Modulation of protein-protein interactions in the p53 pathway

Sonja Srdanovic

Submitted in accordance with the requirements for the degree of

Doctor of Philosophy

The University of Leeds

School of Chemistry

September 2020

Intellectual property and publication statements

The candidate confirms that the work submitted is his/her own and that appropriate credit has been given where reference has been made to the work of others.

Acknowledgment

Firstly, I would like to thank my supervisors, Prof. A. Wilson for the opportunity to work on this engaging project and to Dr. Stuart Warriner for the guidance while writing this thesis. I would also like to thank Prof. C. Ottmann and Dr. Gavin O'Mahony for the warm welcome and the opportunity to carry out secondments in Eindhoven and Gothenburg. I am also grateful for the possibility of joining a TASPPI network and the H2020 Marie Curie Actions for the funding.

The work presented in this thesis would not be possible without assistance of a technical staff at the University of Leeds: Martin Huscroft (HPLC), Dr Iain Manfield (ITC-SPR), Dr Chi Trinh (X-ray), Dr Arnout Kalverda (NMR), Nasir Khan (CD), Astra-Zeneca Gothenburg: Anna Jonson (chiral HPLC). Particular thank you goes to Madita Wolter for your help with crystallography-your magical ability to solve even unsolvable structures, and to Dr Michael Webb for showing me how to express proteins.

Special thank you goes to the Wilson Lab members, past and present, for being excellent coworkers and even greater support system with endless tea breaks when needed the most. Similarly, I would like to thank my TASPPI group, not sure how we immediately clicked as a group after one drink, but I surely looked forward to all the training sessions and conferences with you. Some friendships that started here will last for a lifetime, which I am beyond grateful for.

To my family and friends, thank you for always being here and forcing me to see there is life outside this PhD bubble. And most importantly, to Villi, thank you for all the love and support over the years as this wouldn’t be possible without you.

Abstract

Protein-Protein Interactions (PPIs) are of remarkable significance given their role in the vast majority of cellular processes. The protein p53 is known as “the guardian of the genome” due to its involvement in DNA repair, inhibition of cell proliferation and cell cycle regulation in general. The activation of p53 is triggered by various stress signals, inducing a negative-feedback loop that mediates levels of p53. The structurally similar proteins, *h*DMX and *h*DM2 bind to a transcriptional domain of p53, inhibiting its function in cell cycle repair or apoptosis. p53 is additionally degraded by *h*DM2-mediated ubiquitination, which is amplified by formation of *h*DMX/*h*DM2 heterodimers. Dimeric hub 14-3-3 proteins have a positive feedback effect on p53 activity and prior cellular studies have shown both *h*DMX and *h*DM2 undergo phosphorylation, which is recognized by these phospho-binding 14-3-3 proteins. Stabilizing or inhibiting interactions of *h*DMX and *h*DM2 with 14-3-3 proteins might promote increased or decreased levels of cellular p53 respectively. Firstly, to fully characterize these interactions, a peptide-based approach employing biophysical techniques (including FA, ITC and SPR) was used to determine the binding affinity between *h*DMX/*h*DM2 and 14-3-3 proteins. In addition, X-ray crystallography was used to obtain structural information on the *h*DMX/14-3-3σ and *h*DM2/14-3-3σ interfaces. Finally, small-molecule and fragment screening along with a protein templated fragment ligation approach was used to find novel small-molecules that could modulate this pathway. This work provides better understanding of the role that 14-3-3 proteins and *h*DMX/*h*DM2 play in the p53 pathway, shining light on a novel approach to modulate PPIs in the p53 pathway.

Table of contents

List of figures

List of tables

List of schemes

Abbreviations and symbols

Å	Angstrom
Ac	Acetyl group
Ahx	Aminohexanoic acid linker
AUC	Analytical ultracentrifugation
*t*Bu	Tert-butyl
βME	β-mercaptoethanol
Boc	Tert-butoxycarbonyl
CD	Circular dichroism
CPS	Chemical shift perturbation
DCC	N,N'-Dicyclohexylcarbodiimide
DCM	Dichloromethane
DIPEA	N,N-Diisopropylethylamine
DMF	Dimethylformamide
DMSO	Dimethyl sulfoxide
DNA	Deoxyribonucleic acid
DTT	Dithiothreitol
EC_{50}	Half maximal effective concentration
EDTA	Ethylenediaminetetraacetic acid
ERα	Estrogen Receptor alpha peptide
ExoS	Exoenzyme S
FA	Fluorescence Anisotropy
FAM	(5,6)-carboxyfluorescein
FBDD	Fragment-based drug discovery
FCA	Fusicoccin A
Fmoc	Fluorenylmethoxycarbonyl protecting group
GCP	Guanidinocarbonylpyrrole
h	Hour
HCTU	(2-(6-Chloro-1H-benzotriazole-1-yl)-1,1,3,3-tetramethylaminium hexafluorophosphate)
*h*DM2	Human double minute 2 protein
*h*DMX	Human double minute 4 protein (MDM4)
HBS	HEPES-buffered saline buffer
HRMS	High resolution mass spectrometry

HSQC	Heteronuclear single quantum correlation NMR
HTS	High-throughput screening
IC50	The half maximal inhibitory concentration
IPTG	Isopropyl β-d-1-thiogalactopyranoside
ITC	Isothermal titration calorimetry
Kd	Equilibrium dissociation constant
min	Minute
MeOH	Methanol
kon/koff	Association / Dissociation constant
LB	Lysogeny broth
LC-MS	Liquid chromatography mass spectrometry
mut	Mutated
NMR	Nuclear magnetic resonance
PAGE	Polyacrylamide gel electrophoresis
PDB	Protein Data Bank
PPIs	Protein-protein interactions
PYR	Pyrrolidone1
ppm	Parts per million
QTOF	MS Quadrupole Time-of-Flight Mass Spectrometry
Rus	Response units
SAR	Structure activity relationship
SDS	Sodium dodecyl sulfate
sec	Second
SPPS	Fmoc-solid phase synthesis
SPR	Surface plasmon resonance
STD	Saturation transfer difference NMR
TCEP	Tris(2-carboxyethyl)phosphine
TFA	Trifluoroacetic acid
wt	Wild type

Amino Acid	3 letter abbreviations	1 letter abbreviation
Alanine	Ala	A
Arginine	Arg	R
Asparagine	Asn	N
Aspartic acid	Asp	D
Cysteine	Cys	C
Glycine	Gly	G
Glutamine	Gln	Q
Glutamic acid	Glu	E
Histidine	His	H
Isoleucine	Ile	I
Leucine	Leu	L
Lysine	Lys	K
Methionine	Met	M
Phenylalanine	Phe	F
Proline	Pro	P
Serine	Ser	S
Threonine	Thr	T
Tryptophan	Trp	W
Tyrosine	Tyr	Y
Valine	Val	V
Phosphoserine	pSer	pS
Phosphothreonine	pThr	pT

Chapter 1: Introduction

1.1 Protein-protein interactions

Protein-protein interactions (PPIs) are involved in most biological processes and understanding this complex network of interactions is central to recognizing how their impairment leads to the development of diseases. Many proteins function by interacting selectively with other protein partners in a highly crowded cellular environment. These multiprotein complexes often regulate cellular growth, cell survival and differentiation, and are often deregulated in diseases.[1] Targeting PPIs represents a potentially lucrative strategy in drug discovery, since the human interactome is estimated to include more than 600 000 protein-protein complexes,[2] thus expanding the "druggable genome" drastically. Small-molecule drugs have been exploited extensively against more conventional drug targets bearing well defined ligand-binding sites, such as enzymes, ion channels, or nuclear receptors.[3] In comparison, proteins interact through multiple polar and hydrophobic interactions covering much larger and usually flat surfaces, which creates a difficult task for a small-molecule to recapitulate (Figure 1.1). Over the years, large-molecule drugs or biologics have rapidly emerged on the pharmaceutical market as they could easily overcome these obstacles.[4] Despite the challenges, the field of modulating PPIs by small-molecules has progressed immensely in the recent years, as numerous compounds have reached clinical trials and the first PPI inhibitor, Venetoclax, has been approved.[5]

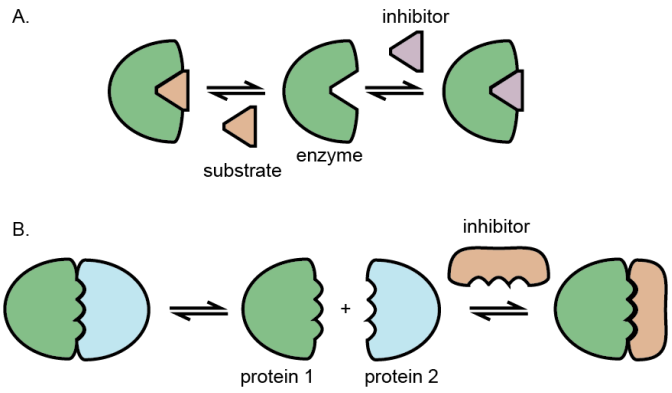

Figure 1.1 Targeting and modulation of enzymes and PPIs. A) Inhibitor displacing a substrate bound to a well-defined pocket on an enzyme. B) Inhibitor binding to a much larger and shallow surface of a protein.

1.2 Modulation of PPIs

Small-molecule modulation of PPIs can be generalized by three different mechanisms: orthosteric inhibition, allosteric regulation, and stabilization (Figure 1.2). Orthosteric inhibition entails direct competition with two partner proteins by a small-molecule that binds at the same pocket as the partner protein, thus completely disrupting the protein-protein complex. This mode of altering PPIs has been exploited the most, as emphasized by several compounds reaching the market including Venclyxto® (**1**), Xiidra® (**2**), Aggrastat® (**3**), with many more currently being tested in clinical trials.[6] Secondly, a small molecule can bind to a protein target at a site that is distant from the binding interface, with two outcomes. In allosteric inhibition, such binding induces conformational and functional changes that prevent the partner protein from forming a complex.[7] Alternatively, small-molecule binding in an allosteric fashion can also enhance the binding of the second partner, as exemplified by the chemotherapy drug Taxol® (**4**).[8] Lastly, an orthosteric or direct stabilization is achieved upon a small molecule binding directly at the binding interface between the proteins, increasing their apparent affinity by acting as "molecular glue" (e.g. Vyndaqel® (**5**)).[9] Although challenging, PPI stabilization has an advantage over PPI inhibition because of its uncompetitive nature and higher selectivity. Assuming formation of the PPI interface is necessary to form a unique pocket for a small molecule to bind to, it is possible to find a specific stabilizer for each PPI interface. Despite the advantages, modulation of PPIs has been recognized mostly in terms of developing small molecule inhibitors. In comparison, examples of PPI stabilization are still rare and rather neglected in the literature.[10]

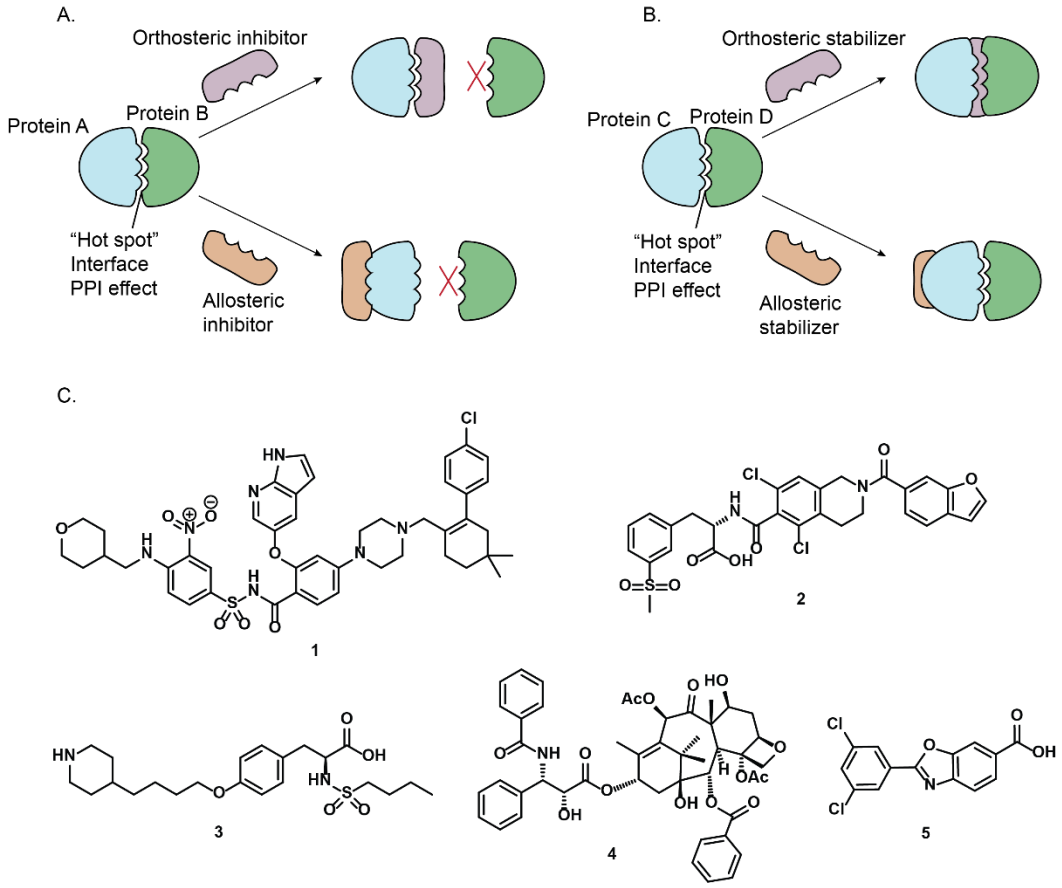

Figure 1.2 Different approaches in altering PPIs. A) Inhibition of PPI achieved by an orthosteric inhibitor directly binding to the same binding site as the partner protein and an allosteric inhibitor causing a conformational change on a protein, thus preventing the PPI. B) Stabilization of PPI by an orthosteric stabilizer acting as a "glue" between partner proteins and an allosteric stabilizer binding to only one partner protein. C) Structures of small molecule PPI modulators in the clinic. Compound **1** is an inhibitor of Bcl-2 protein used to treat various cancers. Compound **2** is an ophthalmic drug that inhibits inflammatory cell binding. Compound **3** inhibits glycoprotein IIb/IIIa receptor which prevents platelet aggregation. Natural product **4** is a stabilizer of microtubule polymers used as a chemotherapy medication. Compound **5** stabilizes transthyretin tetramers whose aggregation subsequently leads to amyloid formation.

1.2.1 Natural products that stabilize PPIs

Natural product PPI stabilizers provide examples of privileged scaffolds for drug discovery or "tool compounds" to probe fundamental biological questions. Natural products have the advantage of recognizing and interacting with biological systems, as they cover a much wider chemical space, and contain a multitude of diverse functional groups and stereogenic centers.[11] Numerous natural products have been shown to stabilize PPIs (Figure 1.3), setting a precedent for small molecule development in this field. Paclitaxel (**4**) is an example of an allosteric stabilizer that is used as a chemotherapy medication. Microtubule polymers consists

of a heterodimer made of α- and β-tubulin that form a cylindrical shape and are of crucial importance to the cell structure. Paclitaxel interferes with (de)polymerization of microtubules by binding to a hydrophobic pocket on β-tubulin resulting in stabilization of the whole structure.[8] Direct stabilization of PPIs is also achieved by natural products such as FK506 (**6**) or Rapamycin (**7**).[12] These structurally different immunosuppressants share highly similar modes of action, stabilizing interactions between FKBP12/protein phosphatase calcineurin and FKBP12/mTOR. In the first step, both FK506 and Rapamycin bind to immunophilin FKBP12. Through the newly formed interface they further bind to calcineurin and mTOR, suppressing other enzymatic activity. Interestingly, without the presence of FK506 or Rapamycin, FKB12 does not interact with calcineurin or mTOR. These few highlighted examples represent different mechanisms in stabilization of PPIs, which offers an alternative perspective for small-molecule drug development.

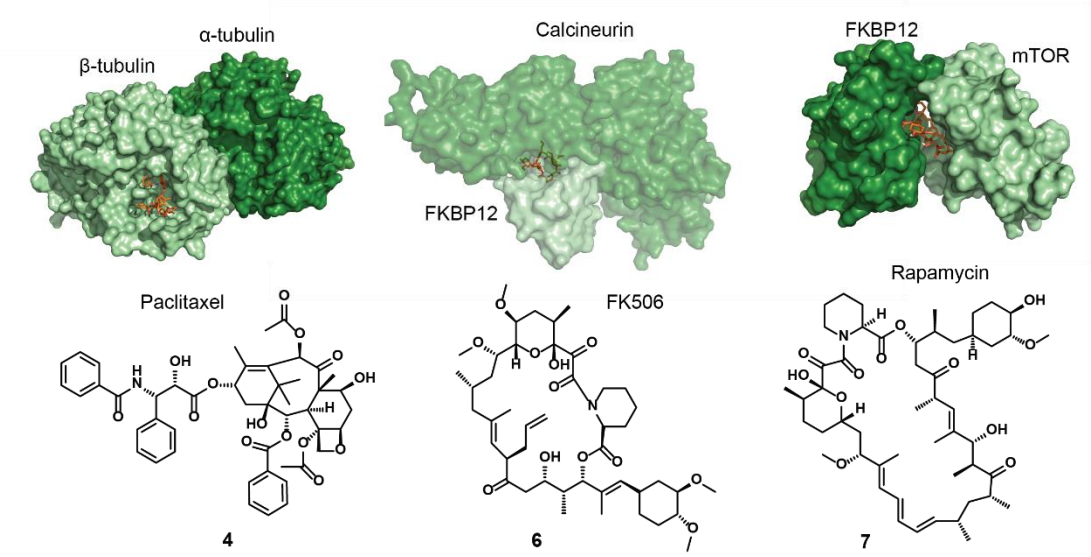

Figure 1.3 Natural products as PPI stabilizers: Paclitaxel, *PDB:1JFF* (**4**), *FK506, PDB:1TCO* (**6**), and Rapamycin, *PDB:1FAP* (**7**)

1.3 Targeting PPIs

Traditionally, small molecule drugs were discovered as enzyme inhibitors or allosteric regulators, and receptor or channel (ant)agonists. They regulate activity of biological targets by mimicking substrates and ligands that bind in a deeply buried and defined binding pockets. These rigid topologies inspired further structure-based design of small molecule drugs to compete with such substrates and ligands, exceeding their affinity towards the target.[13] Since many biological processes are governed by PPIs, developing small molecule drugs with novel modes of action holds

great promise. PPIs are known as more unconventional and challenging drug targets, yet recognition of the key features essential for binding at the protein-protein interface, so called hot-spots, accelerated discovery of small-molecule PPI modulators significantly.[14] Despite protein-protein contact surfaces being relatively large and lacking well defined druggable pockets, it was found that only a cluster of a few residues truly contribute to the overall binding energy. These key residues are known as hot-spots and were initially identified by alanine scanning mutagenesis studies; where the contribution of each residue to the overall binding is determined by its substitution to Ala.[15] However, even when the hot spot residues on the target PPI are known, discovering a small molecule that can access that druggable region while achieving the desirable physiological effect is still challenging. Over the years, different strategies have been employed to identify modulators of PPIs:

Rational design is focused on a distinct class of pharmaceuticals: conformationally constrained peptides, peptidomimetics and mini proteins.[16] This strategy which mimics secondary protein structure motifs has generally been effective in developing PPI inhibitors, as hot spot regions often contain α-helices and β-sheets.[17] More than 60% of published structures in the PDB contain α-mediated interactions, bearing key hot spot residues only on one side of the helix.[18] Here, peptides have the advantage over small molecules in easily matching the key interactions and show superiority in target specificity, but developing peptide therapeutics has its own challenges. The conformation of a short synthetic peptide may differ in solution and upon binding to a target protein, from the conformation it has in the native protein. Conformationally constraining peptides was found to result in increased target affinity and selectivity, proteolytic stability, and cellular uptake.[19] Restricting peptides to their helical bioactive structure can be achieved by introducing a staple that covalently links two amino acid side chains, hydrogen bond surrogates (HBS), or unnatural β-amino acids.[20] Non-peptidic scaffolds can also reproduce the topology of key sidechains without necessarily adopting the α-helical conformation.[21,22] More difficult to develop are β-sheet mimetics because their interactions with the partner protein involves multiple interactions, through the strand itself, side chain recognition or backbone hydrogen bonding. Thus, several “turn- inducing” scaffolds and cyclization strategies have been developed to constrain β-sheet conformation in peptides.[23] Biologically active mini proteins are engineered in the form of antibodies, helical bundles, or β-sheet barrels.[24]

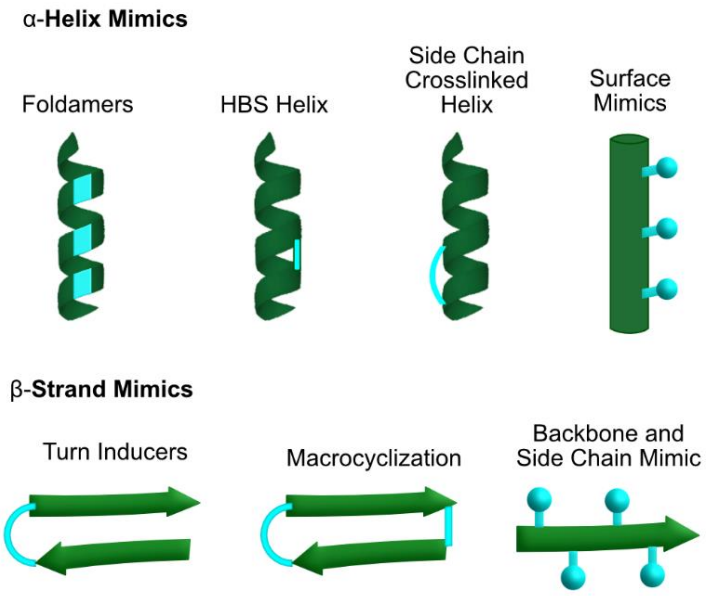

Figure 1.4 Overview of strategies used to mimic secondary protein structure motives. α-helix can be mimicked by using foldamers[25], hydrogen-bond surrogates[26], peptide staples[27] or by surface mimetics[28]. β-strand can be mimicked by turn inducers[29], non-natural backbones[30], or β-peptide macrocycles[31]. Figure adapted with permission from[32]

High-throughput screening (HTS) is a well-recognized discovery approach adopted both by industry and academia. HTS involves for screening compound libraries that contain hundreds of thousands of compounds effectively and at low cost. Success of the screening campaigns relies heavily on high quality and well refined compound libraries, regarding diversity, drug-like properties, low toxicity and target focused compounds.[33] Several initial hits have been identified by this approach, which were then optimized to drug like molecules, such as inhibitors of p53/*h*DM2[34], BCL-2 family of proteins[35], or stabilizers of 14-3-3 hub proteins[36]. The main disadvantage of HTS is a low hit rate, hampered by a high number of false-positives and false-negatives. Biophysical assays such as FRET (Fluorescence Resonance Energy Transfer), ALPHA-screen (Amplified Luminescent Proximity Homogeneous Assay), FA (Fluorescence Anisotropy), or ELISA (Enzyme-linked Immunosorbent Assay) have been optimized for efficient HTS of PPI modulators, but often one partner protein is represented only partially, for example as a peptide. Combined with screening compounds at a single concentration, it can be difficult to replicate the effects of a hit compound in dose-response assays or in vivo studies especially.[37] HTS still remains a go to approach for less well-defined protein-protein complexes or in discovery of allosteric modulators.

Fragment-based drug discovery (FBDD) uses a similar approach to HTS, but screens libraries containing fragments that in comparison have much lower molecular

mass. In principle, screening a lower number of fragments should result in identification of several core motifs binding to the target protein. This is because fragments that inherently have a lower number of heavy atoms will cover greater chemical space than libraries of drug like or natural compounds.[38] Fragments are better at "probing the protein surfaces" and therefore are more likely to bind unbiasedly. Due to their small size and low affinities, usually a combination of more sensitive biophysical techniques (SPR, NMR, X-ray, ITC, or Thermal shift) is required to identify binding and eliminate false-positives. Once a fragment hit has been identified, expanding a fragment into a drug-like compound takes additional effort, typically through fragment-growing or fragment-linking approaches.[39] A selective Bcl-2 inhibitor, Venetoclax, has been developed through linking and optimizing of two fragments identified by protein NMR.[40] The FBDD approach will be discussed in more detail in Chapter 3.

Site-directed ligand discovery or *tethering* approach allows detection of low molecular weight ligands that bind to specific regions of a target protein through disulfide formation.[41] A target protein with a solvent exposed cysteine is incubated and reacts reversibly with a mixture of disulfide-library compounds. Ligands showing intrinsic affinity towards the protein will shift the equilibrium towards protein-ligand formation, thus being detectable by MS. This approach has been applied in discovering novel chemical tools, PPI inhibitors and more recently, stabilizers.[42,43] Site directed ligand discovery approach will be discussed in more detail in Chapter 4.

Computational approaches are frequently used to aid rational drug design and screening campaigns.[44] It is often utilized as an initial cost-reduction step, such as in silico alanine mutation studies or simply filtering large HTS libraries to exclude compounds with undesirable properties. Using the solved structures of protein-protein interfaces, either by X-ray crystallography or NMR, it is possible to identify possible novel binding pockets[45] on the protein complex surfaces or hot spot regions.[46] The limitation of using crystal structures is that they only represent a "snapshot" of a PPI, so often molecular dynamics simulations are performed to gain more accurate representation of protein conformations.[47] Virtual screening is also used as a stand-alone method to predict binding associations between small molecules and a target protein, ranking their affinity by various scoring functions.[48] These predictions have become more accurate as docking algorithms have been developed and customized for challenging PPIs. Another widely used computational approach is pharmacophore modeling, where the key elements for molecular

recognition are classified as pharmacophore fingerprints and used to identify the most similar compounds with the appropriate biological response.[49] Most recently, Artificial Intelligence (AI) has emerged as a useful tool for drug discovery projects, from the initial target validation stage to clinical development.[50]

1.4 The p53 pathway

Transcriptional factor p53 is one of the most studied proteins related to cancer. It was discovered in 1979, but only described as a tumor suppressor a decade later. Since then, more than 50% of cancers were found to have some mutation of p53 and loss of its function was observed in an even greater number of cases.[51] Thus, reactivation of p53's function has been a significant target in developing new cancer treatments.

p53 is often described as "the guardian of the genome" because of its central role in regulating diverse biological processes: DNA repair, cell cycle arrest, apoptosis, and senescence.[52] This is achieved upon p53 binding to DNA and activating downstream gene expression. Functions of the tumor suppressor p53 are negatively regulated by *h*DMX and *h*DM2; structurally and functionally similar proteins, with *h*DM2 bearing an intrinsic E3 ubiquitin ligase activity. Both proteins bind directly to the transactivation domain of p53 and sterically block it. p53 is additionally targeted for nuclear export and proteasomal degradation through *h*DM2 promoted ubiquitination (Figure 1.5b).[53] Although *h*DMX does not induce degradation of p53 directly, E3 ligase activity of *h*DM2 is enhanced through formation of *h*DMX/*h*DM2 heterodimers.[54] Through formation of a heterodimer with *h*DMX, *h*DM2 is additionally prevented from autoubiquitination. This continuous targeting of p53 for degradation keeps the levels of p53 low under normal conditions. It is only under stressed conditions (e.g. DNA damage, hypoxia, oncogene activation and ribosomal stress) that p53 is rapidly activated through multiple post-translational modifications. Most prominent are phosphorylation events on p53 that obstruct *h*DMX(2) binding and acetylation which activates p53 for DNA binding.[55] Subsequently, stabilization and accumulation of p53 upregulates the expression of genes responsible for the cell cycle arrest and/or apoptosis. This balanced autoregulatory loop is of vital importance for regulation of numerous cellular signaling pathways. In-vivo studies have shown that deletion of p53 leads to spontaneous tumor formation, whilst overexpression of

p53 causes toxicity in certain tissues.[56] Knock-out studies of the oncogenes *h*DMX and *h*DM2 manifested lethality in mice studies.[57]

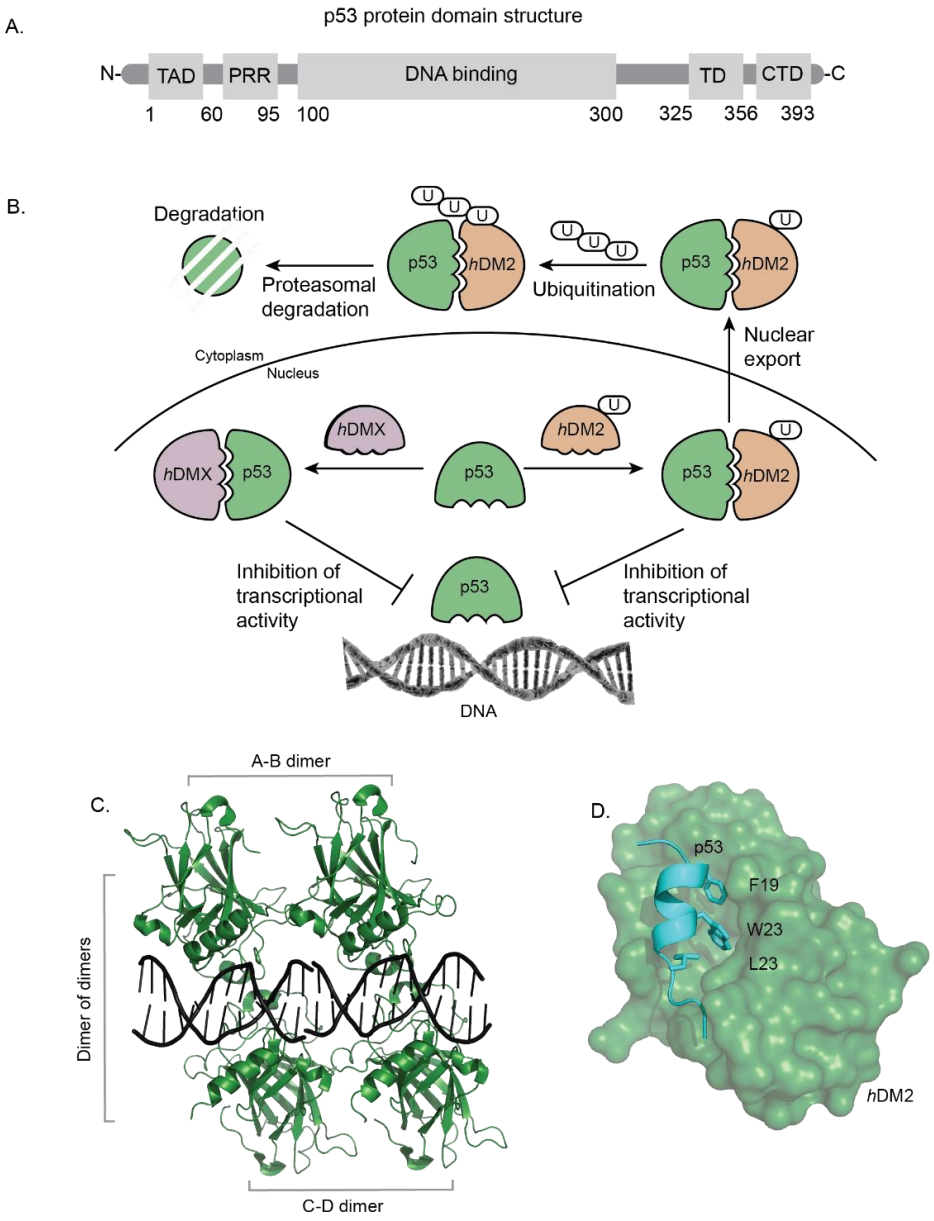

Figure 1.5 A) Domain structure of a tumor suppressor p53: N-terminal transactivation domain (TAD), proline rich region (PRR), structured DNA binding domain (DBD), tetramerization domain (TD), C terminal regulatory domain (CTD). B) Negative feedback-loop of p53 pathway: *h*DMX and *h*DM2 bind p53 and subsequently inhibit its transcriptional activity. *h*DM2 as a ubiquitin ligase additionally tags p53 for degradation. C) Structure of the p53 (dimer of dimers, in green) binding to DNA (black), *PDB: 3EXJ*. D) p53 peptide (cyan) bound to a hydrophobic pocket of *h*DM2 (green), *PDB: 1YCR*.

Structurally, p53 is a homo-tetrameric protein that forms a unique dimer-of-dimers topology. Primary dimers consist of two subunits, each made of a β-strand followed by an α-helix and are stabilized by antiparallel intermolecular β-sheet and helix-packing interactions. The two dimers further pack into a tetrameric

form which is stabilized by protein-protein and base-stacking interactions. Figure 1.5a shows a cartoon representation of distinctive domains on p53: an intrinsically disordered N-terminal transactivation domain (TAD), followed by a proline rich region (PRR), a structured DNA-binding domain (DBD), and a flexible linker connecting tetramerization domain (TD) and the intrinsically disordered C-terminal regulatory domain (CTD).[58]

In a disease state, the ability of p53 to suppress tumors is severely damaged by mutations or its complete inactivation. Mutations mostly occur in the DNA binding domain, preventing correct folding of the tumor suppressor, or removing essential DNA interaction sites, thus affecting the normal transcriptional activity.[59] Secondly, loss of wt-p53 function is observed through overexpression of the *h*DMX and *h*DM2 oncogenes.[60] The first crystal structure of the p53 peptide in complex with *h*DM2 showed the structural motifs necessary for the binding. A hydrophobic pocket of *h*DM2 accommodated the p53 peptide, where three critical amino acids: Phe19, Trp23 and Leu26 were identified as crucial for the molecular recognition by *h*DM2 (Figure 1.5d). Discovery of this druggable pocket has set the precedent for developing small molecule inhibitors of p53/*h*DM2, which could restore active p53 concentrations in a disease situation.[61]

1.4.1 Stabilization of misfolded mutant-p53

Mutated p53 (mut-p53) is overexpressed in tumor cells, partially because of the inability of the p53 to induce expression of the *h*DMX(2) oncogenes. Targeting inactivated tumor suppressor p53 is a noteworthy approach as such high levels of mut-p53 are already present in the cancer cells, readily available to be activated for tumor suppression.[62] Inducing apoptosis in cells expressing mut-p53 can be achieved if the tumor suppressor activity is reactivated by restoring sequence-specific DNA binding and wt-conformation to mut-p53 or by inducing expression of *h*DM2 targets. Such an approach has been exemplified with small-molecules PRIMA[63] (**8**) and COTI-2[64](**9**). PRIMA was shown to restore wt-structure of misfolded p53 through a thiol alkylation mechanism, covalently modifying p53 *in vivo*. The exact mechanism of action for COTI-2 is largely unknown, however it was suggested it could act as a zinc chaperone but also to affect other targets that are independent of p53. These two most prominent small molecules targeting mut-p53 have now entered the later stages of clinical trials. Although wt-p53 has a vital role for many cellular processes, inadvertent activation has harmful consequences on normal cells. Thus, expression

of p53 is kept at low levels with a relatively short half-life under physiological conditions. Cancer related mutations have diverse effects on structure and function of p53, mostly through further decrease of thermodynamic and kinetic properties of the already unstable protein. Several hot spot mutations on the DNA binding domain (DBD), such as R273H and R248Q (Arg to His/Glu substitution, residues directly responsible for interacting with DNA) or R175H and R249S (Arg mutations to His/Ser that alter the folding and structure of p53) have been targeted for therapeutic interventions, particularly in cancers where wt-p53 is not being expressed.[65]

Although mutations on p53 generally occur in DBD, the most frequent p53 germline mutation currently known to predispose to multiple cancers, R337H, is located in the tetramerization domain.[66] This inherited mutation destabilizes the tetrameric structure of p53 by disrupting the ion-paired bridge R337–D352. Multivalent calix[4]arene ligands have been found to stabilize the p53 tetrameric structure under physiological conditions.[67] In particular, tetraguanidiniomethyl-calix[4]arene (**10**) has been found through molecular docking and biophysical characterization to bind at the opposite ends of a p53 tetramer, with guanidinium groups interacting with E336 and E339, and the calixarene scaffold buried in the hydrophobic pocket of the protein (Figure 1.6). Similar calixarene derivatives with the same mode of action restored transcriptional activity of p53 in *in-vivo* studies.[68]

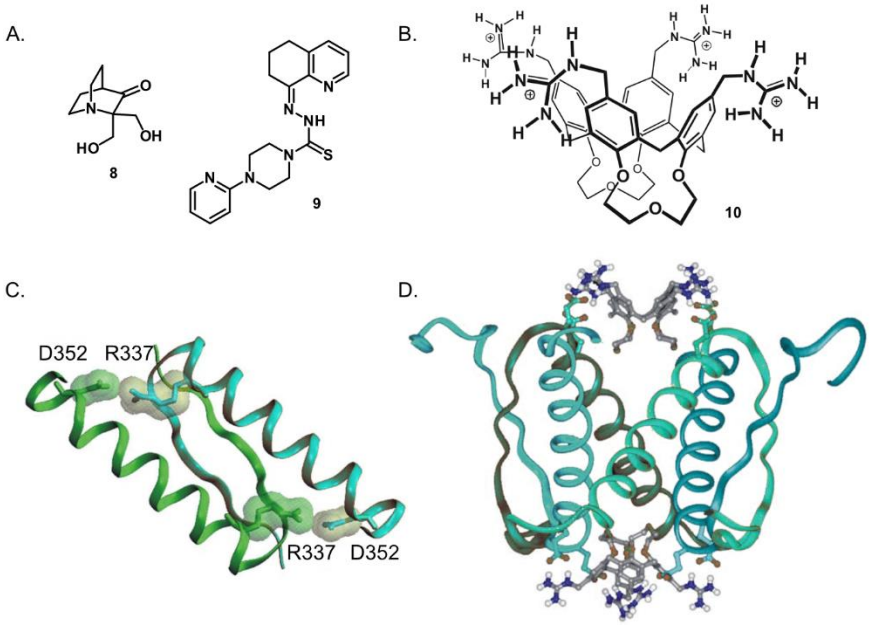

Figure 1.6 A) Structures of small molecules PRIMA (**8**) and COTI-2 (**9**). B) Stabilization of R337H mutant p53 by calixarene scaffolds. Structure of calixarene derivative **10**. C) p53 tetramerization domain is destabilized when the R337–D352 interaction is disrupted by R337H mutation, *PDB: 1AIE*. D) Tetramerization domain is stabilized by two calixerine scaffolds on opposite ends. Figure adapted from.[67]

1.4.2 Modulators of p53 / *h*DMX(2)

Inhibition of the PPI between *h*DM2 and *h*DMX with p53 is an interesting therapeutic approach in cancers where the overexpression of these oncogenes abolishes wt-p53 function. Nutlins were the first potent and selective small molecule inhibitors of the p53/*h*DM2 interaction discovered by Vassilev and colleagues.[69] These cis-imidazoline analogues with in vitro activity, showed a nanomolar affinity displacing p53 by binding to the same hydrophobic pocket on *h*DM2. The crystal structure of Nutlin 3a (**11**) bound to *h*DM2 revealed three aromatic substituents on the imidazole scaffold mimicked the key residues from p53 (F19, W23, L26), which subsequently guided the rational design of the next generation inhibitors.[70] The first Nutlin analogue to reach the clinical trials was Roche compound RG7112 (**12**), but it was discontinued in phase I due to significant toxicities that were observed with the dose increase to attain satisfactory levels of p53.[71] Currently in phase III trials is the most recent Nutlin derivative, the pyrrolidine-based compound Idasanutlin (**13**) with improved affinity and pharmacokinetic properties.[72] AMG-232 (**14**) is the most potent *h*DM2 inhibitor in clinical trials at present, exhibiting picomolar affinity.[73] This novel piperidinone inhibitor from Amgen was further optimized to an improved compound AM-7209 (**15**) (Figure 1.7a).[40] Other *h*DM2 small-molecule antagonists include spiro-oxindoles, morpholinones, benzodiazepinediones, dihydroisoquinolinone and many others, as reviewed by Holak.[74] These classes of compounds prevent *h*DM2 from engaging with p53 through steric hindrance, which subsequently results in the stabilization of 53 and activation of its downstream targets. Structures of example p53/*h*DM2 inhibitors are shown in Figure 1.7a.

Many of the inhibitors designed for *h*DM2 are weak binders for *h*DMX and of limited value in cancers that overexpress *h*DMX, such as melanoma or breast cancers.[75] This is because the p53 binding pocket on *h*DM2 and *h*DMX has the overall hydrophobicity nature of the pocket conserved, but several residues and their conformation differ significantly, especially around the L26 subpocket. The first small molecule found to target *h*DMX was SJ-172550 (**16**), another imidazole compound whose effect on p53 activation was amplified when combined with *h*DM2 inhibitor Nutlin 3a.[76] A benzofuroxan XI-006 (**17**) and psudourea XI-011 (**18**) derivatives were discovered in reporter-based assays as lead compounds that induce p53-independent apoptosis through *h*DMX inhibition and are still in a preclinical stage.[77] The latest compound discovered to target *h*DMX exclusively is CTX1 (**19**), identified in a cell-based screen as a promising lead anti-cancer agent.[78] Figure 1.7b shows structures of p53/*h*DMX inhibitors. Subsequent efforts have been made in

developing the next generation of drugs - dual inhibitors of *h*DMX and *h*DM2 (Figure 17c).[79] Since most of the small-molecule inhibitors were developed to target *h*DM2, they are routinely tested for *h*DMX activity as well. Such an example is compound (**20**), a pyrrolidone derivative discovered as a dual inhibitor through virtual screening.[80] Since the structures of many inhibitors have been elucidated in complex with the proteins, this ample amount of novel crystal structures enabled the design of novel inhibitors through virtual screening and rational design. Many of these published dual inhibitors had modest affinities for *h*DMX and *h*DM2, usually in the lower micromolar range. However, in the past few years, several new patents have emerged from Adamed, St. Jude Children's Research Hospital or Hoffman-La Roche, describing non-peptidomimetic dual *h*DMX(2) inhibitors: 3-pyrrolin-2-on (**21**) and cis-imidazole (**22**, **23**) derivatives, exhibiting much higher affinities.[74]

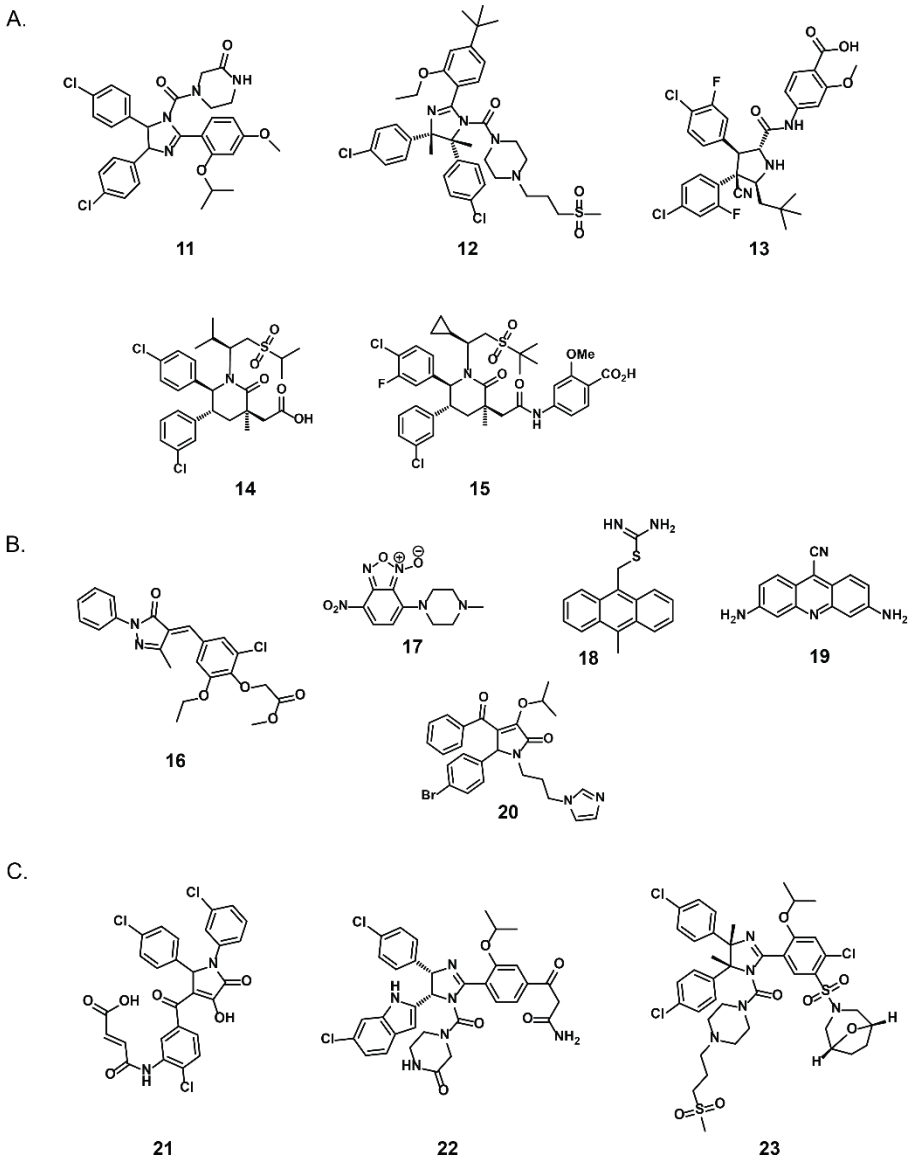

Figure 1.7 Small-molecule modulators of p53/*h*DMX(2) interactions. A) *h*DM2 inhibitors. B) *h*DMX inhibitors C) small-molecule dual *h*DMX(2) inhibitors.

Beside small-molecules, peptide and peptidomimetic approaches have been applied in searching for p53/*h*DMX(2) inhibitors (hereafter abbreviation *h*DMX(2) is used to imply both oncogenes: *h*DMX and *h*DM2).[81] Firstly, p53-derived peptides were used as inhibitors, but many efforts have been made in developing different peptide constraints or incorporation of unnatural amino acids to improve stability, cell penetration and target affinity. SAH-P53-8 peptide was initially developed as an *h*DM2 inhibitor but did not exhibit high potency due to limitations in cell permeability as a result of the overall negative charge of the peptide at the physiological pH.[82] The improved peptide had a hydrocarbon staple introduced and exhibited 25 times higher affinity for *h*DMX than *h*DM2.[83] More peptides have been developed as dual inhibitors than small molecules, due to the advantageous abilities of peptides to make multiple contact points with the two targets that have dissimilarities in the p53 binding domain (such as ATSP-7041, as shown in Figure 1.8a). Several dual *h*DMX(2) peptide inhibitors, their sequences and affinities, have been summarized in Figure 1.8b.[84,85,86,87] Because of the intrinsic instability peptides have as therapeutics, only one dual peptidic inhibitor of *h*DMX(2) has reached clinical trials. The cell penetrating ALN-6924 peptide, developed by Aileron therapeutics, is derived from the transcriptional p53 domain and optimized as a stapled helical peptide currently in phase II.[88]

A.

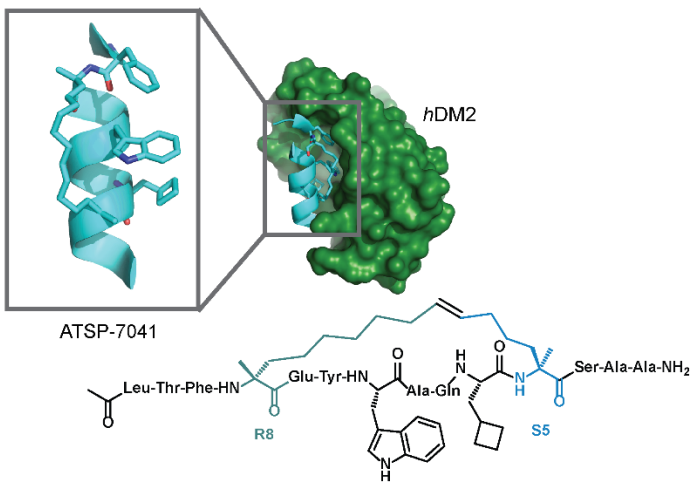

B.

	PEPTIDE	SEQUENCE	*h*DM2	*h*DMX
1	WT-p53	Ac-LSQETFSDLWKLLPEN-NH_2	410.0	646.0
2	SAH-P53-8	Ac-QSQQTFR$_8$NLWRLLS$_5$QN-NH_2	50.2	14.0
3	PDI	Ac-LTFEHYWAQLTS-NH_2	3.3	8.9
4	ATSP-7041	Ac-LTFR$_8$QYWAQZ$_5$SSAA-NH_2	0.9	2.3
5	SMTIDE-02	Ac-TSFR$_8$EYWALLS$_5$-NH_2	34.3	45.7
6	SMTIDE-02A	Ac-TSF$_8$REY(L-6-Cl)WALLS$_5$-NH_2	6.8	1360.0

Figure 1.8 Peptidic modulators of p53/*h*DMX(2) interactions. A) ATSP-7041 peptide (*PDB: 4N5T*). B) peptide sequences of the *h*DMX(2) inhibitors and their K_d affinities in nM

1.4.3 *h*DMX / *h*DMX(2) stabilization

Indolyl hydantoin compounds, RO-2443 (**24**) and RO-5963 (**25**), were discovered by Graves and colleagues as dual antagonists of *h*DMX and *h*DM2, but with a distinct mode of action.[89] Typical p53/*h*DMX(2) inhibitors bind to the oncogenes by mimicking p53 key residues and sterically blocking the interaction. Here, the two small-molecules were found to dimerize the N-terminal p53-binding domains of *h*DMX(2) and activate wt-p53 in cells overexpressing *h*DMX indirectly. The first compound, RO-2443, was discovered through HTS with nanomolar inhibitory potency for both oncogenes. Structural analysis showed two molecules of RO-2443 stacked together stabilizing a pair of *h*DMX dimers (Figure 1.9a). Two inhibitor compounds are initially stabilized through aromatic stacking between the indolyl-hydantoin groups and Y66 from the *h*DMX monomer. Dimerization of *h*DMX is achieved by the indolyl moiety of RO-2443 making contacts with the Phe pocket of one *h*DMX monomer and di-fluoro-phenyl group binding the Trp pocket of the other *h*DMX monomer (Figure 1.9b). Evaluation of the cellular activity with the RO-2443 compound was initially restricted due to solubility issues. However, further optimization led to discovery of an analogue with improved activity and solubility, RO-5963, that showed stabilization and activation of p53 in cancer cells. Inhibitory activity (IC50) of RO-5963 in-vitro was found to be 17 nM for *h*DM2 and 24 nM *h*DMX. In comparison to Nutlin-3, which has similar inhibitory activity towards *h*DM2, RO-5963 was found to be an almost 400 times more potent inhibitor for *h*DMX. Based on this finding, novel dual inhibitors have recently been found through virtual screening and pharmacophore modeling.[48]

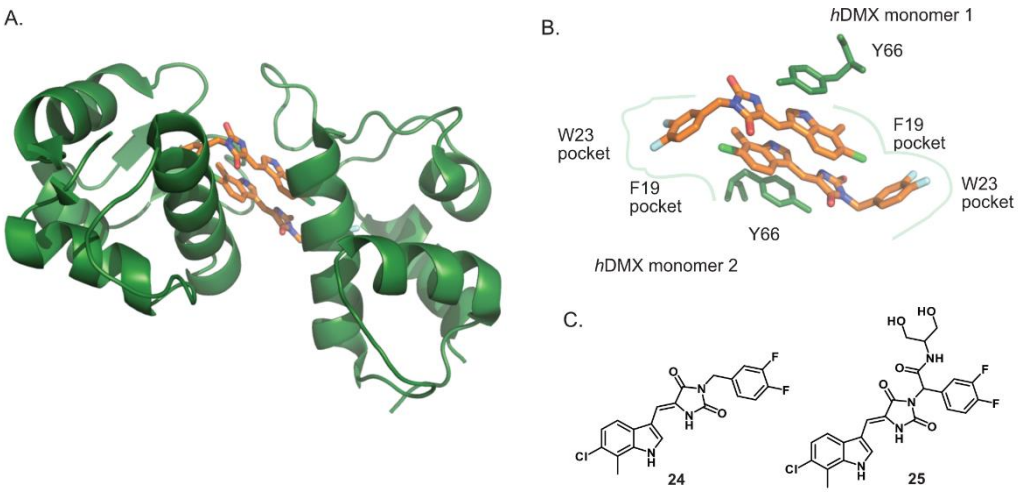

Figure 1.9 Stabilization of *h*DMX(2). A) Crystal structure of small molecule RO-2443 (orange) stabilizing two *h*DMX monomers (green), *PDB: 3U15*. B) Indolyl moiety of RO-2443 binds into the Phe pocket of one *h*DMX monomer and di-fluoro-phenyl group binding the Trp pocket of the other *h*DMX monomer. C) Structures of dual inhibitors.

1.4.4 Motivation to target p53 pathway

Through years of research regarding the transcriptional factor p53, fundamental insights into the safeguarding role that p53 has against cancer have been gained. Detailed structural and functional characterization of p53, along with the network of genes involved in the autoregulatory loops of p53 were elucidated in the mid-1990s. It paved the way for the discovery of nutlins, which then aided the design of novel compounds with greater affinity for *h*DM2 and *h*DMX. Since then many of the small molecule compounds and peptide therapeutics have translated into the clinic. Despite the wealth of knowledge available around targeting p53 in cancer, there are still many questions left unanswered. Drugs rescuing wt-p53 by inhibiting protein-protein interactions with *h*DMX(2) have become a go to approach in modulating an oversimplified regulatory p53 loop. The approach of inhibiting negative regulators has raised concerns since both *h*DMX and *h*DM2 have p53-independent functions in the cell[90–92], but the major concern relating to this treatment is unexpected toxicity for normal cells. These limitations of wt-p53-reactivating compounds are currently being challenged through cyclotherapy with drugs aimed for selective protection of normal tissues.[93] It has become clear that activation of wt-p53 with *h*DMX(2) inhibitors as a monotherapy approach is not sufficient, but to improve the efficiency of drugs in clinic a drug combination therapy is being explored.[94] Another common problem is the ability of cancer cells to evolve and develop resistance in response to *h*DMX(2) inhibitor treatment, thus weakening the therapeutic effect.[95] During the early stage of drug development, identified lead compounds from in-vivo assays often lack desirable physicochemical properties or exhibit general toxicity. Cellular assays may overcome these issues but then determining the mode of action of hit compounds afterwards remains challenging. Detailed molecular mechanisms of the p53 network of proteins are still unclear, especially the role 14-3-3 proteins play in this pathway. Modulation of other proteins involved in the complex p53 network could be explored as a potentially novel approach in restoring the transcriptional function of p53.

1.5 14-3-3 proteins

In recent years, the 14-3-3 family of proteins have arisen as prospective drug targets due to their remarkable network of interacting proteins through which they control diverse physiological functions. 14-3-3 proteins are eukaryotic adapter

proteins mediating multiple biological processes, as they are involved in signal transduction, protein trafficking, apoptosis, and cell-cycle regulation.[96] Moore & Perez first identified 14-3-3 proteins in 1967 during a systematic classification of brain proteins. The name 14-3-3 was given as a combination of protein elution numbers from column fractionation (14) and their electrophoretic mobility (3-3) and were described as small acidic proteins with molecular mass between 27 and 32 kDa, not having a catalytic domain or a specific function.[97] As ubiquitous adapter ("hub") proteins they can bind and change the functions, enzymatic activity, or subcellular localization of their targets. Due to their involvement in multiple signaling pathways, 14-3-3 proteins play an important role in neurodegenerative diseases, cancer, cystic fibrosis, etc.[98,99] The 14-3-3 family of proteins consist of seven isoforms in humans: β, γ, ε, η, ζ, σ and τ/θ, all of which share a high degree of sequence conservation (Figure 1.10*).* Even though sequence conservation between the isoforms usually indicates the redundancy in protein function, this is not the case for 14-3-3 proteins as different affinities towards a target protein are clear between the isoforms. 14-3-3 proteins exist as homo- or heterodimers where each monomer consists of nine α-helices forming an amphipathic binding groove (Figure 1.11a). Four α-helices are directly responsible for dimer formation, while the rest of the α-helices form the "W" shape of the protein dimer. The N-terminal domain of 14-3-3 proteins modulates homo/heterodimerization while the C-terminal domain binds partner proteins.[100]

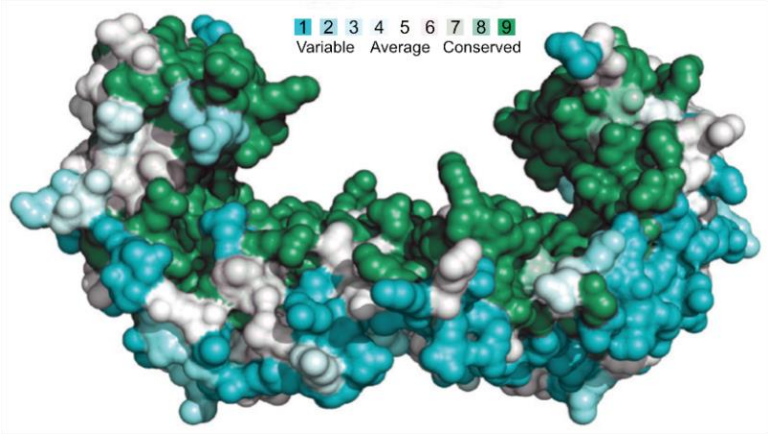

Figure 1.10 14-3-3 proteins share a high degree of conserved amino acids between 7 isoforms. Heat map (1-9) indicates which residues are unchanged across all seven isoforms of 14-3-3, 9 being the most conserved residues in the amphipathic groove of 14-3-3 proteins. Figure adapted from[101]

Activity and modulation of many cellular pathways by 14-3-3 is controlled by phosphorylation events. The W-shaped conformation of a 14-3-3 dimer provides a

groove for phosphorylated partner proteins to bind. One dimer usually accommodates two phosphorylated sites from one target, but there are examples of two different targets simultaneously binding to one dimer of 14-3-3 proteins as well.[102,103] Target proteins are recognized by 14-3-3 through well-defined sequences that can be generalized by three binding modules: I.) RXX-pS/pT-XP, II.) RX(Y/F)X-pS/pT-XP, III.) XX-pS/pT-X-COOH (X-being any amino acid).[104] In mode I and II, proline is always located at position +2 in relation to the central pSer/pThr and arginine is at position -3 in mode I. Mode III represents C-terminal sequences where pSer/pThr are the penultimate amino acid of the partner protein. Phosphorylated Ser/Thr from partner proteins generally bind directly between K49 and R56 in helix α3, and R127 and Y128 in helix α5 as they form a basic binding pocket in otherwise acidic surroundings (Figure 1.10b).

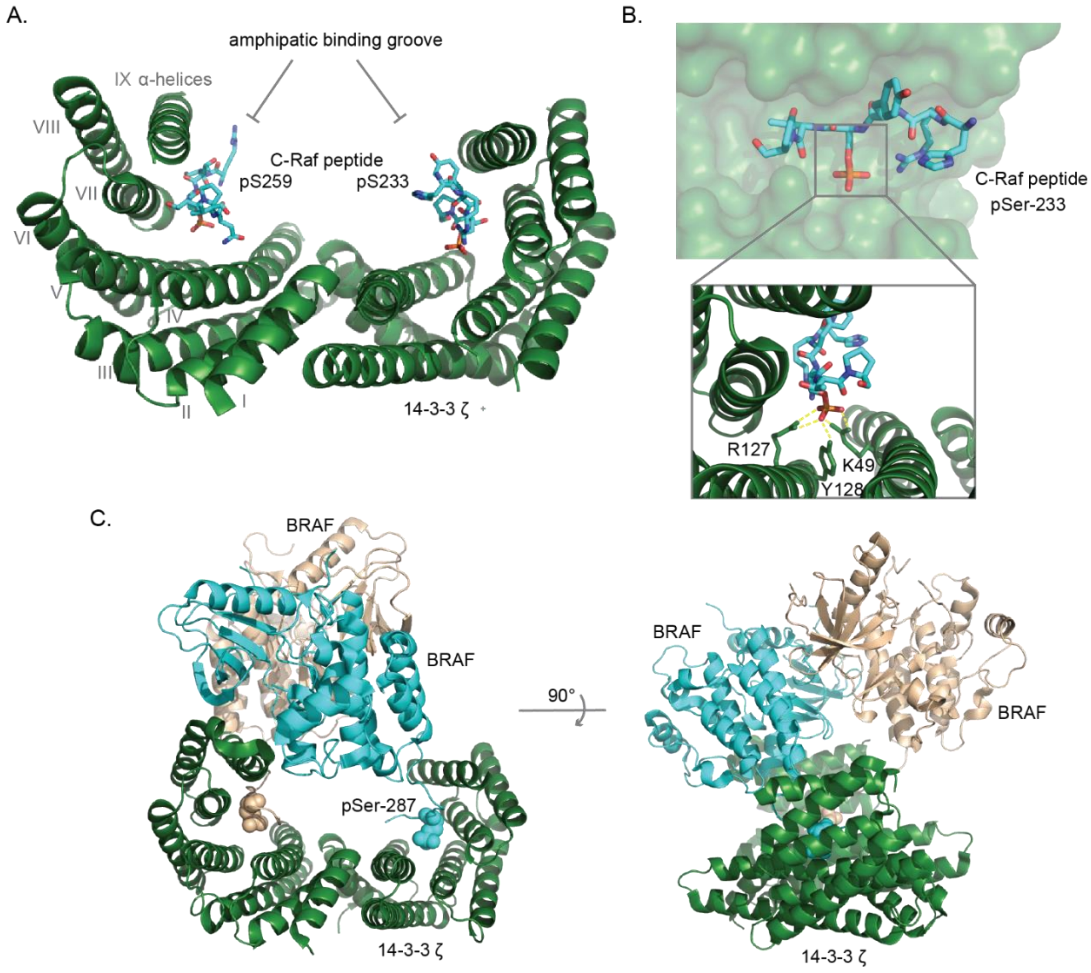

Figure 1.11 An example of 14-3-3 binding targets with Raf kinase interfaces. A) Synergistic binding of the phosphorylated C-RAF peptide with two phosphorylation sites: S233 and S259 (in cyan) to one 14-3-3ζ dimer (green). An example of Mode I. binding peptide. *PDB: 4FJ3.* B) A closer look of C-Raf peptide with pSer-233 binding in a 14-3-3 amphipatic groove, making polar contacts with the key residues from 14-3-3ζ. C) Crystal structure of full length BRAF protein (monomers in cyan and orange) in complex with 14-3-3ζ (green), *PDB: 6U2H.*

Since 14-3-3 proteins act entirely as adaptor proteins all modulators developed for this family of protein should in fact target a specific complex of 14-3-3 with a target protein. 14-3-3 are a ubiquitous class of proteins present in almost every cell and implicated in numerous human diseases. Thus, regulating signaling pathways through inhibition or stabilization of a PPI with 14-3-3 offers a different approach to developing novel therapeutics.

1.5.1 Inhibitors of 14-3-3 proteins

The first 14-3-3 inhibitor was identified from a phage display library, an R18 peptide reported by Fu and colleagues.[105] This 20 amino-acid long peptide (PHCVPRDLS^{1}WLDLE^{5}ANMCLP) exhibited a central unphosphorylated sequence that was bound to a conserved ligand binding site of 14-3-3ζ, blocking the interaction with Raf-1 kinase. As an example of an unconventional 14-3-3 binding mode, the E5 of the peptide R18 appeared to be placed in a crystal structure where the phosphorylated residue is usually located (Figure 1.12a). This interaction was stabilized through a salt bridge between glutamic acid E5 of the peptide and R56 and R60 from helix 3 and R127 from helix 5 on 14-3-3ζ, along with hydrophobic contacts between L172 and L220 on the peptide with multiple hydrophobic residues on 14-3-3ζ. Later, a dimeric version of the R18 peptide was branded as the general 14-3-3 protein antagonist Difopein® with the ability to induce apoptosis when expressed in various cancer cells.[106] A macrocyclic peptide inhibitor was developed recently by the groups of Ottmann and Grossmann, through a ring-closing alkyne metathesis reaction on a previously reported virulence factor ExoS peptide sequence (^{420}QGLLDALDLAS^{430}) known to bind 14-3-3 proteins (Figure 1.12b).[107] The reduction in conformational flexibility of the macrocyclic molecule resulted in 20x increase in affinity for 14-3-3ζ with the inhibitory effect of ExoS being observed in vivo. This study provided evidence for developing 14-3-3 inhibitors through a rational design approach, employing macrocyclic strategies to constrain bioactive peptides having an irregular secondary structure. Another therapeutic area where 14-3-3 proteins could be established as a drug target is in Alzheimer's disease. Dysregulation of Tau protein function to bind and stabilize microtubules results in its aggregation and formation of tangles. 14-3-3 proteins directly contribute to this neurofibrillary tangle formation by interacting with the hyperphosphorylated Tau, especially through pS214 and pS324 phosphorylation sites. Inhibitory Tau peptides have been designed by Milroy, Ottmann, and Landrieu groups in a joint study, by

modifying the C-terminus of the peptide with different benzhydryl pyrrolidine moieties (Figure 1.12c).[108] All novel Tau peptide analogues were found to be 14-3-3/Tau inhibitors and presented a starting point for developing novel nonphosphorylated inhibitors for this system.

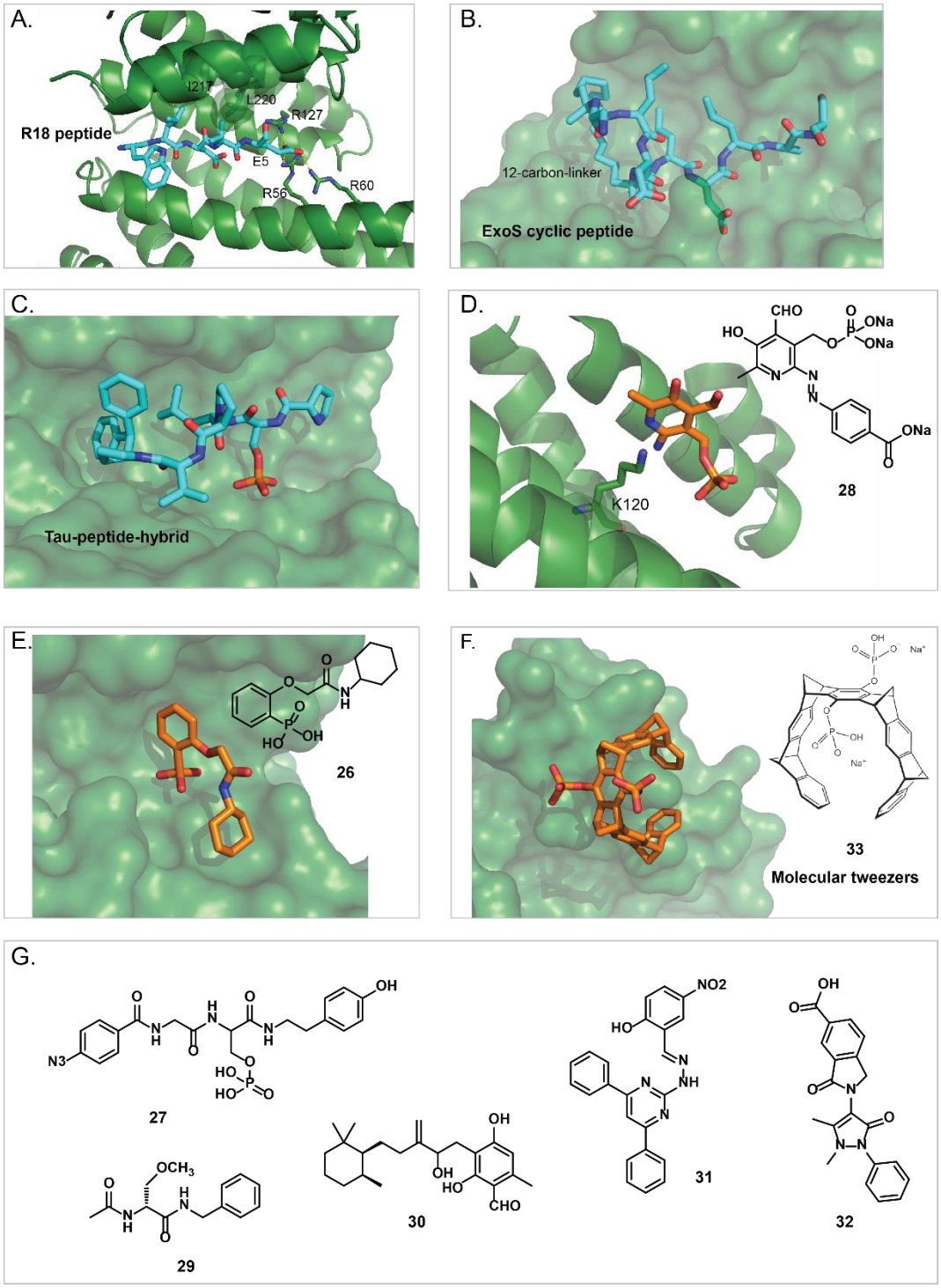

Figure 1.12 Inhibitors of 14-3-3 proteins. Peptides represented in cyan, small-molecules in orange and 14-3-3 proteins in green A) Peptide R18, ^{1}WLDLE^{5}, *PDB: 1A38*. b) Modified Exo-S peptide, PDB: 4N84.C) Tau-peptide hybrid, PDB: 6FI4. D) Small molecule FOBISIN101, *PDB: 3RDH*. E) Small molecule B2, *PDB: 4DHT*. F) Molecular tweezers, *PDB: 5OEG*. G.) Structures of some 14-3-3 protein small-molecule inhibitors

Small molecule non-peptidic inhibitors of 14-3-3 proteins (as shown in Figure 1.12g) usually mimic phosphorylated serine and bind in the basic arginine pocket of 14-3-3 proteins, as is the case of FOBISIN analogues, B2 (**26**) or 2–5 compounds (**27**), reviewed by Stevers *et al*.[109] As an example, FOBISIN101 (**28**) was the first covalent inhibitor of 14-3-3 reported by the Fu group.[110] This pyridoxal-phosphate derivative was discovered from the LOPAC screening library as an inhibitor of the 14-3-3γ/pS259-Raf-1 peptide interaction but was later found to inhibit both phosphorylated as well as unphosphorylated targets. The crystal structure revealed only the pyridoxal-phosphate moiety of the compound covalently linked to a K120 on the 14-3-3ζ protein. This seemed to be a crystallographic artifact, a consequence of exposure to the synchrotron radiation which then caused the N = N diazene bond to cleave and release the paraaminobenzoic acid moiety into solvent (Figure 1.12d).

Small molecules inhibitors which do not mimic phosphorylated serine include Lacosamide (**29**), UTKO1 (**30**) and BV02 (**31**) compounds (Figure 1.12g). These are discussed in more depth in a review article by Stevers *et al*.[109] The group of Botta reported a series of inhibitors targeting the 14-3-3σ/c-Abl interaction in the treatment of chronic myeloid leukemia (CML). The most recent inhibitor **32** has been developed by Iralde-Lorente and colleagues as a next generation inhibitor from a parent compound BV02 (**31**).[111] In comparison, compound 34 exhibited superior chemical stability at physiological conditions and was found to enhance the nuclear translocation of c-Abln in cells. To date, only one 14-3-3 inhibitor binding outside of the amphipathic binding groove was published by Bier *et al.*[112] A supramolecular ligand with molecular tweezer geometry (**33**) was found to bind around the surface exposed residue K214, at the edge of the amphipathic groove and consequently inhibit interactions of 14-3-3 proteins with C-Raf and ExoS peptides (Figure 1.12f).

1.5.2 Stabilizers of 14-3-3 proteins

Natural products Fusicoccanes (FCA) are the most studied “tool compounds” in the field of stabilizing PPIs with 14-3-3 proteins. FCA was isolated as a metabolite from the phytopathogenic fungus *Phomopsis amygdali* in the mid-1960s and described as a wilt-inducing toxin. FCA still has a huge role as a plant toxin today, but its repurpose for drug discovery use began in the mid-1990s and it has been growing ever since.[113] The landmark was the first crystal structure of FCA (**34**) in a ternary complex with a tobacco 14-3-3c (c denotes a 14-3-3 isoform in plants) and the plasma membrane H^+-ATPase (PMA).[114,115] PMA is a proton pump that controls

the nutrient uptake and turgor pressure within a cell. 14-3-3c protein binds the C-terminal domain of PMA (QSYpTV-COOH) upon which the proton pump activates. FCA binds at the rim of the interface between 14-3-3c and PMA, acting as a "molecular glue" (Figure 1.13a). Since FCA increases the affinity between the two proteins 90-fold, it permanently activates the proton pump which has a detrimental effect on plant (de)hydration. FCAs belong to a family of diterpene glycosides sharing a 5-8-5 ring structure. In the crystal structure, the glycoside moiety was solvent exposed making polar contacts with N49 and D222, while the diterpene moiety was buried deeper in the pocket making polar contacts with K129 and D222, and multiple hydrophobic interactions with the protein. The PMA peptide makes additional contacts through the C-terminal valine to the core ring structure of FCA, creating an additional hydrophobic pocket for the PMA peptide (Figure 1.13b). However, the FCA molecule does not exhibit great selectivity as it was found to stabilize multiple targets with 14-3-3: ERα[116], TASK3[117], C-Raf[118], p53[119], etc. Because 14-3-3 proteins regulate so many biological processes, designing novel bioactive compounds around a FCA scaffold would enable development of more selective therapeutic agents. Some of the semi-synthetic FCA analogues developed over the years include: Fusicoccin-THF (**35**) and Fusicoccin-NAc (**36**), Fusicoccin-H (**37**), Fusicoccin-J (**38**), as shown on Figure 1.13c.[117,120] The latest FCA derivative was discovered by Andrei *et al* who used molecular dynamics and rational design approach to develop the FC-NAc molecule (**36**), a selective stabilizer for 14-3-3σ and the TASK peptide.[120] Improved potency and increased anti-tumor activity of the novel analogue was achieved by exchanging the 19-acetoxy group of FCA for an acetamide, a hydrogen-bond donor that interacts with D215 on the 14-3-3σ. Cotylenin A (CN-A, **39**) is another fungal metabolite isolated from the *Cladosporium* fungus, structurally very similar to FCA and believed to target the same 14-3-3/PMA complex in plants. Anticancer activity of CN-A has been observed in human acute myeloid leukemia cells, or in combination with other drugs in breast and lung cancer.[121] The metabolite adenosine monophosphate (AMP, **40**) was recently discovered by the group of Uyeda to stabilize 14-3-3β and the carbohydrate-response element-binding protein.[122] It is a glucose-responsive transcription factor that enables conversion of excess carbohydrates into fat storage, and its subcellular localization in response to glucose levels is controlled through interacting with 14-3-3 proteins. Interestingly, this interaction is mediated through a non-phosphorylated mechanism. The N-terminal region of ChREBP binds in a central groove of 14-3-3, but the phosphate group of the small molecule AMP is located where the phosphorylated serine or threonine of the target protein is normally positioned.

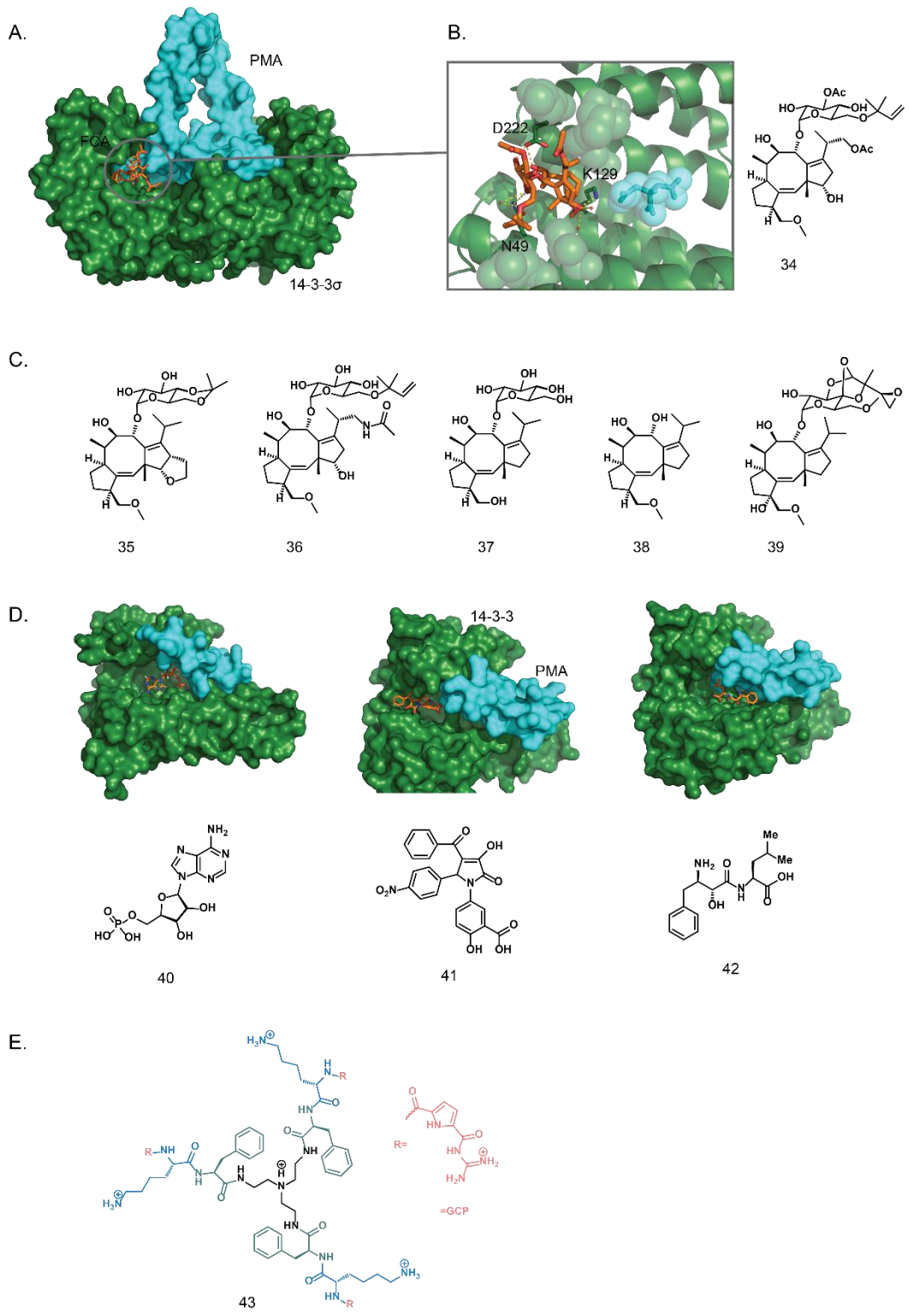

Figure 1.13 Stabilizers of 14-3-3. A) Ternary complex of 14-3-3σ/PMA/FCA.14-3-3 in green, PMA in cyan and FCA in orange, *PDB: 2O98*. B) Stabilization effect of FCA on 14-3-3/PMA peptide, *PDB: 1O9E*. C) Similar structure among FCA analogues. D) Small molecules PYR1 (*PDB: 3M51*), epibastine (*PDB: 3M50*) and AMP (*PDB: 5F74*). E) Supramolecular stabilizer of 14-3-3 proteins

The family of FCs have highly complex scaffolds that are challenging to optimize for achieving selectivity and higher affinity among partner proteins. Current production of the FCs is by isolation from natural sources as only a lengthy

semi-synthetic route of FCA has been published so far. In order to find small molecules that could possibly replace the complex natural products by binding to a well-defined FCA pocket on the 14-3-3/PMA interface, a first high-throughput screening was carried out by Rose et al.[36] Two compounds with a distinctive binding mode were identified, a pyrrolidone1 (PYR1, **41**) and dipeptide epibastin (**42**). The trisubstituted PYR1 compound occupies a pocket that significantly overlaps with the FCA pocket, while epibastin was buried much deeper between in the 14-3-3ζ and PMA interface (Figure 1.12c). Compound **41** will be discussed further in Chapter 3.

Last year, the group of Schmuck and Ottomann published several papers on the topic of using supramolecular stabilizers with 14-3-3 proteins, specifically on molecules containing the guanidinocarbonylpyrrole (GCP) moiety stabilizing interactions with ERα, Tau and C-Raf peptides.[123] As a proof of concept, in-house developed multivalent arginine mimetics were used because of their ability to generate very stable ion pairs with phosphates. Selected compound **43** contains 3 symmetric peptidic arms, each bearing an arginine mimetic GCP-structure. It was found to increase the binding affinity between 14-3-3ζ and ERα 100-fold, but when combined with FCA, the effect doubled. This suggested a quaternary complex formation with compound **43** binding outside the FCA binding pocket on the 14-3-3ζ / ERα interface, which was also confirmed by molecular dynamic simulations. This study offered a novel tool compound for achieving selectivity among 14-3-3 protein mediated interactions through employing a novel synergistic approach.

1.5.3 Motivation to target 14-3-3

14-3-3 have been recognized as an important class of proteins as they are implicated in numerous biological processes. More than 200 protein partners of 14-3-3 are known, some of which are medicinally relevant targets. Therefore, 14-3-3 proteins offer a great therapeutic potential in developing novel small-molecule drugs. The extensive 14-3-3 interactome could also be targeted with small molecules as “tool-compounds” to gain fundamental understanding of the mechanisms of how exactly 14-3-3 proteins mediate PPIs in each pathway. The number of 14-3-3 protein targets currently represents a challenge in developing selective novel small-molecule modulators. This is especially evident in the case of 14-3-3 inhibitors that bind in the pSer binding groove of 14-3-3 and displace any protein target with lower affinity towards 14-3-3 proteins. Although selective stabilization of 14-3-3 proteins is exploited mostly through derivatives of FCs, novel small-molecules are required to address the wide range of pharmacological effects of the 14-3-3 interactome. A

growing number of crystal structures involving 14-3-3 proteins and peptide binding epitopes open an opportunity to develop selective small-molecule modulators.

14-3-3 proteins have also been associated with having a tumor-suppressive role in p53 cell cycle regulation. Expression levels of 14-3-3σ are often downregulated in several types of carcinomas. Following DNA-damage, 14-3-3σ was shown to stabilize levels of p53 and suppress tumor growth by antagonizing *h*DM2-mediated p53 ubiquitination.[124] Other isoforms of 14-3-3 have been associated with enhancing p53 tetramerization and DNA binding.[125] 14-3-3σ recognizes the C-terminal domain of p53 with the key phosphorylated residues (S378, S366 and T387) as a result of post-translational modifications. The molecular mechanism and modest stabilization of FCA on the 14-3-3σ/p53 interaction was recently elucidated by Kuusk and Doveston.[119] Additionally, stabilizing negative regulators of p53, *h*DMX and *h*DM2 with 14-3-3 proteins could have a positive feedback effect on p53's activity, but this approach has not been explored so far.

1.6 Project aims

The aim of this project was to find a novel way of modulating PPIs in the p53 pathway with small molecules, through stabilization of *h*DMX(2)/14-3-3 interactions. A tumor suppressor p53 is regulated during the normal cell cycle through a negative feedback loop by *h*DMX and *h*DM2 inhibiting its transcriptional activity. Upon various stress signals, the function of *h*DMX(2) proteins is now inhibited in order to stop the p53 suppression. However, this feedback loop is dysregulated in a disease state where needed activation of a tumor suppressor p53 is malfunctioned, so is expression of downstream genes dictated by p53. The 14-3-3 family of proteins when bound to a phosphorylated *h*DMX(2) oncogenes could act as positive regulators of this pathway by indirectly preventing p53/*h*DMX(2) interactions, thus stabilizing levels of p53 in the cell (Figure 1.14). As of yet, activation of p53 has not been explored through stabilization of the *h*DMX(2) with 14-3-3 proteins.

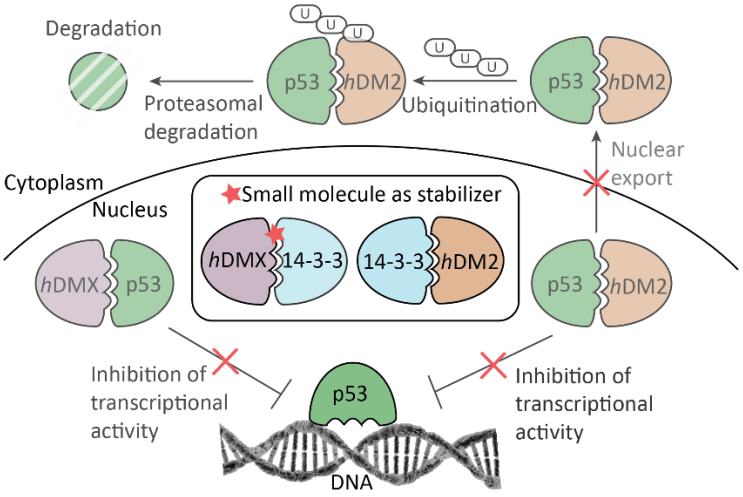

Figure 1.14 Aim of the project: modulating PPIs in the p53 pathway through stabilization of the *h*DMX(2) / 14-3-3 protein interactions. Inhibition of p53's transcriptional activity by *h*DMX(2) could possibly be prevented so as subsequent nuclear export and degradation of p53, when *h*DMX(2) /14-3-3 interactions is stabilized by a small molecule. This thesis focuses mostly on stabilizing *h*DMX /14-3-3 interaction.

Aims:

1. Firstly, in order to gain a better understanding how *h*DMX and *h*DM2 interact with 14-3-3 proteins, biophysical and structural characterization of the peptides mimicking *h*DMX(2) with 14-3-3 proteins will be carried out (Chapter 2). This will include *h*DMX(2) peptide synthesis, 14-3-3 protein expression and developing biophysical assays (FA, ITC and SPR) to determine binding modes between newly synthesized peptides and 14-3-3 proteins so as crystallography studies.

2. In Chapter 3, a FA assay will be developed to screen several small-molecule and fragment containing libraries, followed by confirming the hit compounds using SPR and NMR screening.

3. In addition, Chapter 3 will focus on optimization of a known 14-3-3 stabilizer PYR1 with the objective of gaining specificity towards *h*DMX/14-3-3η complex. This will include synthesis of PYR1 derivatives and determining their affinity and specificity towards *h*DMX/14-3-3η interaction by using FA assay.

4. Chapter 4 will focus on identifying site-specific binding fragments through a protein templated peptide ligation approach, which could provide a basis for further development of inhibitors or stabilizers. Here, *h*DMX-367 hydrazide peptides will be synthesized and used as anchors to detect site-specific binding fragments to 14-3-3η.

Chapter 2: Characterization of *h*DMX(2)/14-3-3 interactions

2.1 Introduction and aims

Even after decades of research on the connection between p53 and cancer, there is still a need to elucidate unexplored molecular interactions within the pathway and develop noninvasive therapeutic strategies to fight cancer progression. The p53 transcriptional factor's role in safeguarding cellular homeostasis is strictly regulated by *h*DMX and *h*DM2, but these two similar proteins have additional independent roles in cell-cycle regulation.[126] Post-translational modifications of *h*DMX(2) such as phosphorylation were found to weaken the interaction between p53 and the two oncogenes.[127] There are dozens of serine and threonine residues in the *h*DMX(2) proteins that can be phosphorylated (protein sequences with highlighted Ser and Thr residues on *h*DMX(2) proteins, as well as their alignment can be found in Appendix, Figure A.1). Several kinases outlined below have been reported to phosphorylate *h*DMX(2) and cellular studies have shown that phosphorylated *h*DMX(2) also interacts with 14-3-3.[3-7] Thus the 14-3-3 proteins are able to indirectly modulate the interaction between *h*DMX(2) and p53. The key phosphorylated residues on *h*DMX(2) recognized by 14-3-3 proteins, as well as their role in cell signaling are outlined in Figure 2.1. Phosphorylation sites on *h*DMX: S342 and S367 are targeted by several kinases (such as AMP[128], chk2[129] or chk1[130]) in response to stress or DNA[131] damage. Phosphorylation was shown to induce *h*DMX binding to 14-3-3 proteins and consequently stabilize p53 from *h*DMX mediated degradation. *h*DM2 phosphorylation on S166 and S186 was promoted by Akt kinase[132] and interaction with 14-3-3 was observed when phosphorylated at the same position by Pim kinase[133]. Interaction between phosphorylated *h*DM2 and 14-3-3 proteins was observed to accelerate the self-ubiquitination of *h*DM2, with a resulting downstream stabilization of p53.

Cellular studies have linked *h*DMX(2) to 14-3-3 proteins, but the mechanisms behind these interactions are still poorly understood. The effect that phosphorylation modifications have on *h*DMX(2) and their association with 14-3-3 proteins have been

known for a while, but haven't been explored yet as stabilization of PPIs is a relatively new concept in drug development, where the majority of known small-molecule stabilizers have been discovered through serendipity.[10] These studies suggest that pharmacological restoration of p53 could be exploited through a novel approach of using 14-3-3 proteins as a promising therapeutic target. By enhancing the association between *h*DMX(2) and 14-3-3 proteins, p53 ubiquitination is suppressed which eventually leads to stabilization and activation of p53.

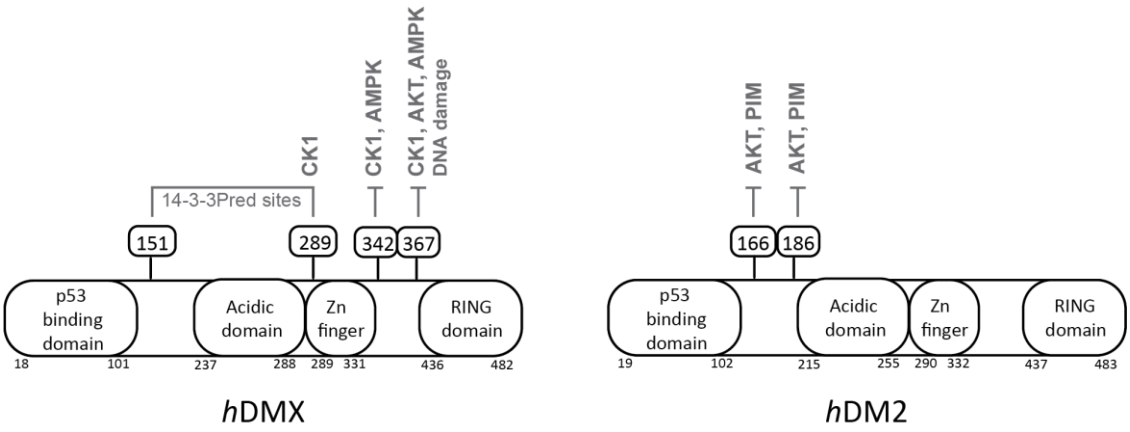

Figure 2.1 Structure of *h*DMX(2) proteins with key amino acids phosphorylated by kinases (highlighted in grey) and their downstream functions include: S289 on *h*DMX is involved in molecular association, S342 and S367 in intracellular localization, protein degradation and ubiquitination, and additionally S367 is associated with cell growth and protein stabilization. pSer on *h*DM2: S166 and S186 are involved in apoptosis, signaling pathway regulation, ubiquitination, etc. (associated downstream functions from www.phosphosite.org)

In this chapter, interactions of *h*DMX and *h*DM2 with 14-3-3 proteins were investigated by various biophysical methods and (in collaboration with Madita Wolter from The Eindhoven University of Technology-Tu/e, Netherlands) structures of these interfaces were solved by X-ray crystallography. In order to find a small molecule that would stabilize *h*DMX or *h*DM2 proteins with the hub family of 14-3-3 proteins and potentially restore transcriptional function of p53, a better understanding of the binding interfaces and affinities between the proteins was required. Therefore, peptides mimicking the key phosphorylation sites from *h*DMX and *h*DM2 were synthesized and all seven human isoforms of 14-3-3 proteins have been expressed for further characterization of these interactions. Using biophysical methods such as FA, ITC and SPR, different binding mechanisms and affinities between *h*DMX(2) peptides and 14-3-3 proteins have been determined. The natural product, FCA (36), known to stabilize numerous 14-3-3 interactions was also tested as a possible stabilizer and a starting point for development of *h*DMX(2)/14-3-3 stabilizers.

2.2 Prediction of *h*DMX(2) binding sites to 14-3-3 proteins

In addition to analysis of the literature, the 14-3-3Pred server[134] was used to identify putative phosphorylated residues on *h*DMX(2) to potentially identify new binding sites (Table 2.1). 14-3-3-Pred[134] is a webserver that predicts binding sites of target proteins if they were to interact with 14-3-3 proteins, based on up to date published examples of 14-3-3 interactions with specific amino acids surrounding pSer or pThr. Scores are assigned to each Ser and Thr residue on the protein target whose sequences in FASTA format were queried, based on three different classification methods: position-specific scoring matrix (PSSM), support vector machines (SVM) and artificial neural network (ANN). End score values are calculated as the average of three independent methods used to calculate the prediction, where a score above 0.5 indicates high probability of the sequence binding 14-3-3 proteins. Additionally, the webserver provides information on the phosphorylation state for each Ser/Thr residue. All previously reported phosphorylated sites on *h*DMX(2) have been confirmed by 14-3-3Pred to have a high probability of binding 14-3-3, except the pSer-342 on *h*DMX, which showed rather low probability of binding to 14-3-3 proteins (score 0.19). Additional unknown phosphorylated residue S151 on *h*DMX has been predicted to be a potentional binding site for 14-3-3 proteins (score 0.75).

Table 2.1 14-3-3-Pred scores for *h*DMX(2) sites predicted to bind 14-3-3.

pSer site	Score (>0.5)
*h*DMX-151	0.75
*h*DMX-289	0.67
*h*DMX-342	0.19
*h*DMX-367	1.28
*h*DM2-166	1.10
*h*DM2-186	0.88

2.3 *h*DMX(2) peptide synthesis

Using the information from the 14-3-3-Pred server several key regions of *h*DMX(2) were identified. Peptides containing these binding regions were designed and synthesized. A key phosphorylated residue was placed in the center of the peptide, surrounded by seven amino acids on each side. Phosphorylated residues close to each other (pS342 and pSer367 from *h*DMX, as well as pSer166 and pSer186 from *h*DM2) were also combined in longer diphosphorylated peptide sequences to determine if phosphorylation at these sites can have a cooperative effect on binding to 14-3-3 proteins.

Table 2.2 List of synthesized *h*DMX(2) peptides

Peptide	sequence
*h*DMX-151	STSRKRT(pT)EDDIPTL
*h*DMX-289	DDLEDSK(pS)LSDDTDV
*h*DMX-342	SKLTHSL(pS)TSDITAI
*h*DMX-367	DCRRTI(pS)APVVRPK
*h*DMX-342+367	SKLTHSL(pS)TSDITAIPEKENEGNDVPDCRRTI(pS)APVVRPK
*h*DM2-166	SRRRAI(pS)ETEENS
*h*DM2-186	QRKRHK(pS)DSISLS
*h*DM2-166+186	SRRRAI(pS)ETEENSDELSGERQRKRHK(pS)DSISLS

All peptides were synthesized manually or via automated Fmoc-solid phase synthesis (SPPS) and modified at the N-terminus by acetylation for ITC, SPR and crystallography studies or with (5,6)-carboxyfluorescein following an Ahx linker to function as a tracer in FA assays (Scheme 2.1).

Briefly, Rink amide resin (0.33 mmol/g loading) was used for single phosphorylated sequences and Rink amide ProTide resin (0.18 mmol/g loading) for diphosphorylated sequences. Lower loading resin was chosen for the longer sequences as it is more suitable for synthesis of difficult or peptides longer than 30 amino acids, as it helps to overcome aggregation issues and higher yields can be achieved. During SPPS the peptide chain was elongated on a solid support through repetitive cycles of Fmoc-deprotection and amide coupling. The phosphorylated residues were introduced using monobenzyl-protected pSer and pThr derivatives, Fmoc-Ser(PO(OBzl)OH)-OH and Fmoc-Thr(PO(OBzl)OH)-OH respectively. Once the peptide sequence was complete, the C-terminus was manually capped by acetylation or reacted with an aminohexanoic acid linker (Ahx) followed by a fluorophore. Peptides were released from the resin through acid mediated cleavage

(using Reagent ‘K’) and protecting groups on the peptide were simultaneously cleaved. All peptides were purified by preparative UV- or mass-directed HPLC. To access the purity of peptides, analytical HPLC and HRMS were carried out and full characterization can be found in Appendix A.2.

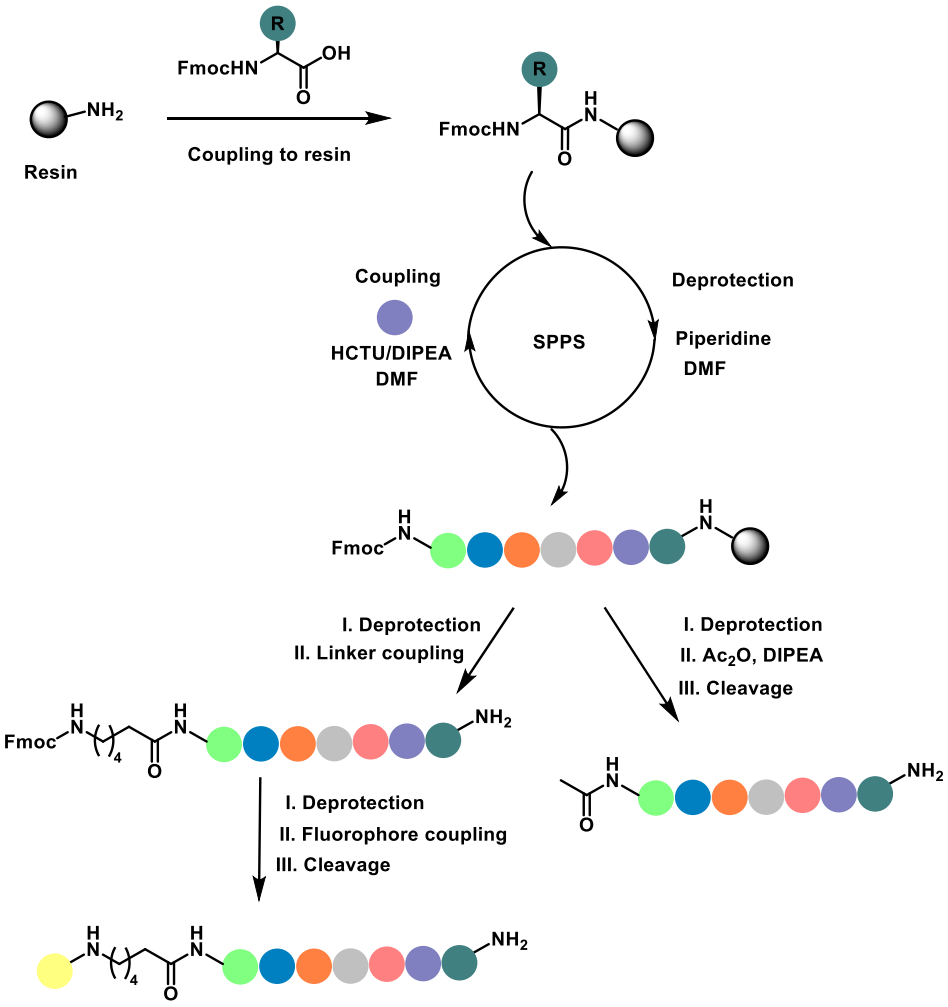

Scheme 2.1 General cycle of solid-phase synthesis of peptides (SPPS).

Additionally, pseudoproline dipeptide Ala-Thr was used for synthesis of the *h*DMX-342+367 peptide (Figure 2.2). Pseudoprolines consist of Ser or Thr oxazolidines, or Cys thiazolidine, and are coupled in the same manner as other amino acids during SPPS. Incorporation of pseudoprolines enhances the solvation of the peptide and subsequently increases the coupling efficiency and overall yield.[135]

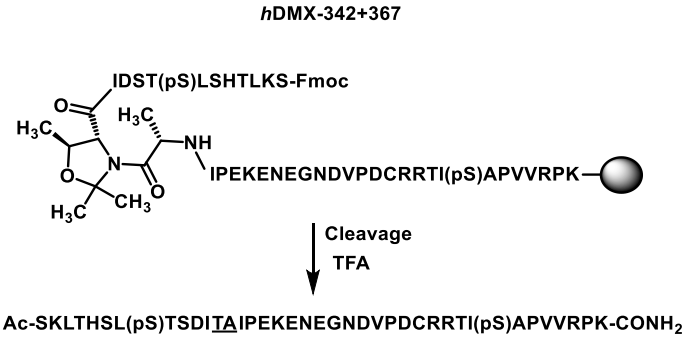

Figure 2.2 Synthesis of *h*DMX-342+367 peptide using pseudoproline (Fmoc-Ala-Thr(Psi(Me,Me)pro)-OH)

2.4 14-3-3 proteins: expression and purification

Plasmids for all 7 human isoforms of 14-3-3 proteins (σ, ζ, η, γ, β, ε and τ, with a His_6-tag, sequence alignment in Appendix A.1) were kindly provided by Prof. Ottmann's group from Technische Universiteit Eindhoven (Tu/e), Netherlands. Firstly, BL21(DE3) cells were transformed with the plasmids and the starter cultures were prepared of all 7 full length 14-3-3 proteins and delta C of σ, ζ, η and τ (meaning 18 amino acids are truncated on the C-terminus for crystallography purposes). The cells were grown in larger cultures (2L), induced by IPTG and left overnight at 18℃. After spinning down the cultures, the cells were lysed by sonication and the protein was isolated and purified by Ni^{2+}-affinity chromatography. Full length 14-3-3 proteins containing fractions were combined, dialyzed overnight and concentrated. Only 14-3-3 isoforms to be used in crystallography, ΔC proteins were dialyzed with TEV protease to remove the expression tag and purified again on Ni^{2+}-NTA column, followed by size-exclusion chromatography. All proteins were analyzed by SDS-PAGE during purification and finally by QTOF MS (Appendix A.2). Circular dichroism (CD) spectroscopy was used to confirm the correct folding of the proteins.

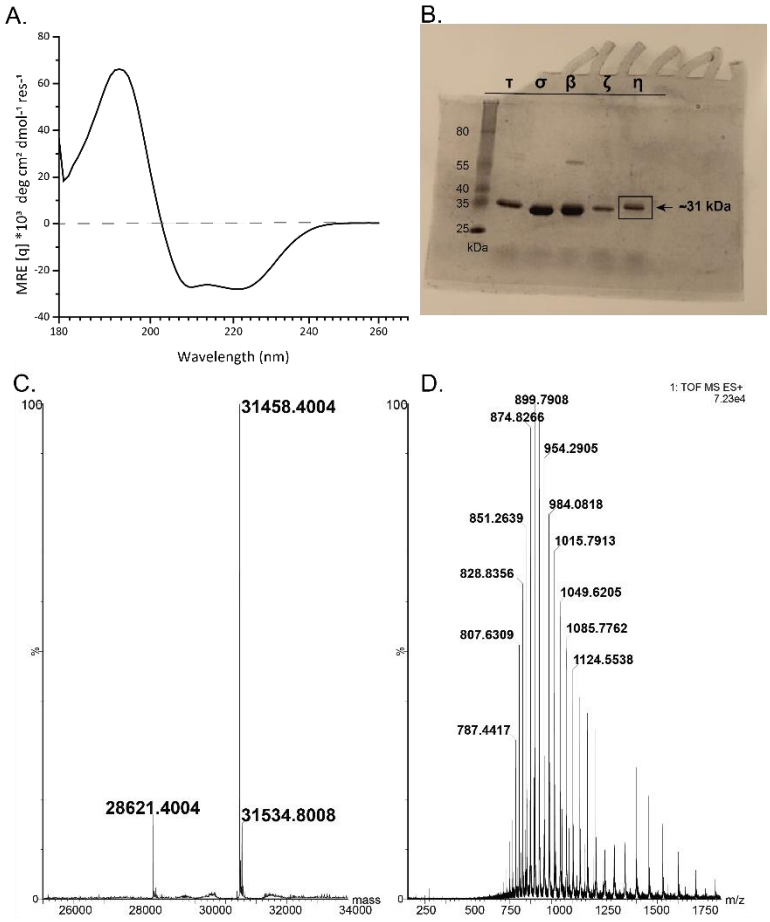

Figure 2.3 14-3-3η analytical characterization: A) CD spectra showing an α-helical structure of the 14-3-3η (71%, theoretical helicity 78%, at 20 ℃, 50 mM sodium phosphate buffer, pH 7.5) B) Coomassie Brilliant Blue stained SDS-PAGE gel after the protein purification C) Deconvoluted spectrum of 14-3-3η D) QTOF MS showing a mass of 31 458.40 kDa (expected: 31 459, mass of 28 621.40 kDa corresponds to 14-3-3η without His_6-tag and the mass of 31 534.80 kDa corresponds to addition of mercaptoethanol)

2.5 Biophysical characterization of the *h*DMX(2)/14-3-3 interactions

2.5.1 Fluorescence anisotropy

To determine the binding affinity between all 7 isoforms of 14-3-3 proteins and *h*DMX(2) peptides, fluorescence anisotropy (FA) experiments were carried out. It was important to develop a robust assay that could be used later for screening small-molecules or fragments that would modulate these interactions. In FA the tracer is a peptide labeled with a fluorophore that binds the protein partner and the binding event is observed through an increase of anisotropy. Anisotropy is a property of the fluorophore to emit light with a certain degree of polarization that is inversely proportional to its rotational rate when exposed to polarized light. As an assay, FA is

a relatively high-throughput and widely used as a primary screen in PPI small-molecule discovery.[136]

14-3-3 proteins were titrated against the constant concentration of the tracer, synthesized fluorescent peptides representing phosphorylated binding sites from *h*DMX(2) proteins (as listed in Table 2.2.). An increase of anisotropy in a shape of the binding curve was observed as peptides were binding to 14-3-3 proteins. The binding affinities (K_d values) were determined by fitting this data to 1:1 model, as described in Chapter 5. Briefly, plotted anisotropy values were fitted using the logistic function while the slope values were constrained between 0.9 and 1.1. With the EC_{50} values determined, min. and max. values were used to convert anisotropy values to ligand fraction bound and fitted to obtain K_d values (see experimental). The constrain to a fitting was set to 50 (tracer concentration used in the assay) to obtain accurate fitting, especially for the peptides where only the very beginning of the binding curve is observed. In some cases, as it is with *h*DM2-186, K_d values with τ, σ and ε could only be estimated to be greater than a limiting values. Similarly, the accurate fitting for diphosphorylated peptides could be obtained only for η, γ and β isoforms.

Table 2.3 K_d values for *h*DMX(2) peptides / 14-3-3 proteins

14-3-3 Proteins: / Peptides:	14-3-3 η	14-3-3 β	14-3-3 τ	14-3-3 ζ	14-3-3 γ	14-3-3 σ	14-3-3 ε
*h*DMX-367	98.8 ± 4.6 nM	507.6 ± 16.3 nM	1.2 ± 0.2 μM	923.8 ± 28.7 nM	533.4 ± 41.6 nM	3.6 ± 0.4 μM	2.7 ± 0.2 μM
*h*DMX-342	20.0 ± 1.2 μM	49.4 ± 11.5 μM	107.8± 6.0 μM	95.8 ± 3.6 μM	37.8± 0.7 μM	135.9 ± 3.6 μM	53.4 ± 2.9 μM
*h*DM2-166	10.2 ± 0.3 μM	11.1 ± 0.5 μM	29.3 ± 2.4 μM	19.6 ± 0.2 μM	3.9 ± 0.3 μM	32.7 ± 1.4 μM	23.0 ± 1.2 μM
*h*DM2-186	31.6 ± 1.9 μM	207.9 ± 6.3 μM	> 250 μM	165.8 ± 5.6 μM	82.9 ± 2.1 μM	> 170 μM	> 260 μM
*h*DMX-342+367 K_{d1}	30.3 ± 6.4 nM	26.5 ± 9.9 nM	-	-	91.5 ± 15.1 nM	-	-
*h*DMX-342+367 K_{d2}	10.67 ± 1.2 μM	7.6 ± 0.8 μM	-	-	18.7 ± 0.7 μM	-	-
*h*DM2-166+186 K_{d1}	49.6 ± 12.1 nM	-	-	-	88.8 ± 10.0 nM	-	-
*h*DM2-166+186 K_{d2}	17.5 ± 2.5 μM	-	-	-	28.0 ± 0.8 μM	-	-

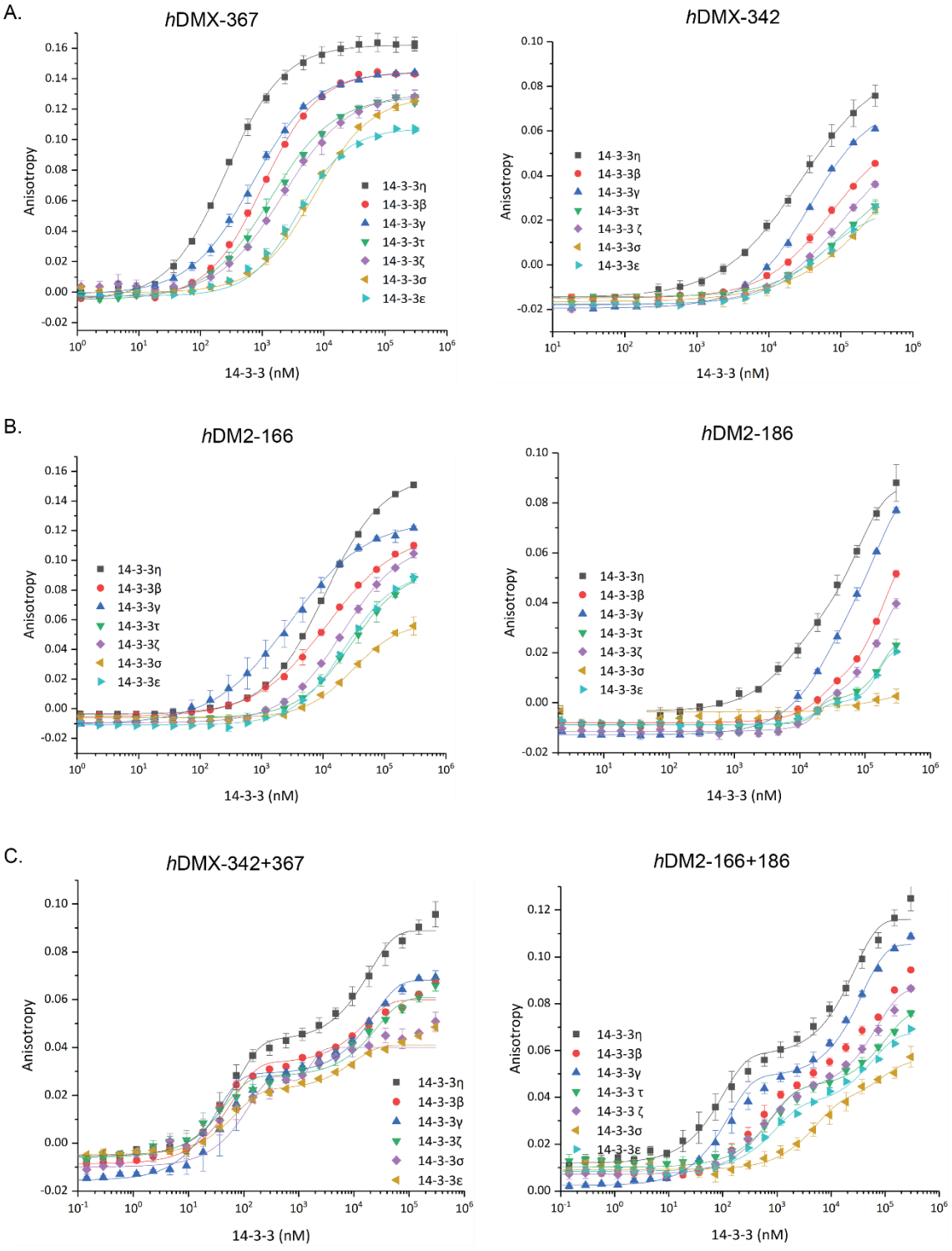

Figure 2.4 Fluorescence anisotropy assays for the two mono-phosphorylated peptides: A) *h*DMX-367 and *h*DMX-342 peptides B) *h*DM2-166 and *h*DM2-186 peptides, and the combined diphosphorylated peptide with all isoforms of 14-3-3: C) *h*DMX-342+367 and *h*DM2-166+186 peptides. (FAM-peptides- tracer 50 nM, 0.1 nM - 300 µM protein, in 10 mM HEPES, 150 mM NaCl, 0.1% Tween 20, 0.1% BSA, pH 7.4, concentration of proteins presented as 14-3-3 monomers)

Peptides representing *h*DMX binding sites pSer-342 and pSer-367 showed high affinity binding with 14-3-3 proteins and similarly, *h*DM2 peptides representing binding sites pSer-166 and pSer-186 showed low micromolar affinities to all 14-3-3 isoforms. A distinct difference in maximum anisotropy levels were observed between *h*DMX(2) peptides and 14-3-3 proteins, reflecting different levels of mobility a fluorophore has. The general trend between isoforms was observed, meaning the tracer is most rigidly bound to 14-3-3η and has more flexibility when binding, for example, 14-3-3σ. Generally, all peptides exhibited the best binding towards 14-3-3η isoform, followed by γ, β, τ, ζ, σ and ε, respectively (Figure 2.4 a-b). These *h*DMX(2) peptides mimicking one phosphorylation site followed a dose-response curve which was fitted to 1:1 model. In this previously described model each 14-3-3 dimer protein can bind two peptides, one peptide per monomer unit of 14-3-3 protein.[100]. K_d values for all 14-3-3 isoforms are reported in Table 2.3, but for simplicity only the 14-3-3η isoform that has the highest affinity will be discussed. The *h*DMX-367 peptide exhibited higher affinity than *h*DMX-342 for 14-3-3η, with K_d of 98.8 ± 4.6 nM versus 20.0 ± 1.2 μM for the corresponding *h*DMX-342 peptide. The observed K_d of *h*DM2-166 peptide was 10.2 ± 0.3 μM and 31.6 ± 1.9 μM for the *h*DM2-186 peptide, with 14-3-3η isoform. The highest affinity was observed with the *h*DMX-367 peptide that is a Mode I 14-3-3 protein binder, with Pro at the +2 position and Arg at the -3 position. Other *h*DMX(2) peptides don't follow the typical 14-3-3 binding motifs as they only have Arg at the -3 or -4 position.

Because of its dimer structure, 14-3-3 is known to bind multiple binding partners simultaneously, either by binding two different phosphorylated residues from the same target or possibly two phosphorylated sites within a multiprotein complex.[137,138] Thus, diphosphorylated *h*DMX(2) peptides were used to determine if there is any cooperativity and increase in affinity between the two targets: *h*DMX(2) and 14-3-3 proteins, if both sites are involved in the binding. Two state binding in FA was observed for both diphosphorylated *h*DMX(2) peptides (Figure 2.4c). The fitting for the observed biphasic-dose response curves was done in the same manner as for the short peptides by fitting each binding event separately to a 1:1 model and K_d values were determined. Accurate fitting was possible for 14-3-3 η, γ and β isoforms as reported in Table 2.3. *h*DMX-342+367 peptide showed two binding events with the K_{d1} of 30.3 ± 6.4 nM and K_{d2} of 10.67 ± 1.2 μM , where the *h*DM2-166+186 peptide had a K_{d1} of 49.6 ± 12.1 nM and K_{d2} of 17.5 ± 2.5 μM. Almost a 200-fold lower K_{d1} was observed diphosphorylated *h*DM2 peptide compared to monophosphorylated *h*DM2-166 and a 3-fold increase in binding affinity for the diphosphorylated *h*DMX peptide compared to monophosphorylated *h*DMX-367. The exact binding mode of

diphosphorylated peptides is difficult to predict solely relying on this FA data. There are several published examples of diphosphorylated peptides exhibiting higher affinity than two individual monophosphorylated peptides and 2:1 binding stoichiometry with 14-3-3 proteins, one dimer of 14-3-3 proteins (two monomers) binding one diphosphorylated peptide.[99,138,139] However, another possible binding mode for diphosphorylated peptides is for one phosphoresidue to bind one monomer of 14-3-3 while another monomer is occupied by a phosphoresidue from a different peptide, keeping 1:1 stoichiometry. To confirm this hypothesis and to exclude possible formation of higher order complexes (tetramers), an analytical ultracentrifugation experiment was performed. 14-3-3η (at the concentration of 14 μM, corresponding to the second binding events on Figure 2.4c) and *h*DMX-342+367 peptide in two different concentration ratios (1:1 and 1:0.5, protein versus peptide) were analyzed. The sedimentation coefficient value remained unchanged for 14-3-3 protein alone and when varying peptide/protein concentrations, indicating that only one dimer of 14-3-3η is involved in the binding (Figure 2.5a). Secondly, peptide length can also have a significant effect on the affinity and binding mode as well. This has been demonstrated in a recent study with p53 peptides with 14-3-3σ, where variation in the peptide length (from 9 to 32 residues) correlated with the improved binding affinities.[140] Two long variants of *h*DMX-342+367 peptide were synthesized, with only one phosphorylation site: pSer-367 or pSer-342, extending the peptide length by 26 amino acids (Figure 2.5b). The two peptides were tested in FA assay to see if both phosphorylation sites bind, but independently as two peptides. *h*DMX-342-long peptide showed increase in binding affinity with 14-3-3η (K_d= 5.4 ± 1.1 μM) as expected, in comparison to the short version of the *h*DMX-342 peptide (K_d= 20.0 ± 1.2 μM). On the other hand, increasing the peptide length for *h*DMX-367 decreased the binding affinity (Kd = 0.8 ± 0.1 μM) and significantly lowered the maximum anisotropy signal. The lower max. signal observed might be due to the fluorophore being moved approximately 20 amino acids further from the binding pSer-367, as the shorter version of the same peptide.

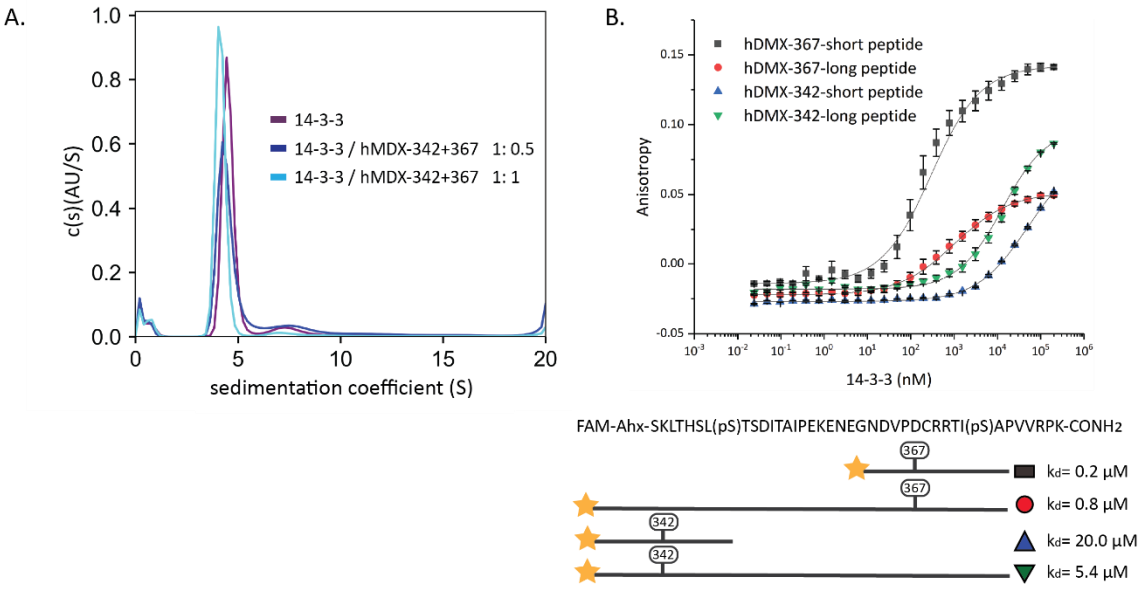

Figure 2.5 A) AUC data for 14-3-3η alone and in mixture with the *h*DMX-342+367 peptides, indicating only one physiological dimer is involved in the binding (14 μM of protein used with two different rations of *h*DMX 342+367 peptide, in the HBS buffer) B) Difference in the affinity between short *h*DMX-367, *h*DMX-342 peptides and their loner singly phosphorylated variants (tracer 50 nM, 200 μM protein, in 10 mM HEPES, 150 mM NaCl, 0.1% Tween 20)

Additionally, peptides representing the sites pSer-151 and pSer-289 (Table 2.2) were synthesized and tested in FA assay as previously described. Neither peptide showed binding to any isoform of 14-3-3, despite the strong indication for binding from the 14-3-3Pred webserver (Figure 2.6).

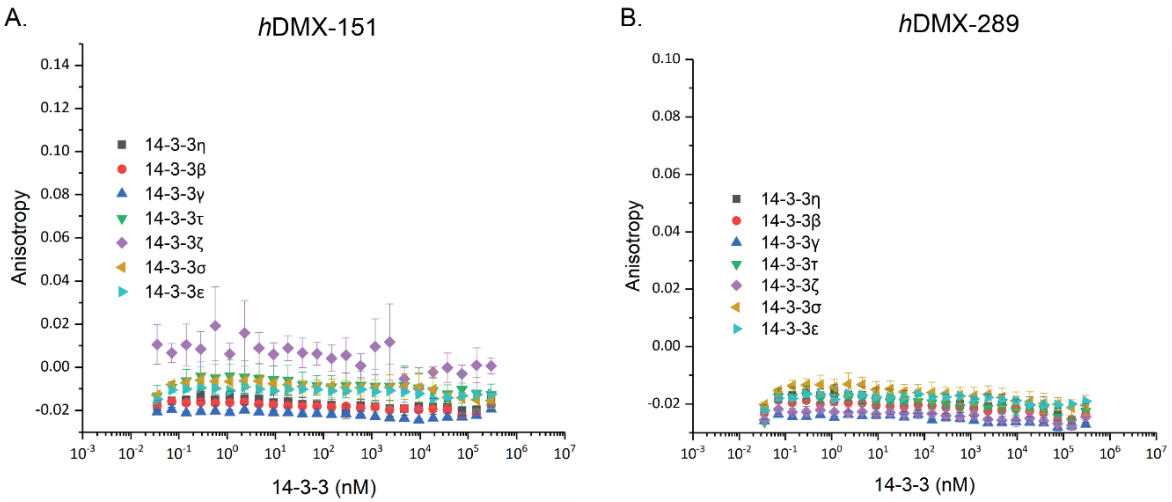

Figure 2.6 Peptides *h*DMX-151 and *h*DMX-289 predicted to bind 14-3-3 proteins by 14-3-3Pred webserver, however no binding was observed to any isoform of 14-3-3.

To test the hypothesis that 14-3-3 proteins require a phosphorylated form of *h*DMX(2) to bind, the same peptides as listed in Table 2.2, but without the pSer were

synthesized as a negative control peptides. As expected, no binding of the negative control peptides to 14-3-3η was observed in FA (Figure 2.7).

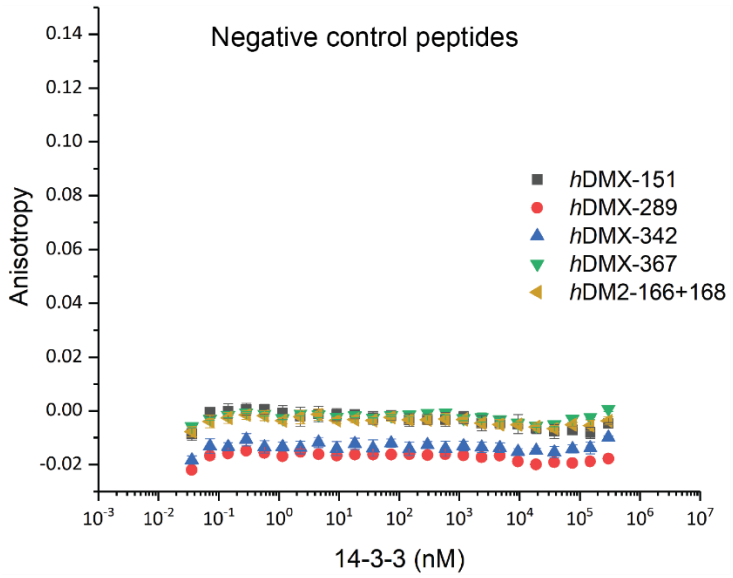

Figure 2.7 Peptides without a pSer were synthesized as negative control peptides to prove the hypothesis about 14-3-3 proteins requiring a pSer residue for binding.

2.5.2 ITC

ITC was used as an orthogonal assay to confirm the binding affinities of *h*DMX(2) peptides to 14-3-3η and to gain additional information about the stoichiometry of the interactions. The advantage of ITC experiments is additional thermodynamic data about the interaction obtained, additionally it is a label free method and requires no immobilization of any of the binding partners.[141] Here, acetylated peptides were injected step wise into a temperature-controlled cell containing 14-3-3η (as described in Chapter 5). In principle, interaction between the protein and peptide affects the temperature of the sample cell and this discrepancy in heat is being matched by the reference cell. Plotting the difference in heat with molar ratio of the protein/peptide gives a binding isotherm. With information about the association constant (Ka), enthalpy (ΔH) and stoichiometry (n) provided, Gibbs Free Energy (ΔG) and changes in entropy (ΔS) can be also calculated.[142] Thermodynamic parameters for *h*DMX(2) peptides / 14-3-3 proteins obtained by ITC are summarized in Table 2.4.

Table 2.4 Thermodynamic parameters for *h*DMX(2) peptides / 14-3-3 proteins

	K_d	ΔG (kJ/mol)	ΔH (kJ/mol)	-TΔS (kJ/mol)	n
*h*DMX-367	870 ± 95 nM	-35	-16 ± 0.2	-18	1.28
*h*DMX-342	21 ± 3 µM	-27	-21 ± 1	-5	0.72
*h*DMX-342+367	14 ± 10 nM	-45	-22 ± 0.7	-23	0.94
*h*DM2-166+186	151 ± 57 nM	-39	-12 ± 0.6	-27	0.94

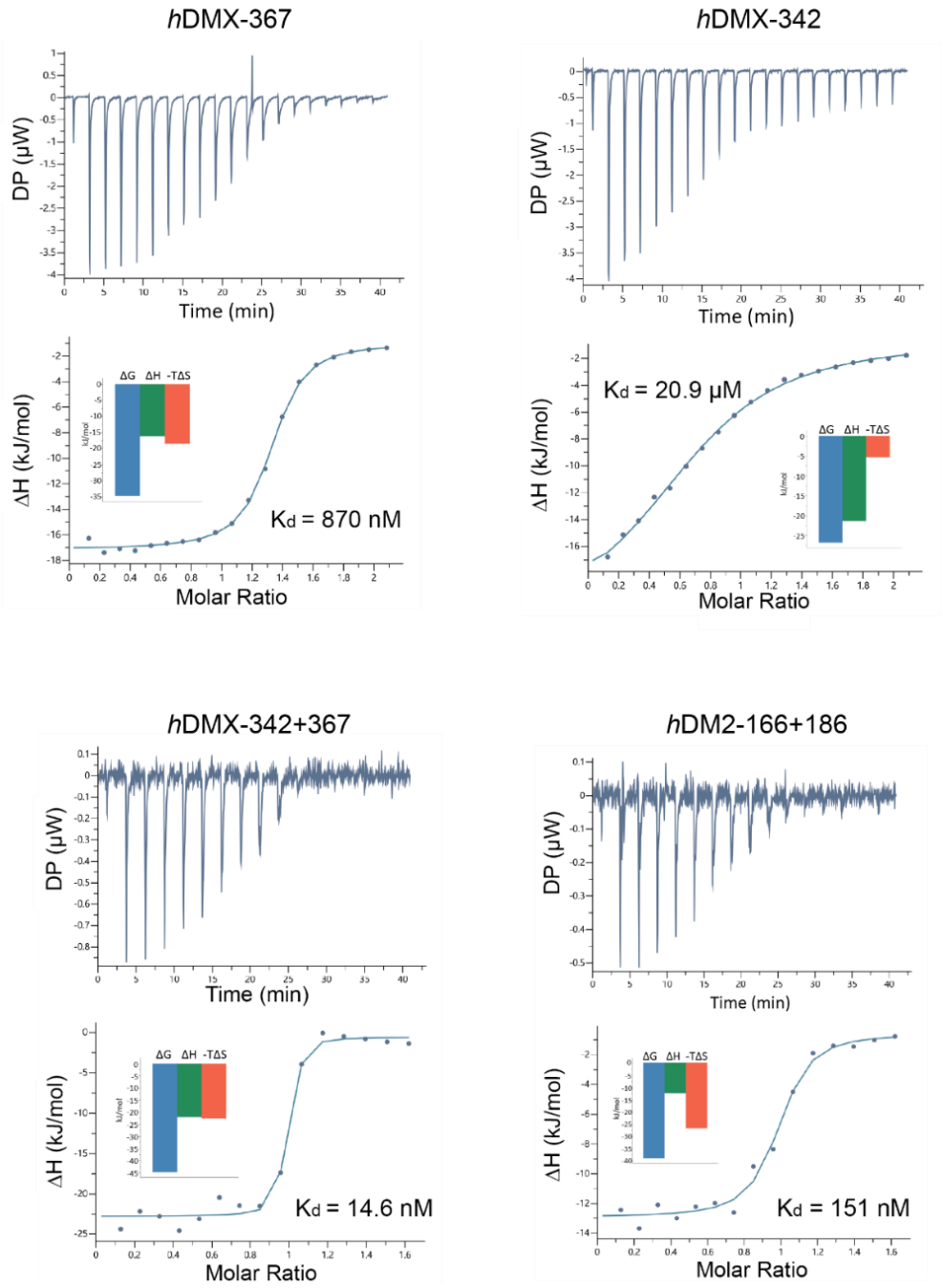

Figure 2.8 ITC experiments for *h*DMX(2) peptides and 14-3-3η. Peptides were titrated into 14-3-3 η (1 mM to 0.1 mM for monophosphorylated peptides and 0.2 mM to 0.02 mM to diphosphorylated peptides) in HBS buffer at 25°C (25 mM HEPES pH 7.5, 100 mM NaCl, 10 mM $MgCl_2$, 0.5 mM TCEP).

ITC data showed the same trend of *h*DMX peptides binding 14-3-3η as in the FA assays, as the binding affinities of *h*DMX-367, *h*DMX-342 and *h*DMX-342+367 were 870 ± 95 nM, 21 ± 3 μM and 14 ± 10 nM. Increase in binding affinity to the nanomolar range when both binding sites of *h*DM2 are present was also confirmed, with the K_d being 151 ± 57 nM. The stoichiometry between diphosphorylated *h*DMX(2) peptides and 14-3-3η was found to be 0.94, which would indicate a 1:1 binding model. If two phosphorylated sites from one peptide were binding simultaneously, the expected stoichiometry would be around 0.5 for 2:1 model. As of thermodynamic data, only *h*DMX-342/14-3-3η interaction was dominated by entropy as all examined *h*DMX(2) sites are quite favorable on enthalpy.

2.5.3 SPR

*h*DMX(2) peptides with similar affinities still might have very different binding kinetics. Association and dissociation rates for *h*DMX(2) peptides were determined by SPR, along with confirming the affinities towards 14-3-3η. SPR is a method that measures biomolecular interactions in real-time and requires no labeling of any components. Increase in response units (RU) are measured while one target is immobilized on a chip surface (14-3-3η) and the analyte (*h*DMX(2) peptide) is flown over the surface until all binding sites are occupied. The reported K_d values are then calculated from plotting the RU values against increasing analyte concentration and fitted to a logistic model. Similar K_d values were confirmed by the Biocore software where the affinities were calculated directly from the k_{on}/k_{off} values (for peptides where kinetics could be calculated, as described in Chapter 5). Developing a robust SPR assay was also important as it will be used as a counter screen to validate small molecules or fragment stabilizers identified as initial hits in Chapter 3.

SPR measured affinities were found to be in agreement with previously determined K_d values from FA and ITC experiments (Table 2.5). *h*DMX-367 and *h*DMX-342 peptides showed a K_d of 189 nM and 37 μM, respectively. For peptides exhibiting lower affinities (*h*DMX-342, *h*DM2-166 and *h*DM2-186) it was only possible to determine steady-state affinities, but not their kinetic profile (example of *h*DMX-342 peptide, Figure 2.9). Diphosphorylated peptides showed a significant increase in affinity, in comparison to the singly phosphorylated peptides: *h*DMX-342+367 (K_d= 9 nM) and *h*DM2-166+186 (K_d= 155 nM). In addition, the biphosphorylated *h*DMX-342+367 peptide was found to have a much slower k_{off} rate than singly

phosphorylated *h*DMX-367 and *h*DMX-342. In stabilizing PPIs, a slow dissociation curve is especially important as it reflects time the bound complex stays intact.

Table 2.5 SPR values for *h*DMX(2) peptides / 14-3-3η

	K_d	k_{on} (1/Ms)	k_{off} (1/s)
*h*DMX-367	189 nM	3.89 x 10^5	0.1208
*h*DMX-342	37 μM	-	-
*h*DMX-342+367	8.6 nM	1.51 x 10^6	0.0048
*h*DM2-166+186	155 nM	1.45 x 10^6	0.1215

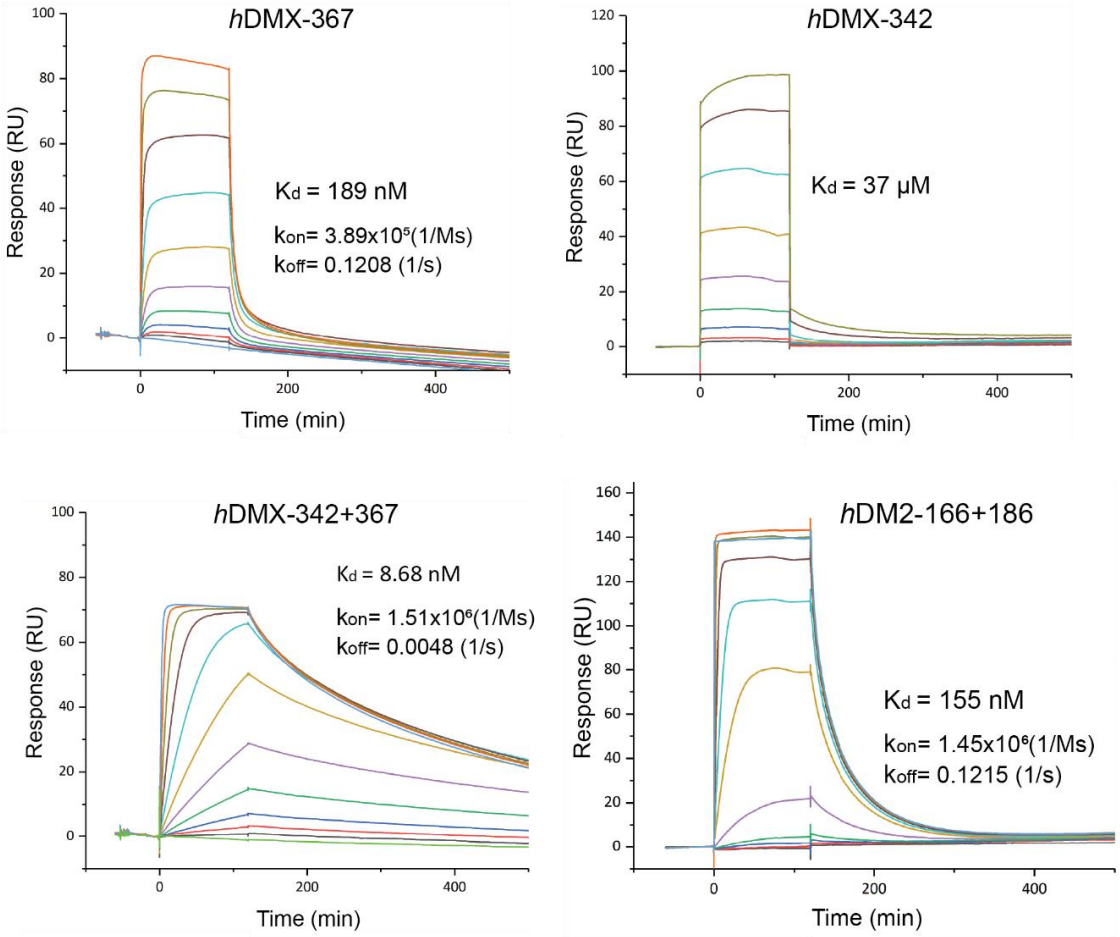

Figure 2.9 SPR experiments for *h*DMX(2) peptides and 14-3-3η. Peptides (concentration at the 10x the K_d for each peptide) were flown over immobilized 14-3-3η, in HBS buffer at 25℃ (25 mM HEPES pH 7.5, 100 mM NaCl, 10 mM $MgCl_2$). Experiment was performed in a multicycle kinetic format and data was fitted to a Langmuir model. K_d values were determined by fitting maximal response level at the end of injection against protein concentration using Steady State Affinity model in Biocore Evaluation software (see Appendix A3)

2.6 Structural characterization of *h*DMX(2)/14-3-3 complexes

Structural data were obtained by solving three novel crystal structures, of *h*DMX-367 (PDB: 6YR5), *h*DMX342+367 (PDB: 6YR7) and *h*DM2-186 (PDB: 6YR6) in complex with 14-3-3σΔC (C-terminus was truncated for the crystallography purposes). Crystallography conditions for *h*DMX-367 were found and final refinement for all structures was done by Madita Wolter. Refinement statistics for all three structure is in Appendix, Table A4. Closer images of each structure with electron density for peptides in each monomer unit of 14-3-3σ are in Appendix A.4.

2.6.1 *h*DMX-367/14-3-3σ

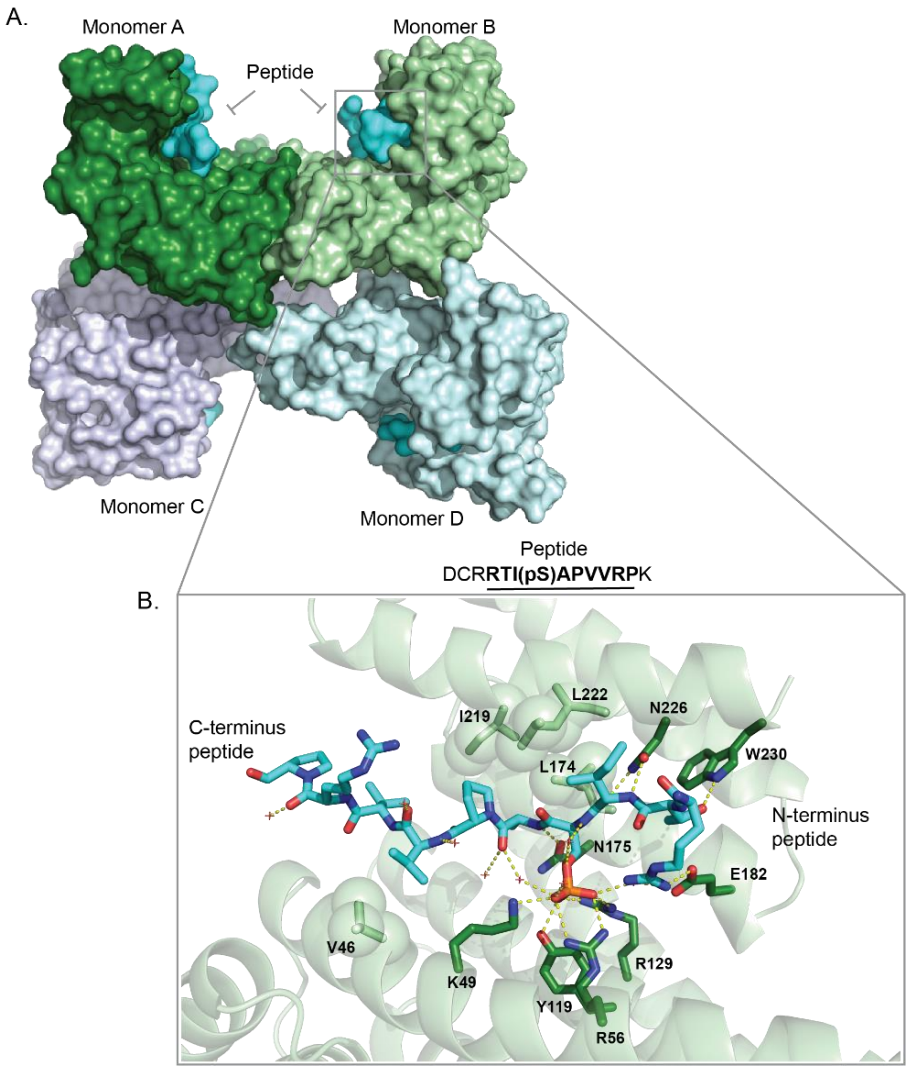

Figure2.10 *h*DMX-367/14-3-3σ structure. *PDB: 6YR5*.

*h*DMX-367/14-3-3σ structure was solved to a resolution of 2.25 Å resolution with a dimer and two additional monomers of 14-3-3σ (in green and blue) in the asymmetric unit, each binding a *h*DMX-367 peptide (cyan) in a conserved amphipathic groove (Figure 2.10a). Ten amino acids from the *h*DMX-367 peptide (RTI pS367 APVVRP) could be built into the electron density map (Figure 2.10b). Phosphoserine of the *h*DMX-367 peptide is positioned in a basic pocket of 14-3-3σ making polar contacts with K49, R56, Y119 and R129 (presented as dashed lines), and N226 makes polar contacts with the backbone of the peptide (Ile365 in the -1 position regarding the pSer-367), which is in agreement with previously published 14-3-3 structures.[100] Additional polar contacts were found between the Arg364 of the *h*DMX-367 peptide and E182 of 14-3-3σ, along with the Ala368 and Thr365 on the peptide backbone with N175 and W230 on the protein respectively. Further contacts of the peptide with the water shell of 14-3-3σ could be observed. Hydrophobic contacts were found between Ile366, Ala368 and Pro369 of the peptide with multiple residues on the protein (presented as spheres).

2.6.2 *h*DMX-342+367/14-3-3σ

The structure of a diphosphorylated peptide *h*DMX-342+367 in complex with 14-3-3σ was solved to a 2.1 Å resolution (Figure 2.11a). 14-3-3σ has crystalized as a dimer in a C121 unit cell (green) and additional electron density for the peptide (cyan) was observed in both monomeric units of 14-3-3σ (Figure 2.11a). Based on previously published structures of diphosphorylated peptides, it was expected to observe pS-342 site binding to monomer B and the pS-367 site to monomer A.[99,138,139] The electron density within the binding groove of monomer B could unambiguously be assigned to the pS-342 site, whereby the eight amino acids of the peptide were built into (HSL pSer342 TSDI), as shown on Figure 2.11b. The peptide was observed to adopt an unusual conformation by taking a sharp turn. A closer examination of the pSer-342 site binding in a monomer B of 14-3-3σ (Figure 2.11b) shows pSer binding to a basic pocket as expected, making polar contacts with R56, R129 and Y130. In this orientation the Ile346 from the peptide makes hydrophobic contacts with L218 and I219 on the protein (represented as spheres). Peptide residues Thr and Ser make polar contacts with K122, N175 and E182, W230, while N226 makes polar contact with the backbone of the peptide. Overall, the C-terminus of the peptide takes a sharp turn after the pSer-Thr residues and this peptide conformation is stabilized by hydrogen bonds between water molecules and Thr, Ser and Asp peptide residues.

This structural information about pSer-342 site contributes to full elucidation of both binding sites from the *h*DMX protein binding to 14-3-3σ.

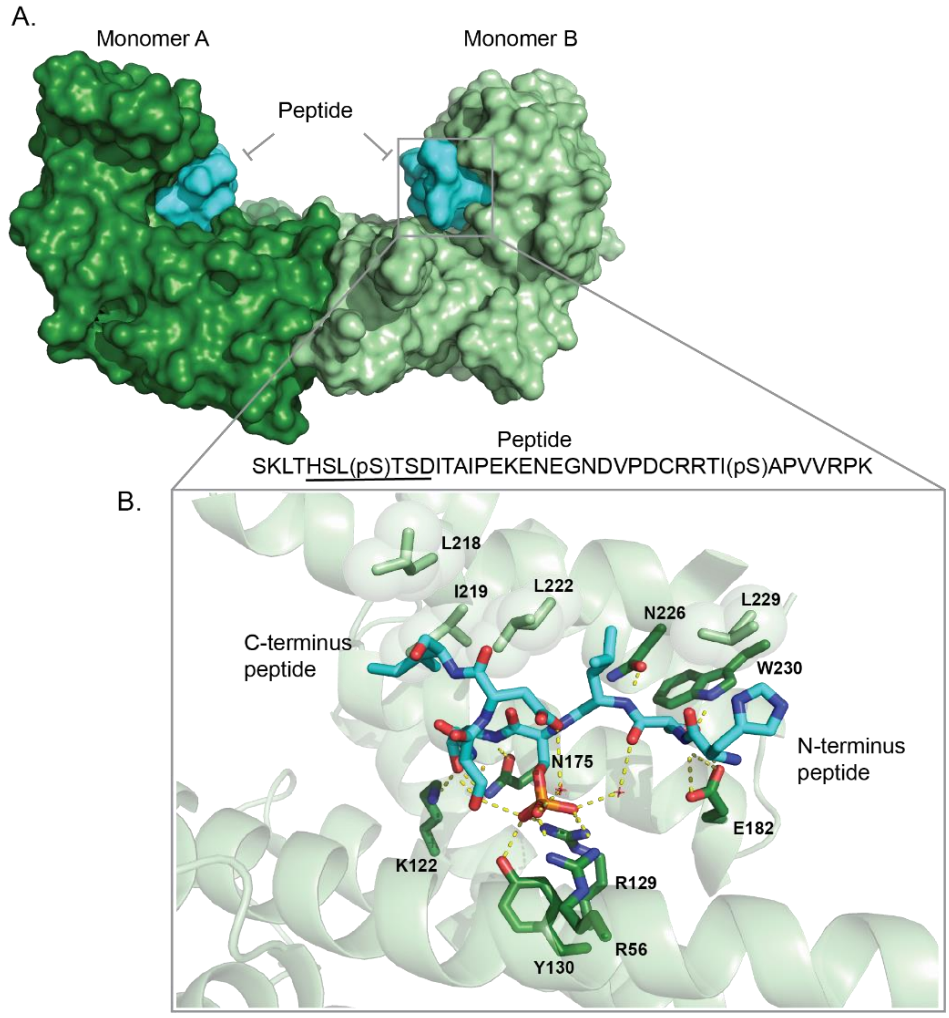

Figure 2.1115 *h*DMX-342+367/14-3-3σ structure. *PDB: 6YR7*.

However, the electron density map within the binding groove of monomer A can be interpreted in different ways, indicating an overlay of multiple conformations (both pSer-342 and pSer-367 sites, Figure 2.12). The dominant electron density map can be assigned to the pSer-342 binding site as the unusually bent conformation is not supported by the Pro369 of the second binding site (pSer-367). Nevertheless, after modeling in the pSer-342 site extra electron density can be observed lateral from Ser344 of the first binding site of the peptide. This extra electron density fits to the sequence of the pSer-342 binding site, confirming the right peptide was built into monomer A.

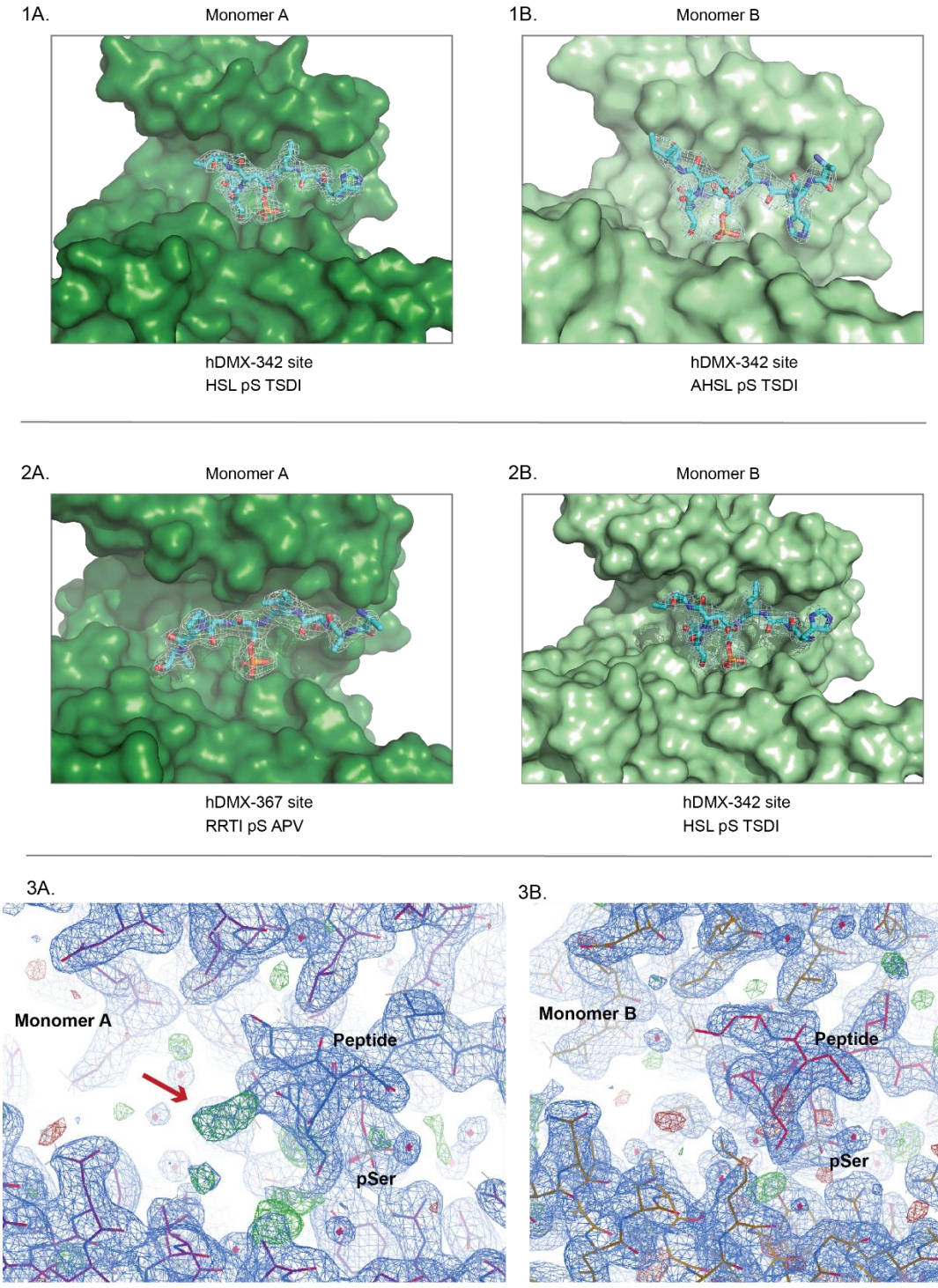

Figure 2.12 *h*DMX-342+367/14-3-3σ structure. 1A-B shows the final refined structure with both pSer-342 in monomer A and B. 2A-B shows electron density during the refinement, where pSer-367 peptide could be in monomer A. 3A-B shows electron density for the final refined structure. An extra electron density can be observed in monomer A (in green) indicating pSer-342 and pSer-367 peptides overlapping

2.6.3 *h*DM2-186/14-3-3σ

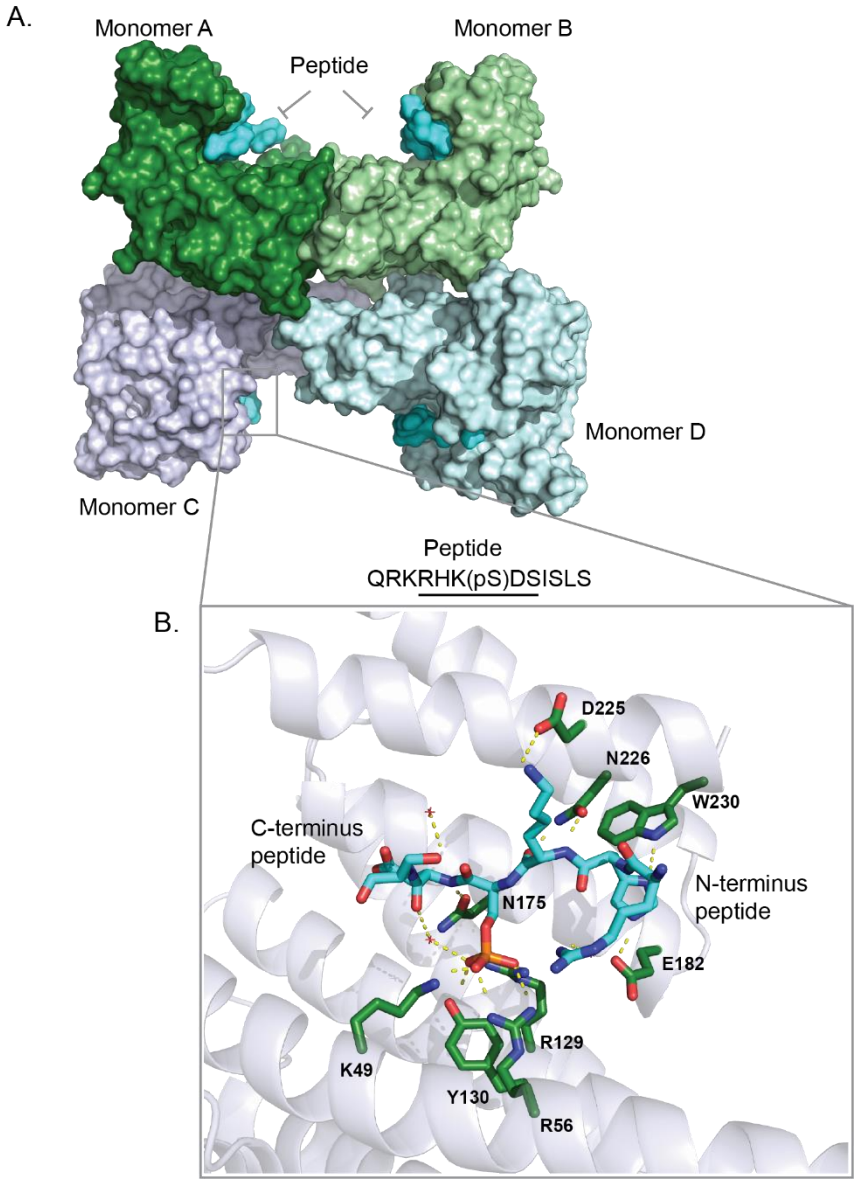

Figure 2.13 *h*DM2-186/14-3-3σ. *PDB: 6YR6*

Crystal trials were set up for all *h*DM2 peptides and the structural proof of *h*DM2 interaction with 14-3-3 proteins was obtained by solving novel crystal structure of the *h*DM2-186 peptide in complex with 14-3-3σ, at the 1.75 Å resolution. *h*DM2-186 peptide crystalized in a P1 unit cell, as a dimer and additional two monomers of 14-3-3σ (monomers A-D) with pSer-186 peptide in each groove (in cyan) as shown in Figure 2.13a. Six amino acids of the peptide were interpretable in electron density: RHK(pS)DS (Figure 2.13b). pSer of the peptide is always located in the same position, between K49, R56, R129 and Y130. The peptide is stabilized by polar contacts between Lys and D225, His and E182, W230, and the peptide backbone

with N175 and N226. Arg and Ser peptide residues are also stabilized through hydrogen bonds with water molecules.

2.7 Stabilization of *h*DMX(2)/14-3-3 by natural product FCA

Modulation of *h*DMX(2)/14-3-3 interactions represents a novel strategy to modulate PPIs in the p53 pathway that has not been fully explored. After fully characterizing *h*DMX and *h*DM2 binding sites with 14-3-3 proteins, a well-known stabilizer of 14-3-3 PPIs, natural product FCA was tested to see if it would act as a stabilizer for these interactions as well.

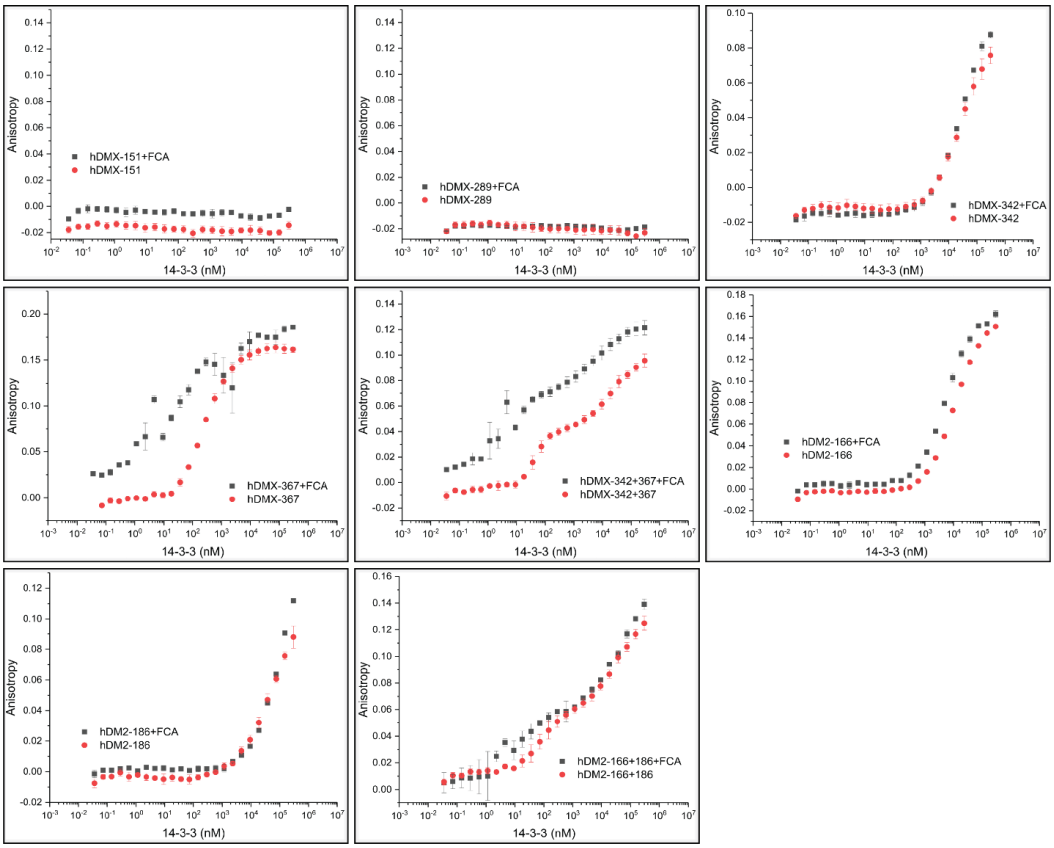

Figure **2.14** No stabilization was observed by testing all *h*DMX and *h*DM2 peptides in the presence of FCA (HBS buffer, 50 nM tracer, 200 μM 14-3-3η, 200 μM FCA)

FCA is a complex natural product that binds in a pocket of 14-3-3 proteins, stabilizing the interaction with its binding partner, making it a great tool that indicates if the same pocket can be targeted by other more drug like compounds. The assays were repeated with titrating 14-3-3η against a constant tracer concentration, with and without 200 μM FCA (Figure 2.14). In the case with *h*DMX(2), FCA showed no stabilization with any of the eight singly or diphosphorylated peptides. The apparent

left shift of the binding curves for diphosphorylated *h*DMX and *h*DMX-367 peptides originated from differences in lower anisotropy, which might be caused by differences in concentrations rather than stabilization effect. No observed stabilization was in some way expected as the FCA stabilizes the mode III (C-terminus) peptides or mode I/II peptides with Pro on +2 position that causes the changes in peptide orientation away from the FCA pocket. However, in novel crystal structure of *h*DMX-367/14-3-3σ, the peptide has a linear shape that extends and occupies the FCA binding pocket (Figure 2.15).

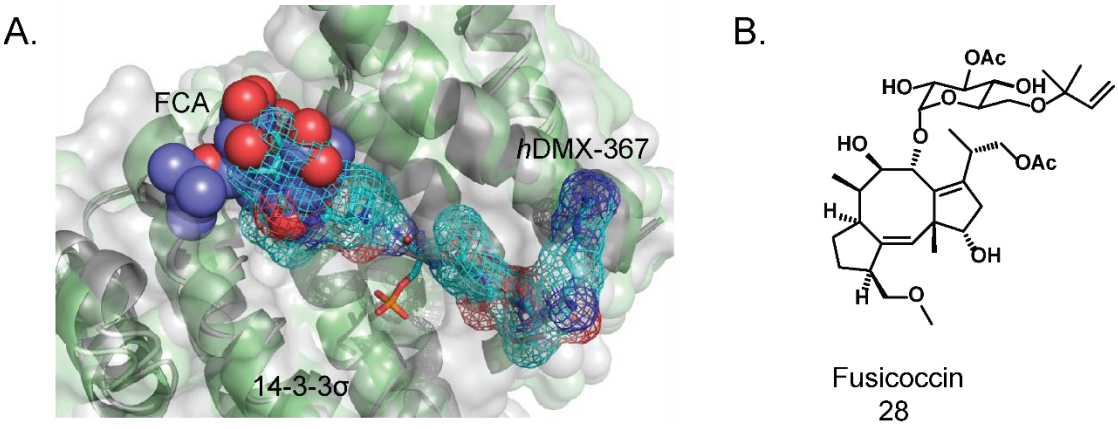

Figure 2.15 A) Overlay of the novel *h*DMX-367 structure and the *3IQV* PDB structure with FCA. Protein is shown in green, peptide in cyan and FCA in purple. B) Fusicoccin structure

2.8 Discussion and summary

In this chapter, an extensive biophysical and structural analysis of the 14-3-3 interactions with phosphorylated peptides mimicking *h*DMX and *h*DM2 was presented. Novel peptides representing *h*DMX(2) binding sites have been synthesized and 14-3-3 proteins have been expressed for these studies. Peptide sequences were designed based on previously reported phosphorylation residues that were involved in binding to 14-3-3 proteins as well predicted sites from using the 14-3-3Pred webserver (as listed in Table 1 and 2). To date, only *in vivo* studies have shown the important role 14-3-3 proteins play in p53 activation by interacting with the phosphorylated *h*DMX(2) oncogenes.[3-7] To exploit this complex network of PPIs in the p53 pathway through stabilization of the 14-3-3 proteins with *h*DMX(2), a precise mechanism of action and the affinities between the proteins had to be determined. Thus, a range of assays were employed to characterize binding between them, starting with FA assays to ITC and SPR.

Firstly, the hypothesis that 14-3-3 requires a phosphorylated residue to bind was confirmed by testing peptides with the identical sequence (as listed in Table 2.2) but lacking the central phosphorylated Ser/Thr, where no binding was observed. 14-3-3Pred predicted sites, *h*DMX-151 and *h*DMX-289, also did not exhibit any binding in the FA assays and were discarded from any future studies. However, all literature reported phosphorylated sites (pSer-342 and pSer-367 from *h*DMX, pSer-166 and pSer-186 from *h*DM2) were confirmed to have affinities in low μM and nM range towards 14-3-3 proteins (as summarized in Table 2.3). Additionally, an enhanced overall binding affinity towards 14-3-3 proteins was observed when the two neighboring phosphorylated sites were combined in longer *h*DMX-342+367 and *h*DM2-166+186 sequences. As a dimer, 14-3-3 binds two monophosphorylated peptides, one per each groove.[143] This 1:1 binding model is demonstrated on Figure 2.16c and it was observed in FA assays for all four monophosphorylated peptides. The K_d values for *h*DMX-342 and *h*DMX-367 peptides with 14-3-3η obtained by SPR and ITC agreed with the FA assay. Only *h*DMX-367 peptide showed slightly higher K_d in ITC experiments (98.8 ± 4.6 nM in FA, 870 nM in ITC), but this discrepancy might be due to inaccurate concentration of either peptide or protein since the observed N value was 1.3 and the K_d obtained from SPR was 189 nM, similar to FA. One limitation in directly comparing results or obtaining the same K_d values by different techniques is the fundamentally different experiment setup. For example, in FA assays proteins were titrated against a fixed concentration of peptide, while ITC experiments were performed in the opposite manner, a peptide was titrated in ten times lower concentration of protein. Similarly, the ratio of peptide/protein concentration varies significantly in the FA and in crystallography. Thus, it is worth noting that different cartoon representation is drawn for the end state in FA assays (Figure 2.16a and 2.16c), to reflect a true nature of the interactions. Towards the end points (highest protein concentration) in FA, tracer is so diluted that for each copy is only possible to occupy one monomer of 14-3-3 protein. On the other hand, for ITC or crystallography experiments, where peptide concentration is much higher in respect to protein concentration, a typical 14-3-3 binding mode drawn on Figure 2.16c applies.

Further, two novel crystal structures of monophosphorylated peptides were solved, providing additional validation of the *h*DMX-367 and *h*DM2-186/14-3-3σ interactions. The two obtained structures showed typical binding to 14-3-3, where peptides were bound in an amphipathic groove of 14-3-3 that acts as a ligand-binding channel (Figure 2.16c).

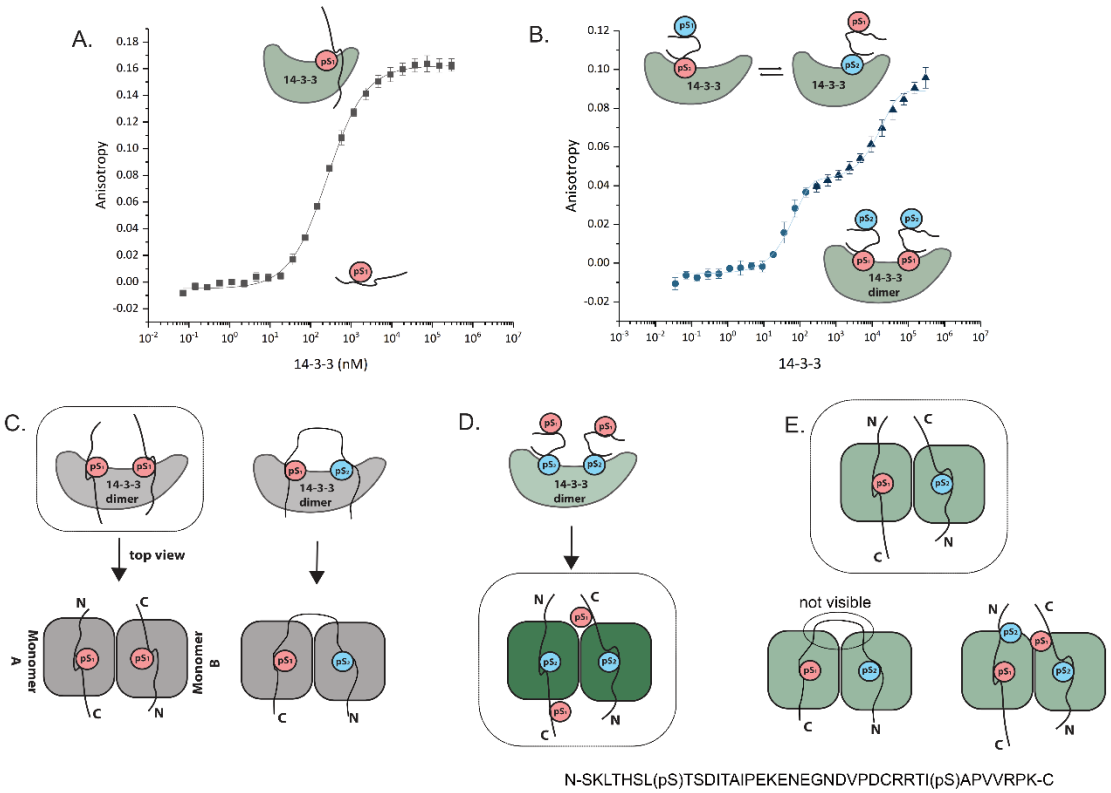

Figure 2.16 Cartoon representation of the 14-3-3 binding modes. A) An S shaped curve was obtained for monophosphorylated peptides binding in 1:1 stoichiometry. B) The double S curve was observed for diphosphorylated peptides. In this proposed binding mechanism two separate peptides bind with a higher affinity pSer residue. With the increase of protein concentration, one peptide binds with either of the two pSer residues. C) Typical 14-3-3 binding mode. Two monomeric peptides bind one dimer of 14-3-3. Diphosphorylated peptide binds with one pSer in monomer A and the second pSer in monomer B, with amino acids in the between them bridging the gap between two monomers. D) Novel crystal structure of diphosphorylated hDMX-342+367 peptide shows pSer-342 site in both monomers of 14-3-3σ. E) The hDMX-342+367/14-3-3σ structure alluded on possible overlay of pSer-367 and pSer-342 sites in monomer A. Impossible to determine the exact binding mode as the electron density for the linker (amino acids between the two pSer sites) is not visible. Probable simultaneous binding of one or two hDMX-342+367 peptides.

An interesting biphasic binding event was observed in FA assays for diphosphorylated peptides *h*DMX-342+367 and *h*DM2-166+186. The K_d values for the two distinct binding events were significantly lower than for each monophosphorylated peptide, especially for the *h*DM2-166+186 peptide. There are several published examples of diphosphorylated peptides exhibiting higher affinity than two individual monophosphorylated peptides and 2:1 binding stoichiometry with 14-3-3 proteins (cartoon representation of that binding on Figure 2.16c).[99,138,139] Usually, these are the cases where monophosphorylated peptides (that follow 1:1 binding) have much lower affinities towards 14-3-3 proteins, in the high micromolar or even lower millimolar range. For example, Raf and CFTR peptides had a several fold increase in affinity when two sites were combined and crystal structures with two

different phosphoserine sites bound to a dimer of 14-3-3σ were solved. However, no apparent biphasic binding events were observed in FA assays or ITC experiments with biphosphorylated peptides so far. In this case, affinities of each monophosphorylated *h*DMX(2) peptides are much higher in comparison, with K_d's being in a low micromolar and even nanomolar range to start with. Here, the proposed 'typical' 2:1 binding mode for *h*DMX-342+367 and *h*DM2-166+186 peptides is not supported by obtained ITC or structural data. ITC experiments confirmed the higher affinity of diphosphorylated peptides, lowering the K_d values to 14 nM for *h*DMX and 151 nM for *h*DM2. These affinities can be directly compared to the first binding event from FA where the observed K_d values were 30.3 ± 6.4 nM for *h*DMX and 49.6 ± 12.1 nM for *h*DM2, as the concentration range of peptide/protein used is similar. ITC experiments also indicated the stoichiometry of the interaction to be 1:1, meaning two diphosphorylated peptides were involved in binding (Figure 2.16b).

Crystal structure of the *h*DMX-342+367 peptide was solved with pSer-342 site in both monomers of 14-3-3 (cartoon representation of the peptide orientation shown on Figure 2.16d). However, the *h*DMX-342+367/14-3-3σ structure refinement alluded to a possible overlay of pSer-367 and pSer-342 sites in monomer A of 14-3-3σ (Figure 2.16e). An extra electron density was observed that would accommodate Pro on +2 position from pSer-367, however, the peptide was not able to extend in the direction of the dominant electron density which was taking a sharp turn not supported by the right orientation of Pro369. This extra electron density fits to the sequence of the pSer-342 binding site. Not only was this observation not expected, it also contradicted the binding data observed with FA, where the pSer-367 binding site binds with a significantly higher affinity than the pSer-342 site. Multiple reasons can cause this phenomenon, one of which is that both binding sequences are equally represented but the C-terminus of the pSer-367 site is more flexible within these buffer conditions, subsequently leading to a lower occupancy of the electron density map. Another reason can be the influence of the crystal formation of the binding affinities of the peptides. The 14-3-3 protein can be crystalized in an "opened" and "closed" conformation which indicates a certain degree of flexibility.[144] The crystal lattice formation limits this flexibility, possibly paying the entropic penalty for fixing the 14-3-3 protein in a single conformation, which might shift the binding affinities of the two sites in favor of the pSer-342 site. This second hypothesis is supported by several examples of peptides with astonishing polar and hydrophobic contacts within crystal structures by almost undetectable binding affinity. Also, the unusual binding mode of the pSer-342 site supports this second hypothesis, since the peptide is folding back to helix 8 and 9 of 14-3-3σ, the part where the highest flexibility is expected.

Seeing that two phosphorylated sites from one peptide are not involved simultaneously in binding 14-3-3, an AUC experiment was performed to exclude any formation of tetramers. Concentration of peptide used to test this hypothesis corresponds to the second binding event observed in FA for diphosphorylated peptides. The unchanged sedimentation coefficient between 14-3-3η alone and in the presence of *h*DMX-342+367 peptide suggested one dimer of 14-3-3η is involved in the second binding step as well. And lastly, the two long variants of *h*DMX-342+367 peptide with only one phosphorylation site: pSer-367 or pSer-342 were tested in the FA, where a higher affinity was correlated with the length of the peptide for pSer-342 site.

Based on the data presented in this chapter, a binding model of diphosphorylated peptides and 14-3-3 proteins is proposed on Figure 2.16b. It could be hypothesized that two peptides bind in the first step, with the higher affinity pSer-site binding in each monomer of 14-3-3. Stoichiometry of this interaction is supported by ITC experiments while lower binding affinities are evident by both ITC and FA. The second binding event would correspond to one peptide binding, with either of the two pSer-sites in each monomer of 14-3-3. One dimer of 14-3-3 protein involved in binding is supported by AUC data, while the overlay of two pSer-sites is supported by crystallography data. Despite striking similarities in the amphipathic groove of 14-3-3 proteins (peptide binding region, Figure 1.10), a range in binding affinities between peptide and 14-3-3 isoforms are always observed. The 14-3-3 proteins were found to follow a trend in binding all *h*DMX(2) peptides, where η isoform was preferentially bound. The isoform-specific interactions of 14-3-3 proteins are usually observed with different peptide partners, often with σ and ε isoforms being the weakest binders. However, there is still no clear distinction between preferential 14-3-3 isoform-partner interaction or their biological relevance (involvement in disease progression).

All together, these results provide an understanding of the *h*DMX(2) interactions with 14-3-3 proteins beyond the scope of *in-vivo* experiments and provide a basis for the developing small-molecule stabilizers of these interactions.

Chapter 3: Towards small molecule modulators of *h*DMX(2)/14-3-3

3.1 Aims and objective

This chapter is divided into two main sections as it describes different approaches in developing small-molecule PPI modulators: I.) assay development and screening of small-molecule and fragment libraries, and II.) SAR of a known stabilizer of 14-3-3 protein mediated interactions, PYR1 (**41**). The overall aim of this chapter was to find a compound that would bind selectively to the *h*DMX(2)/14-3-3 complex and enhance or inhibit the interaction between the two protein targets. Finding a small-molecule stabilizer that binds on the rim of the interface of these interactions as a 'molecular glue' would be of particular interest, as it would potentially enhance the biological effect *h*DMX(2)/14-3-3 interaction has on p53 activity. It is also expected that small-molecule or fragment inhibitors will be found during the screen. Although inhibition of *h*DMX(2)/14-3-3 interactions is not of biological relevance, those compounds could be used as 'tools' to probe the p53 pathway. For example, such compounds would be particularly useful as negative control compounds in future cell-based assays.

Firstly, since there are no compounds reported as modulators of *h*DMX(2)/14-3-3 interactions to date, a robust screening protocol for small-molecule or fragment libraries needs to be developed. The stabilization and/or inhibition effect of possible modulators can be monitored by using biophysical assays as previously developed and described in Chapter 2. Thus, to achieve the first objective, fluorescence anisotropy will be used as a primary assay to screen from the commercially available Maybridge fragment library, PPInet small-molecule library along with compounds and fragments provided by TASPPI-network collaborators. The screening will focus on using 14-3-3η protein and *h*DMX-367 peptide as a mimic of the phosphorylated *h*DMX protein. The screening cascade will consist of testing compounds in a single point FA assay, followed by confirming the selected hits in dose response (stabilizers) or competition assay (inhibitors) using FA, as well as SPR and protein NMR techniques for selected hit compounds (Figure 3.1b).

The novel crystal structure of *h*DMX-367 peptide in complex with 14-3-3σ also opened a possibility to explore a rational drug design approach in stabilizing PPIs within the p53 pathway. The second objective of this chapter is to investigate the possibility of 'repurposing' a known 14-3-3 binding compound to a selective *h*DMX-367/14-3-3 stabilizer. To achieve this aim, a small library of novel PYR1 analogues will be synthesized and activity, as well as selectivity of those compounds will be tested in FA dose-response assays (Figure 3.1c). This work was carried out as a part of a secondment in Astra-Zeneca, Sweden, under supervision of Dr. Gavin O'Mahony.

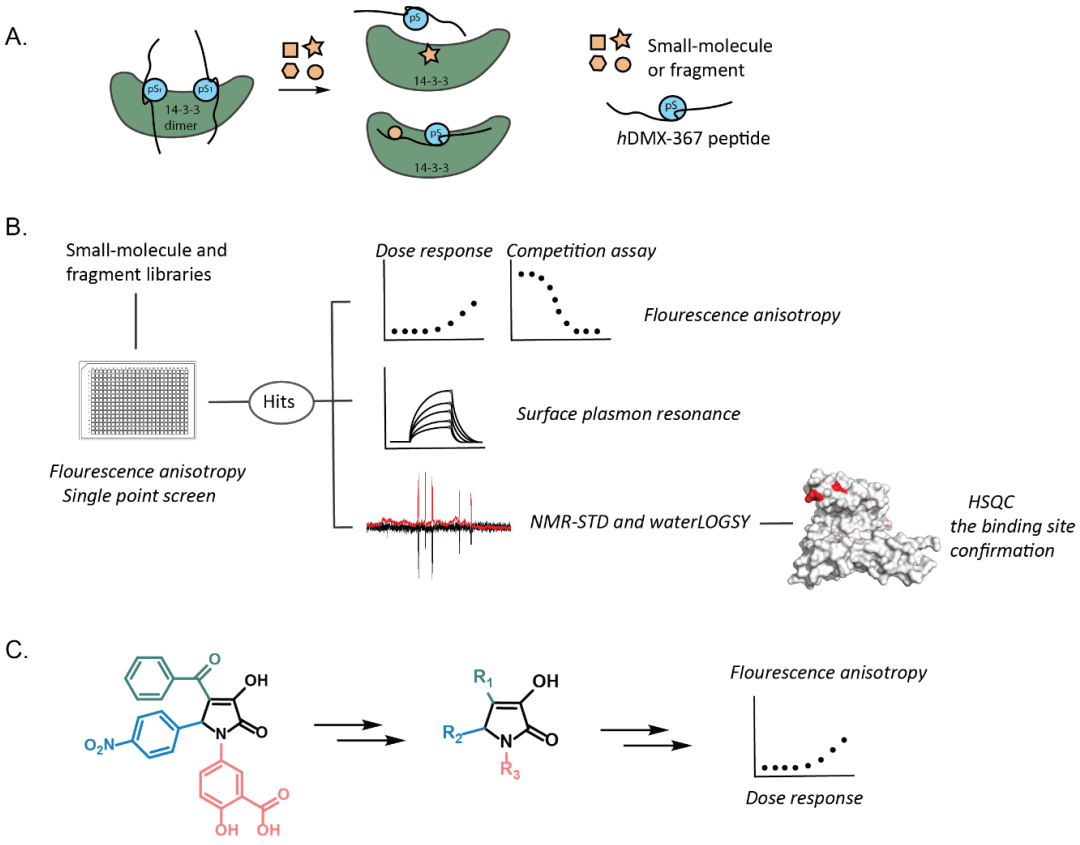

Figure 3.1 Aims of the chapter. A) Finding a compound that modulates *h*DMX-367/14-3-3 by either inhibiting or stabilizing the interaction by: B) Developing a robust screening protocol for small-molecule or fragment libraries. Each compound will be screened in a single-point FA assay and compounds showing an (de)increase in anisotropy will be chosen for further validation. Hit compounds will be then be confirmed in a dose-response or competition assay in FA, but also SPR and NMR. C) Optimizing a known 14-3-3 stabilizer, PYR1, to achieve selectivity towards *h*DMX-367/14-3-3 interaction

3.2 Introduction: biophysical methods to study PPIs

The goal of modern drug discovery is to produce novel therapeutic agents that can selectively target pathways connected to a particular disease, including diseases mediated by PPIs. The perception of PPIs as druggable therapeutic targets has changed drastically over the past decade. Despite once being ignored as 'undruggable' due to the dynamic nature of proteins and their large, featureless surfaces, now small-molecules are routinely developed as PPI modulators owing to refinement of existing bioassay techniques and new ones continuously being developed.[1] Even relatively novel concepts in drug discovery, such as small-molecule stabilizers of PPIs[145] and PROTACs[146] being developed as drugs, are being studied with the existing bioassay techniques.

The cost for a single drug to reach market is staggeringly high, so early stages of drug development are of crucial importance to avoid developing a pipeline leading to expensive failures. After establishing a biologically relevant target, different pathways outlined in Figure 3.1 can be chosen to identify a lead compound that would undertake further optimization to reach a drug candidate stage, depending on the nature of the target and available resources.[147] Usually a combination of several complementary workflows, such as screening campaigns and structure-based design, have helped to overcome the basic molecular recognition problem associated with targeting PPIs: how to selectively target large protein surfaces with small-molecules. Despite protein-protein interfaces lacking small-molecule natural ligands, which are usually a great starting point in drug development, structural biology still has an important role in guiding early stages of drug development.[148] The large number of high-resolution 3D structures of biomolecules available in the PDB allows *in silico* assessment of a protein target. Although some proteins lack obvious hot spot regions, native residues in the protein-protein interfaces can be identified and optimized to maximize the contact surface between the protein-protein complexes.[149] The key residues from one protein involved in binding can also be identified as pharmacophores, and *in silico* screening methods can then be employed to identify a compound that could match those pharmacophoric elements.[150] In contrast to structure guided drug design, a screening approach refers to a process of screening a large number of small-molecules or fragments in biophysical or cell assays with the aim of finding a compound that would ultimately change the biological outcome of a protein target. One difficult task is to establish a robust, reliable, and reproducible screen using appropriate techniques. For HTS, not many biophysical techniques can meet the throughput requirements of HTS.[151] Additionally, identifying

an initial hit compound can be challenging if the techniques used for screening are not sensitive enough, as compounds need to exhibit micromolar affinities or even higher to be detected.[152] In HTS, a second validation screen of active analogues usually follows the hit identification, before the compounds undergo further optimization and biological evaluation to identify a lead compound. Fragment-based approaches to optimizing initial low molecular weight ligand hit include linking two fragments in near proximity into a larger small-molecule compound or progressively growing a fragment to maximize the contact with the protein target (Figure 3.2). Examples of successful fragment approaches have been extensively reviewed in the literature to date.[39,153]

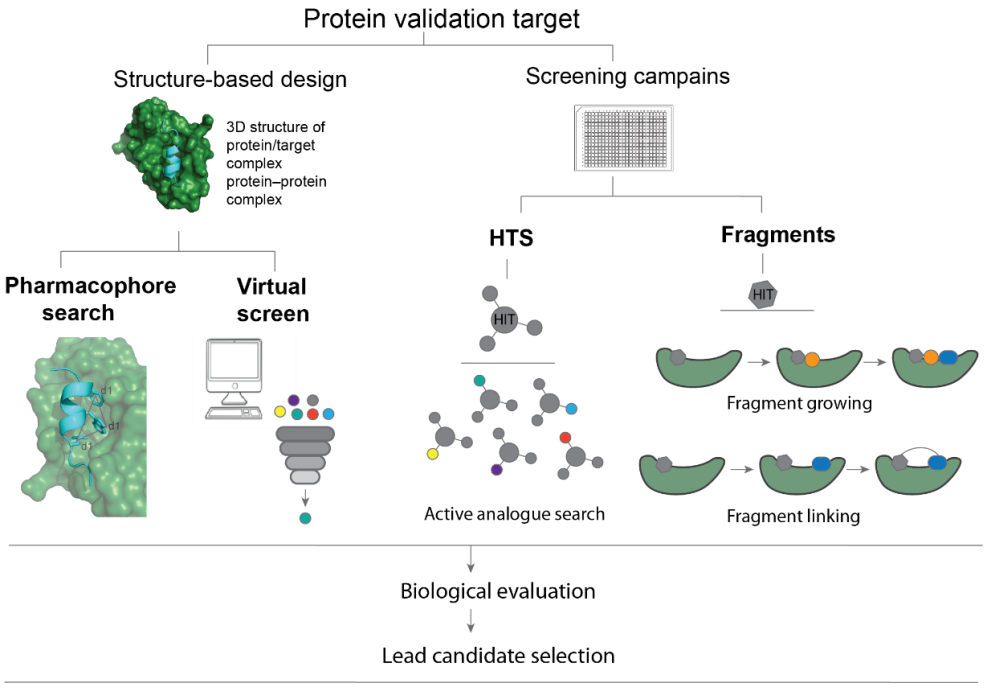

Figure 3.2 Different approaches in PPI drug discovery to identifying a lead compound.

Various biophysical techniques are used to study PPIs, each providing a different set of information from kinetics, thermodynamic to structural information. The different physical principles behind each biophysical technique dictates detection of binding, throughput, assay sensitivity and robustness, and what sample quantity is required to obtain quality data. The requirements these techniques have in common are non-aggregating compounds with high solubility, the protein target needs to be stable and well behaved at higher concentrations and certain techniques might require modification of one component in the assay (such as adding a fluorescent dye, immobilizing protein on a chip, etc).[154] However, the choice of which methods to use greatly depends on the drug discovery phase, as different

approaches will be taken at the hit-generating (HTS and FBS) to lead optimization stage, when the emphasis shifts from throughput to more information content.[155] Screens with readouts such as fluorescence (FA, FRET) or luminescence (AlphaScreen) satisfy the throughput requirements of HTS, but also TS (thermal shift) and MS can be altered to reach throughput and lower sample consumption by, for example, screening compounds in mixtures. After the first assessment to determine if the compound is binding-not binding to the target, complementary techniques are used to confirm the hit compound and answer questions such as: where does the compound bind (X-ray, NMR), what is the stoichiometry of binding (ITC), what are the kinetics of the compound binding (SPR), etc. FBBD usually employs more sensitive binding methods during the initial screening process (such as SPR, TS, NMR or X-ray) since small fragments bind with a millimolar K_d. Structural information about whether fragments bind at the PPI interface can be obtained by X-ray or NMR techniques and it is an important step for further hit optimization. Some of the most used biophysical methods used to study PPIs, their strengths and weaknesses, among other approaches have been extensively reviewed.[142,155]

3.2.1 Assay development

To screen small-molecule and fragment libraries against *h*DMX-367/14-3-3η using fluorescence anisotropy assay, several screening conditions had to be established. Firstly, choosing a protein/peptide concentration for a single-point screen had to be suitable for identification of both inhibitors and stabilizers. If the concentration was chosen around the K_d value, then an increase in anisotropy would indicate the stabilization effect of the interaction and similarly, a decrease in signal would suggest the inhibition effect (Figure 3.3a). With the assumption that a compound binds to the *h*DMX/14-3-3 complex as a 'molecular glue', an increased binding affinity of the complex increases fraction of the tracer bound to the protein and subsequently an increase in anisotropy is observed. Opposite, a decrease in signal would have been caused by a free fluorescent probe tumbling in solution if the compound is blocking the interaction with the protein. Thus, concentrations of 0.2 μM 14-3-3η protein and 50 nM of *h*DMX-367-FAM peptide were selected as suitable screening conditions giving a Z-factor of 0.72 (Figure 3.3b). The Z-factor indicates a statistical confidence of the assay and it was calculated using the equation 1, where σ- and σ+ are the standard deviations of max. and min. anisotropy values observed and μ- and μ+ are the corresponding mean values.[165] The Z-factor values between

0.5 and 1 indicate an excellent assay robustness and great separation between positive and negative controls (assay window).

$$\text{Equation 1.} \quad Z = \frac{3(\sigma- + \sigma+)}{(\mu- + \mu+)}$$

Secondly, the assay stability was tested by monitoring the changes in anisotropy of *h*DMX-367/14-3-3η in the presence of a compound (FCA) over a 24 h period at the rt. The assay plate was read at different time points: immediately after plating the assay, 1 h, 15 h and 24 h. Figure 3.3c shows that no significant change in anisotropy was observed between different time points suggesting that the equilibrium is reached rapidly and the protein stability was maintained. Thirdly, a competition assay was developed to be able to confirm the inhibitory effect of compounds lowering the anisotropy signal from the single-point screen. Acetylated *h*DMX-367 peptide (150 μM) was used to compete the fluorescently labeled analogue for binding to the 14-3-3η at the same concentrations used in the single-point screen (0.2 μM 14-3-3η protein and 50 nM of *h*DMX-367-FAM peptide). IC_{50} value of the unlabeled peptide was determined to be IC_{50}= 2 ± 0.2 μM by fitting the curve using logistic model in Origin. A complete list of screened compounds presented below can be found in the Digital Supplementary Material.

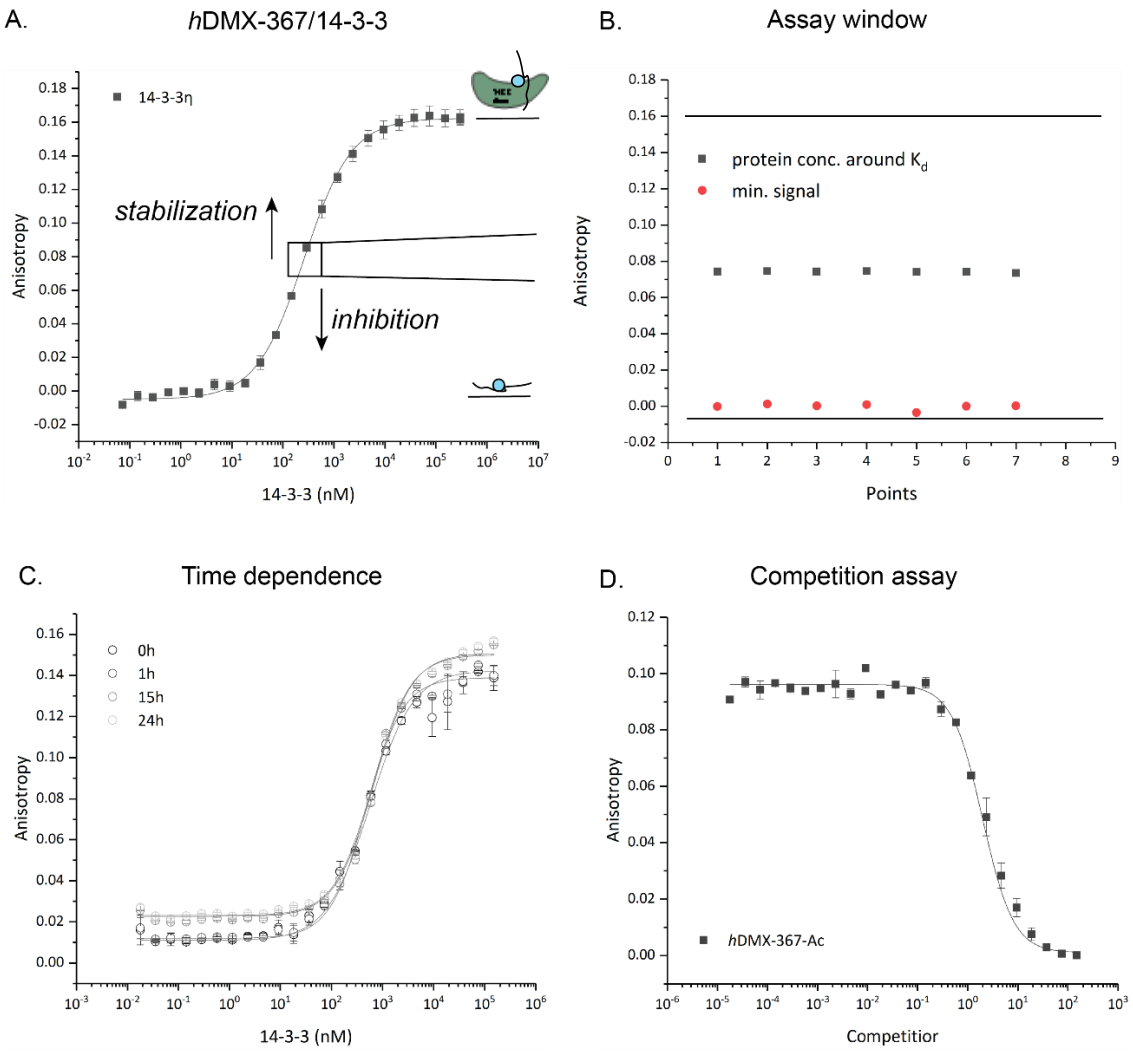

Figure 3.3 Assay development. A) Concentration for a single-point screen of fragments and small-molecules was chosen around the K_d value calculated from the *h*DMX-367/14-3-3η fluorescence anisotropy assay, as previously described in Chapter 2. B) Z-factor of the assay was calculated to be 0.72, with concentrations of 0.2 μM 14-3-3η and 50 nM fluorescently labeled *h*DMX-367 peptide (grey) and 50 nM *h*DMX-367 peptide only (red) as min. and max. points C) Time dependence of fluorescence anisotropy assays on the *h*DMX-367/14-3-3η in the presence of the natural product Fusicoccin-A (25 nM *h*DMX-367, 75 μM 14-3-3η, 25 μM FCA) D) Competition assay of acetylated *h*DMX-367 against fluorescently labeled *h*DMX-367 peptide with 14-3-3η, IC_{50}= 2 ± 0.2 μM (150 μM *h*DMX-367-Ac, 50 nM *h*DMX-367-FAM, 0.2 μM 14-3-3η, in 10 mM HEPES, 150 mM NaCl, 0.1% Tween 20, pH 7.4)

3.2.2 Screening of Maybridge fragments

A library of 1000 fragments provided by the Foster group, commercially available from Maybridge, was used in a blind screen using a FA single-point assay (structures of fragments were provided after hit compounds were identified). In FBBD, weak affinities demonstrated by fragments present a significant challenge for screening, thus a high concentration screening approach was applied. This concept implies performing an assay in typically higher concentrations of fragments than usual (from 250 μM to 5 mM), although using high concentrations of fragments in screening may result in detection of false positives and negatives due to compound aggregation and lack of solubility.[166]

For this primary screen of the Maybridge library, 2.5 mM of each fragment were mixed with 0.2 μM 14-3-3η protein, 50 nM of *h*DMX-367-FAM peptide in a 384-format and resulting anisotropies were compared to a DMSO control wells (DMSO was always kept below 5% in all experiments). The screening results are shown in Figure 3.4a where each dot represents a fragment with error bars representing the standard deviation of 2 repeats. Figure 3.4b shows anisotropy of the same 1000 fragments mixed with protein only as an additional control, i.e. no anisotropy change should be observed for the mixture of fragments and proteins in the absence of peptide. From this, 11 fragments showing an increase in anisotropy (panel A-green dots), but not changing the anisotropy in the absence of the peptide (panel B-green dots) were chosen as initial stabilizing fragment hits. Similarly, 10 fragments showing a decrease in anisotropy (panel A-red dots), but not changing the anisotropy in the absence of the peptide (panel B-red dots) were chosen as initial inhibitory fragment hits. Other fragments showing a clear (de)increase in anisotropy for both test wells (fragment, protein, peptide) and control wells (fragment, protein) were discarded as false positives. An example of such a fragment is showed as a blue color dot on both panels A and B on Figure 3.4.

The first 500 fragments were retested (due to sample availability) in the same setup with a lower protein concentration to expand the ‘stabilization assay window’, to possibly identify more fragments stabilizing the *h*DMX/14-3-3 interaction. The fragment and peptide concentrations were kept the same, while protein concentration was lowered from 50% to fit only 20% occupancy. Figure 3.4c shows an additional 9 fragments exhibiting an increase in anisotropy while not changing the anisotropy in control wells as showed on Figure 3.4d. In total, 21 stabilizing and 10 inhibiting

fragments were chosen for further characterization in direct titration or competition assays and their structures are shown on Figure 3.5.

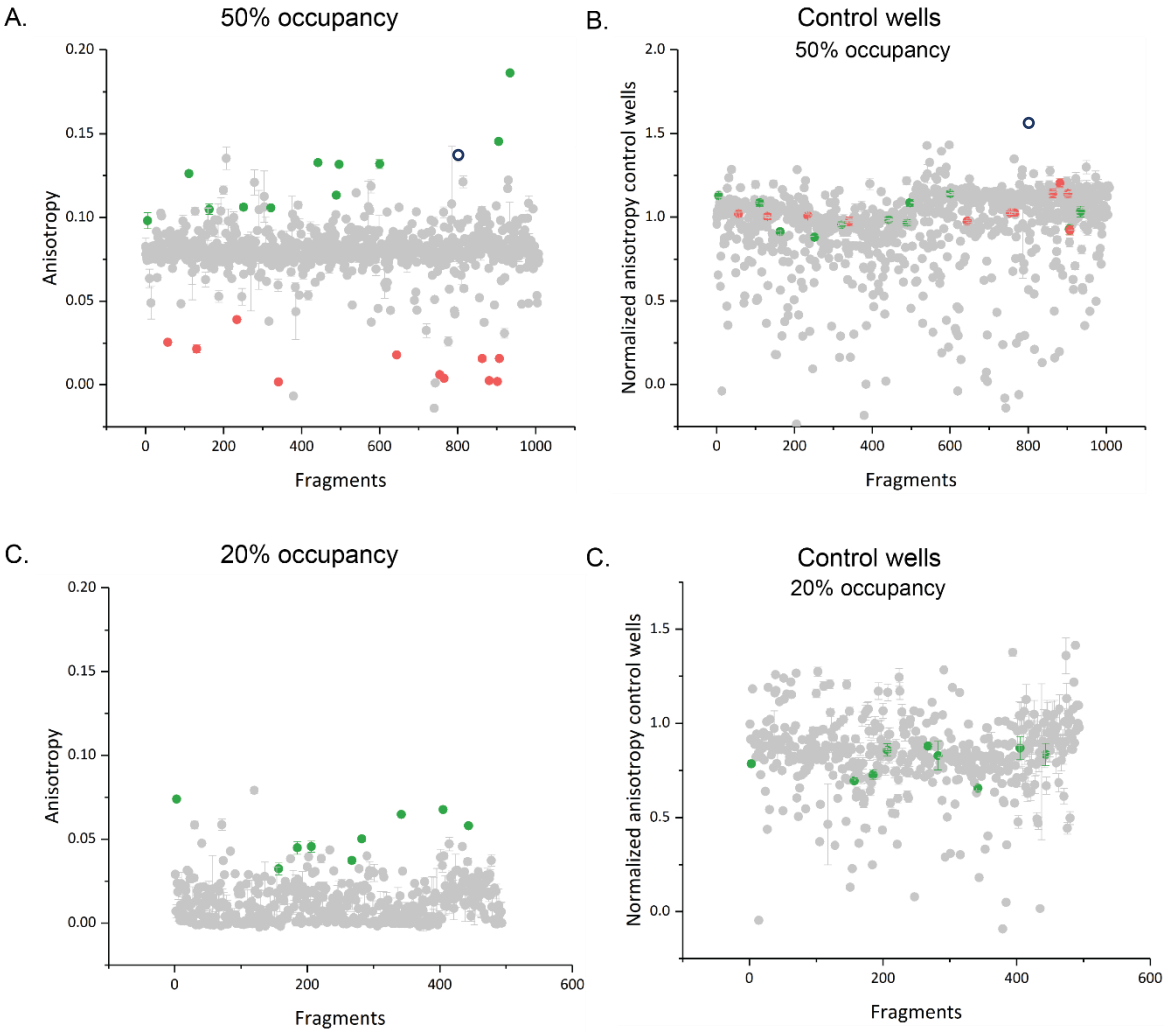

Figure 3.4 Single point screen of Maybridge fragment library. A) Anisotropy calculated for each fragment (fragments tested in duplicates, each fragment represented as a dot) mixed with 14-3-3η and *h*DMX-367 peptide (0.2 μM protein, 50 nM peptide, 2.5 mM compound) and compared to DMSO. 11 fragments were identified as possible stabilizers (green dots) and 10 fragments as inhibitors (red dots). B) Anisotropy of control wells (fragment and protein only, no peptide). Fragments identified as hits changed the anisotropy was observed from panel A, but not caused changes in anisotropy from panel B. C) Anisotropy calculated for fragments with 14-3-3η and *h*DMX-367 peptide at 20% occupancy. Additional 9 fragments were identified as possible stabilizers (green dots) D.) Anisotropy of control wells from panel C.

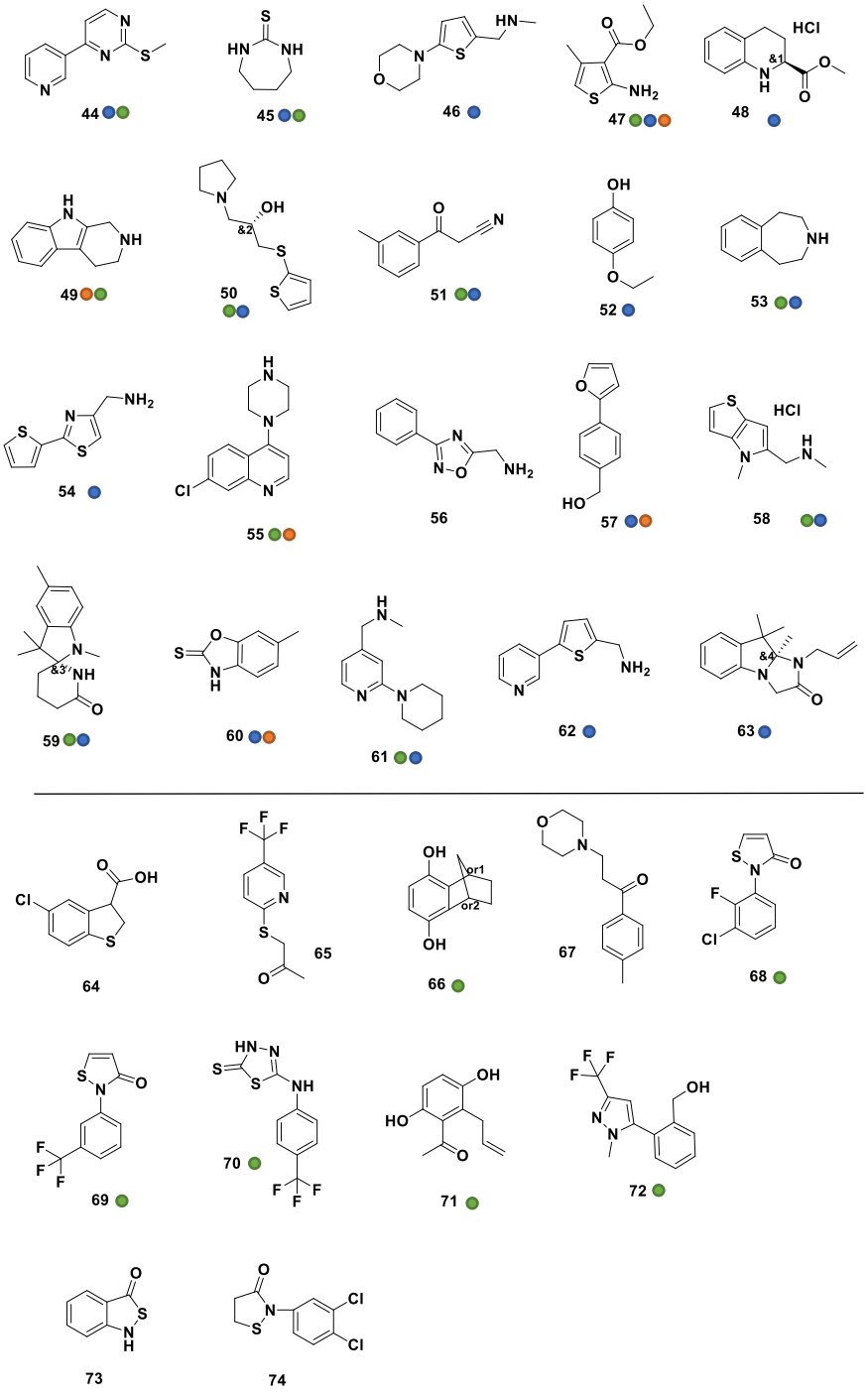

Figure 3.5 Structure of hit compounds identified from a single point FA screen. Fragments **44**-**63** were identified as stabilizers and **64**-**74** as inhibitors. Green dots represent fragments confirmed in a dose-response assays in FA, blue dots by SPR and the orange dots by NMR.

All 20 fragments indicating a stabilization effect were tested in a dose response assay where 14-3-3η protein was titrated against the constant concentration of fragments (2.5 mM) with a *h*DMX-367 peptide and compared to DMSO as a control. As an example, Figure 3.6 shows the modest stabilization effect fragment **55** (in green) had in comparison to a DMSO control (in grey), where the K_d value shifted only from 151.5 ± 11.8 nM to 70.7 ± 1.0 nM in the presence of a fragment. Shifting of the titration curves were expected to reflect the 'stabilization effect' of fragments and the changes in the binding affinities. However, fragments overall had no significant effect on the *h*DMX/14-3-3 interaction in terms of lowering the K_d values, as plotted curves were often overlapped with a DMSO control (see Appendix, Figure A.5.1). This observation is not surprising due to low fragment affinities and molecular weight.

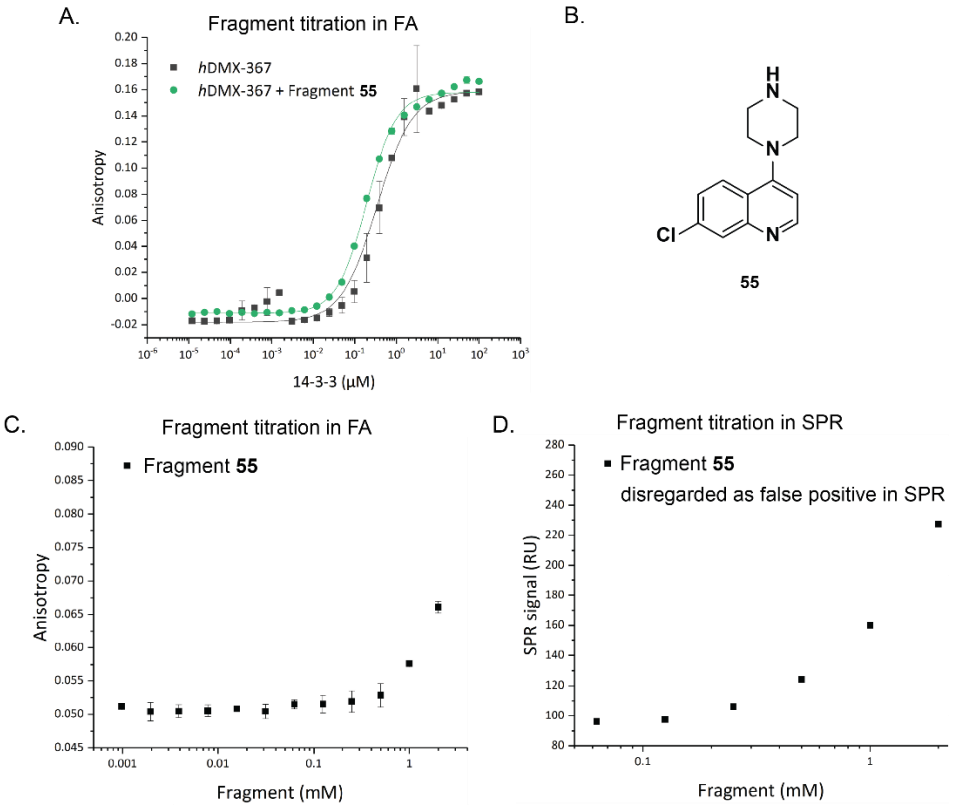

Figure 3.6 Hit conformation of Maybridge fragment **55**. A. Dose response of *h*DMX-367-FAM, 14-3-3η, Fragment **55** in green (100 μM 14-3-3η titrated, 50 nM tracer, 2.5 mM fragment in HBS buffer: 10 mM HEPES, 150 mM NaCl, 0.1% Tween 20, pH 7.4) compared to a DMSO control in grey. Fragment 12 shifted the K_d value form to 151.5 ± 11.8 nM to 70.7 ± 1.0 nM. B. Fragment **55** structure C. Fragment titration using FA (2.5 mM fragment **55** was titrated against the constant concentration of peptide and tracer: 0.2 μM of 14 3 3η and 50 nM of hDMX 367 peptide) D. Fragment titration using SPR (a serial dilution of fragment **55** (2 mM being the highest concentration, 2% (v/v) DMSO) with a constant concentration of 50 nM of acetylated *h*DMX-367 peptide was prepared and flown over the protein immobilized on surface).

Confirming the activity of small size and low affinity fragments using this approach did not seem feasible. Thus, a different approach was taken where the same conditions from the single-point screen were replicated. In this way, 2.5 mM of fragments were titrated against the same fixed concentrations used in the screening: 0.2 μM of 14-3-3η and 50 nM of *h*DMX-367 peptide, and titrations of fragments without the protein were taken as a control (Fragment **55** as an example on Figure 3.6b, all 20 fragment titrations can be found in Appendix, Figure A.5.2). Fragments **46**, **48**, **56** and **57** showing an increase in anisotropy in the absence of protein were disregarded as false positives due to interference with the fluorescent probe (see Appendix, Figure A.5.3). Since the fragments were showing a modest increase in anisotropy only at the highest concentration, accurate estimation of the binding affinities could not be determined. Instead, fragments indicating an increase in anisotropy without interfering with the fluorescent probe were taken forwards as fragments that bind to the *h*DMX/14-3-3 complex. In total 11 fragments were confirmed as stabilizing fragments (marked on Figure 3.5 as green dots), 4 were disregarded as false positives and 5 fragments showed no activity.

Next, SPR was used as an orthogonal assay to counter-screen 20 fragments identified from a single-point FA screen. 14-3-3η was immobilized on a chip surface in much higher density than previously described for kinetic studies to amplify the signal from the binding fragments (as described in Chapter 5). A serial dilution of fragments (2 mM being the highest concentration, 2% (v/v) DMSO) was prepared with 50 nM of acetylated *h*DMX-367 peptide which was kept constant. The same concept of varying the fragment concentration was applied in the screening by SPR, where the analyte (*h*DMX-367 peptide with serially diluted fragments) was flown over the protein immobilized on a surface causing the increase in response units (RU) upon binding. Observed RU signals for all 20 fragments were then plotted against fragment concentration as shown in Appendix, Figure A.5.2 (Fragment 12 as an example on Figure 3.6c). Only 3 fragments (**49**, **55** and **56**) were disregarded as nonspecific binders due to high signal observed on a reference cell with no immobilized protein, leaving 17 fragments to be identified as stabilizers by SPR (marked on Figure 3.5 as blue dots).

NMR was used alongside FA and SPR as a third orthogonal technique to confirm true binders among 20 fragments identified as potentional stabilizers. WaterLOGSY and STD experiments were set up at the Asbury center with the help of Dr Arnout Kalverda. ^{15}N-^{2}H 14-3-3Δσ labeled protein was provided by Dr. Isabelle

Landrieu and Dr. João F. Neves, while HSQC experiments and data analysis were performed by Dr. Fruszina Hobor.

Ligand-based NMR is suitable for fragment screening as low affinity fragments can be detected by measuring the changes in intensity or relaxation of fragment protons in the presence of the target protein.[167] Only low amounts of isotopically unlabeled protein are necessary to determine binding of fragments and multiple NMR experiments can be run on only one prepared sample. Additionally, previously shown benefits of using NMR in screening of fragments libraries targeting 14-3-3 interface was another major reason this approach was taken.[168] Ligand based techniques, Water-LOGSY and STD, were first used to narrow down fragment hits. 19 fragments were subjected to an NMR screen as each fragment has been previously confirmed in either or both, FA and SPR; only fragment **56** was characterized as false positive in both assays and disregarded. Both Water-LOGSY and STD NMR experiments were performed by recording a spectra of fragments (500 µM) in the presence or in the absence of 14-3-3η protein (25 µM) and *h*DMX-367-Ac peptide (50 µM). The two spectra were always overlapped for each experiment, where spectra of fragments alone are showed in black and the second spectra of fragment with protein and peptide is shown in red (Figures 3.7-3.11). Fragments showing binding in both complementary techniques were taken forwards as hit fragments. In Water-LOGSY experiments a signal is observed as a result of magnetization transfer from bulk water upon ligand binding. The binding events are easily identified by peak inversion, as bound fragments can be identified by positive resonances while non-binding fragments remain a negative resonance. Panel A on Figures 3.7-3.11 shows Water-LOGSY signal phased positive indicating binding was confirmed for 5 fragments. A complete inversion of peaks was observed for fragments **47**, **57** and **60**, while fragments **49** and **55** showed disappearance of negative resonances (in red). The control spectra of fragments alone are all phased negative (in black). In STD experiments a signal is observed when ligand protons are in contact with a protein target and consequently receive a higher degree of saturation, as a result of being in close proximity. Thus, a signal would not be observed in non-binding ligands. Panel B on Figures 3.7-3.11 shows STD spectra comparing fragments (in black) in presence of protein and peptide (in red). STD NMR signals were observed for fragments **47**, **49**, **55**, **57** and **60** which were identified as binders.

Lastly, the 5 fragments showing a positive effect in at least two techniques were submitted for final confirmation by ^{1}H-^{15}N HSQC to determine an approximate binding site of the fragments. To do so, spectra was recorded of 50 µM 14-3-3Δσ in the

presence of 2 mM fragment. Each peak in the spectrum reports on the local chemical environment of the resonant nuclei, which is characteristic for each individual protein residue. Upon binding, the chemical shifts of protein residues affected by binding will change (CPS, in ppm). Those changes were compared to the assigned spectrum of 14-3-3Δσ for each fragment (as shown on panel C in each figure) and visualized by marking them in red on a crystal structure of 14-3-3σ in Pymol (as shown on panel D in each figure). In all 5 cases, a significant change in chemical shift perturbation was evident for two peaks, D211 and T217 on 14-3-3σ. Position of D211 is close to the FCA binding pocket and near to the peptide binding groove, which would indicate these fragments bind close to the *h*DMX/14-3-3 interface. Considerable chemical shift perturbations of D211 were detected among three fragments (**47**, **49** and **55**), but the other two fragments (**57** and **60**) were found to bind on multiple sites on the 14-3-3σ, which was again not surprising for an initial fragment screen.

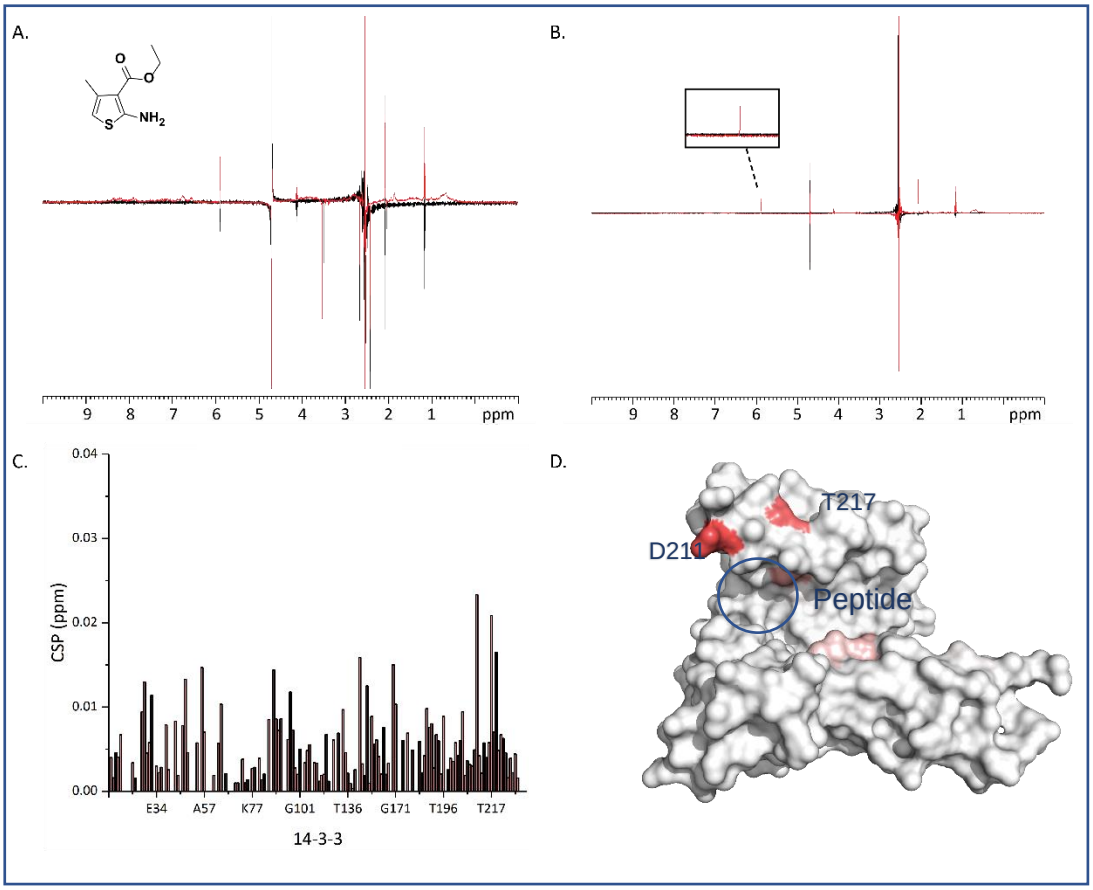

Figure 3.7 NMR screening results for Fragment **47**. A) Water-LOGSY B) STD spectra obtained with 25 µM 14-3-3η, 50 µM *h*DMX-367-Ac, 500 µM fragment, fragment only spectra showed in black; fragment, protein, and peptide in red (100 mM Phosphate buffer, 50 mM NaCl, pH 6.8, 10% dH_2O, 0.5% (v/v) DMSO) C) Chemical shift perturbations (in ppm) of 50 µM 14-3-3Δσ in the presence of 2 mM fragment **47**, plotted (100 mM Phosphate buffer, 50 mM NaCl, 1 mM DTT, 10% dH_2O, pH 6.8) D) Determining the binding site of fragment **47** on a 14-3-3σ by mapping affected resonances upon binding. Blue circle indicates binding site of FCA next to the peptide binding groove on 14-3-3 proteins.

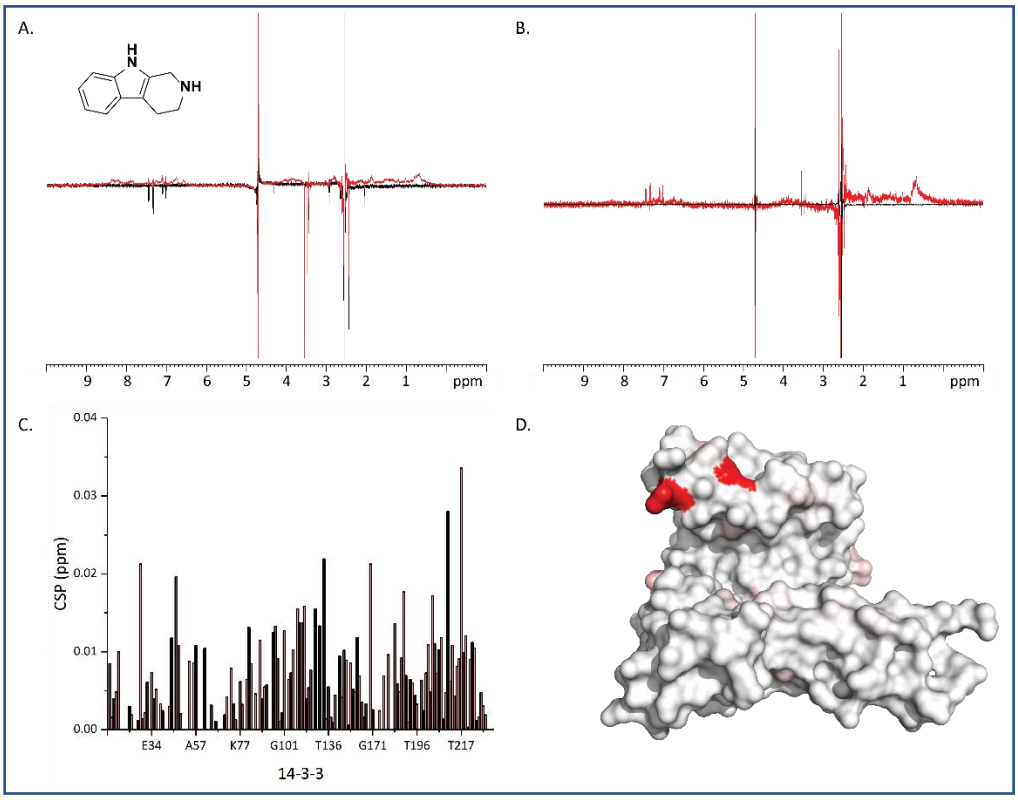

Figure 3.8 NMR screening results for Fragment **49**.

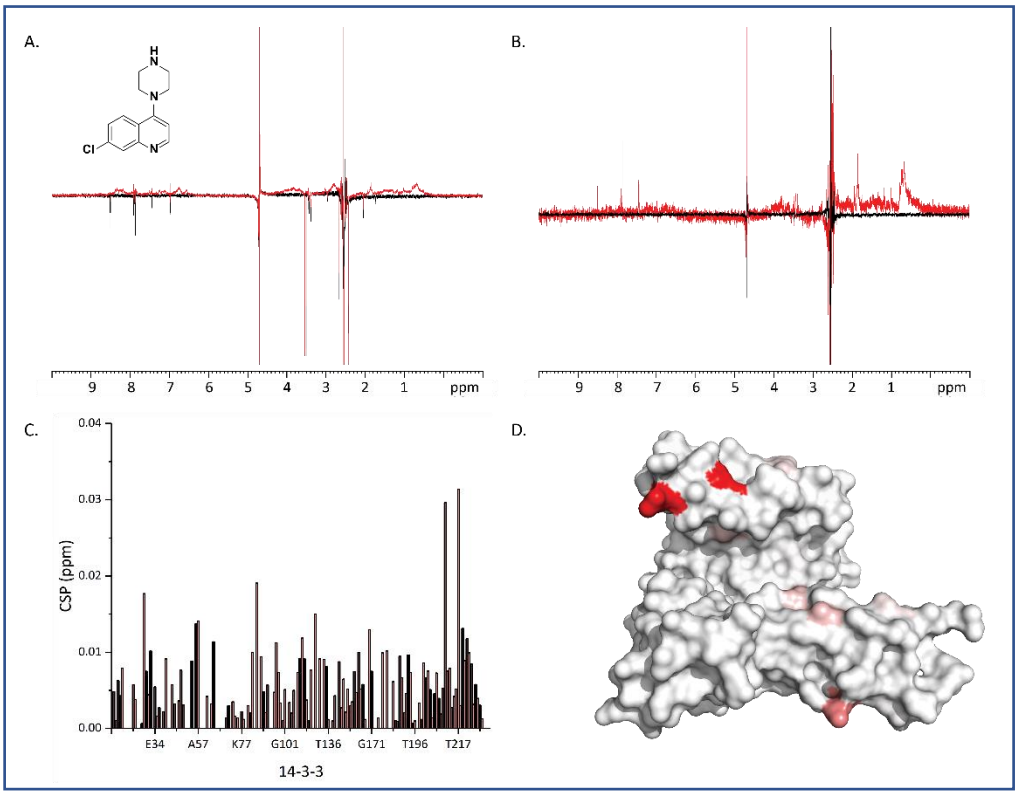

Figure 3.9 NMR screening results for Fragment **55**.

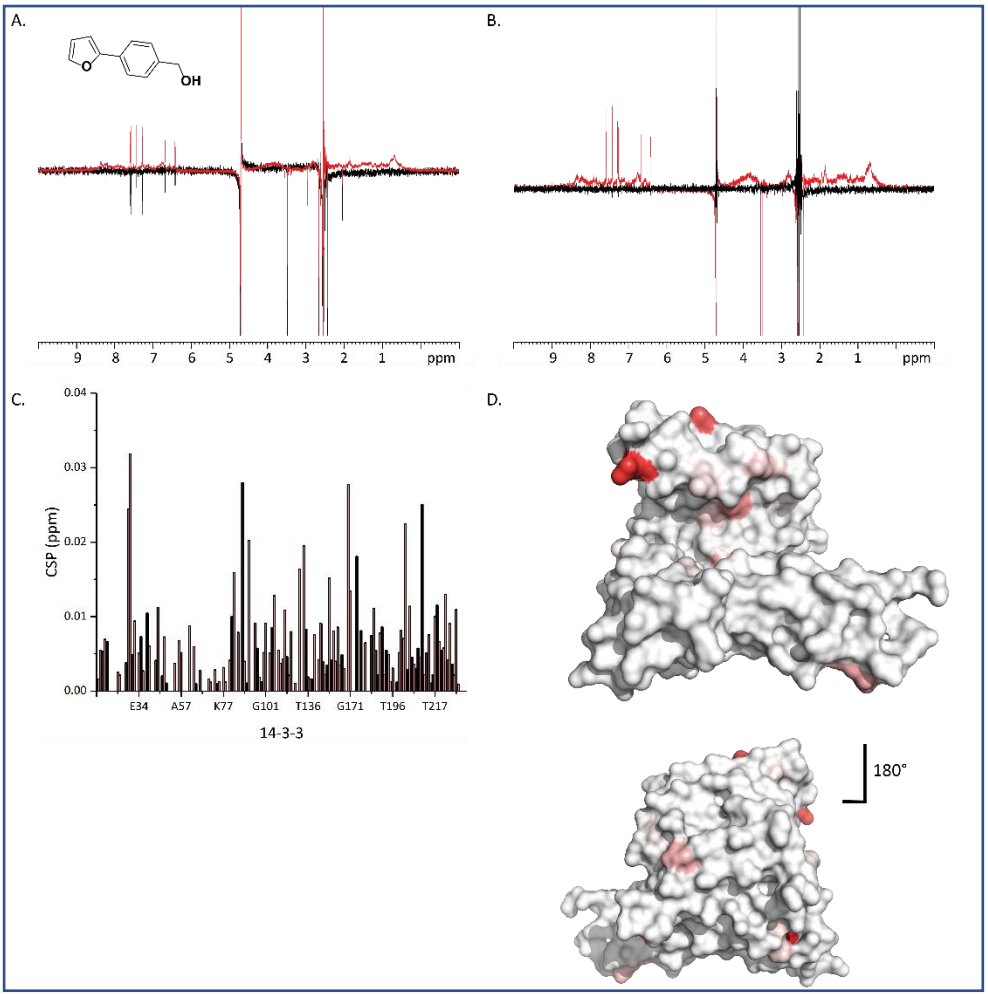

Figure 3.10 NMR screening results for Fragment **57**.

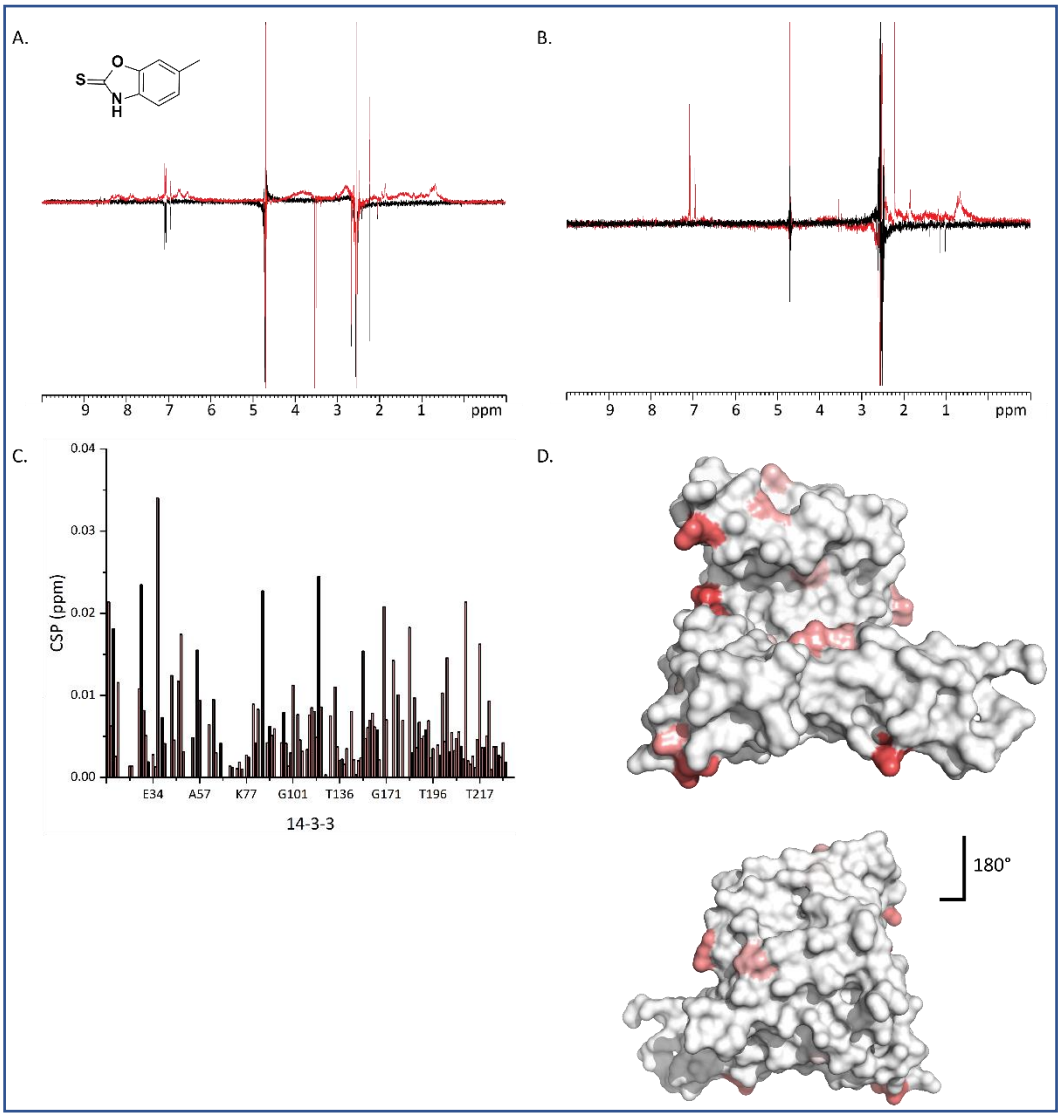

Figure 3.11 NMR screening results for Fragment **60**.

Beside the 20 fragments identified as potentially having a stabilizing effect from the single-point screen, a further 11 fragments were also shown to decrease anisotropy, indicating an inhibitory effect. Those 11 fragments were then tested in a competition assay where fragments were titrated against 14-3-3η and *h*DMX-367, replicating concentrations used in a single-point screen. A decrease in signal is observed as fluorescently labeled peptide is displaced from the protein complex. The obtained data was then fitted using logistic function in Origin and IC_{50} values are reported in Table 3.1. Figure 3.12 shows fragment titrations where the fit followed the titration curve and accurate IC_{50} could be obtained. Competition assay plots of other 5 fragments can be found in Appendix, Figure A.5.4. However, further characterization of fragments in orthogonal assays is needed, especially as the most potent fragments seemed to be the isothiazolones, one of the most commonly identified Pan-Assay Interference Compounds (PAINS).[169]

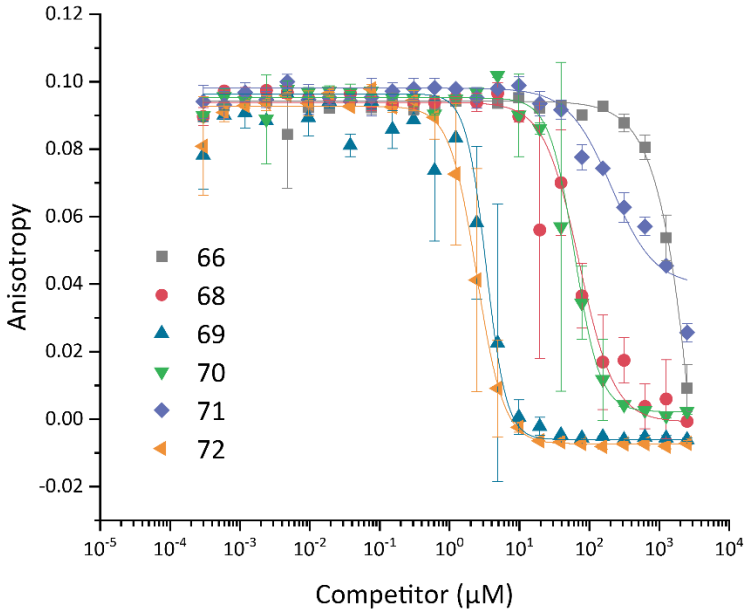

Figure 3.12 Competition assay for fragments identified as inhibitors. 2.5 mM fragments were titrated against a constant concentration of protein and peptide, as used in the a single-point screen (0.2 µM 14-3-3η, 50 nM *h*DMX-367-FAM, in HBS buffer: 10 mM HEPES, 150 mM NaCl, 0.1% Tween 20, pH 7.4).

Table 3.1 The IC_{50} values for Maybridge fragments inhibitors

Fragment	**66**	**68**	**69**	**70**	**71**	**72**
IC_{50}	6.5 ± 1.8 mM	71.3 ± 1.2 µM	3.3 ± 2.4 µM	61.5 ± 6.7 µM	205.9 ± 8.1 µM	2.4 ± 2.6 µM

3.2.3 Screening of PPI-net library

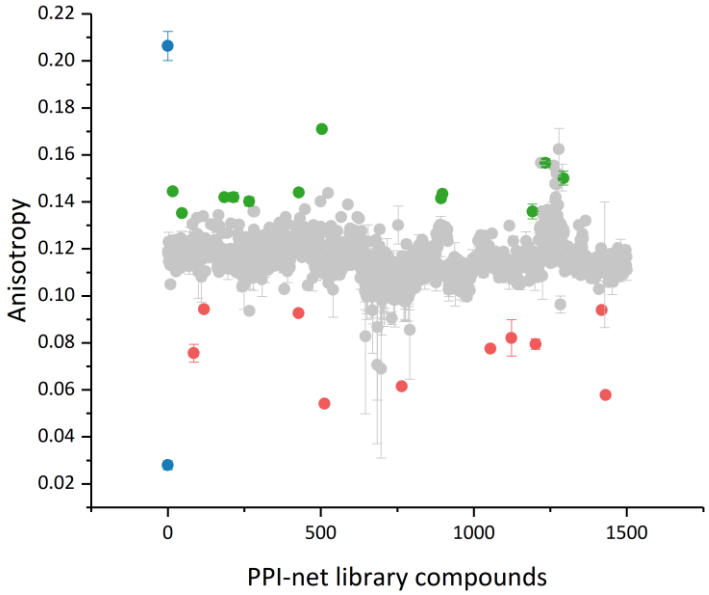

Figure 3.13 Single point assay PPI library. Anisotropy calculated for each compound (compounds tested in duplicates, each fragment represented as a dot) mixed with 14-3-3η and *h*DMX-367 peptide (0.2 μM protein, 50 nM peptide, 500 μM compound, in 10 mM HEPES, 150 mM NaCl, 0.1% Tween 20, pH 7.4). Anisotropy obtained for the compounds was compared to a DMSO control, and the minimal anisotropy was obtained with 50 nM of *h*DMX-367 peptide and maximal anisotropy by 300 μM 14-3-3η and 50 nM of *h*DMX-367 peptide. Error bars represent the standard deviation of 2 repeats. 12 stabilizing (green dots) and 10 inhibitory (red dots) compounds were selected for a follow-up confirmation in dose response and competition assay.

The PPI-net library was screened as a collection of 1534 compounds commercially available from Asinex. Screening was carried out by measuring the anisotropy signal for 500 μM of each compound with 0.2 μM 14-3-3η protein, 50 nM of *h*DMX-367-FAM peptide using 384-format. The raw data was then compared to a DMSO control as shown in Figure 3.13. Additional control experiments with testing the compounds and protein were only carried out for Maybridge library due to availability of the samples. Blue dots on the Figure 3.13 represent minimal (tracer only) and maximal anisotropy (the highest concentration of 300 uM protein and 50 nM tracer), due to lack of known stabilizing and inhibitor compounds that could be used as 'true' positive and negative controls. In total, 12 compounds were chosen for a dose response assay to confirm their stabilization effect, as well as 11 inhibitory compounds to be tested in a competition assay.

In a dose response assays, 50 μM protein was titrated against 50 nM of *h*DMX-367-FAM peptide in the presence of 500 μM of compounds. Overall, titrations of 12 stabilizing compounds significantly overlapped with a DMSO control, indicating

none of the compounds have a significant stabilization of *h*DMX-367/14-3-3η interaction (see Appendix, Figure A.5.5). A maximal left shift of the curve was observed for compound **75** as shown on Figure 3.14, however, the K_d obtained when fitting the data remained similar to a DMSO control (105.8 ± 13.7 nM in comparison to a control of 100.8 ± 9.1 nM). In a competition assay, 150 μM of compounds were titrated against 0.2 μM 14-3-3η and 50 nM of *h*DMX-367-FAM. From 10 compounds tested in a competition assay, only compound **76** has displaced a tracer from the protein complex, while other 9 compounds were shown not to be active (see Appendix, Figure A.5.5). The IC_{50} value for compound **76** was calculated to be 22.0 ± 1.7 μM.

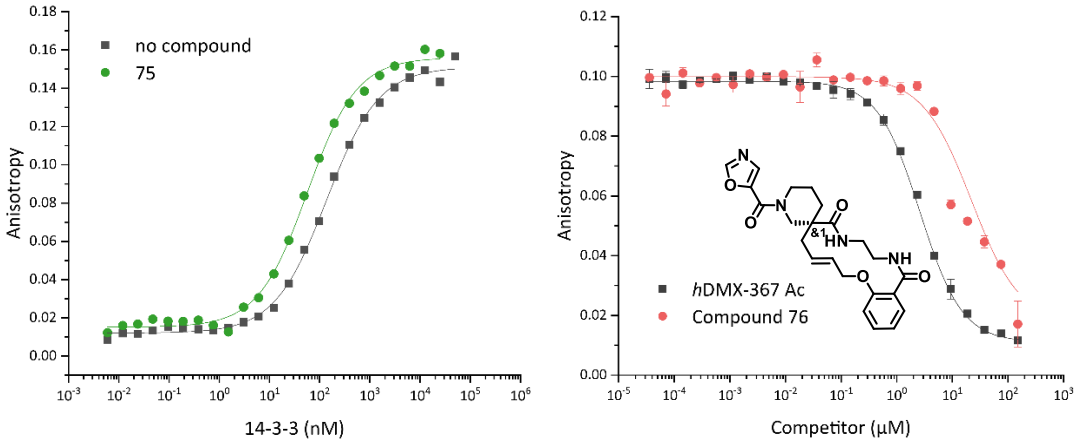

Figure 3.14 Dose response of *h*DMX-367-FAM, 14-3-3η, compound **75** in green (50 μM 14-3-3η, 50 nM tracer, 500 μM compound) compared to a DMSO control in grey. Titrations were carried out with lower amount of protein and in single repeat in an initial testing phase. The K_d value remained unchanged in the presence of compound **75**. Competition assay for a compound **76** identified as an inhibitor. 150 μM of compound (in red) and of *h*DMX-367-Ac (in grey) were titrated against a constant concentration of protein and peptide, as used in the a single-point screen (0.2 μM 14-3-3η, 50 nM *h*DMX-367-FAM, in HBS buffer: 10 mM HEPES, 150 mM NaCl, 0.1% Tween 20, pH 7.4). IC_{50} values were determined by plotting the data using logistic fuction in Origin. Reported IC_{50} for compound **76** was 22.0 ± 1.7 μM in comparison to a peptide control 2.6 ± 0.1 μM

None of the compounds were chosen for a counter screen using other orthogonal techniques since a small stabilizing effect was only observed with already drug like compounds, thus further characterization and optimization was not thought to be a priority in terms of finding a potent and selective small-molecule stabilizer.

3.2.4 Screening of small library of 14-3-3 protein modulators

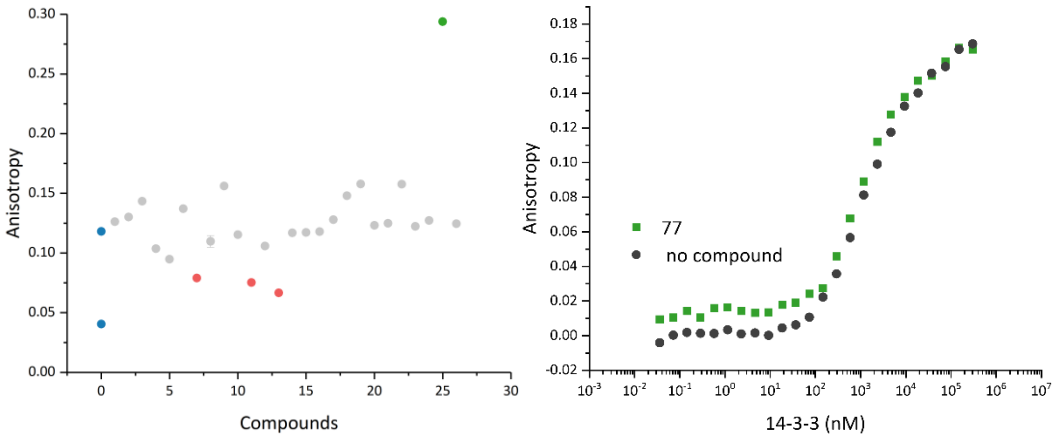

Figure 3.15 Screening of a library of 14-3-3 protein modulators. Anisotropy for a single-point screen was calculated for each compound (each fragment represented as a dot) mixed with 14-3-3η and *h*DMX-367 peptide (0.2 μM protein, 50 nM peptide, 500 μM compound, in 10 mM HEPES, 150 mM NaCl, 0.1% Tween 20, pH 7.4). Anisotropy obtained for the compounds was compared to a DMSO control, and the minimal anisotropy was obtained with 50 nM of *h*DMX-367 peptide (blue dots). 1 stabilizing (green dot) and 3 inhibitory (red dots) compounds were selected for a follow-up confirmation in dose response and competition assay. Dose response of *h*DMX-367-FAM, 14-3-3η, compound **77** in green (50 μM 14-3-3η, 50 nM tracer, 500 μM compound) compared to a DMSO control in grey.

A small library of 29 compounds initially developed as 14-3-3 protein modulators, were provided by TASPPI consortium members (University of Sienna) to be screened against *h*DMX and 14-3-3 proteins. Exact structures of the compounds were not disclosed. The same principle and concentrations from the single-point screen was used as with compounds from the PPI-net library. Figure 3.15 shows anisotropy of compounds to a DMSO control. Compound **77** was tested in a dose-response assay, but no activity was observed (compound **77** in green, control in grey). This might be identified as the assay interference compound since the anisotropy values were observed outside of the usual maximal signal range. 3 compounds were also tested in a competition assay as potential inhibitors (shown as red dots on Figure 3.11). None of the compounds were found active outside of a single-point screen, see competition assay titrations in Appendix, Figure A.5.7.

3.2.5 Screening of Taros fragments

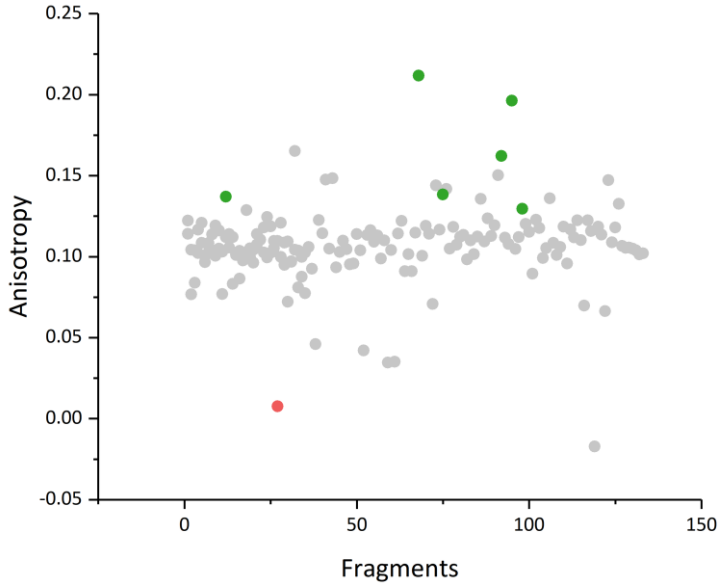

Figure 3.16 Single point assay Taros fragment library. Anisotropy calculated for each compound (compounds tested in duplicates, each fragment represented as a dot) mixed with 14-3-3η and *h*DMX-367 peptide (0.2 μM protein, 50 nM peptide, 2.5 mM compound, in 10 mM HEPES, 150 mM NaCl, 0.1% Tween 20, pH 7.4). 6 stabilizing (green dots) and 1 inhibitory (red dots) fragment cocktails were selected for a follow-up confirmation in dose response and competition assay.

A Taros collection of 136 fragment cocktails, each containing 5 fragments, were provided by TASPPI collaborators (Taros, Dario Valenti) without disclosing the structure of fragments. A FA assay was used to screen all fragment cocktails in the same manner as described previously. Figure 3.16 shows anisotropies for each cocktail fragments in comparison to a DMSO control. In total, 7 cocktail fragments were chosen depending on sample availability to be screened in dose response assay. For each fragment cocktail, five dose response titrations were performed where the protein was titrated against tracer in the presence of a fragment. No stabilization effect was observed for any of the fragments, as presented by titration curves overlapping with a DMSO control (see Appendix, Figure A.5.8). However, fragment **80** showed a significant right shift of the curve indicating an inhibitory effect. This fragment was tested in a competition assay, as shown on Figure 3.17, and IC_{50} was compared to a *h*DMX-367-Ac peptide (fragment IC_{50}= 20.3 ± 1.0 μM, peptide control IC_{50}= 1.7 ± 0.1 μM).

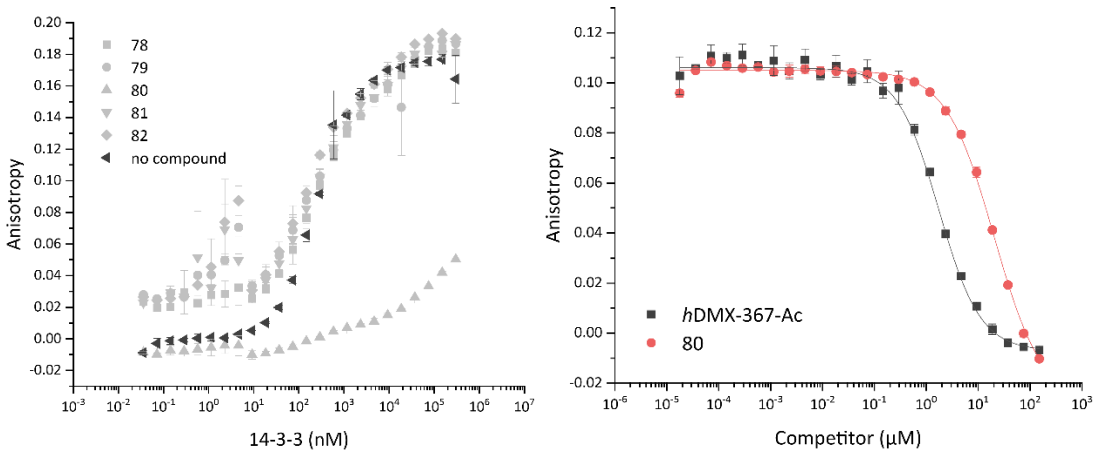

Figure 3.17 Taros fragments were tested in a direct titration. 14-3-3η protein (200 μM) was titrated against the constant concentration of fragments (2.5 mM) and tracer (50 nM *h*DMX-367). In competition assay fragment was titrated against protein and tracer (150 μM fragment and *h*DMX-367-Ac, 0.2 μM 14-3-3η and 50 nM *h*DMX-367-FAM)

3.2.6 Discussion and summary of the screening efforts

To summarize, an FA assay was developed to screen libraries of fragments (Maybridge and Taros) and small-molecules (PPI-net library and a library of 14-3-3 protein modulators) in hopes of finding a compound stabilizing the *h*DMX-367/14-3-3η interaction. To efficiently screen compounds using FA as a primary screen, a Z factor was calculated to determine appropriate concentrations where both inhibitors and stabilizers can be detected. By choosing a concentration around the K_d value, an excellent assay window was found with the Z factor of 0.72. However, when choosing a concentration where the inhibitors would be detected it is done at the expense of detecting stabilizers, and vice versa (Figure 3.3a-b). Next, time course measurements confirmed 14-3-3η protein stability over the period of 24 h and the competition assay was developed where the acetylated *h*DMX-367 peptide was competing off its fluorescently labelled analogue prior to any screening being done.

FA was chosen as a screening method as discovery of compounds altering the anisotropy values through changes in the tumbling rate of the fluorescent probe is relatively straightforward. In practice, determining true hits from the single-point screen turned out to have its challenges, especially for the detection of stabilizers. Although FA is a widely accessible technique in HTS, it was not proved to be an ideal first choice for screening challenging PPIs, such as *h*DMX-367/14-3-3 protein

interactions. A blind screening of PPI-net library and small library of 14-3-3 protein modulators resulted in the detection of numerous false-positive compounds. This screening was carried out prior to solving the crystal structure of *h*DMX-367/14-3-3σ, where now the structural information is available for a better designed approach. In the crystal structure *h*DMX-367 peptide has more of a linear shape and occupies the whole amphipathic groove of 14-3-3σ, not leaving any space for a drug like molecule to bind (Figure 2.14). Specifically, PPI-net library[170] was designed to target challenging PPIs, consisting of α-mimetics and macrocycles, which was not found suitable for stabilization of the *h*DMX-367/14-3-3η system. The lack of appropriate (positive) controls is another reason that has made the screening even more challenging. All 14-3-3 stabilizing compounds up to date bind in the FCA binding pocket of the C-terminus peptide binding 14-3-3 proteins, thus FCA is often used as a positive control and this was not applicable for the *h*DMX-367/14-3-3η interaction.

Another challenge was to confirm identified fragments from the single-point screen in a dose response assays. A clear left shift of the titration curves in the presence of fragments was not observed due to the lower affinities small molecular weight fragments have. This was the case for 35 individually tested Taros and 20 Maybridge fragments. To confirm that the increase of signal from the single point screen was accurate, fragment titrations were performed for the 20 Maybridge initial hits instead of protein titrations in the presence of fragments. Even then the increase in signal was observed towards the highest concentrations of fragments, indicating high micromolar affinity. Orthogonal assays were implemented as counter-screens to confidently identify binding fragments by combining SPR and NMR screening, where the number of binding fragments were narrowed down to five. In comparison to other screening techniques, NMR was found to be the most reliable in detecting the binding of fragments and minimize detection of false positives. This was most evident in case of fragment **55**, which was characterized as a false positive in SPR assay, but NMR indeed confirmed the fragments weak activity initially detected by FA screen. Also, protein NMR experiments show 5 fragments binding near the FCA binding pocket, which would offer a possibility to develop small-molecule compounds at the peptide/protein interface. The next steps would include solving a crystal structure of the soaked fragments as additional step to start fragment optimization. Nevertheless, this substantive screening campaign of more than 3000 compounds has identified 5 fragments binding with the modest stabilization effect on the *h*DMX-367/14-3-3 complex and narrowed down the number of fragments worth pursuing in further structural elucidation studies (fragment soaking) and subsequently the optimization of the fragments towards more potent and selective compounds.

3.3 Optimization of Pyrrolidone-based PPI stabilisers for selective *h*DMX/14-3-3 stabilization

Pyrrolidone1 (PYR1, **41**) was first identified as a small-molecule stabilizer of 14-3-3/plasma membrane H^+-ATPase (PMA) interaction showing *in vivo* activity as an activator of the plant proton pump.[171] The crystal structure of the ternary complex with 14-3-3 (the tobacco 14-3-3e isoform) and the C-terminal 30 amino acid long PMA2 peptide with PYR1 shows a small-molecule partially occupying the FCA binding pocket on the 14-3-3 protein, making minimal contact with the peptide (Figure 1.13d, same pocket occupied in Figure 3.18a). Most recently, SAR of PYR1 has been explored through a metal-ion chelation approach to selectively stabilize the 14-3-3/ERα interaction.[172] The highest resolution crystal structure of PYR1 was solved in complex with 14-3-3σ/ERα peptide which revealed a Mg^{2+} ion chelated by the carboxylate moiety of PYR1 (as shown on Figure 3.18b). Subsequently, this observation drove compound design employing intramolecular hydrogen bonds to mimic the observed chelation stabilization effect. In general, PYR1 was found to bind in the FCA binding pocket with its three phenyl groups pointing in different directions, occupying different pockets on 14-3-3 proteins (Figure 3.18b). Figure 3.18c shows a more detailed representation of the PYR1 binding mode, where the salicylate moiety makes contact with 14-3-3σ through interactions with R41, N42 and E155, and the hydrogen bond between nitro group of PYR1 and K122 on 14-3-3σ.

As part of a secondment carried out at Astra-Zeneca, a small library of 20 PYR1 analogues was synthesized and screened as potential stabilizers of *h*DMX-367/14-3-3η using FA assay.

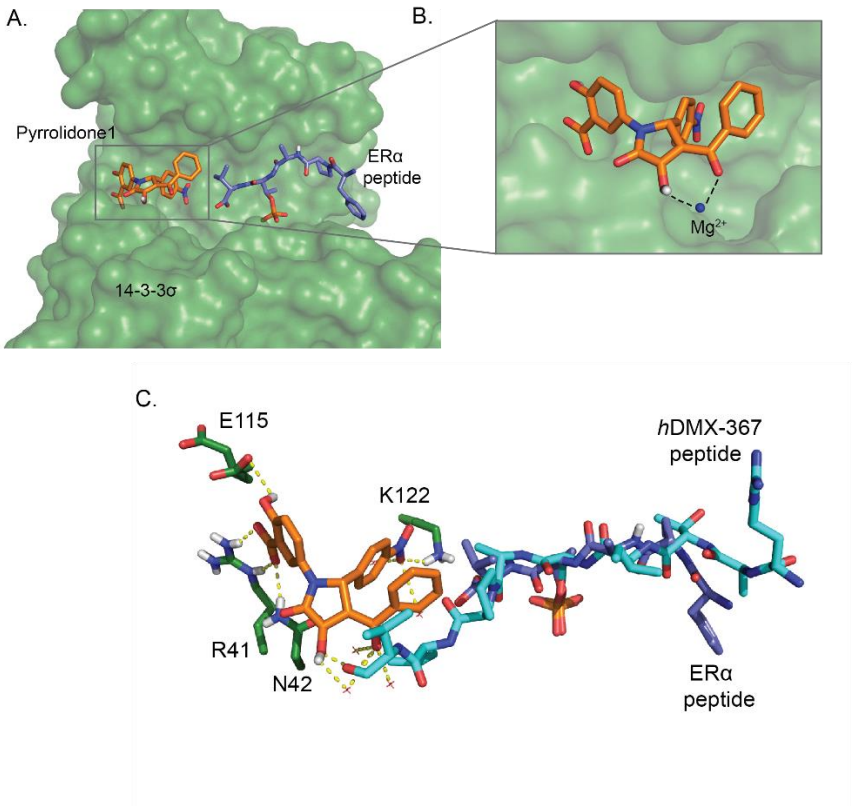

Figure 3.18 Pyrrolidone1 as 14-3-3/ERα stabilizer A) PYR1 (in orange) binds in the amphipathic groove of 14-3-3σ (in green) next to the C-terminus ERα peptide (in purple), *PDB: 6TJM*. B) Three phenyl groups of PYR1 occupy different subpockets of 14-3-3σ and Mg^{2+} ion chelated by carboxylate moieties. C) Overlay of ERα and *h*DMX-367 (in cyan) peptides next to PYR1. 14-3-3σ residues that make polar contacts with PYR1 are shown in green.

3.3.1 Optimization of Pyrrolidone1

Firstly, a library of 55 PYR1 analogues provided by Dr. Gavin O'Mahony was screened using FA to establish if any of the compounds could be used as a starting point for further optimization and also to confirm if the PYR1 itself has any effect on *h*DMX/14-3-3 interaction, inhibitory or stabilizing. Overlaying the crystal structures of *h*DMX-367 and ERα peptides, PYR1 was assumed to be most likely an inhibitor of *h*DMX-367/14-3-3η interaction as the phenyl moiety of PYR1 was clashing with the *h*DMX-367 peptide backbone (Figure 3.18c). All compounds were screened as racemic mixtures in a dose-response assay with compounds titrated against the constant concentration of protein and peptide, as described previously. Four compounds, **83**-**85**, were found to be active with micromolar EC_{50} values, as shown on Figure 3.19.

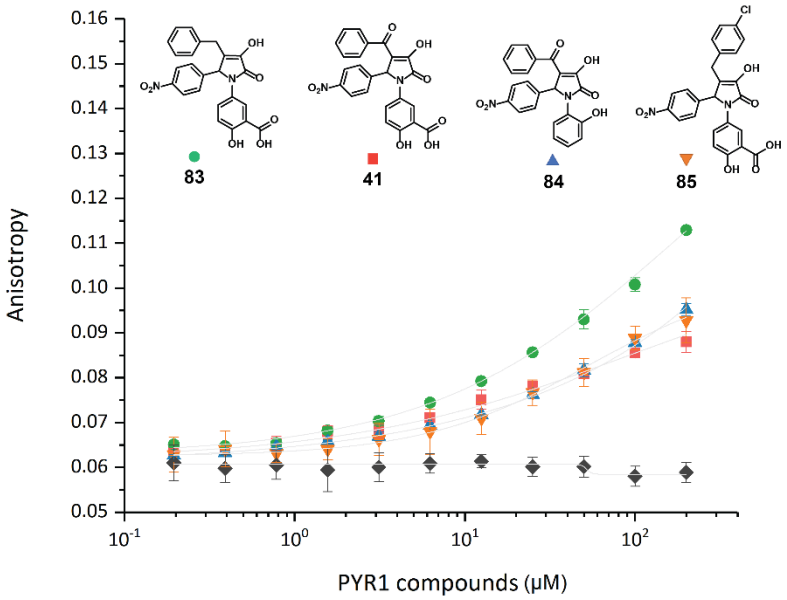

Figure 3.19 Screening results of PYR1 analogue Astra-Zeneca library. Titration of 200 μM compounds with 0.1 μM of 14-3-3η and 50 nM *h*DMX-367-FAM, in 1/3 dilution in HBS buffer: 10 mM HEPES, 150 mM NaCl, 0.1% Tween 20, pH 7.4. Activity of compounds compared to a DMSO control (represented as black diamonds).

Compound **83** was found to be the most active, followed by compounds **41**, **84** and **85**. Although not expected, PYR1 (**41**) showed increase in anisotropy indicating a modest stabilization effect on *h*DMX/14-3-3. However, even higher activity of analogue **83** might be explained by a more flexible phenyl group that would avoid clashes with the *h*DMX-367 peptide backbone. This assay was repeated in the HBS buffer containing 10 mM Mg^{2+} to test the hypothesis of metal chelation increasing the stabilization effect, but no difference was observed on anisotropy from an addition of Mg^{2+} ions (see Appendix, Figure A.5.9).

In order to identify novel PYR1 stabilizers, a small library of 20 compounds containing a central pyrrolidone unit with different substituents inspired by the active structures was synthesized (as listed in Figure 3.20). The synthesis was carried out as outlined in Scheme 3.1a, by one pot Doebner condensation of benzaldehyde, aniline and dicarbonyl derivatives in acetic acid.[173] All starting materials were commercially available except compounds **86**, **87**, **88** and **89** that were prepared following synthetic procedures outlined in Scheme 3.1b for the synthesis of the following compounds: **90**-**93**, **107**-**108**, **100**-**101**, **98**-**99**.

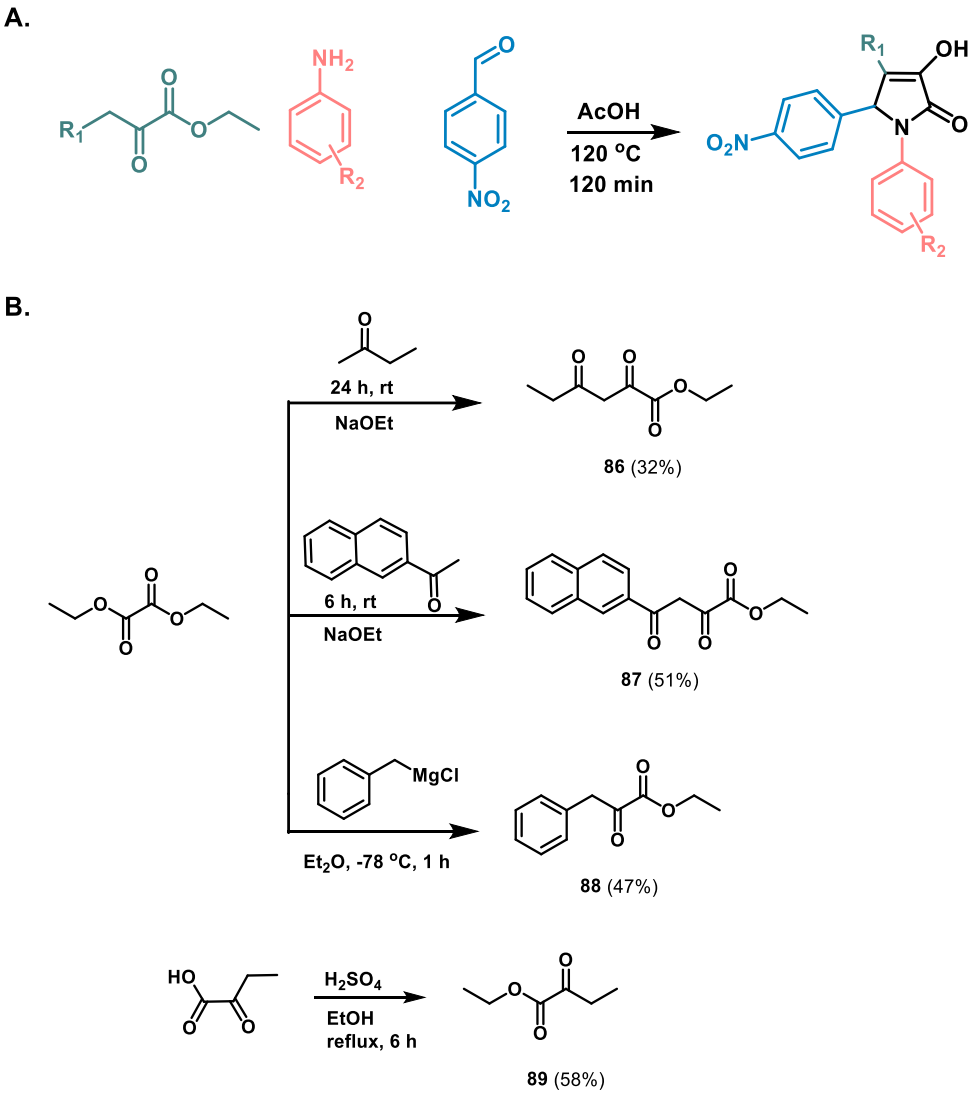

Scheme 3.1 A) Synthesis of Pyrrolidone1 analogues by Doebner condensation. B) Synthetic procedure for preparation of starting material for compounds **90**-**93**, **107**-**108**, **100**-**101**, **98**-**99**.

In more detail, the nitro group was preserved in all novel derivatives of PYR1, as it was previously found crucial to drive the interaction with 14-3-3 proteins.[172,173] The R_1 substituent was introduced without the phenyl ring in compounds **90**-**93**, **94**-**97**, **98**-**99**, or it being directly attached to the pyrrolidone in **100** and **101**. The carbonyl group at R_1 was only kept in compounds **107** and **108**, where a naphthyl moiety was introduced to increase lipophilicity of the compounds. An initial hit identified from the screen, compound **83**, was also resynthesized and similar analogues were prepared (**102**, **103**, **104**, **105**, **106**) without the carbonyl group in R_1 to increase flexibility as this moiety was most likely interacting with the peptide. The salicylic group in R_2 originally found in hit compounds was kept in 7 analogues (**90**, **94**, **98**, **100**, **83**, **105**, **107**), changed to hydroxy group at the ortho (**92**, **96**, **99**, **101**, **102**, **106**, **108**) or para position (**91**, **95**, **105**), or omitted in compounds **93** and **97**.

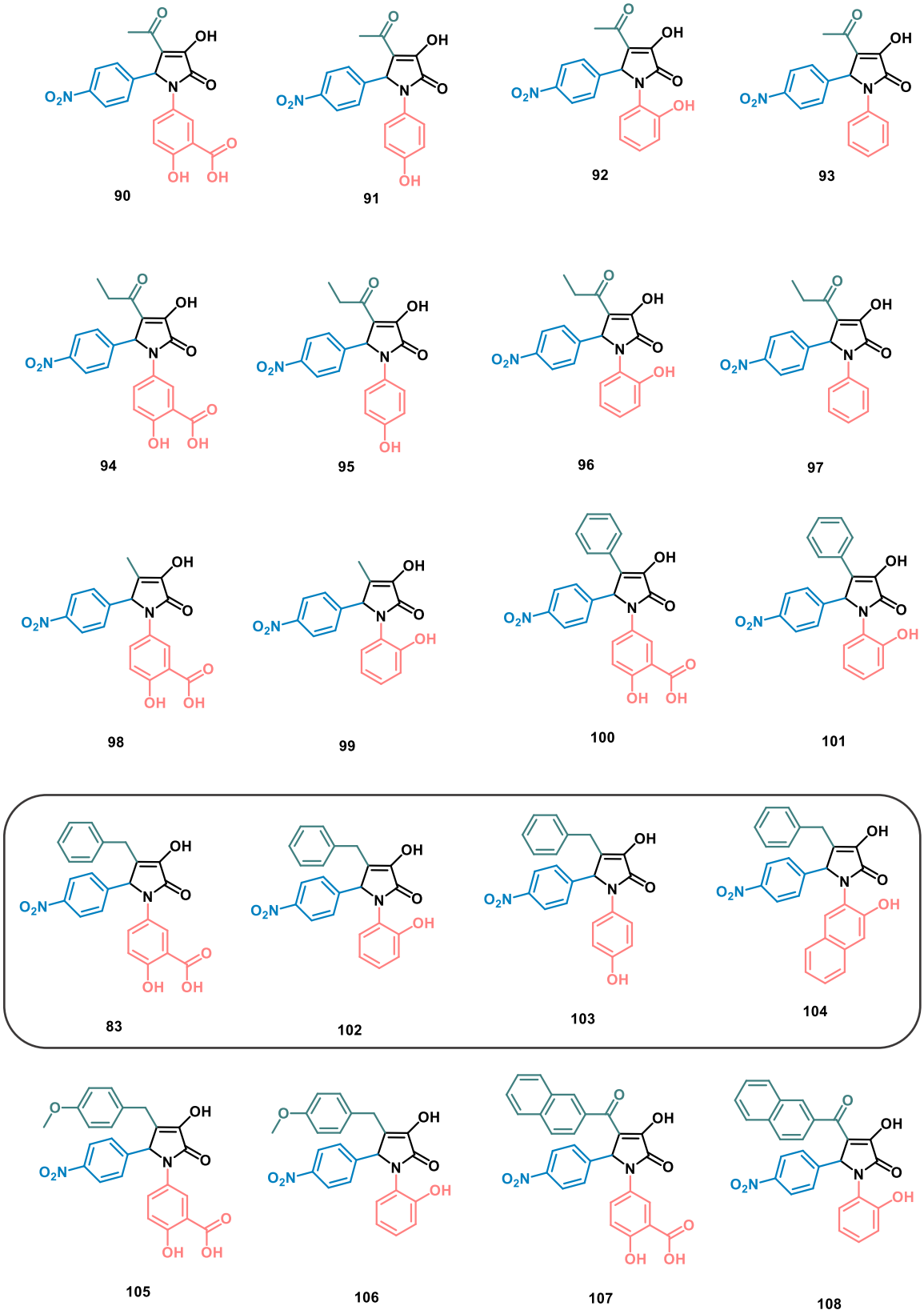

Figure 3.20 Figure of all 20 novel PRY1 analogues. Four compounds highlighted in black showed activity in FA assays.

3.3.2 Biophysical characterization of PYR1 derivatives

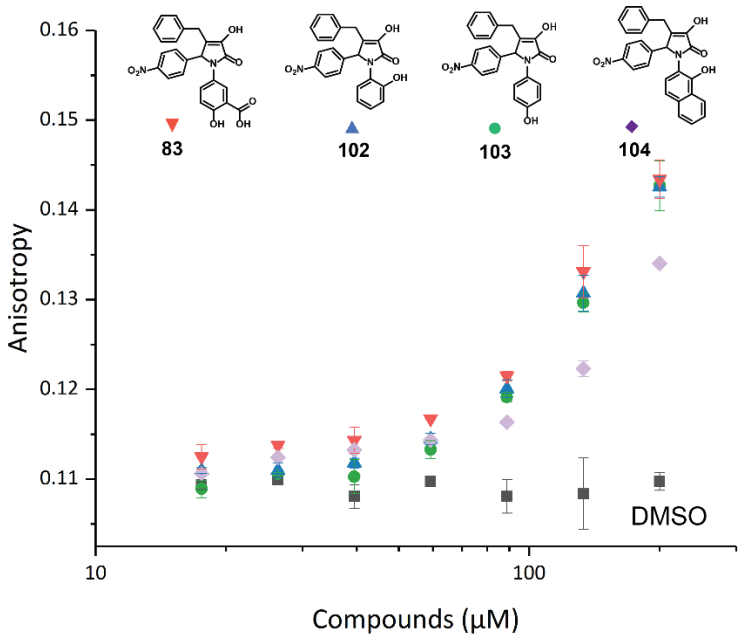

Figure 3.21 Screening of novel analogues identified four compounds showing activity for *h*DMX/14-3-3 complex. Compounds titrated in 1/3 dilutions against constant concentration of protein and peptide in HBS buffer (100 nM 14-3-3η, 50 nM *h*DMX-367-FAM, 200 µM max. concentration of compounds

Table 3.1 Apparent EC_{50} values for hit compounds

Compound	**83**	**102**	**103**	**105**
EC_{50} (µM)	157.12 ± 36.7	141.9 ± 7.3	176.8 ± 30.8	> 200

From 20 compounds listed on Figure 3.20, only four were found active in the FA assay: **83**, **102**, **105** and **104**. Figure 3.21 shows a dose-response assay where compounds (200 µM) were titrated against 14-3-3η (200 nM) and *h*DMX-367 peptide (50 nM). The apparent EC_{50} values were calculated by fitting the data in Origin using the logistic function and are reported in Table 3.1. These low potency stabilizers of *h*DMX-367/14-3-3η interaction were found to have the same phenyl group as R_1 moiety and the affinity was not affected by different substituents at the R_2 position. Next, the racemic mixture of a compound exhibiting the highest affinity, **83** was then separated by chiral HPLC and both enantiomers were tested in the same dose-response assay. Figure 3.22 shows one enantiomer of **83** clearly not having any activity, however, the active enantiomer showed similar activity in comparison to a racemic mixture.

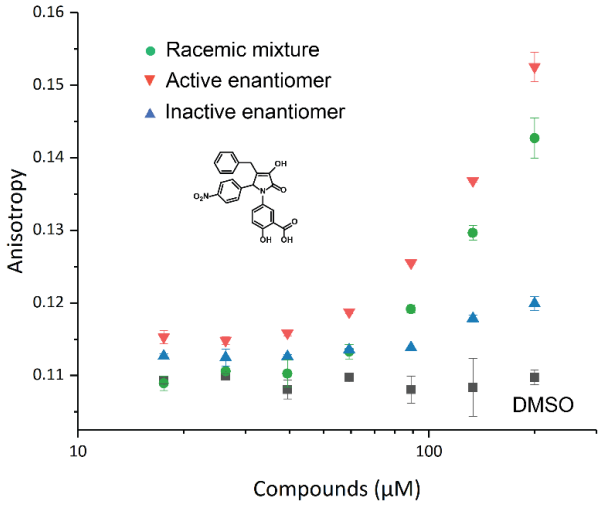

Figure 3.22 Screening of enantiomers and racemic compound **83**. Compounds were titrated in 1/3 dilutions against constant concentration of protein and peptide in HBS buffer (100 nM 14-3-3η, 50 nM *h*DMX-367, 200 µM max concentration of compounds). EC_{50} (active enantiomer) = 159.8 ± 23.3 µM.

Lastly, since PYR1 was found to stabilize multiple 14-3-3 protein interactions and 14-3-3 itself interacts with multiple phosphorylated target proteins, selectivity of the active enantiomer **83** towards *h*DMX-367/14-3-3η interaction was of importance. To investigate this, **83** was subjected to a FA dose-response assay against 14-3-3η and two different peptide constructs: *h*DMX-342 and *h*DM2-166. Figure 3.23 shows the active enantiomer of **83** having no effect on *h*DMX-342 and *h*DM2-166 interactions with 14-3-3, indicating selectivity towards pS-367 site on *h*DMX.

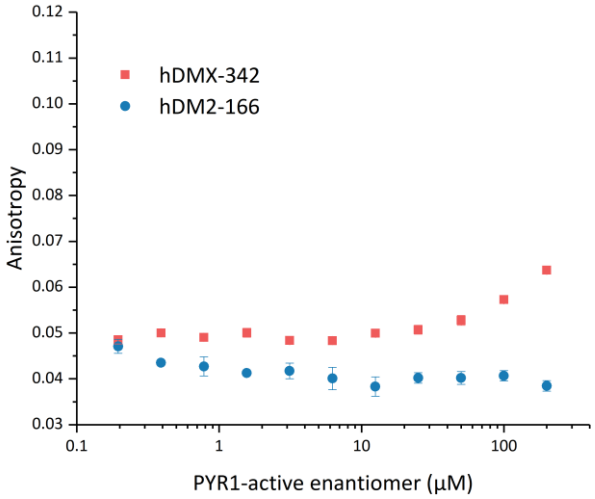

Figure 3.23 Selectivity test for compound **83** (active enantiomer). Compound was titrated in 1/3 dilutions against constant concentration of protein and *h*DMX-342 (in red) and *h*DM2-166 (in blue) peptide in HBS buffer (9 µM and 4 µM 14-3-3η, 50 nM peptide, 200 µM max. concentration of compounds)

3.3.3 Dicussion and summary

Examples of small-molecule stabilizers of PPIs to date are scarce, including 14-3-3 mediated interactions that are mostly explored by natural products such as FCA and its derivatives. Identifying a novel compound that would stabilize *h*DMX-367/14-3-3 interaction through screening campaigns was found to be challenging. Instead, a different approach was taken where the possibility of using known 14-3-3 small-molecule stabilizer, PYR1 as a starting point to develop a compound that would be selective for *h*DMX-367/14-3-3 interaction, was explored. To do so, a library of PYR1 derivatives provided by Astra-Zeneca, including newly synthesized compounds was screened in FA dose-response assays. In the absence of the PYR1- *h*DMX-367 peptide crystal structure, overlays of the two structures with ERα and *h*DMX-367 peptide was used as an initial guideline in determining if PYR1 compounds could be further optimized. Since docking was not performed, the flexibility of the C-terminus *h*DMX-367 peptide in solution was unknown at this stage. The novel compounds were designed simply by removing either the keto or phenyl group on the R_1 position of PYR1 which was solvent/peptide exposed, and by replacing the salicylic group in R_2 that was binding to the negatively charged pocket of 14-3-3σ.. From compounds that were identified as having moderate stabilizing activity, **83**, **102**, **103** and **104,** it was evident that the removal of the keto group increases affinity for the *h*DMX-367/14-3-3 interaction and substituents in the R_2 group have no diminishing effect on the activity. Further, the active enantiomer was shown to be selective for *h*DMX over *h*DM2. Taken together, these preliminary results provide a basis for further exploration of optimizing PYR1 analogues to gain selectivity towards *h*DMX-367/14-3-3 interaction. This preliminary screen of a total of 75 derivatives of PYR1 has allowed active enantiomer of **83** to be identified as a starting point for further crystallography studies (*h*DMX-367/14-3-3σ crystal soakings) and optimization based on potential novel structural data.

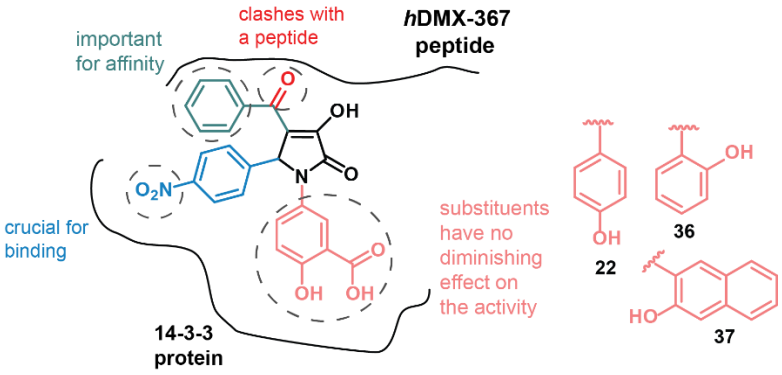

Figure 3.24 The most active derivatives of PYR lack carbonyl group on R_1 position.

Chapter 4: Protein-templated fragment ligation approach as a novel concept in stabilizing PPIs

4.1 Introduction and aim

Despite considerable progress being made in the field of fragment-based drug discovery over the years, challenges in detecting starting points for drug development remain present, especially for targeted stabilization of PPIs. As mentioned previously, several clinically approved drugs have resulted from fragment-based lead molecules. However, identification of weak, low molecular weight binders on the solvent exposed protein surface using biophysical characterization methods is extremely difficult for some targets. Often observation of two binding fragments is necessary for the signal to be observed in the first place, otherwise the low affinity binding can easily be lost in the background error range of the screen. Secondly, the identified hits need to exhibit functionalities that would allow the covalent linkage of the two binding fragments. To overcome these problems, a protein-templated fragment ligation approach has been explored over the years as an alternative strategy to provide leads and their optimization into potent molecules for previously undruggable targets.[174] The largest advantage of a protein-templated fragment ligation approach is that it merges the traditional chemical synthesis and bioassay approach of medicinal chemistry into one single step.

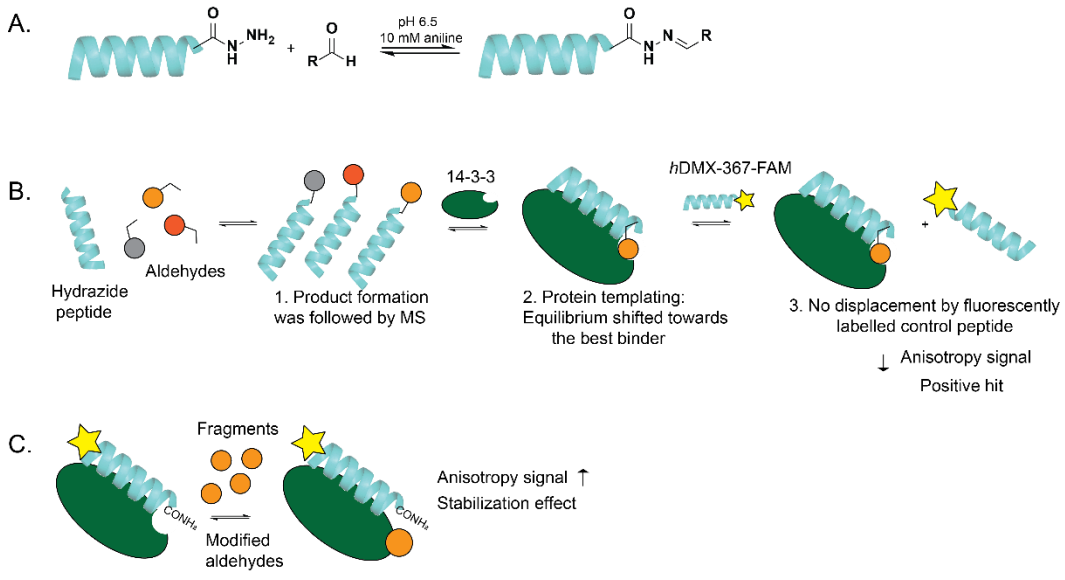

Figure 4.1 Aim of the chapter. A) The acylhydrazone formation can be carried out at physiological conditions with aniline as a catalyst B) Schematic representation of the assay development to detect binding hit hydrazone peptides C) Hit validation step will include testing fragments that are not covalently bound to the peptide probe.

Thus, the aim of this chapter was to discover fragments as a starting point for further optimization towards selective stabilization of *h*DMX/14-3-3 interaction through a protein-templated ligation approach. Reversible acylhydrazone formation was of particular interest for this study as the *h*DMX-367 peptide could easily be synthesized as a hydrazide peptide, and when combined with a diverse library of aldehydes it could be used as an anchor to identify novel small-molecule moieties binding in a predefined pocket of 14-3-3 proteins. (Figure 4.1). This could be done in two ways, by combining a hydrazide peptide with a mixture of aldehydes and employing dynamic covalent chemistry principle (Figure 4.2) or screening aldehydes separately. A novel crystal structure of *h*DMX-367/14-3-3σ was used for determining the novel targetable pockets at the peptide/protein binding interface by using a 'solvent mapping' approach. Different length of hydrazide *h*DMX-367 peptides were synthesized and used to target a specific site on 14-3-3 proteins, either pockets discovered by solvent mapping approach or a well-known FCA/PYR pocket (Figure 4.1b). The idea was that 14-3-3 proteins direct the synthesis of the novel hydrazone peptides with the highest intrinsic affinity, which could be followed by fluorescence anisotropy assays. Novel fragment moieties that otherwise would not be detected without the hydrazide peptide anchor directing the binding could then be modified to increase the affinity and specificity for the particular pocket on the protein (Figure 4.1c).

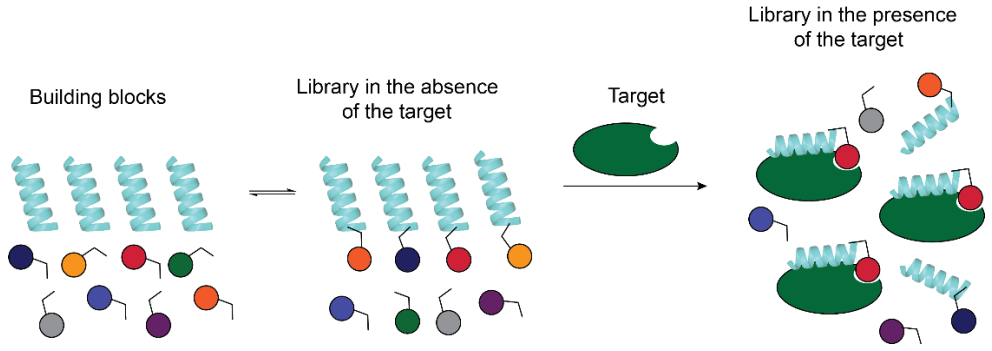

Figure 4.2 Schematic representation of dynamic protein-templated fragment ligation approach. The reversible reactions are used to generate assemblies of molecules (fragments, here: peptide and aldehydes) in thermodynamic equilibrium. The addition of a template (protein, here: 14-3-3η) then shifts the equilibrium towards the best binding molecule, thus the binding of molecules with the highest affinity towards the protein are amplified at the expense of other, less active library members. Adapted from[175]

One of the most frequently used reactions for dynamic covalent chemistry, acylhydrazone formation was used. This technique was first introduced as reversible linkage strategy in non-biological context by the Sanders group.[176] Acylhydrazone formation and exchange is slow at the physiological conditions (at neutral pH and at

rt) but works best at pH around 4. The general application in a biological context was introduced by Greaney *et al*, when aniline was used as a nucleophilic catalyst to rapidly equilibrate the dynamic libraries at pH 6.2 and the rate of reactions can be controlled by increasing or decreasing pH.[177] The acylhydrazone ligation was also established and used by the Wilson lab to develop modulators of β-mediated PPIs (unpublished results). Other common reversible reactions used for protein templated fragment ligation can be carried out in aqueous media around neutral pH and an appropriate temperature which makes them biocompatible and are summarized in Table 4.1.

Table 4.1 Biocompatible reactions used in protein-templated fragment ligation studies[175]

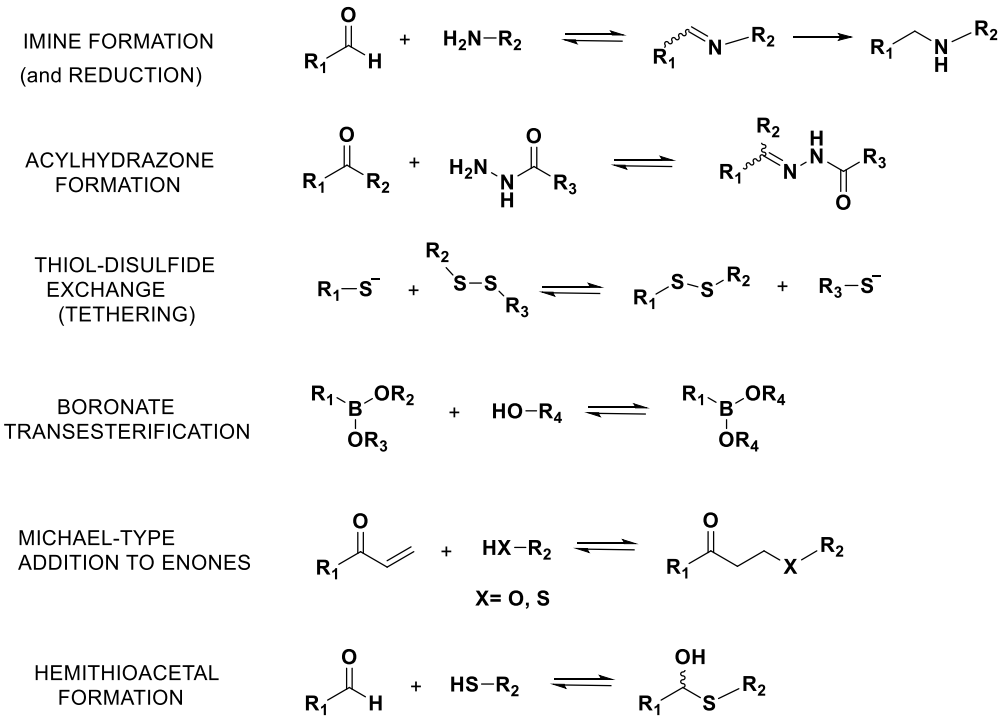

Prominent examples of site-directed ligation studies employing 14-3-3 proteins were published by groups of Ottmann[43] and Ohkanda[178]. In the first example, disulfide tethering was explored as an alternative FBDD method to find site-directed binding fragments on the 14-3-3σ/ERα binding interface. Native (C38) and two engineered (C42 and C45) cysteine residues on 14-3-3σ were used as a reactive handle to identify binding disulfide fragments. A 40-fold stabilization effect was achieved in the presence of the C-terminal ERα peptide (Figure 4.3a). Tethered product formation around each cystine residues, all placed in the FCA binding pocket of 14-3-3σ, was monitored by mass spectrometry where amplification of signal was noted for the binding fragments that were not just being tethered but found to interact

with the ERα peptide through non-covalent interactions. The disulfide trapping strategy was introduced over 20 years ago[179], however this was the first example of it being applied to the discovery of PPI stabilizers.

In the second example, oxime ligation approach was applied in a rational design approach to develop a bivalent diterpene-peptide **109** as an intracellular 14-3-3ζ inhibitor. To allow 1 to be formed in cells, FCA (28) was first modified with an o-formyl benzyl group and the C-terminus peptide of the PMA2 (plasma membrane H^+-ATPase) peptide was modified to an oxyamino group, while phosphothreonine was replaced with aspartic acid to increase membrane permeability. Upon FCA and the PMA2 peptide entering the cells, 14-3-3ζ would act as a template for oxime ligation to yield amphiphilic diterpene-peptide conjugate **109**. It was also shown that chemically synthesized **109** would not penetrate the cells mostly due to its large molecular size and the two components independently are not potent enough to inhibit 14-3-3 mediated interactions, in this case cRaf/14-3-3ζ interaction.

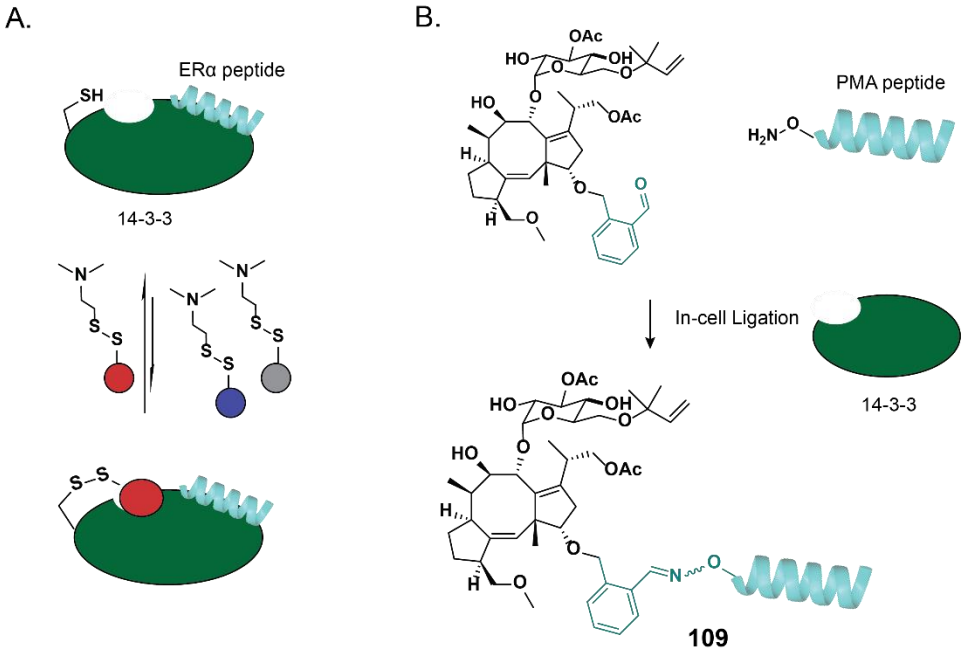

Figure 4.3 Protein-templated ligation approaches including 14-3-3 proteins. A) Tethering B) Oxime ligation

4.2 Identifying targetable pockets on 14-3-3 proteins

The central binding groove of 14-3-3 proteins, which accommodates phosphorylated peptides, share a high degree of conservation among all 14-3-3 isoforms (Figure 1.10). Beside a phospho-binding groove on 14-3-3 proteins, the FCA

pocket is well defined and has been explored for targeted stabilization of 14-3-3 mediated interactions previously, both by small-molecules and natural products.[109] However, the *h*DMX-367 peptide was found to partially occupy the FCA binding pocket in the crystal structure with 14-3-3σ, as discussed in detail in Chapter 2. Thus, the challenge was to identify novel ligandable sites between 14-3-3 proteins and *h*DMX-367 peptide. Ligandable sites referrs to specific regions on a protein surface that are most likely to interact with small-molecules.[180] Here, a computational 'solvent mapping' server FTMap[45] was used to identify suitable targetable pockets on the *h*DMX-367/14-3-3σ interface. The newly solved protein/peptide crystal structure was submitted in a PDB format (code: 6YR5) for analysis (http://ftmap.bu.edu).

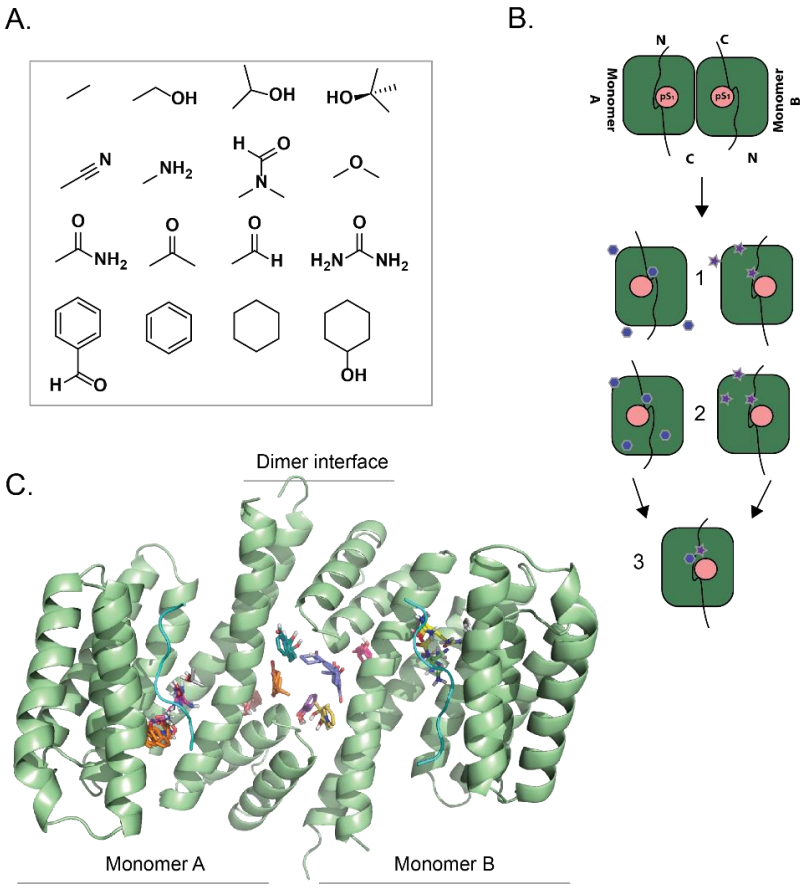

Figure 4.4 FTMap solvent mapping software. A) Solvent probe molecules B) Principle of FTMap server: 1. Docking of probe molecules, 2. Favorable positions of probe molecules are energy minimized and clustered, 3. A site with most probe clusters is defined as a consensus site i.e. main hot-spot region. C) Results obtained from using FTMap server on hDMX-367/14-3-3σ structure. Only one interesting pocket between protein and peptide was observed with a cluster of probes (protein shown in green, peptide in cyan)

The FTMap software firstly removes all water molecules and ligands from the structure and preforms rigid body docking using 16 simple solvent molecules (as shown on Figure 4.4a) varying in polarity and shape on the *h*DMX-367/14-3-3σ complex. The algorithm then finds lowest energy binding fragments, groups them into clusters and finally ranks all probe clusters into so-called consensus sites. The region with most probe clusters in a consensus site is defined as a hot-spot (Figure 4.4b). For the *h*DMX-367/14-3-3σ structure, several consensus sites have been identified on the 14-3-3 protein dimer interface (Figure 4.4c) but only one high quality consensus site was found to occupy a pocket on 14-3-3 protein enveloped with *h*DMX-367 peptide (Figure 4.5a, fragment probes shown as orange spheres in between protein shown in green and peptide in cyan). Targeting this pocket on the protein/peptide interface was brought forward as it offered a possibility of developing orthosteric stabilizers for this interaction. In order to reach and probe this pocket, a truncated version of *h*DMX-367 peptide was synthesized using hydrazone resin (Fmoc-NH-N=Pyv-OH, Iris Biotech[181]) as shown in Figure 4.5b. The key residues (Arg on position -3 and Pro at position +2) that would significantly impact binding were kept, and Gly was used as a first amino acid to maximize coupling efficiency of the resin (coupling of Pro as first amino acid was difficult or resulted in low yields). The peptide chain was elongated using standard protocols of Fmoc chemistry and coupling conditions identical to those discussed in Chapter 2, Scheme 2.1. Following acetylation, the peptide was cleaved and protecting groups were removed by again using ‘Reagent K’. After purification, *h*DMX-367 peptide with a hydrazine linker on the C-terminus was used as an anchor to react with aldehyde moieties, in FA assays (peptide synthesis and general scheme of arylhydrazine reaction is shown on Figure 4.5b).

A.

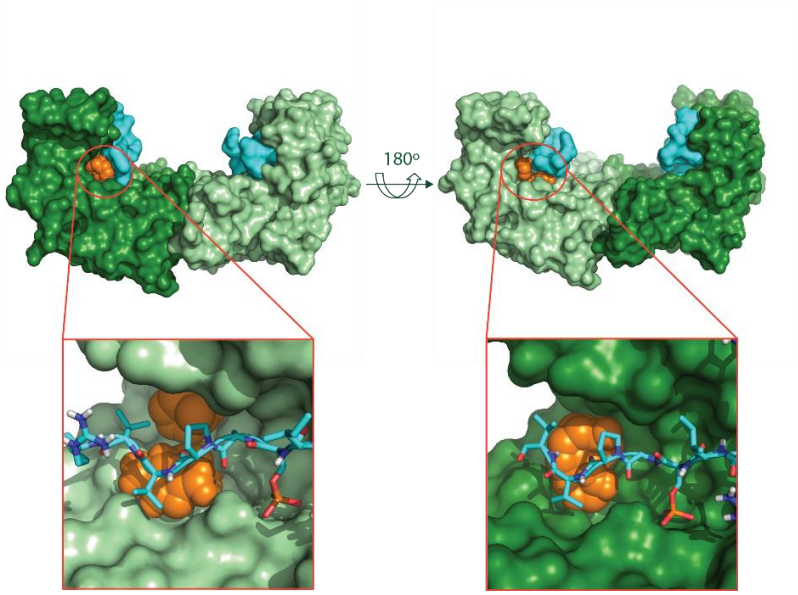

Ac-DCRRTI(pS)APVVRPK-CONH₂

Ac-DCRRTI(pS)APG-CONH-NH₂

B.

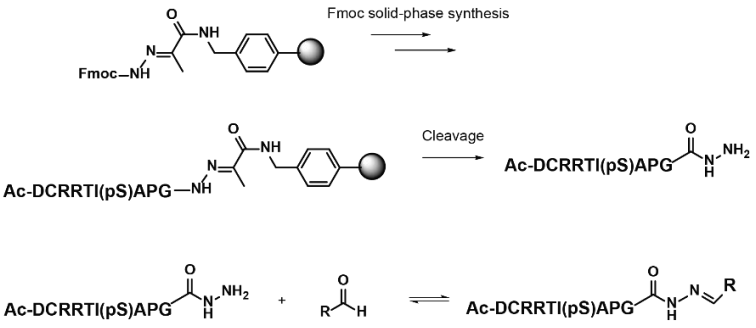

Figure 4.5 Peptide synthesis based on a solvent mapping approach. A) A cluster of small organic probes (shown as orange spheres) were found using FTMap at the interface of hDMX-367 peptide (showed as sticks, in cyan) and 14-3-3σ (protein dimer in green). B) Schematic representation of hydrazide *h*DMX-367 peptide synthesis using standard solid-phase Fmoc chemistry on a hydrazone resin (Fmoc NH N=Pyv OH). Following cleavage from the resin and purification, peptide was incubated with 5 eq. of aldehydes to yield different hydrazone peptides.

4.3 Assay development to target newly identified pocket on 14-3-3 proteins

The assay for protein-templated ligation reactions can take several days, as equilibrating library members and protein templating steps are carried out in separate phases. Thus, to check if the protein is stable enough to withstand the predicted assay time span, in this case 24 h, it was important to establish no or a minimal change in anisotropy between 1 h and 24 h readings for newly synthesized hydrazide *h*DMX-367 peptide and 14-3-3η. The competition assay was carried out using buffer conditions previously found suitable for acylhydrazone formation[177]: NH_4OAc (50 mM), aniline (10 mM) as a catalyst and DTT (1 mM) as a reducing agent since a Cys residue was present in the peptide sequence, at pH 6.5. Hydrazide *h*DMX-367 peptide (150 μM) was used to compete the fluorescently labeled *h*DMX-367 peptide for binding to the 14-3-3η (50 nM of tracer, 1 μM protein) and the resulting IC_{50} values were similar over the 24 h span indicating good stability of a peptide probe and 14-3-3 protein (as shown on Figure 4.6). For all further assays presented in this chapter NH_4OAc buffer was used and experiments were performed at room temperature with the final DMSO concentration below 5%.

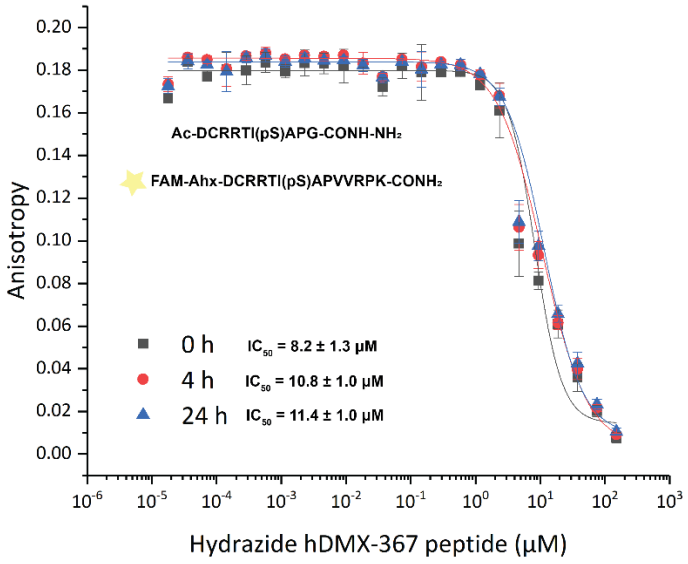

Figure 4.6 Competition assay for the hydrazide *h*DMX-367 peptide in ammonium acetate buffer (150 μM acetylated hydrazide *h*DMX-367 peptide as competitor, 50 nM tracer, 1 μM 14-3-3η in 50 mM NH_4OAc, 10 mM aniline and 1 mM DTT)

A small library used in the experiments described below contained 129 commercially available aldehydes that were provided by Dr. Zsófia Hegedüs (aldehydes purchased from Sigma Aldrich and Fluorochem, a complete list is available in Digital Supplementary Material). Initial attempts to develop a novel assay to screen low

affinity binders for targeted stabilization of PPIs included employing a dynamic ligation approach. Here, 13 screening cocktails were designed from 129 aldehydes, each cocktail containing 10 different aldehydes. The screening was performed in three steps, first being mixing the hydrazide peptide (100 μM) with 5-fold excess of aldehydes (all 13 libraries tested separately in duplicates) in a 384-well plate, followed by adding the 14-3-3η (1 μM) as a template after 24 h of equilibration. The equilibrium is shifted towards the bound hydrazones to 14-3-3η if the aldehyde moiety has the inherent affinity towards protein, thus increasing the concentration of the hit hydrazones at the expense of the other non-binding library members. After another 24 h fluorescently labelled *h*DMX-367 peptide (50 nM) was added as a competitor and plates were read immediately. The acetylated *h*DMX-367 peptide and buffer were used as controls, to which anisotropies of generated hits from aldehyde libraries were compared to, as shown in Figure 4.7. Additionally, a combination of protein and aldehydes was included as another control to determine if the binding is (un)specific and to exclude possible false positives. If the bound hydrazones were not displaced by a fluorescent probe and low anisotropy signal was observed, those libraries of hydrazones were exceeding the activity of the parent *h*DMX-367 peptide (positive control) and were taken as hits.

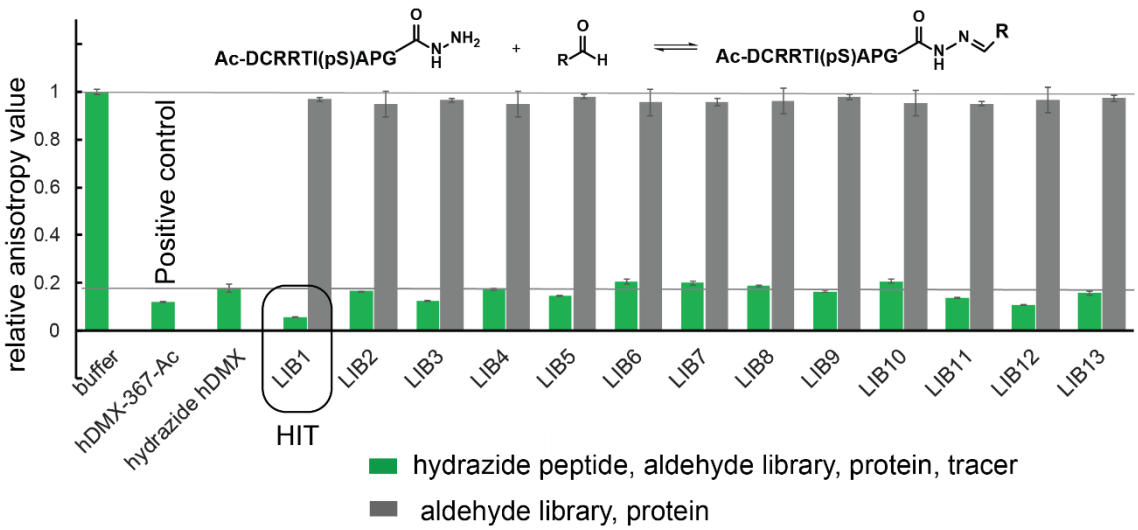

Figure 4.7 Assay development. Testing aldehydes in mixtures of 10 with hydrazide *h*DMX-367 peptide (100 μM). Anisotropy is showed as relative to buffer controls, hydrazone libraries are compared to a hydrazide *h*DMX peptide and *h*DMX-367-Ac as a positive control (all in green).

The lowest anisotropy was evident within Library 1, which confirmed formation of a novel hydrazone peptide exceeding the affinity of a positive control. Subsequently,

Library 1 was submitted to HRMS analysis to determine which library member was a true binder. This could be detected by identifying an amplified peak corresponding to a binding hydrazone peptide, so the relative peak area was compared of hydrazone peptides alone and templated with 14-3-3η. Surprisingly, no amplification was observed for any particular hydrazide peptide in response to 14-3-3η templating effect, despite a clear indication of binding having been observed in the FA assay. The assay development and screening by applying the concept of dynamic covalent chemistry was promising in terms of straightforward FA assay, however it was not found possible to fully implement this strategy as further optimization was needed as binding aldehydes could not be detected by HRMS if screened in mixtures. The assay was hence then repeated where each aldehyde was screened individually with the hydrazide *h*DMX-367 peptide (Figure 4.8a). This way a decrease in anisotropy can be directly attributed to a particular hydrazone product, avoiding the bottleneck of product identification by HRMS. In addition, the equilibration step for hydrazone formation and 14-3-3η were combined into one step, reducing the overall duration of the assay. The two hydrazones exhibiting lower anisotropy than *h*DMX-367-Ac peptide were selected as hits, FC-45 (**110**) and SIG-17 (**111**) (Figure 4.8a, black box), and to confirm the single-point assay results along with their affinities, a competition assay was carried out next (Figure 4.8b). To do so, a hydrazide *h*DMX-367 peptide (150 μM) was incubated with 5 equivalents of each aldehyde (completion of products formation followed by LC-MS, Figure 4.8c), serially diluted and templated by 14-3-3η protein (1 μM). Fluorescently labelled *h*DMX-367 peptide probe (50 nM) was used to compete hydrazine hits. The obtained IC_{50} values, IC_{50}(FC-45)= 10.4 ± 0.3 μM and IC_{50}(SIG-17)= 13.7 ± 0.5 μM were found to be similar to the *h*DMX-367-Ac peptide ($IC_{50=}$ 8.5 ± 0.2 μM) or hydrazide ($IC_{50=}$ 8.2 ± 1.3 μM, Figure 4.6). Both fragment moieties had intrinsic affinity towards 14-3-3η as the affinity of the full length *h*DMX-367-Ac binding peptide was recapitulated, but not exceeded as indicated in a single-point screen.

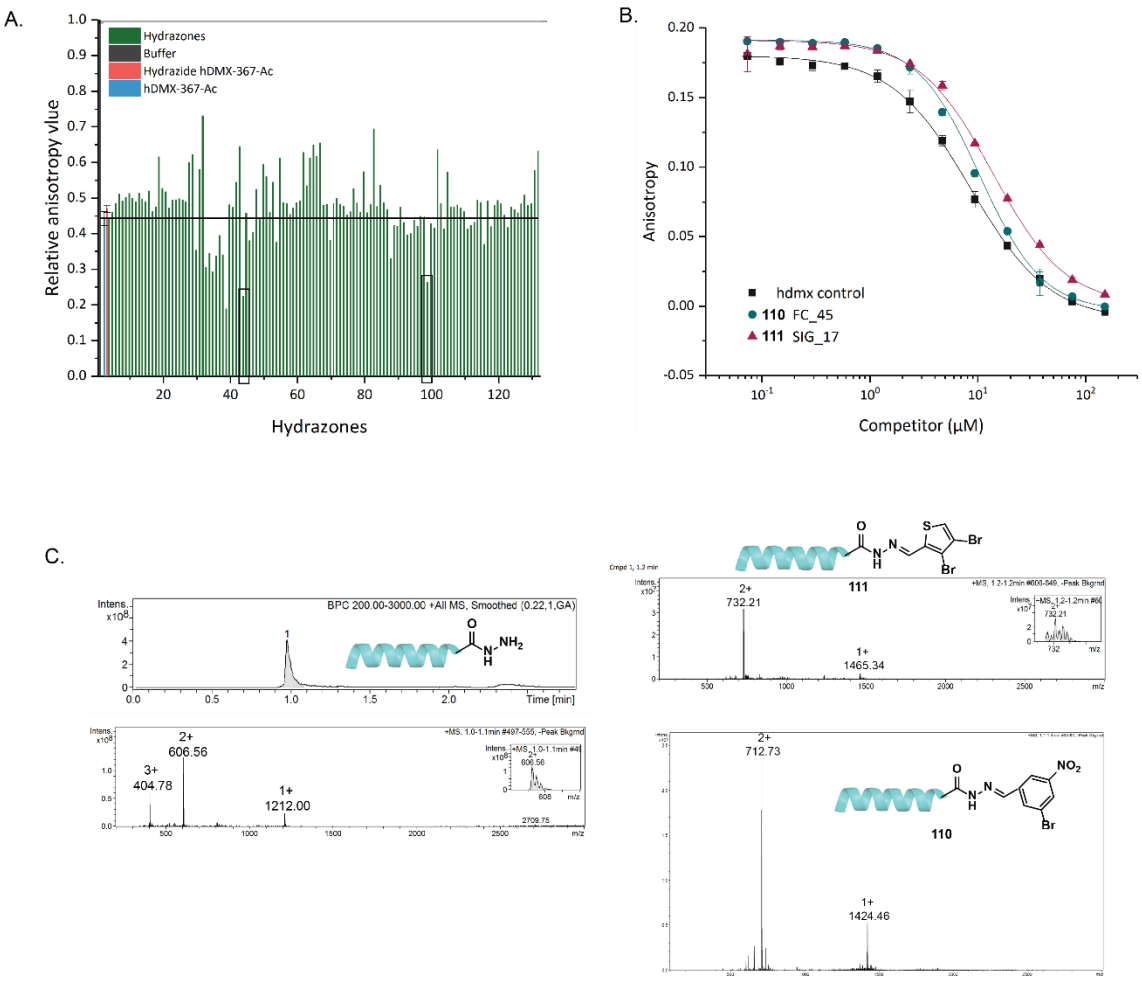

Figure 4.8. A) Plotted relative anisotropy of individually screened hydrozides. Anisotropy is relative to buffer (no activity, negative control in grey), *h*DMX-367-Ac (blue) and hydrazide *h*DMX-367 (red) as positive controls. Two hydrazides taken forwards as hits: FC-45 and SIG-17 (in black box). Assay conditions: 10 μM acetylated hydrazide peptides mixed with 5 eq. of aldehydes and 1 μM 14-3-3η, 50 nM tracer. B) Validation of FC-45 and SIG-17 hydrazone hits in a competition assay (150 μM acetylated hydrazone peptides as competitors in comparison to a parent hDMX-367-Ac peptide, 50 nM tracer, 1 μM 14-3-3η in 50 mM NH_4OAc, 10 mM aniline and 1 mM DTT). C) Hydrazone formation was confirmed by mass spectroscopy before validating the hits in a competition assay.

4.4 Targeting FCA/PYR binding pocket on 14-3-3η

Beside targeting a newly discovered pocket on the *h*DMX-367/14-3-3σ interface by a solvent mapping approach, a conserved FCA/PYR binding pocket on 14-3-3 proteins was probed next with the extended library of aldehydes (165 in total). As a proof of concept, to demonstrate the acylhydrazone ligation could be used to target any specific pockets on a protein, two newly extended hydrazide *h*DMX-367 peptides were synthesized. In order to reach the FCA pocket, the hydrazide peptide was extended by one (PVG) and two (PVVG) Val residues to resemble the natural sequence of *h*DMX protein and the screening assays were repeated using the same conditions as established previously (aldehydes being screened individually). Because of similar results obtained between two peptides and for clarity, only representable data for hydrazide peptide PVG are presented on Figure 4.9a (all screening and validation, including PVVG peptide can be found in the Appendix, Figure A.5.9). In comparison to a previously targeted pocket, considerably more hydrazone hits with higher affinities towards FCA/PYR pocket on 14-3-3η were identified. To a certain extent this was an expected observation as a larger surface pocket was probed and subsequently different hits were observed when compared to PG-hydrazide peptide screen (Figure 4.8). However, the fact that different fragments were identified as hits in each pocket is a great indication of potential selectivity. To further validate hits from a single-point screen, a competition assay for 10 of the hits were carried out (highlighted in a black box on Figure 4.9a, results in Appendix, Figure A.5.10). Figure 4.9b summarizes four hydrazone hits that exceeded affinities of the parent *h*DMX-367 and hydrazide peptide (controls) which was apparent by a three-fold decrease in their IC_{50} values. In comparison to a previously carried out screening with a PG peptide to target solvent-map identified pocket, the dose-response assays validated single-point screening results when FCA/PYR pocket was targeted. For some hydrazone peptides, such as FC-32 (**115**, Figure 4.9c, bottom right panel), the observed hill slope was greater than expected value of 1-usually indication of an independent 1:1 binding. This would allude that cooperative binding occurs, possibly boronic acid binding to Ser/Thr residues on the protein[182], beside regular pSer binding to 14-3-3 proteins. The four hydrazone peptides presented in Figure 3.9c were also subjected to crystallography trials performed by Madita Wolter (Eindhoven University of Technology, Netherlands). Several crystals were observed for COOH-4 (**112**) and COOH-28 (**113**) complex, but this work is still underway (Figure 4.9c). The confirmation of aldehyde moieties occupying desired pocket would provide valuable structural information in atomic resolution and would

allow further medchem optimization of fragments into more potent small-molecule stabilizing compounds.

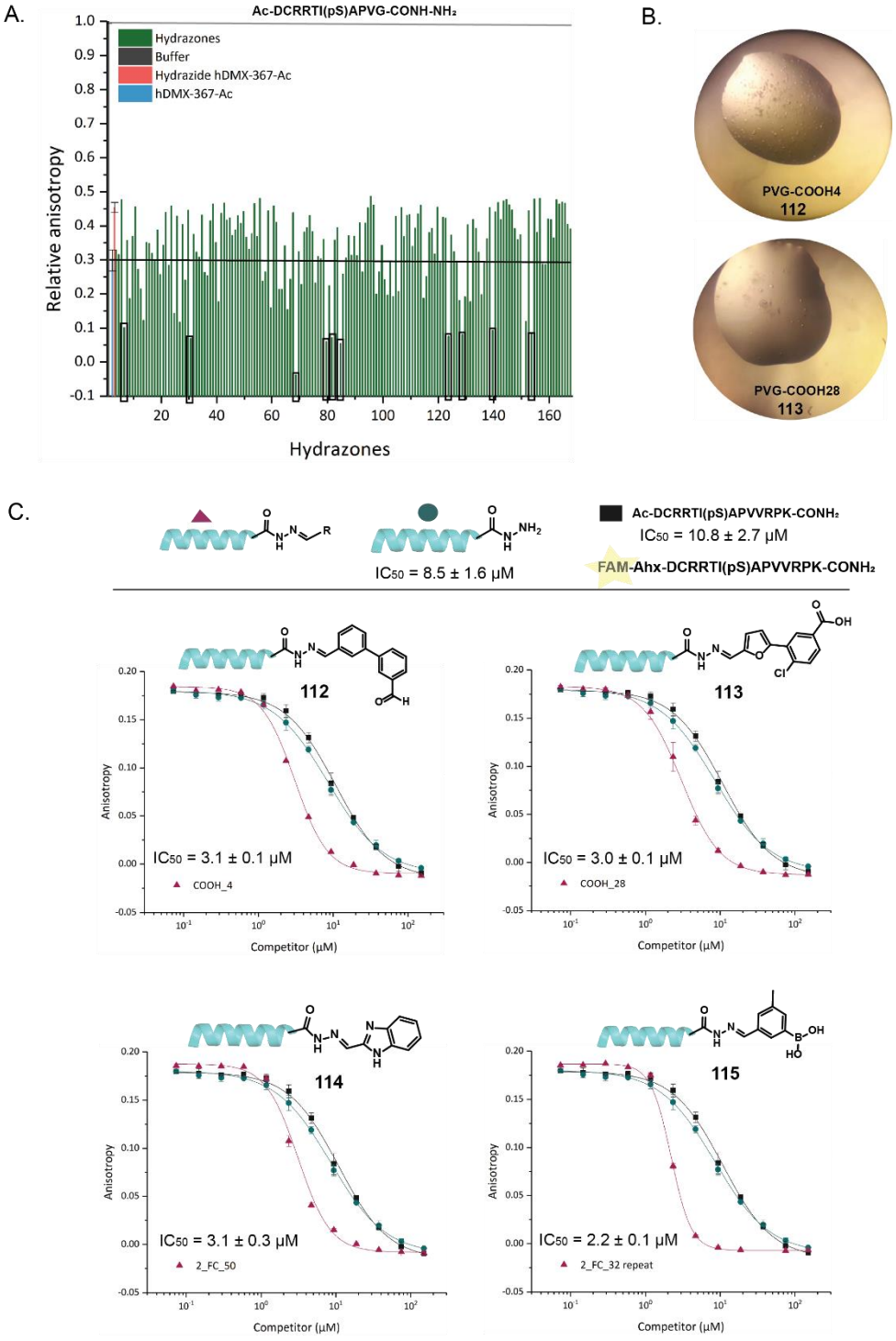

Figure 4.9 A) Plotted relative anisotropy of individually screened hydrozides. Anisotropy is relative to buffer (no activity, negative control in grey), *h*DMX-367-Ac (blue) and hydrazide *h*DMX-367 (red) as positive controls. Several hydrazides were taken forwards as hits, as identified by a black box. Assay conditions: 10 μM acetylated hydrazide peptides mixed with 5 eq. of aldehydes and 1 μM 14-3-3η, 50 nM tracer (*h*DMX-367-FAM). B) Crystals obtained for hydrazone peptides in complex with 14-3-3σ. C) Validation of four hydrazone hits in a competition assay (150 μM acetylated hydrazone peptides as competitors in comparison to a parent *h*DMX-367-Ac peptide, 50 nM *h*DMX-367-FAM tracer, 1 μM 14-3-3η in 50 mM NH_4OAc, 10 mM aniline and 1 mM DTT).

All hydrazone peptides exceeding the affinity of a parent *h*DMX-367 peptide consist of two parts, a natural sequence of *h*DMX peptide and a covalently linked fragment, which is suitable for chemical probe or assay development and a great indication of a fragment starting point for further development. However, the aim is to develop a small-molecule stabilizer of this interaction. Thus, to further explore the effect of non-linked fragments, a small library of 5 fragments resembling the reduced aldehyde form of COOH-4 (**112**), FC-50 (**114**) and FC-32 (**115**) were purchased. The commercially available analogues were alcohol or methyl derivatives, as presented on Figure 4.10a. The same peptide PVG was synthesized but using Rink amide resin (as previously used for peptide synthesis) and was fluorescently labelled to be used as a tracer in FA titration assays. It would be expected that interactions between 14-3-3 protein and fragments would be recapitulated without the acylhydrazone bond to the peptide. Additional contacts with the C-terminus amide peptide would be expected for **116** and **120** through a possible hydrogen bond. Following determination of a K_d value for this novel peptide (K_d= 172.2 ± 9.3 nM, Figure 4.10b), the activity of fragments were tested in serial dilution starting with a concentration of 2 mM against a constant concentration of 14-3-3η protein (0.1 μM) and PVG-FAM tracer (50 nM) as shown on a Figure 4.11c. The indication of binding was observed as the anisotropy slightly increased at the highest fragment concentration, indicating millimolar affinities.

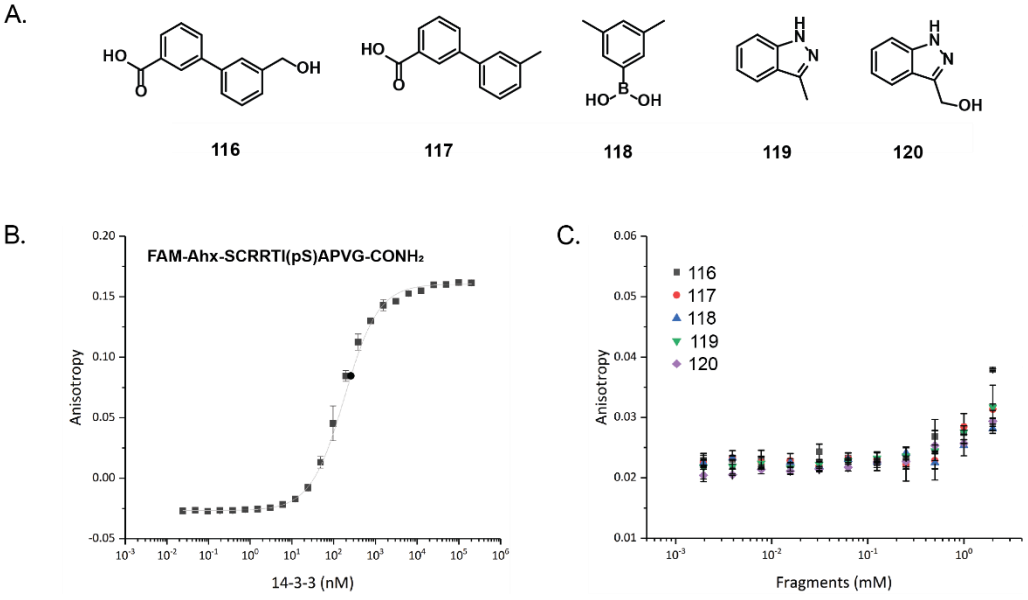

Figure 4.10 From hydrazone peptides towards small-molecule stabilizers A) Reduced fragments resembling hit aldehydes were chosen to see if binding will be detected without a covalent linkage to the hydrazide peptide B) Direct titration of a negative control peptide (FAM peptide tracer 50 nM, 0.1 nM - 300 μM protein, in 10 mM HEPES, 150 mM NaCl, 0.1% Tween 20, 0.1% BSA, pH 7.4. C) Fragment titrations with a negative control peptide as a tracer (2 mM fragments, 0.1 μM 14-3-3η, 50 nM PVG-FAM tracer in 10 mM HEPES, 150 mM NaCl, 0.1% Tween 20, 0.1% BSA, pH 7.4)

4.5 Summary and future work

Based on the overall findings from the initial screening studies, including evaluation of PYR1 derivatives as potential stabilizers discussed in Chapter 3, a significant stabilization of the *h*DMX-367/14-3-3η interaction as an aim of this thesis was challenging to achieve. Many screening techniques lack sensitivity in detecting compounds with low affinities or require optimization to do so. Instead, a protein-templated ligation approach was employed to identify those weaker binding compounds suitable for subsequent optimization towards potential stabilizers of the *h*DMX-367/14-3-3η interaction. This chapter describes an application of an acylhydrazone exchange, a covalent bond formation between hydrazine peptides and aldehydes utilizing the 14-3-3 proteins surface, as a fundamentally different approach for discovery of small-molecule stabilizers. Here, the formation of the thermodynamically most favored hydrazide-fragment combination in the presence of the protein target is easily monitored by FA assay. The advantage of this approach is that it allows fragments to bind to a predefined pocket on 14-3-3 proteins and the binding will be amplified only if the fragment is recognized by a protein template. The new hydrazide peptides varying in length were designed and synthesized to target two distinctive pockets on the 14-3-3 amphipathic groove, the FCA/PYR pocket and one closer to the central binding pSer residue, identified by the FTMap solvent map server. Subsequently, a FA assay protocol was also established close to physiological pH and suitable for acylhydrazone exchange to identify fragments binding in those pockets. The FA assay results were encouraging as different hydrazone hits were observed to bind in each pocket with a stabilization effect in comparison to a parent *h*DMX-367 sequence, but also an indication of fragments binding without being covalently linked to a hydrazide peptide anchor. This is an exciting initial proof of concept study that provides a solid basis for a further development and validation. For example, solving the crystal structure will offer definitive proof of binding and structural insights why the specific fragment is favored by 14-3-3 protein. Since FA assay were not found to be an ideal technique to observe binding fragments, a water-LOGSY or STD NMR would provide clearer proof of binding and direct K_d values along with thermodynamic parameters for the hit hydrazones could be obtained by ITC measurements.

Thesis summary

Targeting PPIs has been proven to be a promising drug-discovery approach, but in the p53 pathway this approach was mostly exploited through inhibition of p53/*h*DM2 interaction or restoration of mutated forms of p53. This thesis explored the possibility of stabilizing the interaction of negative regulators of p53, *h*DMX and *h*DM2, with the 14-3-3 family of proteins as an alternative option of activating a tumor suppressor p53. The introductory Chapter 1 offers an overview of different approaches in modulating PPIs through inhibition or stabilization, and the role transcriptional factor p53 has in cancer. The most exploited strategies to rescue the mutated or wt-p53 have been reviewed. Since this thesis focuses on using specific class of proteins, hub 14-3-3 proteins that bind phosphorylated protein partners, specific examples of interactions involving 14-3-3 proteins were discussed.

Chapter 2 presents an extensive biophysical proof of the 14-3-3 interactions with phosphorylated peptides mimicking *h*DMX(2). It was found that all reported phosphorylated sites (pSer-342 and pSer-367 from *h*DMX, pSer-166 and pSer-186 from *h*DM2) have low μM affinity towards 14-3-3 proteins in 1:1 binding stoichiometry. An enhanced overall binding affinity was observed when the two neighboring phosphorylated sites were combined in a longer diphosphorylated peptide. Further, three novel crystal structures were solved, providing an additional validation of the *h*DMX-367, *h*DMX-342 and *h*DM2-186 / 14-3-3σ binding.

To broaden the protentional druggability of the p53's pathway by stabilizing *h*DMX/14-3-3 interaction, screening of fragment and small-molecule libraries is presented in Chapter 3. By employing FA assay for a single-point screen and confirming the identified hits by complementary techniques, SPR and NMR, five fragment starting points have been identified that bind near the peptide/protein interface. The Chapter 3 additionally discuses SAR of a PYR1 compound, where 20 novel compounds were synthesized to gain selectivity towards *h*DMX/14-3-3η interaction.

In Chapter 4, a conceptually novel method for screening low molecular weight compounds is presented. A protein templated fragment ligation approach was explored by employing reversible acylhydrazone formation between hydrazide *h*DMX-367 peptide and library of aldehydes. Several fragments have been identified

to bind in a predefined pocket on 14-3-3η, setting a precedent for a novel approach of screening for PPIs modulators.

The data presented here hopefully offers validation of the *h*DMX(2) binding sites with 14-3-3 proteins and a different approach to PPI modulation leading to reactivation of the p53 pathway. Overall, this thesis combines initial characterization of the target complexes, screening cascades employing robust methods used in the field of working with PPIs, as well as an attempt to develop a novel way to identify starting points for inhibitor or stabilizer development.

Chapter 5: Experimental

5.1 Small-molecule synthesis

(all carried out in AstraZeneca, Gothenburg)

General remarks:

All solvents and reagents were purchased from major providers such as Sigma-Aldrich or Alfa-Aesar and used without further purification. The microwave syntheses were performed in a Biotage Initiator with an external surface IR probe. Products purified by flash column chromatography on prepacked silica gel columns supplied by Biotage, using Biotage automated flash systems with UV detection. Preparative HPLC was performed by Waters Fraction Lynx with ZQ MS detector on either a Waters Xbridge C18 OBD 5 µm column (19 × 150 mm, flow rate 30 mL/min or 30 × 150 mm, flow rate 60 mL/min) using a gradient of 5–95% MeCN with 0.2% NH3 at pH 10 or a Waters SunFire C18 OBD 5 µm column (19 × 150 mm, flow rate 30 mL/min or 30 × 150 mm, flow rate 60 mL/min) using a gradient of 5–95% MeCN with 0.1 M formic acid or on a Gilson Preparative HPLC with a UV/VIS detector 155 on a Kromasil C8 10 µm column (20 × 250 mm, flow rate 19 mL/min, or 50 × 250 mm, flow rate 100 mL/min) using a varying gradient of MeCN with 0.1% formic acid (FA) in water or 0.2% trifluoroacetic acid (TFA) in water or 0.2% acetic acid (AcOH) in water or 0.2% ammonia (NH_3) in water. Mass spectrometry (HR-ESI-MS) was conducted on a Shimadzu LCMS-2020 instrument (ESI+).

^{1}H NMR was carried out on a Bruker Avance II, III, AV300, AV400 or AVIII500 spectrometer at a proton frequency of 400, 500 or 600 MHz at 25 °C or at a temperature and frequency stated in each experiment. ^{13}C NMR spectra were carried out at 101 MHz or 126 MHz. Chemical shifts (δ) are expressed as parts per million (ppm) with residual solvent signal used as a reference ($(CD_3)_2SO$ at 2.50 ppm for ^{1}H NMR and 39.52 ppm for ^{13}C NMR, CD_2Cl_2 at 5.32 ppm for ^{1}H NMR and 53.84 ppm for ^{13}C NMR, $CDCl_3$ at 7.26 ppm for ^{1}H NMR and 77.16 ppm for ^{13}C NMR), and coupling constants are expressed in Hz. The following abbreviations are used: br = broad, s = singlet, d = doublet, t = triplet, q = quartet, m = multiplet.

Synthetic procedures:

Ethyl 2,4-dioxohexanoate, **86**

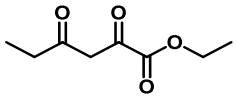

A mixture of diethyl oxalate (0.9 mL, 6.8 mmol) and butan-2-one (0.6 mL, 6.8 mmol) was added dropwise to a stirred solution of sodium ethanolate (3.8 mL, 10.2 mmol) at 0 ℃ and left stirring at room temperature for 24 h. The reaction was quenched with aqueous H_2SO_4 and extracted with ethyl acetate (3 x 20 ml). The combined organic layers were washed with saturated $NaHCO_3$ (3 x 25 ml), dried in a phase separator, and concentrated under vacuum. Purification on silica using Reveleris X2 flash chromatography system (EtOAc, heptane) provided the desired product as a colorless oil (230 mg, 20%). LC-MS m/z $[M^+ H]^+$ calc ($C_8H_{12}O_4$): 172.2, found: 172.1. ^{1}H NMR (500 MHz, Chloroform-d) δ 6.37 (s, 2H), 4.35 (q, J = 7.1 Hz, 2H), 2.53 (q, J = 7.4 Hz, 2H), 1.37 (t, J = 7.1 Hz, 3H), 1.17 (t, J = 7.4 Hz, 3H). Data matches previous characterization.[183]

Ethyl 4-(naphthalen-2-yl)-2,4-dioxobutanoate, **87**

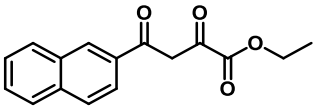

Diethyl oxalate (0.9 ml, 6.8 mmol) and 1-(naphthalen-2-yl)ethan-1-one (1.2 g, 6.8 mmol) were added to a solution of sodium ethanolate (0.7 g, 10.3 mmol). The mixture was left at room temperature and the reaction was quenched with dilute HCl after 6 h. Product was extracted with EtOAc (3 x 20 ml), washed with water and brine (3 x 25 ml), dried in a phase separator before concentrating to yield ethyl 4-(naphthalen-2-yl)-2,4-dioxobutanoate (0.98 g, 51%). LC-MS m/z [M + H]+ calc ($C_{16}H_{14}O_4$): 271.1, found: 271.3. Product was used in the next step without further purification.

Ethyl 2-oxo-3-phenylpropanoate, **88**

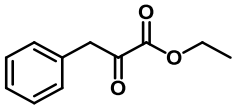

To diethyl oxalate (0.9 ml, 6.8 mmol) in diethyl ether, benzylmagnesium chloride as 2M solution in THF (3.4 ml, 6.8 mmol) was added dropwise while maintaining a temperature of -78 ℃. The mixture was stirred for 1 h and quenched with HCl. The

aqueous layer was extracted with EtOAc (3 x 20 ml), the organic layer was washed, dried in a phase separator, and concentrated to yield ethyl 2-oxo-3-phenylpropanoate (0.62 g, 47%). LC-MS m/z $[M^+ H]^+$ calc ($C_{11}H_{12}O_3$): 192.1, found: 192.2. Product was used without further purification.

Ethyl 2-oxobutanoate, **89**

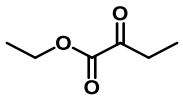

To a solution of 2-oxobutanoic acid (1.0 g, 9.8 mmol) in ethanol (absolute, 99.5%) (10 mL) was added sulfuric acid (0.05 mL, 0.98 mmol) at room temperature. The mixture was stirred for 6 h under reflux. The solvent was removed, residue was diluted with water and pH adjusted to 7 with NaOH. The product was extracted with EtOAc and dried in a phase separator before concentrating (744 mg, 57%). LC-MS m/z $[M^+ H]^+$ calc ($C_6H_{10}O_3$): 131.1, found: 131.2. Product was used in the next step without further purification.

General procedure for synthesis of PYR1 derivatives:

In a 20 mL microwave reactor, to a suspension of aniline derivative (1.0 equiv) in acetic acid (5 mL) was added benzaldehyde derivative (1.0 equiv), followed by dicarbonyl derivatives (1.00 equiv). The vial was capped and heated at 120 °C for 120 min in a single node microwave reactor. The pressure monitored was 1 bar. Biotage V10 was used to evaporate acetic acid and the crude material was dissolved in DMSO for HPLC purification. The compound was purified by preparative HPLC on a Kromasil C8 column (10 µm 250 x 20 ID mm) using a gradient of acetonitrile in H_2O/ACN/FA 95/5/0.2 buffer, over 20 minutes with a flow of 19 mL/min. The compounds were detected by UV at 254 nm.

5-(3-benzyl-4-hydroxy-2-(4-nitrophenyl)-5-oxo-2,5-dihydro-1H-pyrrol-1-yl)-2-hydroxy benzoic acid, **83**

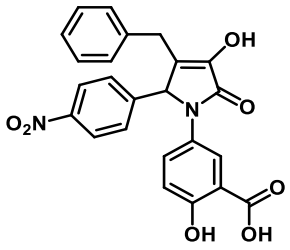

General procedure A was followed, using ethyl 2-oxo-4-phenylbutanoate (185 µl, 0.97 mmol), 5-amino-2-hydroxybenzoic acid (149 mg, 0.97 mmol) and 4-nitrobenzaldehyde (147 mg, 0.97 mmol) to give **83** (195 mg, 45%) HRMS (ESI) m/z $[M^+ H]^+$ calcd ($C_{24}H_{18}N_2O_7$): 447.1192, found: 447.1169. ^{1}H NMR (500 MHz, DMSO) δ 9.94 (s, 1H, OH), 9.73 (s, 1H, OH), 8.03 (d, J = 8.2 Hz, 2H, Ar), 7.34 (d, J = 8.2 Hz, 2H, Ar), 7.24 – 7.17 (m, 2H, Ar), 7.17 – 7.10 (m, 1H, Ar), 7.11 – 6.91 (m, 3H, Ar), 6.78 (d, J = 8.1 Hz, 1H, Ar), 6.65 (t, J = 7.7 Hz, 1H, Ar), 5.63 (s, 1H, CH), 3.70 (d, J = 15.0 Hz, 1H, CH_2), 3.07 (d, J = 14.9 Hz, 1H, CH_2). ^{13}C NMR (151 MHz, DMSO) δ 164.4, 151.0, 145.5, 142.9, 141.6, 136.9, 127.4, 127.3, 126.8, 126.6, 126.4, 124.4, 122.8, 121.9, 121.8, 117.3, 116.4, 114.8, 61.1, 28.1.

4-benzyl-3-hydroxy-1-(2-hydroxyphenyl)-5-(4-nitrophenyl)-1,5-dihydro-2H-pyrrol-2-one, **102**

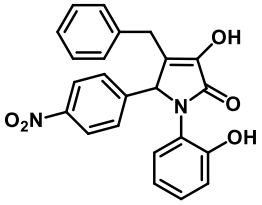

General procedure A was followed, using ethyl 2-oxo-4-phenylbutanoate (138 µl, 0.73 mmol), 4-nitrobenzaldehyde (110 mg, 0.73 mmol) and 2-aminophenol (79 mg, 0.73 mmol) to give **102** (53.8 mg, 18%) HRMS (ESI) m/z $[M^+ H]^+$ calcd ($C_{23}H_{18}N_2O_5$): 403.1294, found: 403.1269. ^{1}H NMR (500 MHz, DMSO) δ 9.97 (s, 1H, OH), 9.76 (s, 1H, OH), 8.04 (dd, *J* = 8.7, 2.1 Hz, 2H, Ar), 7.38 – 7.31 (m, 2H, Ar), 7.24 – 7.18 (m, 2H, Ar), 7.18 – 7.11 (m, 1H, Ar), 7.07-7.01 (m, 3H, Ar), 6.99 (t, *J* = 7.9 Hz, 1H, Ar), 6.79 (d, *J* = 8.2 Hz, 1H, Ar), 6.66 (t, *J* = 7.7 Hz, 1H, Ar), 5.64 (s, 1H, CH), 3.70 (d, *J* = 15.0 Hz, 1H, CH_2), 3.07 (d, *J* = 15.0 Hz, 1H, CH_2). ^{13}C NMR (126 MHz, DMSO) δ 166.5, 153.1, 147.6, 145.0, 143.7, 139.0, 129.5, 129.4, 128.9, 128.8, 128.5, 126.5, 124.9, 124.0, 124.0, 119.4, 116.9, 63.2, 30.2.

4-benzyl-3-hydroxy-1-(4-hydroxyphenyl)-5-(4-nitrophenyl)-1,5-dihydro-2H-pyrrol-2-one, **103**

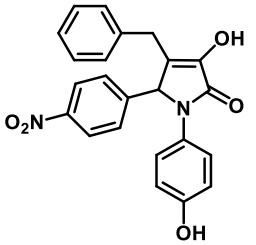

General procedure A was followed, using ethyl 2-oxo-4-phenylbutanoate (185 µl, 0.97 mmol), 4-aminophenol (106 mg, 0.97 mmol) and 4-nitrobenzaldehyde (147 mg,

0.97 mmol) to give **103** (163 mg, 42%) HRMS (ESI) m/z $[M^+ H]^+$ calcd ($C_{23}H_{18}N_2O_5$): 403.1294, found: 403.1299. ^{1}H NMR (500 MHz, DMSO) δ 9.98 (s, 1H, OH), 9.31 (s, 1H, OH), 8.06 (d, *J* = 8.2 Hz, 2H, Ar), 7.38 (d, *J* = 8.2 Hz, 2H, Ar), 7.33 – 7.25 (m, 2H, Ar), 7.20 (t, *J* = 7.4 Hz, 2H, Ar), 7.16-7.13 (m, 1H, Ar), 7.05 (d, *J* = 7.4 Hz, 2H, Ar), 6.64 – 6.58 (m, 2H, Ar), 5.73 (s, 1H, CH), 3.64 (d, *J* = 15.1 Hz, 1H, CH_2), 3.06 (d, *J* = 15.0 Hz, 1H, CH_2). ^{13}C NMR (126 MHz, DMSO) δ 165.9, 154.9, 147.6, 145.3, 143.5, 138.9, 129.3, 129.0, 128.9, 128.8, 126.5, 124.3, 124.2, 124.0, 115.6, 62.5, 30.1.

4-benzyl-3-hydroxy-1-(3-hydroxynaphthalen-2-yl)-5-(4-nitrophenyl)-1,5-dihydro-2H-pyrrol-2-one, **104**

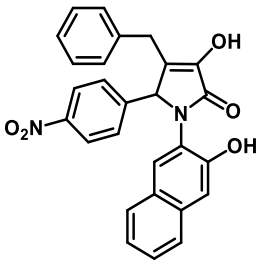

General procedure A was followed, using ethyl 2-oxo-4-phenylbutanoate (200 mg, 0.97 mmol), 3-aminonaphthalen-2-ol (154 mg, 0.97 mmol) and 4-nitrobenzaldehyde (147 mg, 0.97 mmol) to give **104** (38.7 mg, 9%) HRMS (ESI) m/z $[M^+ H]^+$ calcd ($C_{27}H_{20}N_2O_5$): 453.1445, found: 453.1477. ^{1}H NMR (600 MHz, DMSO) δ 10.12 (s, 1H, OH), 9.95 (s, 1H, OH), 8.00 – 7.89 (m, 2H, Ar), 7.61 (s, 1H, Ar), 7.57 (d, *J* = 8.2 Hz, 1H, Ar), 7.52 (d, *J* = 8.3 Hz, 1H, Ar), 7.33 – 7.29 (m, 2H, Ar), 7.25 (dd, *J* = 8.3, 1.4 Hz, 1H, Ar), 7.16 – 7.13 (m, 3H, Ar), 7.11 – 7.07 (m, 1H, Ar), 7.05 (s, 1H, Ar), 7.01 – 6.95 (m, 2H, Ar), 5.71 (s, 1H, CH), 3.69 (d, *J* = 15.0 Hz, 1H, CH_2,), 3.00 (d, *J* = 15.0 Hz, 1H, CH_2). ^{13}C NMR (126 MHz, DMSO) δ not obtained

5-(3-acetyl-4-hydroxy-2-(4-nitrophenyl)-5-oxo-2,5-dihydro-1H-pyrrol-1-yl)-2-hydroxy benzoic acid, **90**

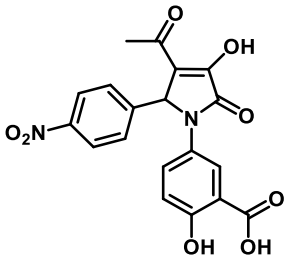

General procedure A was followed, using ethyl 2,4-dioxopentanoate (0.133 mL, 0.95 mmol), 4-nitrobenzaldehyde (143 mg, 0.95 mmol) and 5-amino-2-hydroxybenzoic acid (145 mg, 0.95 mmol) to give **90** (215 mg, 57%), HRMS (ESI) m/z $[M^+ H]^+$ calcd

($C_{19}H_{14}N_2O_8$): 399.0828, found: 399.0808. ^{1}H NMR (500 MHz, DMSO) δ 8.10 – 8.03 (m, 2H, Ar), 7.97 (d, *J* = 2.8 Hz, 1H, Ar), 7.63 (d, *J* = 2.7 Hz, 1H, Ar), 7.62 (d, *J* = 2.8 Hz, 1H, Ar), 7.60 – 7.50 (m, 1H, Ar), 6.87 (d, *J* = 9 Hz, 1H, Ar), 6.18 (s, 1H, CH), 2.33 (s, 3H, CH_3), OH signals not observed. ^{13}C NMR (151 MHz, DMSO) δ 169.4, 162.7, 157.1, 145.4, 143.3, 128.7, 127.7, 125.6, 123.2, 122.2, 121.7, 116.43, 115.8, 111.4, 58.3, 38.8.

4-acetyl-3-hydroxy-1-(4-hydroxyphenyl)-5-(4-nitrophenyl)-1,5-dihydro-2H-pyrrol-2-one, **91**

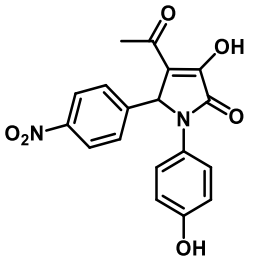

General procedure A was followed, using ethyl 2,4-dioxopentanoate (0.266 mL, 1.90 mmol), 4-nitrobenzaldehyde (287 mg, 1.90 mmol) and 4-aminophenol (166 mg, 1.52 mmol) to give **91** (443 mg, 66%). HRMS (ESI) m/z [M $^+$ H]$^+$ calcd ($C_{18}H_{14}N_2O_6$): 355.0925, found: 355.0917. ^{1}H NMR (500 MHz, DMSO) δ 9.28 (s, 1H, OH), 8.06 – 7.92 (m, 2H, Ar), 7.47 – 7.37 (m, 2H, Ar), 7.37 – 7.27 (m, 2H, Ar), 6.67 – 6.51 (m, 2H, Ar), 5.80 (s, 1H, CH), 2.18 (s, 3H, CH_3). 1 OH not observed. ^{13}C NMR (126 MHz, DMSO) δ 188.0, 171.4, 168.2, 154.9, 149.3, 145.7, 128.7, 124.8, 123.9, 122.8, 115.1, 60.1, 28.1.

4-acetyl-3-hydroxy-1-(2-hydroxyphenyl)-5-(4-nitrophenyl)-1,5-dihydro-2H-pyrrol-2-one, **92**

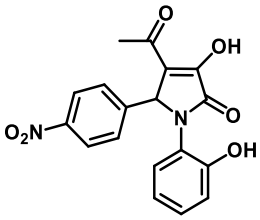

General procedure A was followed, using ethyl 2,4-dioxopentanoate (0.178 mL, 1.26 mmol), 4-nitrobenzaldehyde (191 mg, 1.26 mmol) and 2-aminophenol (110 mg, 1.01 mmol) to give **92** (157 mg, 35%). HRMS (ESI) m/z [M$^+$ H]$^+$ calcd ($C_{18}H_{14}N_2O_6$): 355.0925, found: 355.0908. ^{1}H NMR (500 MHz, DMSO) δ 8.03 – 7.91 (m, 2H, Ar), 7.40 – 7.33 (m, 2H, Ar), 7.02 – 6.91 (m, 2H, Ar), 6.79 (dd, *J* = 8.1, 1.4 Hz, 1H, Ar), 6.64 (td, *J* = 7.6, 1.4 Hz, 1H, Ar), 5.79 (s, 1H, CH), 2.16 (s, 3H, CH_3). 1 OH not observed. ^{13}C NMR (126 MHz, DMSO) δ 186.82, 171.39, 170.05, 168.19, 152.29,

150.68, 145.81, 128.74, 128.01, 127.51, 124.80, 122.56, 118.91, 116.99, 112.04, 60.40, 27.33.

4-acetyl-3-hydroxy-5-(4-nitrophenyl)-1-phenyl-1,5-dihydro-2H-pyrrol-2-one, **93**

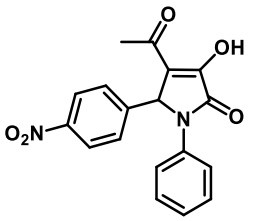

General procedure A was followed, using ethyl 2,4-dioxopentanoate (0.133 mL, 0.95 mmol), 4-nitrobenzaldehyde (143 mg, 0.95 mmol) and aniline (0.086 mL, 0.95 mmol) to give **93** (162 mg, 51%). HRMS (ESI) m/z $[M^+ H]^+$ calcd ($C_{18}H_{14}N_2O_5$): 339.0981, found: 339.0966. ^{1}H NMR (500 MHz, DMSO) δ 9.32 (s, 1H, OH), 8.10 – 7.97 (m, 2H, Ar), 7.61-7.56 (m, 4H, Ar), 7.34 – 7.22 (m, 2H, Ar), 7.09 (t, *J* = 7.4 Hz, 1H, Ar), 6.23 (s, 1H, CH), 2.33 (s, 3H, CH_3). ^{13}C NMR (126 MHz, DMSO) δ 187.8, 171.7, 168.6, 154.6, 150.2, 146.26, 129.2, 129.0, 123.9, 122.9, 115.2, 60.2, 27.9.

2-hydroxy-5-(3-hydroxy-5-(4-nitrophenyl)-2-oxo-4-propionyl-2,5-dihydro-1H-pyrrol-1-yl)benzoic acid, **94**

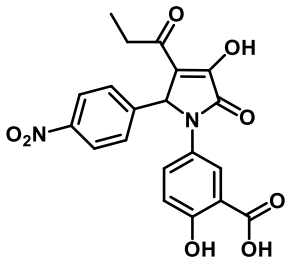

General procedure A was followed, using ethyl 2,4-dioxohexanoate (200mg, 1.16 mmol), 4-nitrobenzaldehyde (176 mg, 1.16 mmol) and 5-amino-2-hydroxybenzoic acid (178 mg, 1.16 mmol) to give **94** (187 mg, 39%). HRMS (ESI) m/z $[M^+ H]^+$ calcd ($C_{20}H_{16}N_2O_8$): 413.0985, found: 413.0964. ^{1}H NMR (500 MHz, DMSO) δ 8.20 (d, J = 8.7 Hz, 1H, OH), 8.12 – 8.02 (m, 2H, Ar), 7.96 (d, J = 2.7 Hz, 1H, Ar), 7.68 – 7.58 (m, 1H, Ar), 7.61 – 7.50 (m, 2H, Ar), 6.88 (d, J = 8.9 Hz, 1H, Ar), 6.19 (s, 1H, CH), 2.92 – 2.73 (m, 1H, CH_2), 2.71 – 2.57 (m, 1H, CH_2), 0.90 (t, J = 7.3, 3H, CH_3). ^{13}C NMR (126 MHz, DMSO) δ 194.2, 171.0, 165.3, 160.0, 146.8, 146.3, 129.1, 128.3, 126.1, 125.1, 123.2, 116.6, 60.3, 34.61, 7.9.

3-hydroxy-1-(4-hydroxyphenyl)-5-(4-nitrophenyl)-4-propionyl-1,5-dihydro-2H-pyrrol-2-one, **95**

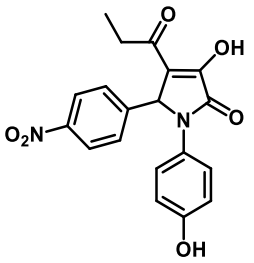

General procedure A was followed, using ethyl 2,4-dioxohexanoate (200 mg, 1.16 mmol), 4-nitrobenzaldehyde (176 mg, 1.16 mmol) and 4-aminophenol (101 mg, 0.93 mmol) to give **95** (172 mg, 40%). HRMS (ESI) m/z $[M^+ H]^+$ calcd ($C_{19}H_{16}N_2O_6$): 369.1086, found: 369.1082. ^{1}H NMR (500 MHz, DMSO) δ 9.46 (s, 1H, OH), 8.07 – 8.01 (m, 2H, Ar), 7.55 – 7.48 (m, 2H, Ar), 7.32 – 7.27 (m, 2H, Ar), 6.66 – 6.61 (m, 2H, Ar), 6.09 (s, 1H, CH), 2.85 – 2.75 (m, 1H, CH_2), 2.68 (dq, *J* = 17.5, 7.3 Hz, 1H, CH_2), 0.90 (dd, *J* = 7.3, 5.8 Hz, 3H, CH_3), 1 OH not observed. ^{13}C NMR (126 MHz, DMSO) δ 164.7, 155.8, 148.1, 147.3, 145.7, 129.6, 129.4, 127.7, 125.10, 124.0, 123.7, 115.6, 60.7, 35.4, 8.1.

3-hydroxy-1-(2-hydroxyphenyl)-5-(4-nitrophenyl)-4-propionyl-1,5-dihydro-2H-pyrrol-2-one, **96**

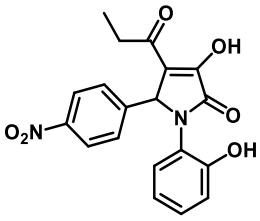

General procedure A was followed, using ethyl 2,4-dioxohexanoate (150 mg, 0.87 mmol), 4-nitrobenzaldehyde (132 mg, 0.87 mmol) and 2-aminophenol (76 mg, 0.70 mmol) to give **96** (73 mg, 23%). HRMS (ESI) m/z $[M^+ H]^+$ calcd ($C_{19}H_{16}N_2O_6$): 369.1086, found: 369.1078. ^{1}H NMR (500 MHz, DMSO) δ 10.05 (s, 1H, OH), 8.10 – 7.97 (m, 2H, Ar), 7.48 – 7.38 (m, 2H, Ar), 7.09 – 6.95 (m, 2H, Ar), 6.83 (d, *J* = 8.1 Hz, 1H, Ar), 6.68 (t, *J* = 7.6 Hz, 1H, Ar), 5.91 (s, 1H, CH), 2.86 – 2.75 (m, 1H, CH_2), 2.74 – 2.68 (m, 1H, CH_2), 0.91 (dd, *J* = 8.2, 6.3 Hz, 3H, CH_3), 1 OH not observed.^{13}C NMR (126 MHz, DMSO) δ 193.6, 163.1, 151.0, 145.3, 143.6, 127.6, 127.3, 127.2, 121.6, 120.7, 117.4, 116.5, 114.9, 59.2, 33.4, 6.1.

3-hydroxy-5-(4-nitrophenyl)-1-phenyl-4-propionyl-1,5-dihydro-2H-pyrrol-2-one, **97**

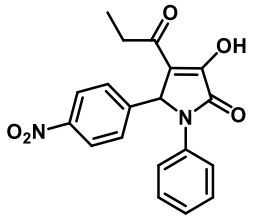

General procedure A was followed, using ethyl 2,4-dioxohexanoate (200 mg, 1.16 mmol), 4-nitrobenzaldehyde (176 mg, 1.16 mmol) and aniline (0.106 mL, 1.16 mmol) to give **97** (126 mg, 31%). HRMS (ESI) m/z $[M^+ H]^+$ calcd ($C_{19}H_{16}N_2O_5$): 353.1137, found: 353.1133. ^{1}H NMR (500 MHz, DMSO) δ 8.13 – 8.03 (m, 2H, Ar), 7.62 – 7.58 (m, 4H, Ar), 7.37 – 7.22 (m, 2H, Ar), 7.11 (t, *J* = 7.4 Hz, 1H, Ar), 6.26 (s, 1H, CH), 2.89 – 2.64 (m, 2H, CH_2), 0.91 (t, *J* = 7.3 Hz, 3H, CH_3), OH not observed. ^{13}C NMR (126 MHz, DMSO) δ 195.0, 164.7, 146.9, 145.3, 135.9, 129.2, 128.9, 125.7, 123.8, 122.4, 120.9, 59.5, 35.2, 7.7.

2-hydroxy-5-(3-hydroxy-4-methyl-5-(4-nitrophenyl)-2-oxo-2,5-dihydro-1H-pyrrol-1-yl) benzoic acid, **98**

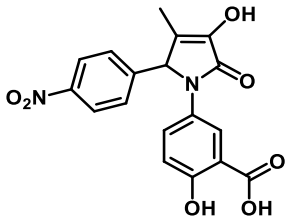

General procedure A was followed, using ethyl 2-oxobutanoate (200 mg, 1.54 mmol), 5-amino-2-hydroxybenzoic acid (235 mg, 1.54 mmol) and 4-nitrobenzaldehyde (232 mg, 1.54 mmol) to give **98** (199 mg, 35%). HRMS (ESI) m/z $[M^+ H]^+$ calcd ($C_{18}H_{14}N_2O_7$): 371.0879, found: 371.0876. ^{1}H NMR (500 MHz, DMSO) δ 10.17 (s, 1H, OH), 9.64 (s, 1H, OH), 8.42 (d, *J* = 8.6 Hz, 1H, Ar), 8.17 - 8.15 (m, 2H, Ar), 7.94 (d, *J* = 2.7 Hz, 1H, Ar), 7.60 (dd, *J* = 9.0, 2.7 Hz, 1H, Ar), 7.52 - 7.49 (m, 1H, Ar), 6.86 (d, *J* = 9.0 Hz, 1H, Ar), 5.90 (s, 1H, CH), 1.64 (s, 3H, CH_3), 1 OH not observed. ^{13}C NMR (126 MHz, DMSO) δ 171.3, 165.8, 157.7, 147.3, 144.9, 142.0, 129.0, 128.8, 128.5, 124.1, 122.9, 122.0, 117.4, 112.8, 62.7, 9.1.

3-hydroxy-1-(2-hydroxyphenyl)-4-methyl-5-(4-nitrophenyl)-1,5-dihydro-2H-pyrrol-2-one, **99**

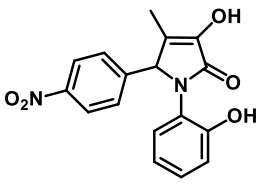

General procedure A was followed, using ethyl 2-oxobutanoate (200 mg, 1.54 mmol), 2-aminophenol (168 mg, 1.54 mmol) and 4-nitrobenzaldehyde (232 mg, 1.54 mmol) to give **99** (59 mg, 12%). HRMS (ESI) m/z $[M^+ H]^+$ calcd ($C_{17}H_{14}N_2O_5$): 327.0981, found: 327.095. ^{1}H NMR (600 MHz, DMSO) δ 9.67 (s, 1H, OH), 9.48 (s, 1H, OH), 8.07 – 8.04 (m, 2H, Ar), 7.45 – 7.35 (m, 2H, Ar), 6.99 (dd, *J* = 7.9, 1.6 Hz, 1H, Ar), 6.93 (td, *J* = 8.1, 1.6 Hz, 1H, Ar), 6.74 (dd,J = 8.1, 1.2 Hz, 1H, Ar), 6.61 (td, *J* = 7.7, 1.3 Hz, 1H, Ar), 5.64 (s, 1H, CH), 1.53 (d, *J* = 0.6 Hz, 3H, CH_3). ^{13}C NMR (126 MHz, DMSO) δ 171.29, 165.88, 157.78, 147.18, 144.96, 141.88, 129.08, 128.47, 124.05, 122.89, 121.98, 117.40, 112.78, 62.66, 9.29.

2-hydroxy-5-(3-hydroxy-5-(4-nitrophenyl)-2-oxo-4-phenyl-2,5-dihydro-1H-pyrrol-1-yl) benzoic acid, **100**

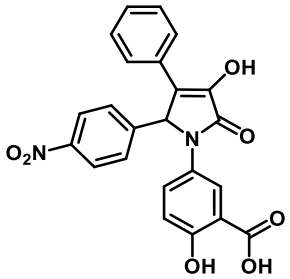

General procedure A was followed, using ethyl 2-oxo-3-phenylpropanoate (150 mg, 0.78 mmol), 5-amino-2-hydroxybenzoic acid (120 mg, 0.78 mmol) and 4-nitrobenzaldehyde (118 mg, 0.78 mmol) to give **100** (201 mg, 60%). HRMS (ESI) m/z $[M^+ H]^+$ calcd ($C_{23}H_{16}N_2O_7$): 433.1036, found: 433.1027. ^{1}H NMR (500 MHz, DMSO) δ 10.78 (s, 1H, OH), 8.08 – 8.04 (m, 2H, Ar), 8.00 (d, *J* = 2.7 Hz, 1H, Ar), 7.72 – 7.69 (m, 3H, Ar), 7.67 – 7.62 (m, 2H, Ar), 7.31 (t, *J* = 7.8 Hz, 2H, Ar), 7.21 – 7.15 (m, 1H, Ar), 6.91 (d, *J* = 9.0 Hz, 1H, Ar), 6.71 (s, 1H, CH). 2 OH not observed. ^{13}C NMR (126 MHz, DMSO) δ 171.2, 165.1, 147.2, 145.4, 143.5, 131.1, 129.9, 129.0, 128.4, 127.5, 127.2, 124.1, 123.7, 121.8, 117.5, 60.7. 2 C not observed.

3-hydroxy-1-(2-hydroxyphenyl)-5-(4-nitrophenyl)-4-phenyl-1,5-dihydro-2H-pyrrol-2-one, **101**

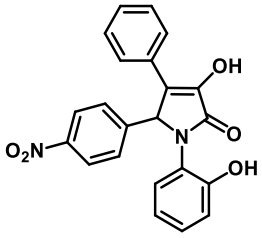

General procedure A was followed, using ethyl 2-oxo-3-phenylpropanoate (150 mg, 0.78 mmol), 2-aminophenol (85 mg, 0.78 mmol) and 4-nitrobenzaldehyde (118 mg, 0.78 mmol) to give **101** (139 mg, 46%). HRMS (ESI) m/z $[M^+ H]^+$ calcd ($C_{22}H_{16}N_2O_5$):

389.1137, found: 389.1133. ^{1}H NMR (500 MHz, DMSO) δ 10.76 (s, 1H, OH), 9.80 (s, 1H, OH), 8.06 – 7.99 (m, 2H, Ar), 7.68 – 7.61 (m, 2H, Ar), 7.61 – 7.53 (m, 2H, Ar), 7.29 (t, *J* = 7.8 Hz, 2H, Ar), 7.23 – 7.13 (m, 1H, Ar), 7.08 – 7.01 (m, 1H, Ar), 6.94 (dd, *J* = 7.9, 1.7 Hz, 1H, Ar), 6.86 (dd, *J* = 8.2, 1.4 Hz, 1H, Ar), 6.68 (td, *J* = 7.6, 1.4 Hz, 1H, Ar), 6.30 (s, 1H, CH). ^{13}C NMR (151 MHz, DMSO) δ 166.0, 153.5, 147.6, 145.9, 144.7, 132.0, 129.5, 129.4, 128.9, 128.8, 127.6, 127.4, 124.0, 123.5, 121.6, 119.4, 117.0, 61.6.

2-hydroxy-5-(3-hydroxy-4-(4-methoxybenzyl)-5-(4-nitrophenyl)-2-oxo-2,5-dihydro-1 H-pyrrol-1-yl)benzoic acid, **105**

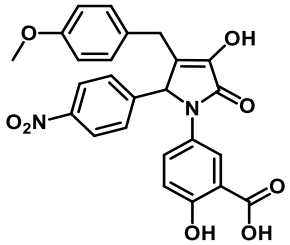

General procedure A was followed, using ethyl 4-(4-methoxyphenyl)-2-oxobutanoate (150 mg, 0.63 mmol), 5-amino-2-hydroxybenzoic acid (97 mg, 0.63 mmol) and 4-nitrobenzaldehyde (96 mg, 0.63 mmol) to give **105** (9 mg, 2.98%). HRMS (ESI) m/z $[M^+ H]^+$ calcd ($C_{25}H_{20}N_2O_8$): 477.1298, found: 477.1261. ^{1}H NMR (500 MHz, DMSO) δ 9.88 (s, 1H, OH), 9.72 (s, 1H, OH), 8.04 – 8.02 (m, 2H, Ar), 7.33 – 7.30 (m, 2H, Ar), 7.03 (dd, J = 7.8, 1.7 Hz, 1H, Ar), 6.97 (td, J = 7.8, 1.7 Hz, 1H, Ar), 6.94 – 6.89 (m, 2H, Ar), 6.81 – 6.72 (m, 3H, Ar), 5.61 (s, 1H, CH), 3.68 (s, 3H, CH_3), 3.63 (d, J = 15.0 Hz, 1H, CH_2), 2.99 (d, J = 15.0 Hz, 1H, CH_2), 1 OH not observed. ^{13}C NMR (151 MHz, DMSO) δ 166.6, 158.1, 153.2, 147.6, 145.1, 143.4, 130.8, 129.9, 129.5, 129.4, 128.5, 125.5, 124.0, 123.9, 119.4, 116.9, 114.2, 63.2, 55.4, 29.3. 1 C not observed.

3-hydroxy-1-(2-hydroxyphenyl)-4-(4-methoxybenzyl)-5-(4-nitrophenyl)-1,5-dihydro-2 H-pyrrol-2-one, **106**

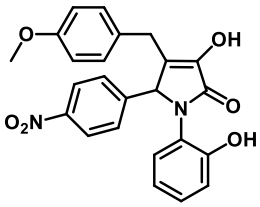

General procedure A was followed, using ethyl 4-(4-methoxyphenyl)-2-oxobutanoate (150 mg, 0.63 mmol), 2-aminophenol (69.3 mg, 0.63 mmol) and 4-nitrobenzaldehyde (96 mg, 0.63 mmol) to give **106** (104 mg, 38%).LCMS m/z $[M^+ H]^+$ calcd ($C_{24}H_{20}N_2O_6$): 433.1, found: 433.2. ^{1}H NMR (500 MHz, DMSO) δ 9.96 (s, 1H, OH), 8.10 – 8.04 (m, 2H, Ar), 7.95 (d, *J* = 2.8 Hz, 1H, Ar), 7.59 (dd, *J* = 9.0, 2.8 Hz, 1H, Ar), 7.38 (d, *J* =

8.3 Hz, 2H, Ar), 7.00 – 6.92 (m, 2H, Ar), 6.87 – 6.79 (m, 2H, Ar), 6.78 – 6.70 (m, 2H, Ar), 5.82 (s, 1H, CH), 3.68 (s, 3H, CH_3), 3.64 – 3.54 (m, 1H, CH_2), 3.00 (d, *J* = 15.2 Hz, 1H, CH_2), 1 OH not observed. ^{13}C NMR (151 MHz, DMSO) δ 171.7, 166.1, 158.4, 158.1, 147.6, 144.98, 143.1, 130.6, 129.9, 129.8, 129.2, 129.0, 125.5, 124.3, 123.7, 117.7, 114.2, 62.2, 55.4, 29.2.

5-(3-(2-naphthoyl)-4-hydroxy-2-(4-nitrophenyl)-5-oxo-2,5-dihydro-1H-pyrrol-1-yl)-2-hydroxybenzoic acid, **107**

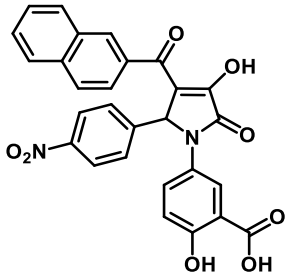

General procedure A was followed, using ethyl 4-(naphthalen-2-yl)-2,4-dioxobutanoate (200 mg, 0.74 mmol), 5-amino-2-hydroxybenzoic acid (113 mg, 0.74 mmol) and 4-nitrobenzaldehyde (112 mg, 0.74 mmol) to give **107** (151 mg, 40%) HRMS (ESI) m/z $[M^+ H]^+$ calcd ($C_{28}H_{18}N_2O_8$): 511.1141, found: 511.1135. ^{1}H NMR (600 MHz, DMSO) δ 8.68 (d, J = 1.6 Hz, 1H, Ar), 8.40 (d, J = 1.7 Hz, 1H, Ar), 8.10 – 8.04 (m, 4H, Ar), 8.03 – 7.91 (m, 4H, Ar), 7.76 (dd, J = 8.7, 1.9 Hz, 2H, Ar), 7.74 – 7.69 (m, 1H, Ar), 6.91 (d, J = 8.9 Hz, 1H, Ar), 6.51 (s, 1H, CH).OH not observed. ^{13}C NMR (151 MHz, DMSO) δ 171.6, 165.0, 159.3, 147.6, 135.6, 135.5, 135.3, 134.6, 132.7, 132.4, 131.0, 130.8, 130.0, 129.9, 129.8, 129.08, 128.7, 128.1, 127.4, 127.2, 125.4, 124.9, 118.0, 61.4.

4-(2-naphthoyl)-3-hydroxy-1-(2-hydroxyphenyl)-5-(4-nitrophenyl)-1,5-dihydro-2H-pyrrol-2-one, **108**

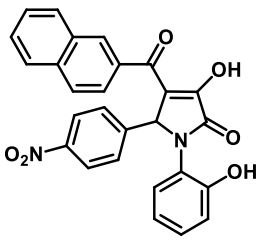

General procedure A was followed, using ethyl 4-(naphthalen-2-yl)-2,4-dioxobutanoate (150 mg, 0.55 mmol), 2-aminophenol (60.6 mg, 0.55 mmol) and 4-nitrobenzaldehyde (84 mg, 0.55 mmol) to give **108** (54.7 mg, 21%) HRMS (ESI) m/z $[M^+ H]^+$ calcd ($C_{27}H_{18}N_2O_6$): 467.1243, found: 467.1228. ^{1}H NMR (500 MHz, DMSO) δ 9.97 (s, 1H, OH), 8.43 (d, *J* = 1.7 Hz, 1H, Ar), 8.15 – 8.04 (m, 2H, Ar), 7.97 (dd, *J* = 8.5, 5.8 Hz, 2H, Ar), 7.85 – 7.79 (m, 1H, Ar), 7.76 (dd, *J* =

8.5, 1.8 Hz, 1H, Ar), 7.73 – 7.68 (m, 2H, Ar), 7.66 – 7.59 (m, 2H, Ar), 7.16 (dd, *J* = 7.9, 1.7 Hz, 1H, Ar), 7.10 – 7.05 (m, 1H, Ar), 6.88 (dd, *J* = 8.2, 1.4 Hz, 1H, Ar), 6.73 (td, *J* = 7.6, 1.4 Hz, 1H, Ar), 6.31 (s, 1H, CH), 1 OH not observed. ^{13}C NMR (151 MHz, DMSO) δ 165.1, 153.3, 147.7, 144.9, 135.6, 135.3, 132.4, 131.1, 129.9, 129.8, 129.4, 129.3, 129.3, 128.9, 128.2, 128.1, 127.2, 124.9, 124.1, 123.8, 123.0, 119.5, 117.1, 62.1.

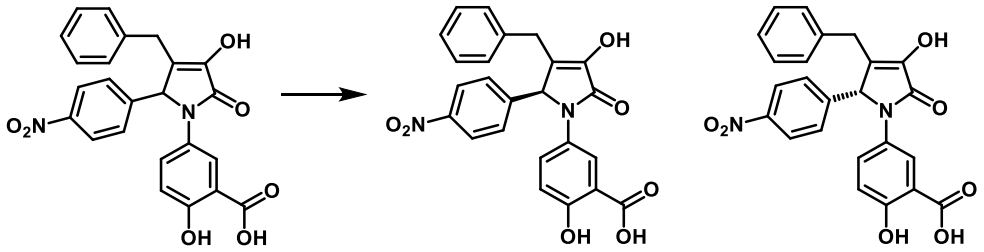

Enantiomers of 20 were separated by chiral chromatography on Chiralpak column (250 x 3 mm 5 µM), using Heptane:EtOH solvents in 60:40 ratio.

The first eluted compound was collected, and solvent was evaporated to give an enantiomer 1 (28 mg). [α]D^{20}: -77.3 (c = 0.5, ACN, 589 nM, 20℃). The second eluted compound was collected, and solvent was evaporated to give enantiomer 2 (32 mg). [α]D^{20}: +83.4 (c = 0.5, ACN, 589 nM, 20℃).

Chiral separation report: **83**

Project: 1test
Sample Name: 30566

Project Name: ARC 2\ARC2_2019-07-01 1
Date Acquired: 2019-07-01 14:10:14

Column:	Chiralpak ID	**Column ID:**	
Mobile Phase A:	Hep/TEA 100/0.1	**Column Dimension:**	150*4.6 mm
Mobile Phase B:	EtOH/TEA 100/0.1	**Particle Size:**	3
Gradient:	40% B	**Injection volume:**	8.00 ul
		Flow:	0.8 ml/min
Temperature:	25°C	**Wavelength:**	2998 PDA 270.0 nm
Sample Concentration:	Sample in EtOH	**Vial:**	2:A,2

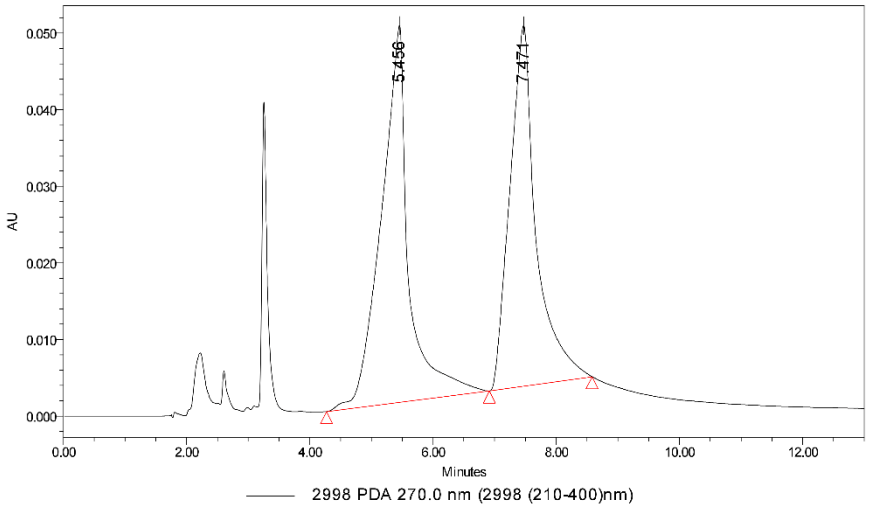

	Retention Time	Area	% Area	k'	N	USP Resolution	Width @ 50%
1	5.456	1521162	52.09	0.000	838.0		3.914876e-001
2	7.471	1399206	47.91	0.369	1616.5	2.532	4.009124e-001

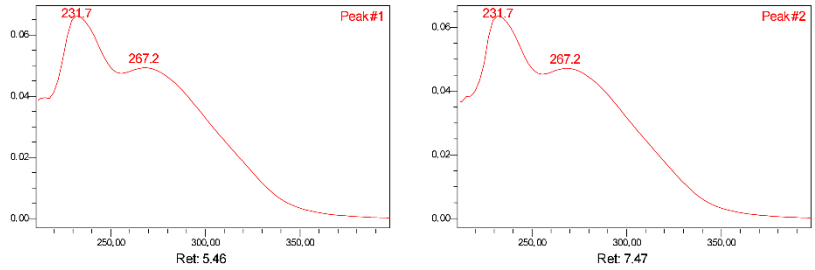

Report Method: normal_spektrum
Acq Method Set: A_C_60_40_25C

Injection Id 4231

5.2 Peptide synthesis

General remarks : Resins and amino acids were purchased from either Sigma–Aldrich or Novabiochem. All amino acids were N -Fmoc protected and side chains protected with Boc (His, Lys), t-Bu (Asp, Glu, Ser, Thr), Pbf (Arg), Trt (Asn, Gln). Peptides were synthesized either manually or using a microwave assisted automated peptide synthesizer (CEM Liberty Blue) on a 0.05 or 0.1 mmol scale. DMF used in peptide synthesis was of ACS grade and from Sigma–Aldrich.

Manual peptide synthesis

Manual peptide synthesis followed this cycle: swelling of a resin (20 min) in cartridge used for solid-phase synthesis, washing (DMF, 3 x 2 ml x 2 min), deprotection (Method A), and coupling of a desired amino acid (Method B), where successful coupling and deprotection were determined by a color test (Method C). Acetylation (Method D) or coupling of a fluorescent dye (Method E) were performed prior to cleavage (Method F).

Method A: Deprotection N-terminal Fmoc-protecting groups were removed by adding 20% piperidine in DMF (5 × 2 mL × 2 min) and washed with DMF (5 × 2 mL × 2 min) after.

Method B: Manual coupling of amino acid and Ahx

The desired amino acid or Ahx (5 equiv.), DIPEA (10 equiv.) and HCTU (5 equiv.) were dissolved in DMF (2 mL) and added to the resin, followed by agitation for 1 h. Reagents were removed by filtration and the resin was washed with DMF (3 × 2 mL × 2 min).

Method C: Kaiser test

Successful coupling or deprotection for any residue coupled manually was determined by Kaiser test. A few resin beads were transferred into a vial and mixed with 2 drops of each of the solutions:

1) Ninhydrin (5% w/v) in ethanol

2) Phenol (80% w/v) in ethanol

3) 1 mM KCN (aq.) in pyridine (2% v/v)

The solution was heated at 100 °C for five minutes before observing the change in color. Successful deprotection was observed by color of the beads changing into blue, where successful coupling gave no change in color.

Method D: N-terminal acetylation

Acetic anhydride (10 equiv.) and DIPEA (10 equiv.) were dissolved in DMF (2 mL) and the solution was transferred to the resin. After 2 h, the resin was drained and washed with DMF (3 × 2 mL × 2 min). Successful capping was determined by color test (Method C).

Method E: N-terminal Fluorescent Dye coupling

5,6-carboxyfluorescein (5 equiv.), DIPEA (5 equiv.) and HCTU (5 equiv.) were dissolved in DMF (2 mL) and added to the resin, followed by agitation for 1 h. Reagents were filtered and the resin was washed with DMF (3 × 2 mL × 2 min) ahead of cleavage and deprotection.

Method F: Cleavage and deprotection of peptides of the resin

After elongation and acetylation or fluorescent dye coupling was complete, the resin was washed with CH_2Cl_2 (5 × 2 mL × 2 min), Et_2O (5 × 2 mL × 2 min) and dried under vacuum. Peptides were cleaved and side-chain deprotected using 'Reagent K' TFA:EDT:Thioanisole:Phenol:H_2O 82:3:5:5:5 (2 mL × 3 h). The peptide was precipitated in ice-cold Et_2O (10 mL) and placed in a centrifuge (3000 rpm × 5 min). The supernatant was removed, the precipitate resuspended in ice-cold Et_2O and placed in a centrifuge again (3x). The precipitate was dried under a stream of nitrogen overnight, before being dissolved in H_2O and lyophilized.

Automated peptide synthesis method

Peptides prepared using automated peptide synthesizer followed cycles described below. Resin loading cycle cleans the reaction vessel, washes with DMF:DCM (1:1), transfers resin to reaction vessel, washes with DMF:DCM (1:1), and drains the vessel at the end of a cycle. Deprotection and coupling cycle consist of: washing with DMF (4 ml), adding 20% piperidine in DMF (6 ml), microwave deprotection cycle (30 sec), washing with DMF (4+4+4+4 mL), addition of amino acid (2.5 ml, 5 eq or 3 eq for phosphorylated amino acids), coupling reagent (1 ml, 5 eq) and activator base (0.5 ml, 5 eq), coupling microwave cycle (5 min), washing with DMF (2 ml) and draining. HCTU and DIPEA were used during automated peptide synthesis as well. As a rule, all amino acids were coupled using 75°C coupling and deprotection cycles up to Ser(PO(OBzl)OH)-OH or Thr(PO(OBzl)OH)-OH, where conventional coupling and deprotection method was used (coupling at the rt for 2 h, deprotection at rt for 15 min) as well for every amino acid following pSer/pThr. After the final residue was coupled, the resin was ejected from the reaction vessel. Ahx coupling, deprotection,

acetylation or florescent dye coupling, and cleavage was performed manually using methods described above.

Peptide purification

Crude peptides were dissolved in H_2O or DMSO and purified by UV- or MS- directed HPLC. Jupiter Proteo (250 x 21.2 mm) or a Kinetex EVO C18 (250 x 21.2 mm) preparative column (reversed phase) was used with increasing gradient of acetonitrile in water with 0.1% formic acid, over 30 min at the flowrate of 10 ml/min. Fractions containing peptide were combined, concentrated, and lyophilized. Purity of peptides was assessed by analytical HPLC and HRMS.

5.3 Protein expression and purification

The pProEx HTb-His-14-3-3 constructs were expressed in BL21(DE3) cells. A single colony from a freshly made agar plate (8 g LB broth mixed with 8 g agar in 400 ml, autoclaved and poured into petri dishes to use for transformation of plasmids) was picked and mixed with 5 ml of LB media with ampicillin to inoculate a starter culture overnight at 37℃. The cells were grown in 2 L of TB media (48 g peptone, 24 g yeast, 4.6 g KH_2PO_4, 24 g $KHPO_4$, 5 ml glycerol in 2 L of dH_2O, autoclaved for 20 min at 121℃) at 37℃ until the OD reached 0.4-0.6. Expression was induced by adding 0.4 mM IPTG and agitating overnight at 18℃. The expression culture was spun down (8000 rpm, 20 min, 4℃), resuspended in 200 ml of lysis buffer (50 mM Tris, 300 mM NaCl, 12.5 mM imidazole, 2 mM β-mercaptoethanol) with 5 mM $MgCl_2$ and DNAse (1:1000). The cells were lysed by French press or sonication and the solid fragments were removed by centrifugation (20000 rpm, 30 min, 4℃). The cleared lysate was loaded on a Ni^{2+}-NTA column, washed with 50 mM Tris, 300 mM NaCl, 12.5 mM imidazole, 2 mM β-mercaptoethanol, 0.1% triton X-100, and the protein was eluted with 50 mM Tris, 300 mM NaCl, 250 mM imidazole, 2 mM β-mercaptoethanol. Imidazole was removed by overnight dialysis using the Tris buffer (50 mM Tris, 300 mM NaCl, 2 mM β-mercaptoethanol), full length proteins were concentrated by centrifugation, rebuffered in HEPES buffer (25 mM HEPES pH 7.5, 100 mM NaCl, 10 mM $MgCl_2$, 0.5 mM TCEF) and stored in -80℃ freezer. ΔC proteins were dialyzed with TEV protease to remove the expression tag and purified again on Ni^{2+}-NTA column, followed by size-exclusion chromatography (HiLoad 16/600 Superdex 75 pg column) in HEPES buffer (20 mM HEPES, 150 mM NaCl, 2 mM DTT). ΔC proteins were concentrated and rebuffered for -80℃ storage. All proteins were analyzed by QTOF MS.

5.4 Fluorescencet anisotropy

Direct titration assay

All assays were performed in 384 well plates (each experiment was run in triplicates) and data were collected by Perkin Elmer EnVision 2013 plate reader with with excitation at 480 nm (30 nm bandwidth), polarised dichroic mirror at 505 nm and emission at 535 nm (40 nm bandwidth, S and P polarised). All experiments in Chapter 2 and 3 were carried out in HBS buffer (10 mM HEPES, 150 mM NaCl, pH 7.4) + 0.1% Tween 20 + 0.1% BSA. The assays regarding acylhydrazone formation were carried out in ammonium acetate buffer (50 mM NH_4OAc, 10 mM aniline, 1 mM DTT, pH 6.5).

General procedure for direct titration:

1) 20 µL buffer was added to every well
2) 20 µL of protein solution was added to the first well of each row and diluted ½ across the plate
3) 20 µL of fluorescently labelled peptide was added to each well within first three rows
4) 20 µL of buffer was added to each well in three rows bellow was a control
5) Plates were left to incubate, and data was collected after 30 min, 4 h and 20-24h

Collected data were processed in Microsoft Excel using equations bellow. Total intensity I and anisotropy r were calculated using Equations 1 and 2 for each well. Average anisotropy was plotted against protein concentration using OriginPro and logistic curve was fitted to give r_{min} and r_{max}. Using Equation 3 anisotropy was converted into fraction bound and multiplied by peptide concentration to be fitted in Origin using Equation 5 to obtain K_d values.

Equation 1. $\mathrm{I} = 2\mathrm{PG} + \mathrm{S}$

Equation 2. $r = \frac{S-PG}{I}$

Equation 3. $L_b = \frac{(r-r_{min})}{\lambda(r_{max}-r)+r-r_{min}}$

Equation 4. $y = r_{min} + \frac{r_{max}-r_{min}}{1+10^{(x-logx_0)}}$

Equation 5. $y = \frac{((K+X+FL)-\sqrt{((K+X+FL)^2-4xFL))}}{2}$

r = anisotropy, I = total intensity, P = perpendicular intensity, S = parallel intensity, L_b = fraction ligand bound, $\lambda = I_{bound}/I_{unbound} = 1$, FL = fluorescent ligand concentration, K = K_d

Competition assay

General procedure for competition assay:

1) 20 µL buffer was added to every well
2) 20 µL of competitor solution was added to the first well of each row and diluted ½ across the plate
3) 20 µL of protein was added to every well
4) 20 µL of fluorescently labelled peptide was added to each well within first three rows
5) 20 µL of buffer was added to each well in three rows bellow was a control
6) Plates were left to incubate, and data was collected after 30 min, 4 h and 20-24h

Collected data were processed as described above. Average anisotropy was plotted against competitor concentration using OriginPro and logistic curve was fitted to give IC_{50} values.

Screening assay

PPI-net library containing of 1534 small molecules and 1000 Maybridge fragments were screened in a single point assay to identify a protentional stabilizer of *h*DMX-367 / 14-3-3η interaction. Concentration of the protein in a single point screen was chosen around K_d value and each compound was screened in duplicates. Each well consisted of 0.2 µM of the protein, 50 nM of the fluorescently labelled peptide and either 500 µM of the small molecule or 2.5 mM fragment. Control well consisted of 0.2 µM of the protein, 50 nM of the fluorescently labelled peptide and DMSO. Negative control well consisted of fluorescently labelled peptide alone (minimal anisotropy) and the positive control well consisted of the protein-peptide concentration at the highest binding affinity (maximal anisotropy). Anisotropy for each compound was calculated in Excel document using the Equation 2. Each compound identified as a hit from a single point screen was further confirmed in a dose response assay. Protein-peptide concentration was kept constant (concentration replicated from the single-point screen) and the compounds were titrated from the highest concentration of 2.5 mM for fragments to give apparent EC_{50} values.

5.5 Surface plasmon resonance

Experiments were performed at 25°C using a Biacore T200 instrument (GE Healthcare). For immobilization, the running buffer was HBS buffer (HEPES, NaCl, Tween-20, pH 7.4). 14-3-3η was immobilized on an NTA sensor chip (Series S Sensor Chip GE Healthcare) using NTA reagent and Biacore Amine Coupling Kit.

Briefly, 14-3-3η was diluted to 0.2 mg/ml and 200 µL was injected over a chip surface that had been activated with an injection of Ni^{2+}, followed by 140 µL of 1:1 NHS/EDC. 30 µL of 0.5 M ethanolamine was then injected to cap the excess free amine groups. Immobilization levels of the 14-3-3η were found to be around 2000 response units (RU) for kinetics measurements and 5000 RUs for fragment screening. *h*DMX and *h*DM2 peptides were serially diluted 11 times from the concentrations 10 times the K_d values measured in FA, on a 96-well plate. Then, 20 µL of these solutions were injected over an 14-3-3η immobilized surface for 1 min at the 20 ml/min flowrate, followed by a 4 min regeneration period with HBS buffer. Kinetics and the binding affinity have been calculated by using a Biacore evaluation software. Fragments were diluted 6 times from the 2 mM starting concentration in HBS buffer with 100 nM *h*DMX-367 peptide (2% DMSO as final conc.) on a 96-well plate. 20 µL of these solutions were injected over an 14-3-3η immobilized surface for 1 min at the 20 ml/min flowrate, followed by a 4 min regeneration period with HBS buffer. Standard dose response curves were fitted by plotting RUs against the fragment concentration.

5.6 Isothermal titration calorimetry

ITC experiments were carried out on a MicroCal iTC200 in HBS buffer at 25℃ (25 mM HEPES pH 7.5, 100 mM NaCl, 10 mM $MgCl_2$, 0.5 mM TCEP). Peptides (0.2-1 M) in the syringe were titrated into a cell containing 14-3-3η (0.02-0.1 M). Data was fitted by using MicroCal software to give binding constant (K_d), enthalpy (ΔH), entropy (ΔS) and binding stoichiometry (n).

5.7 Protein crystallography

A solution of 14 mg/ml 14-3-3σ ΔC with *h*DMX-367 peptide in 1:2 ratio was incubated overnight in crystallization buffer (20 mM HEPES pH 7.5, 2 mM $MgCl_2$, and 2 mM BME). Crystals were obtained at 4℃ in 0.2 M sodium sulfate, 0.1 M Bis-Tris propane, 20 % w/v PEG 3350 at pH 8.5. Diffraction pattern data was collected at the DESY, Petra III P11, Hamburg with the 2.2 Å resolution. *h*DMX-342+367 crystals were obtained at 4℃ after overnight incubation of 12 mg/ml 14-3-3σ ΔC with *h*DMX-342+367 peptide (1:2 ratio) in sodium citrate dihydrate, bis-tris propane, pH 8, 20% PEG 3350. *h*DM2-186 crystals were obtained at 4℃ after overnight incubation of 12 mg/ml 14-3-3σ ΔC with *h*DM2-186 peptide (1:2 ratio) in 0.0375 M $CdSO_4$ H_20, 0.075 M HEPES, pH 7.5, 0.75 M NaAc $3H_20$, 25% glycerol. Diffraction pattern data for *h*DMX-342+367 and *h*DM2-186 crystals were collected at Diamond Light source, UK with 2.1 Å resolution for *h*DMX-342+367 and 1.75 Å resolution for *h*DM2-186. CCP4i software package was used for molecular replacement using 4DAT as a template of 14-3-3σ structure. Further refinement was done by using COOT software.

Refinement statistics for each structure are provided in Supplementary info (Table A.4).

5.8 Protein NMR

STD and WaterLOGSY spectra were acquired using a 600 MHz Oxford NMR spectrometer equipped with a QCI-P-cryogenic probe. Samples were prepared and run in a phosphate buffer (100 mM sodium phosphate, 50 mM NaCl, pH 6.8 and 10% (v/v) D_2O) at the temperature of 16 °C in 3 mm tubes (sample volume 200 µL). The samples contained 25 µM of 14-3-3η, 50 µM of hDMX-367 peptide and 500 µM of fragments. The final DMSO concentration was 0.5% and was kept constant. WaterLOGSY spectra were recorded with 32768 complex data points, 512 scans per increment and with a mixing time of 1.7s (acquisition time of 51 minutes). STD spectra were recorded with 32768 complex data points and with 256 scans per increment (acquisition time of 34 minutes). Additional ^{1}H spectrum with water suppression and t1rho (with 64 scans per increment and 4 min acquisition time) experiments were recorded for each sample. Topspin 3.6 was used for data collection and analysis.

HSQC spectra were acquired using a 950 MHz Bruker Ascend Aeon NMR spectrometer equipped with a TXO-cryogenic probe. Samples were prepared and run in a phosphate buffer (100 mM sodium phosphate, 50 mM NaCl, 1mM DTT, pH 6.8 and 10% (v/v) D_2O) at the temperature of 32 °C in 5 mm tubes (sample volume 320 µL). The samples contained 50 µM of 14-3-3η and 2 mM of fragments, with and without 100 µM of hDMX-367 peptide. The final DMSO concentration was 2% and was kept constant. HSQC experiments were recorded by using BestTROSY pulse program, with 1620 complex data points, 80 scans per increment and with a mixing time of 0.07 s (acquisition time of 126 minutes). Topspin 3.6 was used for data acquisition and Sparky for data analysis.

Chemical shift value modifications (CSPs in ppm) on the ^{1}H-^{15}N TROSY-HSQC were calculated using the equation (6):

$$\Delta\delta = \sqrt{\Delta\delta(^{1}H)^{2} + [0.14 * \Delta\delta(^{15}N)^{2}]} \qquad (6)$$

5.9 Analytical ultracentrifugation

AUC-SV experiments were performed using a Beckman Coulter Optima XL-I ultracentrifuge. Samples were prepared in HBS buffer (10 mM HEPES, 150 mM NaCl, pH 7.4) and loaded into 12 mm aluminum centerpieces with sapphire windows. Three samples were run: I. 14 µM 14-3-3η, II. 14 µM 14-3-3η + 7 µM hDMX-342+367, III. 14 µM 14-3-3η + 14 µM hDMX-342+367, with buffer as a reference, and recorded

at 48 000 rpm in the An50-Ti rotor, at the 25℃. The diffusion-deconvoluted sedimentation coefficient distributions c(s) were calculated using the SEDFIT program.

5.10 Circular dichroism (CD) spectroscopy

Spectra were recorded on a Chirascan circular dichroism spectropolarimeter (Applied Photophysics), using 1 mm cells, scan speed of 5 nm/min, 2 nm bandwith, and 180 nM to 260 nM range. The experiments were preformed in a 50 mM sodium phosphate buffer, pH 7.5 at 20 °C. The spectra were averaged over three repeats with a buffer baseline subtracted. Protein concentrations of approximately 0.2 mg/mL were used for all proteins. The helicity of each protein was determined from the mean residue ellipticity at 222 nm, [θ] (deg cm^2 $dmol^{-1}$).

5.12 SDS page

A stacking and separation gel were prepared according to Table 1. Tetramethylethylenediamine (TEMED) was added last to a separation gel mixture, which was thoroughly mixed and poured into BioRad's tray. Top layer was covered with isopropanol and the gel was left for 30 min to polymerize. The isopropanol layer was then removed and stacking gel was prepared by again mixing the TEMED last, adding the mixture on top of the separation gel. A comb was added to make suitable wells and the gel was left for 30 min to polymerize. Proteins were mixed with loading buffer and boiled for 5 min at 95 ℃ prior loading onto the gel. Electrophoresis was run at the constant voltage at 180 V for 45 min. Proteins were visualized using Coomassie blue stain (45% (v/v) methanol, 10% (v/v) acetic acid, 0.25% (w/v) Coomassie brilliant blue R-250) and destained in 30% (v/v) methanol, 10% (v/v) acetic acid.

Table 5.1 Composition of a 10% SDS-PAGE gel

	STACKING GEL	SEPARATING GEL (10%)
H_20	6.26 ml	5 ml
1.5 M TRIS	2.5 ml pH 6.8	2.5 ml pH 8.8
10% APS	100 µM	100 µM
10% SDS	100 µM	100 µM
40% (w/v) acrylamide	1.24 ml	2.5 ml
TEMED	10 µl	10 µl

References

1. Scott, D. E., Bayly, A. R., Abell, C. & Skidmore, J. Small molecules, big targets: drug discovery faces the protein-protein interaction challenge. *Nat. Rev. Drug Discov.* 15, 533–550 (2016).
2. Estimating the size of the human interactome. http://www.pnas.org/content/105/19/6959.full.
3. Mullard, A. 2019 FDA drug approvals. *Nat. Rev. Drug Discov.* 19, 79–84 (2020).
4. Carter, P. J. & Lazar, G. A. Next generation antibody drugs: pursuit of the 'high-hanging fruit'. *Nat. Rev. Drug Discov.* 17, 197–223 (2018).
5. Mabonga, L. & Kappo, A. P. Protein-protein interaction modulators: advances, successes and remaining challenges. *Biophys. Rev.* 11, 559–581 (2019).
6. Arkin, M. R., Tang, Y. & Wells, J. A. Small-molecule inhibitors of protein-protein interactions: progressing towards the reality. *Chem. Biol.* 21, 1102–1114 (2014).
7. Ni, D., Lu, S. & Zhang, J. Emerging roles of allosteric modulators in the regulation of protein-protein interactions (PPIs): A new paradigm for PPI drug discovery. *Med. Res. Rev.* 39, 2314–2342 (2019).
8. Zhu, L. & Chen, L. Progress in research on paclitaxel and tumor immunotherapy. *Cell. Mol. Biol. Lett.* 24, 40 (2019).
9. Commissioner, O. of the. FDA approves new treatments for heart disease caused by a serious rare disease, transthyretin mediated amyloidosis. *FDA* http://www.fda.gov/news-events/press-announcements/fda-approves-new-treatments-heart-disease-caused-serious-rare-disease-transthyretin-mediated (2020).
10. Andrei, S. A. *et al.* Stabilization of protein-protein interactions in drug discovery. *Expert Opin. Drug Discov.* 12, 925–940 (2017).
11. Rodrigues, T., Reker, D., Schneider, P. & Schneider, G. Counting on natural products for drug design. *Nat. Chem.* 8, 531–541 (2016).
12. Kolos, J. M., Voll, A. M., Bauder, M. & Hausch, F. FKBP Ligands—Where We Are and Where to Go? *Front. Pharmacol.* 9, 1425 (2018).
13. Ferguson, F. M. & Gray, N. S. Kinase inhibitors: the road ahead. *Nat. Rev. Drug Discov.* 17, 353–377 (2018).
14. Rosell, M. & Fernández-Recio, J. Hot-spot analysis for drug discovery targeting protein-protein interactions. *Expert Opin. Drug Discov.* 13, 327–338 (2018).
15. Ibarra, A. A. *et al.* Predicting and Experimentally Validating Hot-Spot Residues at Protein–Protein Interfaces. *ACS Chem. Biol.* 14, 2252–2263 (2019).
16. Valeur, E. *et al.* New Modalities for Challenging Targets in Drug Discovery. *Angew. Chem. Int. Ed.* 56, 10294–10323 (2017).
17. Pelay-Gimeno, M., Glas, A., Koch, O. & Grossmann, T. N. Structure-Based Design of Inhibitors of Protein–Protein Interactions: Mimicking Peptide Binding Epitopes. *Angew. Chem. Int. Ed Engl.* 54, 8896–8927 (2015).
18. Watkins, A. M., Wuo, M. G. & Arora, P. S. Protein–Protein Interactions Mediated by Helical Tertiary Structure Motifs. *J. Am. Chem. Soc.* 137, 11622–11630 (2015).
19. Räder, A. F. B. *et al.* Orally Active Peptides: Is There a Magic Bullet? *Angew. Chem. Int. Ed.* 57, 14414–14438 (2018).
20. Skowron, K. J., Speltz, T. E. & Moore, T. W. Recent structural advances in constrained helical peptides. *Med. Res. Rev.* 39, 749–770 (2019).
21. Horne, W. S. & Grossmann, T. N. Proteomimetics as protein-inspired scaffolds with defined tertiary folding patterns. *Nat. Chem.* 1–8 (2020)
22. Pasco, M., Dolain, C. & Guichard, G. Foldamers. in *Supramolecular Chemistry in Water* 337–374 (John Wiley & Sons, Ltd, 2019).
23. Hill, T. A., Shepherd, N. E., Diness, F. & Fairlie, D. P. Constraining cyclic peptides to mimic protein structure motifs. *Angew. Chem. Int. Ed Engl.* 53, 13020–13041 (2014).

24. Baker, E. G., Bartlett, G. J., Porter Goff, K. L. & Woolfson, D. N. Miniprotein Design: Past, Present, and Prospects. *Acc. Chem. Res.* 50, 2085–2092 (2017).
25. Maity, D., Kumar, S., Curreli, F., Debnath, A. K. & Hamilton, A. D. α-Helix-Mimetic Foldamers for Targeting HIV-1 TAR RNA. *Chem. – Eur. J.* 25, 7265–7269 (2019).
26. Joy, S. T. & Arora, P. S. An optimal hydrogen-bond surrogate for α-helices. *Chem. Commun.* 52, 5738–5741 (2016).
27. Grison, C. M. *et al.* Double quick, double click reversible peptide “stapling”. *Chem. Sci.* 8, 5166–5171 (2017).
28. Lanning, M. E. & Fletcher, S. Multi-Facial, Non-Peptidic α-Helix Mimetics. *Biology* 4, 540–555 (2015).
29. Ricardo, M. G. *et al.* Improved Stability and Tunable Functionalization of Parallel β-Sheets via Multicomponent N-Alkylation of the Turn Moiety. *Angew. Chem.* 132, 265–269 (2020).
30. Jouanne, M. *et al.* β-Strand Mimicry: Exploring Oligothienylpyridine Foldamers. *Eur. J. Org. Chem.* 2016, 5686–5696 (2016).
31. Hubert, J. G., Stepek, I. A., Noda, H. & Bode, J. W. Synthetic fermentation of β-peptide macrocycles by thiadiazole-forming ring-closing reactions. *Chem. Sci.* 9, 2159–2167 (2018).
32. Modell, A. E., Blosser, S. L. & Arora, P. S. Systematic Targeting of Protein–Protein Interactions. *Trends Pharmacol. Sci.* 37, 702–713 (2016).
33. Volochnyuk, D. M. *et al.* Evolution of commercially available compounds for HTS. *Drug Discov. Today* 24, 390–402 (2019).
34. Zhao, Y., Aguilar, A., Bernard, D. & Wang, S. Small-molecule inhibitors of the MDM2-p53 protein-protein interaction (MDM2 Inhibitors) in clinical trials for cancer treatment. *J. Med. Chem.* 58, 1038–1052 (2015).
35. Mady, A. S. A. *et al.* Discovery of Mcl-1 inhibitors from integrated high throughput and virtual screening. *Sci. Rep.* 8, 1–15 (2018).
36. Rose, R. *et al.* Identification and structure of small-molecule stabilizers of 14-3-3 protein-protein interactions. *Angew. Chem. Int. Ed Engl.* 49, 4129–4132 (2010).
37. Wildey, M. J., Haunso, A., Tudor, M., Webb, M. & Connick, J. H. Chapter Five - High-Throughput Screening. in *Annual Reports in Medicinal Chemistry* (ed. Goodnow, R. A.) vol. 50 149–195 (Academic Press, 2017).
38. Reymond, J.-L., Visini, R. & Awale, M. Enumeration of Chemical Fragment Space. in *Fragment-based Drug Discovery Lessons and Outlook* 57–74 (John Wiley & Sons, Ltd, 2016).
39. Erlanson, D. A., Fesik, S. W., Hubbard, R. E., Jahnke, W. & Jhoti, H. Twenty years on: the impact of fragments on drug discovery. *Nat. Rev. Drug Discov.* 15, 605–619 (2016).
40. Fairbrother, W. J., Leverson, J. D., Sampath, D. & Souers, A. J. Discovery and Development of Venetoclax, a Selective Antagonist of BCL-2. in *Successful Drug Discovery* 225–245 (John Wiley & Sons, Ltd, 2019).
41. Hallenbeck, K. K., Turner, D. M., Renslo, A. R. & Arkin, M. R. Targeting Non-Catalytic Cysteine Residues Through Structure-Guided Drug Discovery. *Curr. Top. Med. Chem.* 17, 4–15 (2017).
42. Kathman, S. G. & Statsyuk, A. V. Covalent tethering of fragments for covalent probe discovery. *MedChemComm* 7, 576–585 (2016).
43. Sijbesma, E. *et al.* Site-Directed Fragment-Based Screening for the Discovery of Protein-Protein Interaction Stabilizers. *J. Am. Chem. Soc.* 141, 3524–3531 (2019).
44. Schneider, G. & Clark, D. E. Automated De Novo Drug Design: Are We Nearly There Yet? *Angew. Chem. Int. Ed.* 58, 10792–10803 (2019).
45. Kozakov, D. *et al.* The FTMap family of web servers for determining and characterizing ligand-binding hot spots of proteins. *Nat. Protoc.* 10, 733–755 (2015).
46. Wang, H., Liu, C. & Deng, L. Enhanced Prediction of Hot Spots at Protein-Protein Interfaces Using Extreme Gradient Boosting. *Sci. Rep.* 8, 1–13 (2018).

47. Kuhlman, B. & Bradley, P. Advances in protein structure prediction and design. *Nat. Rev. Mol. Cell Biol.* 20, 681–697 (2019).
48. Chen, S. *et al.* Rapid identification of dual p53-MDM2/MDMX interaction inhibitors through virtual screening and hit-based substructure search. *RSC Adv.* 7, 9989–9997 (2017).
49. Seidel, T., Wolber, G. & Murgueitio, M. S. Pharmacophore Perception and Applications. in *Applied Chemoinformatics* 259–282 (John Wiley & Sons, Ltd, 2018).
50. Schneider, P. *et al.* Rethinking drug design in the artificial intelligence era. *Nat. Rev. Drug Discov.* 1–12 (2019)
51. Pitolli, C. *et al.* Do Mutations Turn p53 into an Oncogene? *Int. J. Mol. Sci.* 20, 6241 (2019).
52. Hafner, A., Bulyk, M. L., Jambhekar, A. & Lahav, G. The multiple mechanisms that regulate p53 activity and cell fate. *Nat. Rev. Mol. Cell Biol.* 20, 199–210 (2019).
53. Karni-Schmidt, O., Lokshin, M. & Prives, C. The Roles of MDM2 and MDMX in Cancer. *Annu. Rev. Pathol. Mech. Dis.* 11, 617–644 (2016).
54. Linares, L. K., Hengstermann, A., Ciechanover, A., Müller, S. & Scheffner, M. HdmX stimulates Hdm2-mediated ubiquitination and degradation of p53. *Proc. Natl. Acad. Sci.* 100, 12009–12014 (2003).
55. Liu, Y., Tavana, O. & Gu, W. p53 modifications: exquisite decorations of the powerful guardian. *J. Mol. Cell Biol.* 11, 564–577 (2019).
56. Kastenhuber, E. R. & Lowe, S. W. Putting p53 in Context. *Cell* 170, 1062–1078 (2017).
57. Tackmann, N. R. & Zhang, Y. Mouse modelling of the MDM2/MDMX−p53 signalling axis. *J. Mol. Cell Biol.* 9, 34–44 (2017).
58. Kamada, R., Toguchi, Y., Nomura, T., Imagawa, T. & Sakaguchi, K. Tetramer formation of tumor suppressor protein p53: Structure, function, and applications. *Pept. Sci.* 106, 598–612 (2016).
59. Bouaoun, L. *et al.* TP53 Variations in Human Cancers: New Lessons from the IARC TP53 Database and Genomics Data. *Hum. Mutat.* 37, 865–876 (2016).
60. Wade, M., Li, Y.-C. & Wahl, G. M. MDM2, MDMX and p53 in oncogenesis and cancer therapy. *Nat. Rev. Cancer* 13, 83–96 (2013).
61. Liu, Y. *et al.* The past, present and future of potential small-molecule drugs targeting p53-MDM2/MDMX for cancer therapy. *Eur. J. Med. Chem.* 176, 92–104 (2019).
62. Bykov, V. J. N., Eriksson, S. E., Bianchi, J. & Wiman, K. G. Targeting mutant p53 for efficient cancer therapy. *Nat. Rev. Cancer* 18, 89–102 (2018).
63. Bykov, V. J. N. *et al.* Restoration of the tumor suppressor function to mutant p53 by a low-molecular-weight compound. *Nat. Med.* 8, 282–288 (2002).
64. Salim, K. Y., Vareki, S. M., Danter, W. R. & Koropatnick, J. COTI-2, a novel small molecule that is active against multiple human cancer cell lines in vitro and in vivo. *Oncotarget* 7, 41363–41379 (2016).
65. Sabapathy, K. & Lane, D. P. Therapeutic targeting of p53: all mutants are equal, but some mutants are more equal than others. *Nat. Rev. Clin. Oncol.* 15, 13–30 (2018).
66. Park, J.-H. *et al.* Mouse Homolog of the Human TP53 R337H Mutation Reveals Its Role in Tumorigenesis. *Cancer Res.* 78, 5375–5383 (2018).
67. Gordo, S. *et al.* Stability and structural recovery of the tetramerization domain of p53-R337H mutant induced by a designed templating ligand. *Proc. Natl. Acad. Sci.* 105, 16426–16431 (2008).
68. Kamada, R. *et al.* Enhancement of transcriptional activity of mutant p53 tumor suppressor protein through stabilization of tetramer formation by calix[6]arene derivatives. *Bioorg. Med. Chem. Lett.* 20, 4412–4415 (2010).
69. Vassilev, L. T. *et al.* In Vivo Activation of the p53 Pathway by Small-Molecule Antagonists of MDM2. *Science* 303, 844–848 (2004).

70. Estrada-Ortiz, N., Neochoritis, C. G. & Dömling, A. How To Design a Successful p53–MDM2/X Interaction Inhibitor: A Thorough Overview Based on Crystal Structures. *ChemMedChem* 11, 757–772 (2016).
71. Andreeff, M. *et al.* Results of the Phase 1 Trial of RG7112, a Small-molecule MDM2 Antagonist in Leukemia. *Clin. Cancer Res. Off. J. Am. Assoc. Cancer Res.* 22, 868–876 (2016).
72. Montesinos, P. *et al.* MIRROS: a randomized, placebo-controlled, Phase III trial of cytarabine ± idasanutlin in relapsed or refractory acute myeloid leukemia. *Future Oncol. Lond. Engl.* 16(13), 807–815 (2020)
73. Erba, H. P. *et al.* Phase 1b study of the MDM2 inhibitor AMG 232 with or without trametinib in relapsed/refractory acute myeloid leukemia. *Blood Adv.* 3, 1939–1949 (2019).
74. Skalniak, L., Surmiak, E. & Holak, T. A. A therapeutic patent overview of MDM2/X-targeted therapies (2014–2018). *Expert Opin. Ther. Pat.* 29, 151–170 (2019).
75. Haupt, S., Mejía-Hernández, J. O., Vijayakumaran, R., Keam, S. P. & Haupt, Y. The long and the short of it: the MDM4 tail so far. *J. Mol. Cell Biol.* 11, 231–244 (2019).
76. Reed, D. *et al.* Identification and characterization of the first small molecule inhibitor of MDMX. *J. Biol. Chem.* 285, 10786–10796 (2010).
77. Wang, H., Ma, X., Ren, S., Buolamwini, J. K. & Yan, C. A Small-molecule Inhibitor of MDMX Activates p53 and Induces Apoptosis. *Mol. Cancer Ther.* 10, 69–79 (2011).
78. Karan, G. *et al.* Identification of a Small Molecule That Overcomes HdmX-Mediated Suppression of p53. *Mol. Cancer Ther.* 15, 574–582 (2016).
79. Espadinha, M., Barcherini, V. & Santos*, E. A. L. and M. M. M. An Update on MDMX and Dual MDM2/X Inhibitors. *Current Topics in Medicinal Chemistry*, 18, 8, 647 - 660 (2018).
80. Zhuang, C. *et al.* Discovery, Synthesis, and Biological Evaluation of Orally Active Pyrrolidone Derivatives as Novel Inhibitors of p53–MDM2 Protein–Protein Interaction. *J. Med. Chem.* 55, 9630–9642 (2012).
81. Teveroni, E. *et al.* Peptides and peptidomimetics in the p53/MDM2/MDM4 circuitry - a patent review. *Expert Opin. Ther. Pat.* 26, 1417–1429 (2016).
82. Bernal, F. *et al.* A Stapled p53 Helix Overcomes HDMX-Mediated Suppression of p53. *Cancer Cell* 18, 411–422 (2010).
83. Bernal, F., Tyler, A. F., Korsmeyer, S. J., Walensky, L. D. & Verdine, G. L. Reactivation of the p53 Tumor Suppressor Pathway by a Stapled p53 Peptide. *J. Am. Chem. Soc.* 129, 2456–2457 (2007).
84. Philippe, G. *et al.* Development of cell-penetrating peptide-based drug leads to inhibit MDMX:p53 and MDM2:p53 interactions. *Pept. Sci.* 106, 853–863 (2016).
85. Chang, Y. S. *et al.* Stapled α−helical peptide drug development: A potent dual inhibitor of MDM2 and MDMX for p53-dependent cancer therapy. *Proc. Natl. Acad. Sci.* 110, E3445–E3454 (2013).
86. Brown, C. J. *et al.* Stapled Peptides with Improved Potency and Specificity That Activate p53. *ACS Chem. Biol.* 8, 506–512 (2013).
87. Lee, J.-H. *et al.* Protein grafting of p53TAD onto a leucine zipper scaffold generates a potent HDM dual inhibitor. *Nat. Commun.* 5, 1–12 (2014).
88. Carvajal, L. A. *et al.* Dual inhibition of MDMX and MDM2 as a therapeutic strategy in leukemia. *Sci. Transl. Med.* 10, (2018).
89. Graves, B. *et al.* Activation of the p53 pathway by small-molecule-induced MDM2 and MDMX dimerization. *Proc. Natl. Acad. Sci. U. S. A.* 109, 11788–11793 (2012).
90. Arena, G. *et al.* Mitochondrial MDM2 Regulates Respiratory Complex I Activity Independently of p53. *Mol. Cell* 69, 594-609.e8 (2018).
91. Eischen, C. M. Role of Mdm2 and Mdmx in DNA repair. *J. Mol. Cell Biol.* 9, 69–73 (2017).

92. Wienken, M., Moll, U. M. & Dobbelstein, M. Mdm2 as a chromatin modifier. *J. Mol. Cell Biol.* 9, 74–80 (2017).
93. Rao, B., Lain, S. & Thompson, A. M. p53-Based cyclotherapy: exploiting the 'guardian of the genome' to protect normal cells from cytotoxic therapy. *Br. J. Cancer* 109, 2954–2958 (2013).
94. Izetti, P. *et al.* PRIMA-1, a mutant p53 reactivator, induces apoptosis and enhances chemotherapeutic cytotoxicity in pancreatic cancer cell lines. *Invest. New Drugs* 32, 783–794 (2014).
95. Tannock, I. F. & Hickman, J. A. Limits to Personalized Cancer Medicine. 375:1289-1294 (2016)
96. Aghazadeh, Y. & Papadopoulos, V. The role of the 14-3-3 protein family in health, disease, and drug development. *Drug Discov. Today* 21, 278–287 (2016).
97. Aitken, A. 14-3-3 proteins: A historic overview. *Semin. Cancer Biol.* 16, 162–172 (2006).
98. Fan, X. *et al.* 14-3-3 Proteins Are on the Crossroads of Cancer, Aging, and Age-Related Neurodegenerative Disease. *Int. J. Mol. Sci.* 20, 3518 (2019).
99. Stevers, L. M. *et al.* Characterization and small-molecule stabilization of the multisite tandem binding between 14-3-3 and the R domain of CFTR. *Proc. Natl. Acad. Sci.* 113, E1152–E1161 (2016).
100. Obsil, T. & Obsilova, V. Structural basis of 14-3-3 protein functions. *Semin. Cell Dev. Biol.* 22, 663–672 (2011).
101. Bartel, M., Schäfer, A., Stevers, L. M. & Ottmann, C. Small molecules, peptides and natural products: getting a grip on 14-3-3 protein-protein modulation. *Future Med. Chem.* (2014)
102. Vincenz, C. & Dixit, V. M. 14-3-3 Proteins Associate with A20 in an Isoform-specific Manner and Function Both as Chaperone and Adapter Molecules. *J. Biol. Chem.* 271, 20029–20034 (1996).
103. Agarwal-Mawal, A. *et al.* 14-3-3 Connects Glycogen Synthase Kinase-3β to Tau within a Brain Microtubule-associated Tau Phosphorylation Complex. *J. Biol. Chem.* 278, 12722–12728 (2003).
104. Gardino, A. K., Smerdon, S. J. & Yaffe, M. B. Structural determinants of 14-3-3 binding specificities and regulation of subcellular localization of 14-3-3-ligand complexes: A comparison of the X-ray crystal structures of all human 14-3-3 isoforms. *Semin. Cancer Biol.* 16, 173–182 (2006).
105. Wang, B. *et al.* Isolation of High-Affinity Peptide Antagonists of 14-3-3 Proteins by Phage Display. *Biochemistry* 38, 12499–12504 (1999).
106. Masters, S. C. & Fu, H. 14-3-3 Proteins Mediate an Essential Anti-apoptotic Signal. *J. Biol. Chem.* 276, 45193–45200 (2001).
107. Glas, A. *et al.* Constrained Peptides with Target-Adapted Cross-Links as Inhibitors of a Pathogenic Protein–Protein Interaction. *Angew. Chem. Int. Ed.* 53, 2489–2493 (2014).
108. Andrei, S. A. *et al.* Inhibition of 14-3-3/Tau by Hybrid Small-Molecule Peptides Operating via Two Different Binding Modes. *ACS Chem. Neurosci.* 9, 2639–2654 (2018).
109. Stevers, L. M. *et al.* Modulators of 14-3-3 Protein–Protein Interactions. *J. Med. Chem.* 61, 3755–3778 (2018).
110. Zhao, J. *et al.* Discovery and structural characterization of a small molecule 14-3-3 protein-protein interaction inhibitor. *Proc. Natl. Acad. Sci. U. S. A.* 108, 16212–16216 (2011).
111. Iralde-Lorente, L. *et al.* Chemically stable inhibitors of 14-3-3 protein–protein interactions derived from BV02. *J. Enzyme Inhib. Med. Chem.* 34, 657–664 (2019).
112. Bier, D. *et al.* Molecular tweezers modulate 14-3-3 protein–protein interactions. *Nat. Chem.* 5, 234–239 (2013).

113. Camoni, L., Visconti, S., Aducci, P. & Marra, M. From plant physiology to pharmacology: fusicoccin leaves the leaves. *Planta* 249, 49–57 (2019).
114. Ottmann, C. *et al.* Structure of a 14-3-3 Coordinated Hexamer of the Plant Plasma Membrane H+-ATPase by Combining X-Ray Crystallography and Electron Cryomicroscopy. *Mol. Cell* 25, 427–440 (2007).
115. Würtele, M., Jelich-Ottmann, C., Wittinghofer, A. & Oecking, C. Structural view of a fungal toxin acting on a 14-3-3 regulatory complex. *EMBO J.* 22, 987–994 (2003).
116. De Vries-van Leeuwen, I. J. *et al.* Interaction of 14-3-3 proteins with the estrogen receptor alpha F domain provides a drug target interface. *Proc. Natl. Acad. Sci. U. S. A.* 110, 8894–8899 (2013).
117. Anders, C. *et al.* A Semisynthetic Fusicoccane Stabilizes a Protein-Protein Interaction and Enhances the Expression of K+ Channels at the Cell Surface. *Chem. Biol.* 20, 583–593 (2013).
118. Molzan, M. *et al.* Impaired Binding of 14-3-3 to C-RAF in Noonan Syndrome Suggests New Approaches in Diseases with Increased Ras Signaling. *Mol. Cell. Biol.* 30, 4698–4711 (2010).
119. Doveston, R. G. *et al.* Small-molecule stabilization of the p53 - 14-3-3 protein-protein interaction. *FEBS Lett.* 591, 2449–2457 (2017).
120. Andrei, S. A. *et al.* Rationally Designed Semisynthetic Natural Product Analogues for Stabilization of 14-3-3 Protein–Protein Interactions. *Angew. Chem. Int. Ed.* 57, 13470–13474 (2018).
121. Kasukabe, T. *et al.* Combined treatment with cotylenin A and phenethyl isothiocyanate induces strong antitumor activity mainly through the induction of ferroptotic cell death in human pancreatic cancer cells. *Oncol. Rep.* 36, 968–976 (2016).
122. Sato, S. *et al.* Metabolite Regulation of Nuclear Localization of Carbohydrate-response Element-binding Protein (ChREBP): role of AMP as an allosteric inhibitor. *J. Biol. Chem.* 291, 10515–10527 (2016).
123. Gigante, A. *et al.* A Supramolecular Stabilizer of the 14-3-3ζ/ERα Protein-Protein Interaction with a Synergistic Mode of Action. *Angew. Chem.* n/a,.
124. Yang, H.-Y. *et al.* Roles for negative cell regulator 14-3-3 σ in control of MDM2 activities. *Oncogene* 26, 7355–7362 (2007).
125. Rajagopalan, S., Jaulent, A. M., Wells, M., Veprintsev, D. B. & Fersht, A. R. 14-3-3 activation of DNA binding of p53 by enhancing its association into tetramers. *Nucleic Acids Res.* 36, 5983–5991 (2008).
126. Wang, W. *et al.* Targeting MDM2 for novel molecular therapy: Beyond oncology. *Med. Res. Rev.* 40, 856–880 (2020).
127. de Polo, A., Vivekanandan, V., Little, J. B. & Yuan, Z.-M. MDMX under stress: the MDMX-MDM2 complex as stress signals hub. *Transl. Cancer Res.* 5, 725-732–732 (2016).
128. He, G. *et al.* AMP-Activated Protein Kinase Induces p53 by Phosphorylating MDMX and Inhibiting Its Activity. *Mol. Cell. Biol.* 34, 148–157 (2014).
129. Pereg, Y. *et al.* Differential roles of ATM- and Chk2-mediated phosphorylations of Hdmx in response to DNA damage. *Mol. Cell. Biol.* 26, 6819–6831 (2006).
130. Jin, Y. *et al.* 14-3-3γ binds to MDMX that is phosphorylated by UV-activated Chk1, resulting in p53 activation. *EMBO J.* 25, 1207–1218 (2006).
131. Okamoto, K. *et al.* DNA damage-induced phosphorylation of MdmX at serine 367 activates p53 by targeting MdmX for Mdm2-dependent degradation. *Mol. Cell. Biol.* 25, 9608–9620 (2005).
132. Milne, D. *et al.* A novel site of AKT-mediated phosphorylation in the human MDM2 onco-protein. *FEBS Lett.* 577, 270–276 (2004).
133. Wood, N. *et al.*14-3-3 Binding to Pim-phosphorylated Ser166 and Ser186 of human Mdm2 – Potential interplay with the PKB/Akt pathway and p14ARF, 518, 4, 615-620 (2009)

134. Madeira, F. *et al.* 14-3-3-Pred: improved methods to predict 14-3-3-binding phosphopeptides. *Bioinformatics* 31, 2276–2283 (2015).
135. Paradís-Bas, M., Tulla-Puche, J. & Albericio, F. The road to the synthesis of “difficult peptides”. *Chem. Soc. Rev.* 45, 631–654 (2016).
136. Rinken, A., Lavogina, D. & Kopanchuk, S. Assays with Detection of Fluorescence Anisotropy: Challenges and Possibilities for Characterizing Ligand Binding to GPCRs. *Trends Pharmacol. Sci.* 39, 187–199 (2018).
137. Kalabova, D. *et al.* Human procaspase-2 phosphorylation at both S139 and S164 is required for 14-3-3 binding. *Biochem. Biophys. Res. Commun.* 493, 940–945 (2017).
138. Molzan, M. *et al.* Stabilization of physical RAF/14-3-3 interaction by cotylenin A as treatment strategy for RAS mutant cancers. *ACS Chem. Biol.* 8, 1869–1875 (2013).
139. Molzan, M. & Ottmann, C. Synergistic Binding of the Phosphorylated S233- and S259-Binding Sites of C-RAF to One 14-3-3ζ Dimer. *J. Mol. Biol.* 423, 486–495 (2012).
140. Kuusk, A. *et al.* Adoption of a Turn Conformation Drives the Binding Affinity of p53 C-Terminal Domain Peptides to 14-3-3σ. *ACS Chem. Biol.* 15, 262–271 (2020).
141. Conn, G. L. Application of Isothermal Titration Calorimetry (ITC) to Biomolecular Interactions. in *Biomolecular and Bioanalytical Techniques* 279–305 (John Wiley & Sons, Ltd, 2019).
142. Kairys, V., Baranauskiene, L., Kazlauskiene, M., Matulis, D. & Kazlauskas, E. Binding affinity in drug design: experimental and computational techniques. *Expert Opin. Drug Discov.* 14, 755–768 (2019).
143. Pennington, K. L., Chan, T. Y., Torres, M. P. & Andersen, J. L. The dynamic and stress-adaptive signaling hub of 14-3-3: emerging mechanisms of regulation and context-dependent protein–protein interactions. *Oncogene* 37, 5587–5604 (2018).
144. Yang, X. *et al.* Structural basis for protein–protein interactions in the 14-3-3 protein family. *Proc. Natl. Acad. Sci.* 103, 17237–17242 (2006).
145. Vink, P. J. de *et al.* Cooperativity basis for small-molecule stabilization of protein–protein interactions. *Chem. Sci.* 10, 2869–2874 (2019).
146. Sun, X. *et al.* PROTACs: great opportunities for academia and industry. *Signal Transduct. Target. Ther.* 4, 1–33 (2019).
147. Nero, T. L., Morton, C. J., Holien, J. K., Wielens, J. & Parker, M. W. Oncogenic protein interfaces: small molecules, big challenges. *Nat. Rev. Cancer* 14, 248–262 (2014).
148. Renaud, J.-P. The Evolving Role of Structural Biology in Drug Discovery. in *Structural Biology in Drug Discovery* 1–22 (John Wiley & Sons, Ltd, 2020).
149. London, N., Raveh, B. & Schueler-Furman, O. Druggable protein–protein interactions – from hot spots to hot segments. *Curr. Opin. Chem. Biol.* 17, 952–959 (2013).
150. Briels, B., Graaf, C. de & Bender, A. Structural Chemogenomics. in *Structural Biology in Drug Discovery* 53–77 (John Wiley & Sons, Ltd, 2020).
151. Folmer, R. H. A. Integrating biophysics with HTS-driven drug discovery projects. *Drug Discov. Today* 21, 491–498 (2016).
152. Janzen, W. P. Screening Technologies for Small Molecule Discovery: The State of the Art. *Chem. Biol.* 21, 1162–1170 (2014).
153. Coyle, J. & Walser, R. Applied Biophysical Methods in Fragment-Based Drug Discovery: *SLAS Discov. Adv. Sci. Drug Discov.* 25(5):471-490 (2020)
154. Holdgate, G. A. & Phillips, C. Combining Structural, Thermodynamic, and Kinetic Information to Drive Hit-to-Lead Progression. in *Structural Biology in Drug Discovery* 99–124 (John Wiley & Sons, Ltd, 2020).
155. Renaud, J.-P. *et al.* Biophysics in drug discovery: impact, challenges and opportunities. *Nat. Rev. Drug Discov.* 15, 679–698 (2016).
156. Hall, M. D. *et al.* Fluorescence polarization assays in high-throughput screening and drug discovery: a review. *Methods Appl. Fluoresc.* 4, 022001 (2016).

157. Gao, K., Oerlemans, R. & Groves, M. R. Theory and applications of differential scanning fluorimetry in early-stage drug discovery. *Biophys. Rev.* 12, 85–104 (2020).
158. Ferenczy, G. G. & Keserű, G. M. Thermodynamic profiling for fragment-based lead discovery and optimization. *Expert Opin. Drug Discov.* 15, 117–129 (2020).
159. Chavanieu, A. & Pugnière, M. Developments in SPR Fragment Screening. *Expert Opin. Drug Discov.* 11, 489–499 (2016).
160. Aguirre, C., Cala, O. & Krimm, I. Overview of Probing Protein-Ligand Interactions Using NMR. *Curr. Protoc. Protein Sci.* 81, 17.18.1-17.18.24 (2015).
161. Bortoluzzi, A. & Ciulli, A. Protein-Based NMR Methods Applied to Drug Discovery. in *Applied Biophysics for Drug Discovery* 153–173 (John Wiley & Sons, Ltd, 2017).
162. Maveyraud, L. & Mourey, L. Protein X-ray Crystallography and Drug Discovery. *Molecules* 25, 1030 (2020).
163. Wienken, C. J., Baaske, P., Rothbauer, U., Braun, D. & Duhr, S. Protein-binding assays in biological liquids using microscale thermophoresis. *Nat. Commun.* 1, 100 (2010).
164. Leney, A. C. & Heck, A. J. R. Native Mass Spectrometry: What is in the Name? *J. Am. Soc. Mass Spectrom.* 28, 5–13 (2017).
165. Zhang, J.-H., Chung, T. D. Y. & Oldenburg, K. R. A Simple Statistical Parameter for Use in Evaluation and Validation of High Throughput Screening Assays. *J. Biomol. Screen.* 4, 67–73 (1999).
166. Lamoree, B. & Hubbard, R. E. Current perspectives in fragment-based lead discovery (FBLD). *Essays Biochem.* 61, 453–464 (2017).
167. Harner, M. J., Metzler, G., Fanslau, C. A., Mueller, L. & Metzler, W. J. 1D NMR Methods for Hit Identification. in *Applied Biophysics for Drug Discovery* 131–152 (John Wiley & Sons, Ltd, 2017).
168. Valenti, D. *et al.* Set-up and screening of a fragment library targeting the 14-3-3 protein interface. *MedChemComm* 10, 1796–1802 (2019).
169. Baell, J. B. & Nissink, J. W. M. Seven Year Itch: Pan-Assay Interference Compounds (PAINS) in 2017—Utility and Limitations. *ACS Chem. Biol.* 13, 36–44 (2018).
170. Protein Protein Interaction – Asinex.com. https://www.asinex.com/ppi/.
171. Rose, R. *et al.* Identification and Structure of Small-Molecule Stabilizers of 14–3–3 Protein–Protein Interactions. *Angew. Chem. Int. Ed.* 49, 4129–4132 (2010).
172. Bosica, F. *et al.* Design of Drug-Like Protein–Protein Interaction Stabilizers Guided By Chelation-Controlled Bioactive Conformation Stabilization. *Chem. – Eur. J.* 26, 7131–7139 (2020).
173. Richter, A., Rose, R., Hedberg, C., Waldmann, H. & Ottmann, C. An optimised small-molecule stabiliser of the 14-3-3-PMA2 protein-protein interaction. *Chem. Weinh. Bergstr. Ger.* 18, 6520–6527 (2012).
174. Jaegle, M., Nawrotzky, E., Wong, E. L., Arkona, C. & Rademann, J. Protein-Templated Fragment Ligation Methods: Emerging Technologies in Fragment-Based Drug Discovery. in *Fragment-based Drug Discovery Lessons and Outlook* 293–326 (John Wiley & Sons, Ltd, 2016).
175. Frei, P., Hevey, R. & Ernst, B. Dynamic Combinatorial Chemistry: A New Methodology Comes of Age. *Chem. – Eur. J.* 25, 60–73 (2019).
176. Cousins, G. R. L., Poulsen, S.-A. & Sanders, J. K. M. Dynamic combinatorial libraries of pseudo-peptide hydrazone macrocycles. *Chem. Commun.* 1575–1576 (1999)
177. Bhat, V. T. *et al.* Nucleophilic catalysis of acylhydrazone equilibration for protein-directed dynamic covalent chemistry. *Nat. Chem.* 2, 490–497 (2010).
178. Parvatkar, P., Kato, N., Uesugi, M., Sato, S. & Ohkanda, J. Intracellular Generation of a Diterpene-Peptide Conjugate that Inhibits 14-3-3-Mediated Interactions. *J. Am. Chem. Soc.* 137, 15624–15627 (2015).

179. Erlanson, D. A. *et al.* Site-directed ligand discovery. *Proc. Natl. Acad. Sci.* 97, 9367–9372 (2000).
180. Zerbe, B. S., Hall, D. R., Vajda, S., Whitty, A. & Kozakov, D. Relationship between Hot Spot Residues and Ligand Binding Hot Spots in Protein–Protein Interfaces. *J. Chem. Inf. Model.* 52, 2236–2244 (2012).
181. Chelushkin, P. S. *et al.* Convenient method of peptide hydrazide synthesis using a new hydrazone resin. *Tetrahedron Lett.* 56, 619–622 (2015).
182. Bandyopadhyay, A. & Gao, J. Targeting Biomolecules with Reversible Covalent Chemistry. *Curr. Opin. Chem. Biol.* 34, 110–116 (2016).
183. Dai, H. *et al.* Development of novel bis-pyrazole derivatives as antitumor agents with potent apoptosis induction effects and DNA damage. *Eur. J. Med. Chem.* 143, 1066–1076 (2018).

Appendix

A.1: Protein alignment

*h*DMX and *h*DM2

UniProt code: Q00987, *h*DM2_HUMAN E3 ubiquitin-protein ligase

MCNTNMSVPTDGAVTTSQIPASEQETLVRPKPLLLKLLKSVGAQKDTYTMKEVLFYLGQY
IMTKRLYDEKQQHIVYCSNDLLGDLFGVPSFSVKEHRKIYTMIYRNLVVVNQQESSDSGT
SVSENRCHLEGGSDQKDLVQELQEEKPSSSHLVSRPSTSSRRRAISETEENSDELSGERQ
RKRHKSDSISLSFDESLALCVIREICCERSSSSESTGTPSNPDLDAGVSEHSGDWLDQDS
VSDQFSVEFEVESLDSEDYSLSEEGQELSDEDDEVYQVTVYQAGESDTDSFEEDPEISLA
DYWKCTSCNEMNPPLPSHCNRCWALRENWLPEDKGKDKGEISEKAKLENSTQAEEGFDVP
DCKKTIVNDSRESCVEENDDKITQASQSQESEDYSQPSTSSSIIYSSQEDVKEFEREETQ
DKEESVESSLPLNAIEPCVICQGRPKNGCIVHGKTGHLMACFTCAKKLKKRNKPCPVCRQ
PIQMIVLTYFP

UniProt code: O15151,*h*DMX_HUMAN Protein

MTSFSTSAQCSTSDSACRISPGQINQVRPKLPLLKILHAAGAQGEMFTVKEVMHYLGQYI
MVKQLYDQQEQHMVYCGGDLLGELLGRQSFSVKDPSPLYDMLRKNLVTLATATTDAAQTL
ALAQDHSMDIPSQDQLKQSAEESSTSRKRTTEDDIPTLPTSEHKCIHSREDEDLIENLAQ
DETSRLDLGFEEWDVAGLPWWFLGNLRSNYTPRSNGSTDLQTNQDVGTAIVSDTTDDLWF
LNESVSEQLGVGIKVEAADTEQTSEEVGKVSDKKVIEVGKNDDLEDSKSLSDDTDVEVTS
EDEWQCTECKKFNSPSKRYCFRCWALRKDWYSDCSKLTHSLSTSDITAIPEKENEGNDVP
DCRRTISAPVVRPKDAYIKKENSKLFDPCNSVEFLDLAHSSESQETISSMGEQLDNLSEQ
RTDTENMEDCQNLLKPCSLCEKRPRDGNIIHGRTGHLVTCFHCARRLKKAGASCPICKKE
IQLVIKVFIA

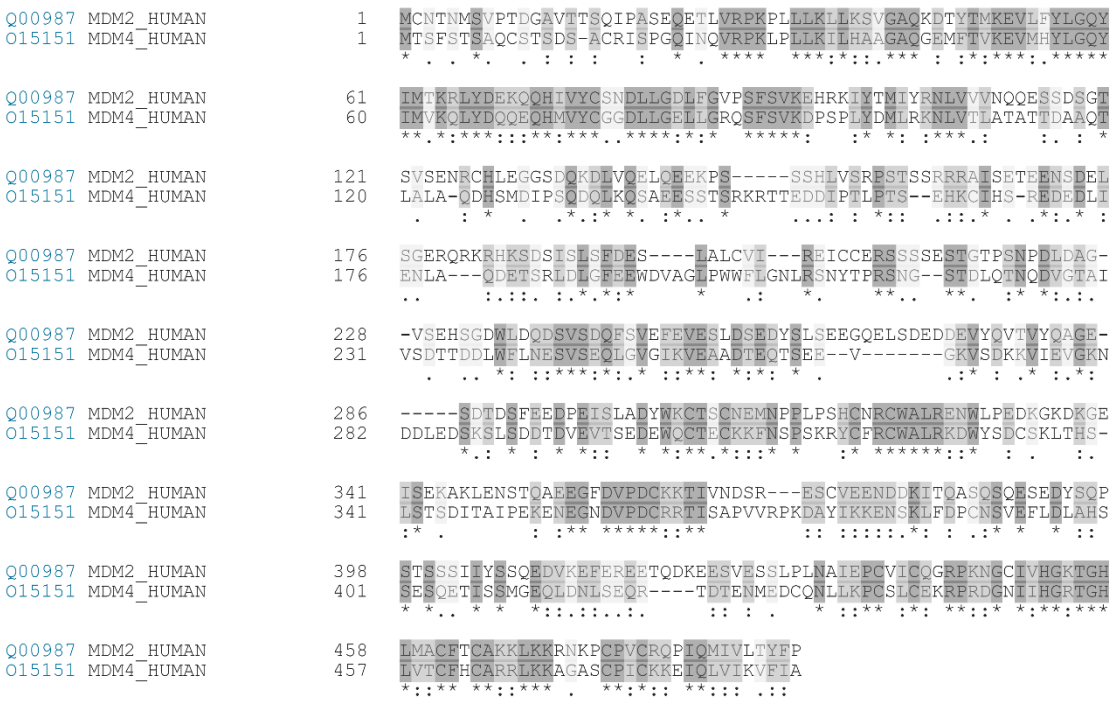

Sequence of *h*DM2 and *h*DMX proteins with Ser and Thr residues highlighted in bold and their alignment (similar amino acids in grey)

14-3-3 proteins alignment

UniProt codes for seven human 14-3-3 isoforms: τ- P27348, η- Q04917, σ- P31947, ε-P62258, β- P31946, γ- P61981, ζ- P63104.

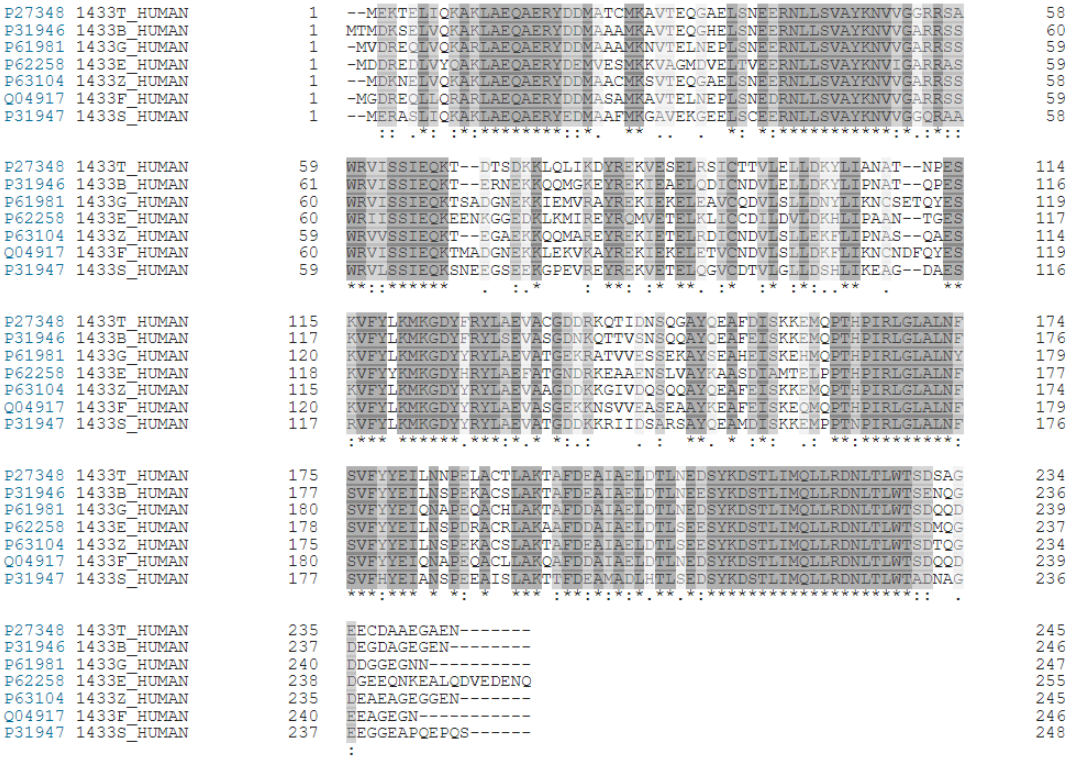

A.2 Peptides and proteins analytical characterization

Table A.2 List of synthesized peptides

	Peptide	Sequence	Purity
1	*h*DMX-367-Ac	Ac-DCRRTI(pS)APVVRPK-$CONH_2$	95.2%
2	*h*DMX-367-FAM	FAM-Ahx-DCRRTI(pS)APVVRPK-$CONH_2$	100%
3	*h*DMX-367-FAM neg cntrl	FAM-Ahx-DCRRTISAPVVRPK-$CONH_2$	90.1%
4	*h*DMX-342+367-Ac	Ac-SKLTHSL(pS)TSDITAIPEKENEGNDV PDCRRTI(pS)APVVRPK-$CONH_2$	77.4%
5	*h*DMX-342+367-FAM	FAM-Ahx-SKLTHSL(pS)TSDITAIPEKENEG NDVPDCRRTI(pS)APVVRPK-$CONH_2$	100%
6	*h*DMX-342-FAM long	FAM-Ahx-SKLTHSL(pS)TSDITAIPEKENEG NDVPDCRRTISAPVVRPK-$CONH_2$	100%
7	*h*DMX-367-FAM long	FAM-Ahx-SKLTHSLSTSDITAIPEKENEG NDVPDCRRTI(pS)APVVRPK-$CONH_2$	100%
8	*h*DM2-166-Ac	Ac-SRRRAI(pS)ETEEN-$CONH_2$	100%
9	*h*DM2-166-FAM	FAM-Ahx-SRRRAI(pS)ETEEN-$CONH_2$	100%
10	*h*DMX-342-Ac	Ac-SKLTHSL(pS)TSDITAI-$CONH_2$	100%
11	*h*DMX-342-FAM	FAM-Ahx-SKLTHSL(pS)TSDITAI-$CONH_2$	93.2%
12	*h*DMX-342-FAM neg cntrl	FAM-Ahx-SKLTHSLSTSDITAI-$CONH_2$	89.2%
13	*h*DM2-186-Ac	Ac-QRKRHK(pS)DSISLS-$CONH_2$	100%
14	*h*DM2-186-FAM	FAM-Ahx-QRKRHK(pS)DSISLS-$CONH_2$	100%
15	*h*DM2-166+186-Ac	Ac-SRRRAI(pS)ETEENSDELSGE RQRKRHK(pS)DSISLS-$CONH_2$	98.3%
16	*h*DM2-166+186-FAM	FAM-Ahx -SRRRAI(pS)ETEENSDELSGE RQRKRHK(pS)DSISLS-$CONH_2$	92.7%
17	*h*DM2-166+186-FAM neg cntrl	FAM-Ahx -SRRRAISETEENSDELSGE RQRKRHKSDSISLS-$CONH_2$	95.2%
18	*h*DMX-289-Ac	Ac-DDLEDSK(pS)LDSSTDV-$CONH_2$	100%
19	*h*DMX-289-FAM	FAM-Ahx- DDLEDSK(pS)LDSSTDV-$CONH_2$	100%
20	*h*DMX-289-FAM neg cntrl	FAM-Ahx- DDLEDSKSLDSSTDV-$CONH_2$	78.59%
21	*h*DMX-151-Ac	Ac-STSRKRT(pS)EDDIPTL-$CONH_2$	100%
22	*h*DMX-151-FAM	FAM-Ahx- STSRKRT(pS)EDDIPTL -$CONH_2$	99.1%
23	*h*DMX-151-FAM neg cntrl	FAM-Ahx- STSRKRTSEDDIPTL-$CONH_2$	93.0%
24	Hydrozide PG-*h*DMX-367-Ac	Ac-DCRRTI(pS)APG-CONH-NH_2	92%
25	Hydrozide PVG-*h*DMX-367-Ac	Ac-DCRRTI(pS)APVG-CONH-NH_2	96%
26	Hydrozide PVVG-*h*DMX-367-Ac	Ac-DCRRTI(pS)APVVG-CONH-NH_2	100%
27	Hydrozide PVG-*h*DMX-367-Ac neg cntrl	Ac-DCRRTI(pS)APVG-$CONH_2$	91.3%

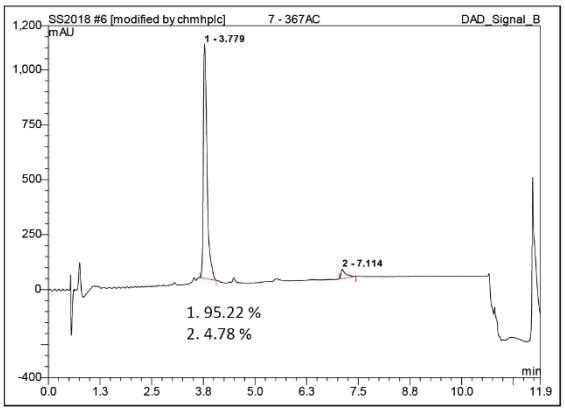

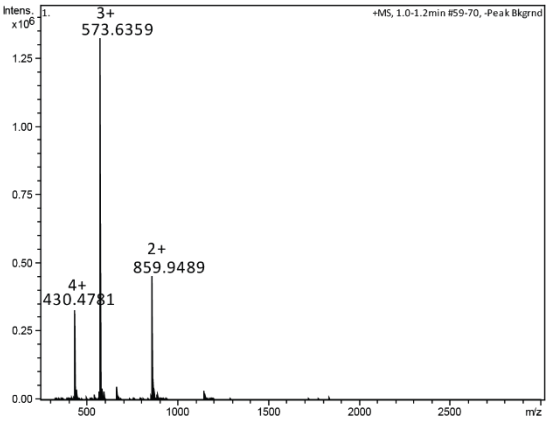

hDMX-367-Ac

DCRRTI(pS)APVVRPK

Mw theoretical= 1717.88 +2: 859.94 +3: 573.63

+2: 859.95 +3: 573.63

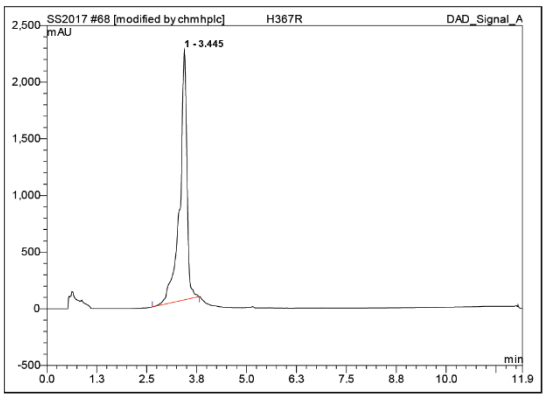

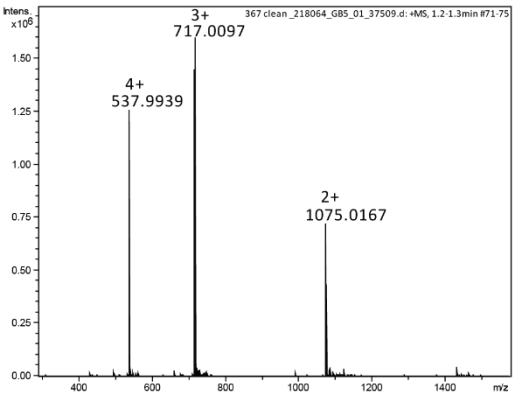

hDMX-367-FAM

DCRRTI(pS)APVVRPK

Mw theoretical= 2149.02 +2: 1075.51 +3: 717.34

+2: 1075.02 +3: 717.01

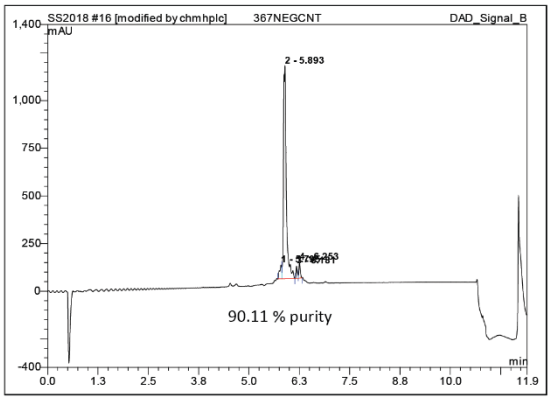

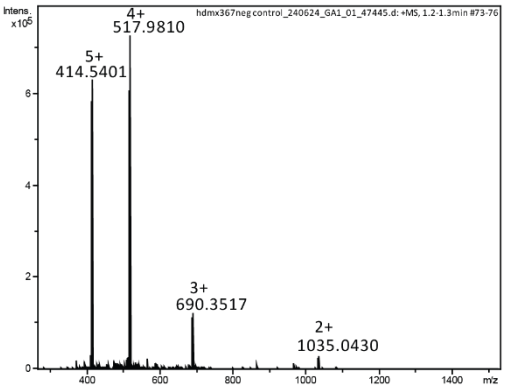

hDMX-367-FAM Negative control

DCRRTISAPVVRPK

Mw theoretical= 2069.05 +2: 1035.52 +3: 690.68

+2: 1035.04 +3: 690.35

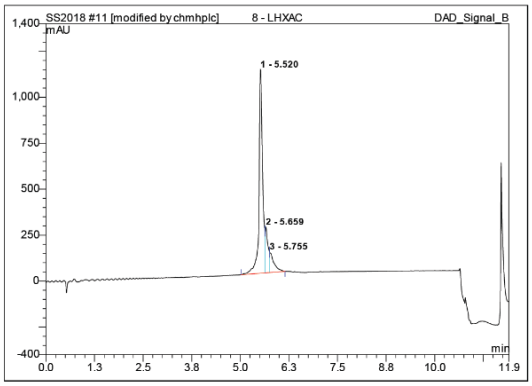

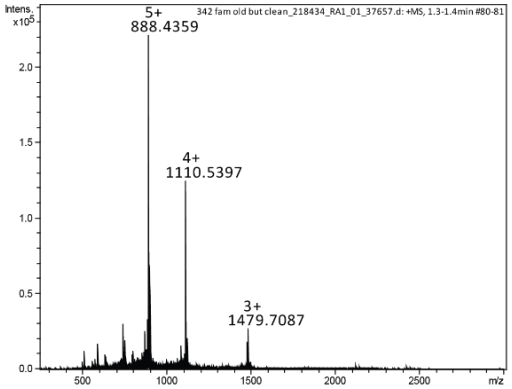

hDMX-342+367-Ac

Mw theoretical= 4435.67 +3: 1479.56 +4: 1109.92

SKLTHSL(pS)TSDITAIPEKENEGNDVPDCRRTI(pS)APVVRPK

+2: 1479.71 +3: 110.54

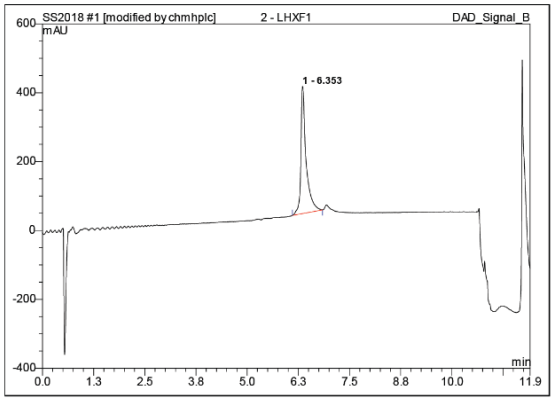

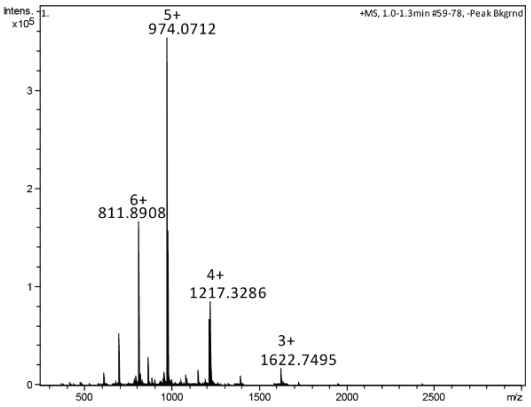

hDMX-342+367-FAM

Mw theoretical= 4864.26 +3: 1622.42 +4: 1217.06

SKLTHSL(pS)TSDITAIPEKENEGNDVPDCRRTI(pS)APVVRPK

+3: 1622.75 +4: 1217.36

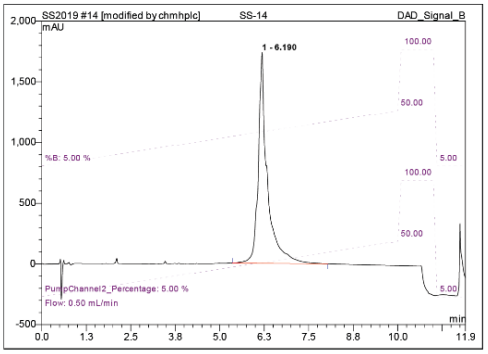

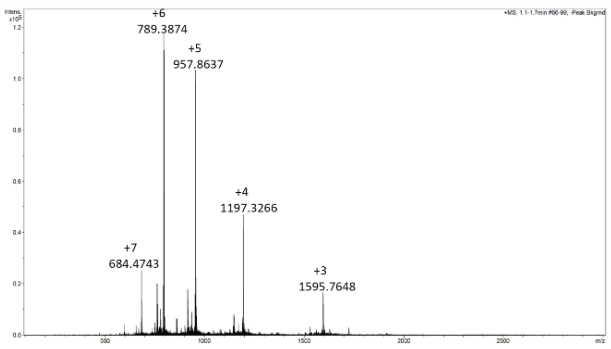

hDMX-342-long peptide-FAM

Mw theoretical= 4784.28 +3: 1595.76 +4: 1197.07

SKLTHSL(pS)TSDITAIPEKENEGNDVPDCRRTISAPVVRPK

+3: 1595.76 +4: 1197.33

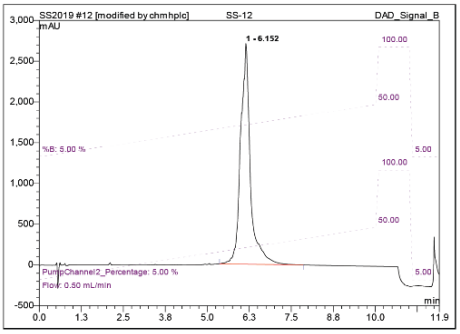

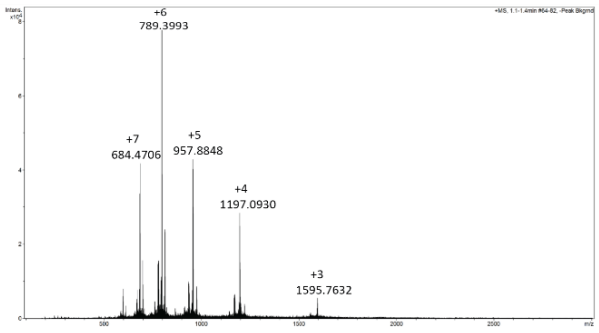

hDMX-367-long peptide-FAM

SKLTHSLSTSDITAIPEKENEGNDVPDCRRTI(pS)APVVRPK

Mw theoretical= 4784.28 +3: 1595.76 +4: 1197.07

+3: 1595.76 +4: 1197.09

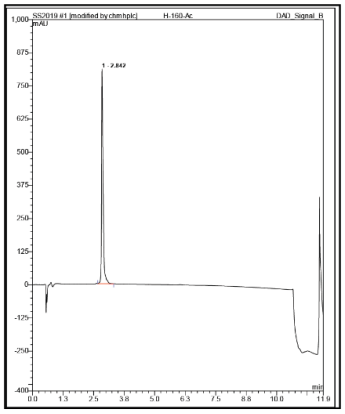

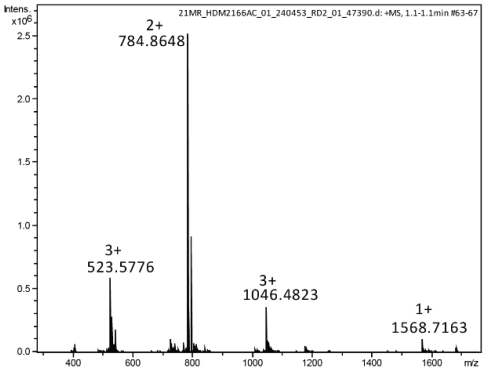

hDM2-166-Ac

S R R R A I (pS) E T E E N

Mw theoretical= 1567.71 +2: 784.85 +3: 523.57

+2: 784.86 +3: 523.58

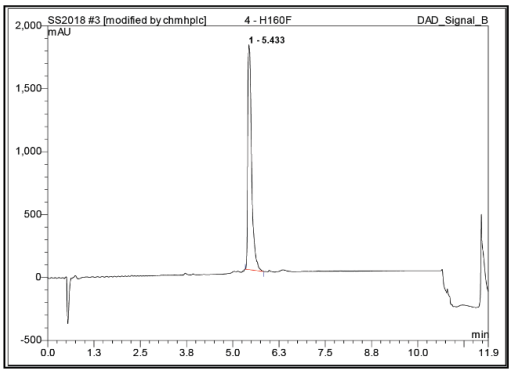

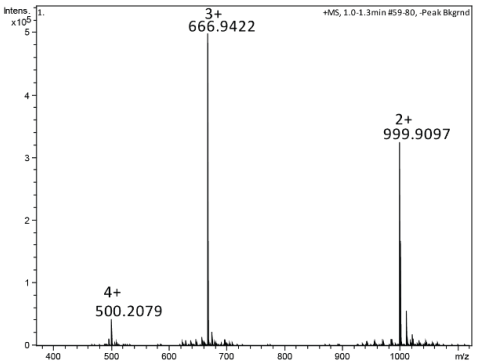

hDM2-166-FAM

S R R R A I (pS) E T E E N

Mw theoretical= 1998.85 +2:1000.42 +3:667.28

+2:999.91 +3:666.94

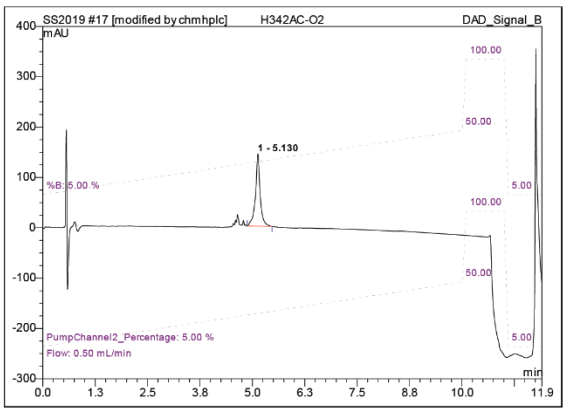

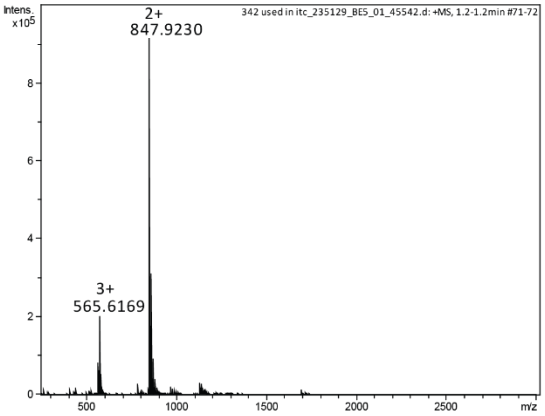

hDMX-342-Ac

SKLTHSL(pS)TSDITAI

Mw theoretical= 1693.83 +2: 847.91 +3: 565.61

+2: 847.92 +3: 565.62

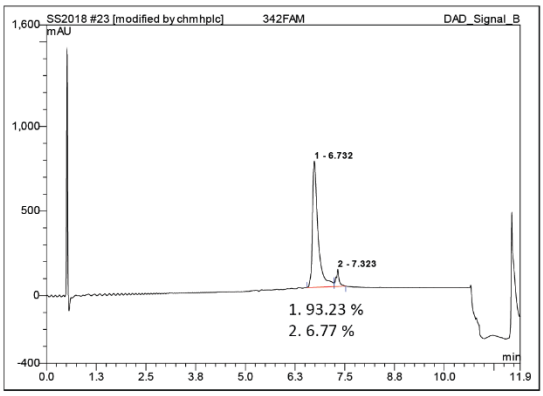

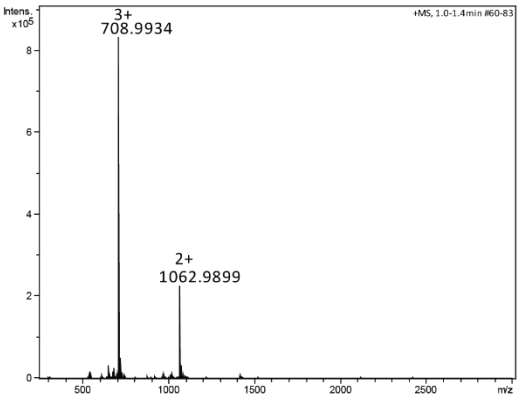

hDMX-342-FAM

SKLTHSL(pS)TSDITAI

Mw theoretical= 2124.97 +2: 1063.48 +3: 709.32

+2: 1062.98 +3: 708.99

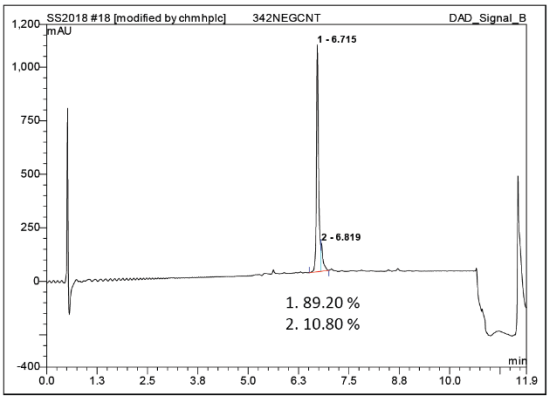

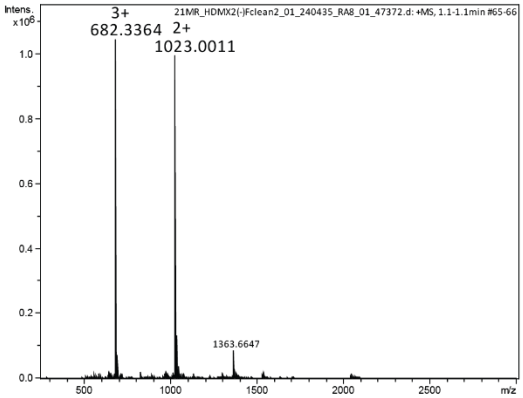

hDMX-342-FAM Negative control

SKLTHSLSTSDITAI

Mw theoretical= 2045.00 +2: 1023.50 +3: 682.67

+2: 1023.00 +3: 682.34

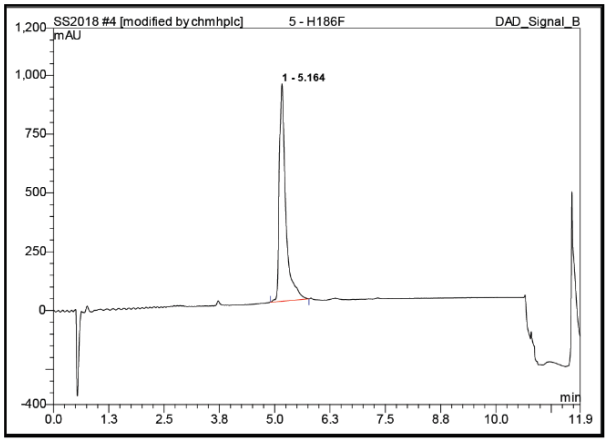

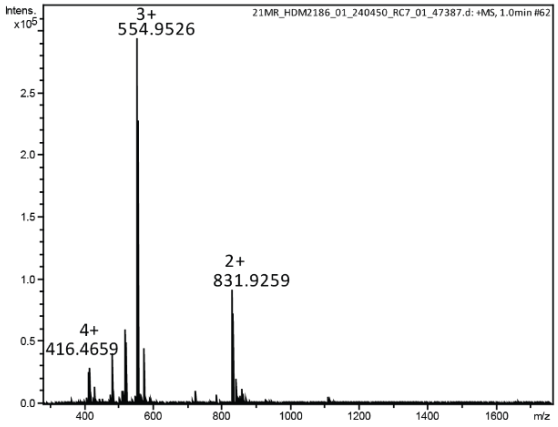

hDM2-186-Ac

Q R K R H K (pS) D S I S L S

Mw theoretical=1661.84 +2:831.92 +3:554.95

+2:831.92 +3:554.95

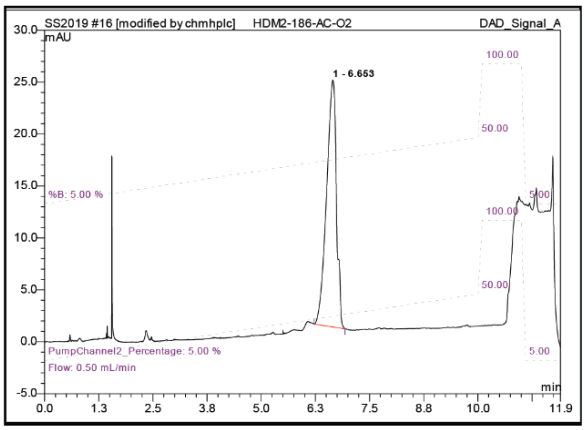

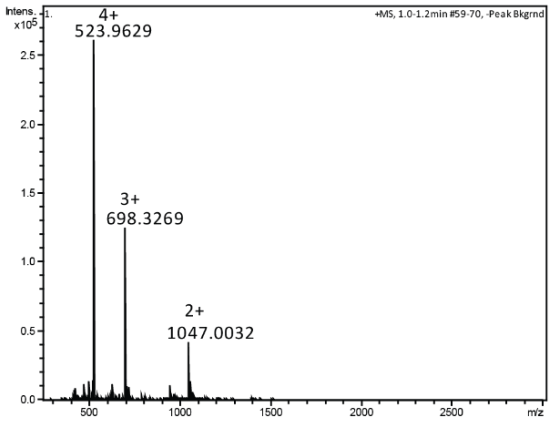

hDM2-186-FAM

Q R K R H K (pS) D S I S L S

Mw theoretical= 2092.97 +2: 1047.48 +3:698.65

+2: 1047.00 +3: 698.32

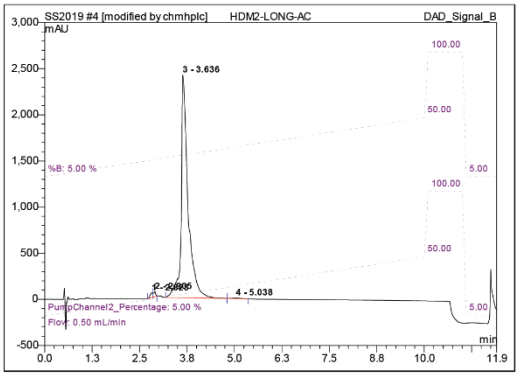

hDM2-166+186-Ac

SRRRAI(pS)ETEENSDELSGERQRKRHK(pS)DSISLS

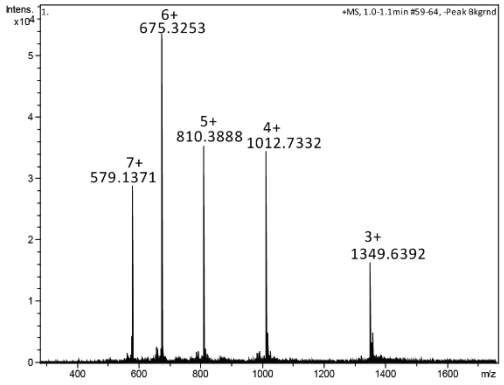

Mw theoretical 4046.14 +3: 1349.7 +4: 1012.5 +5: 810.22

Mw_{found} +3:1349.64 +4: 1012.73

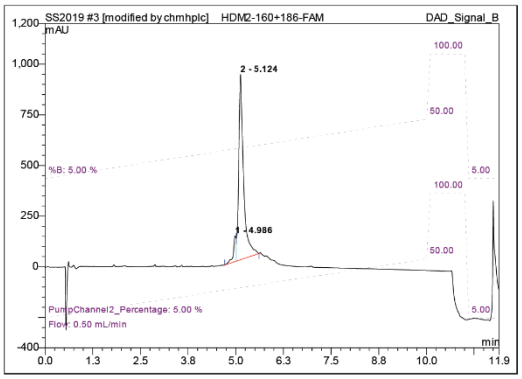

hDM2-166+186-FAM

SRRRAI(pS)ETEENSDELSGERQRKRHK(pS)DSISLS

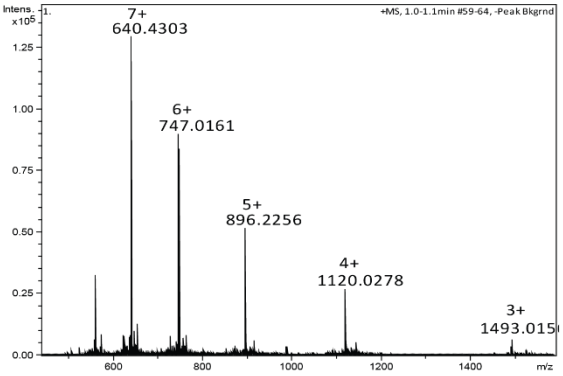

Mw theoretical = 4477.58 +3: 1493.5 +4: 1120.39 +5: 896.5

Mw_{found} +3: 1493.01 +4: 1120.03

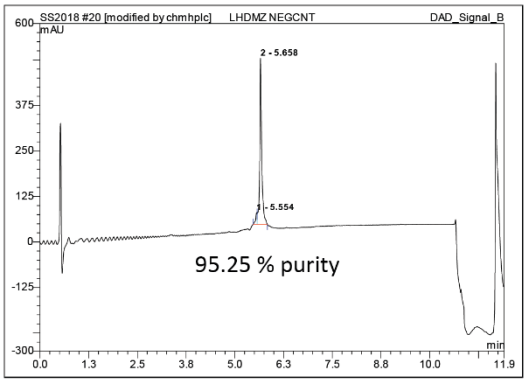

hDM2-166+186-FAM Negative control

SRRRAISETEENSDELSGERQRKRHKSDSISLS

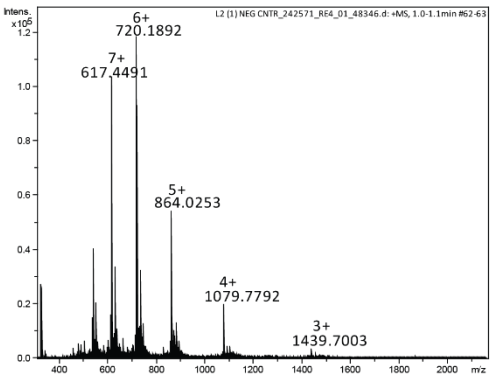

Mw theoretical= 4315.10 +3: 1439.37 +4: 1079.77

+3: 1439.70 +4: 1079.78

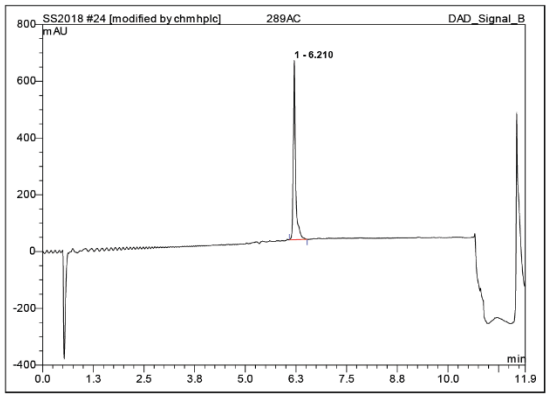

hDMX-289-Ac

DDLEDSK(pS)LSDDTDV

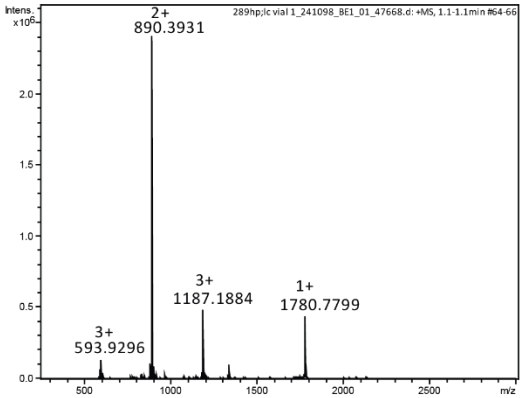

Mw theoretical= 1774.66 +2: 888.33 +3: 592.55

+2: 890.39 +3: 593.93

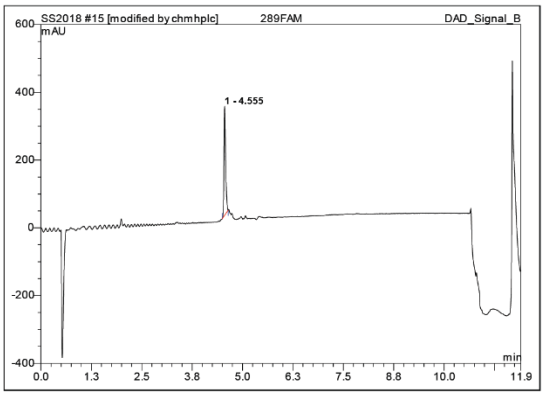

hDMX-289-FAM

DDLEDSK(pS)LSDDTDV

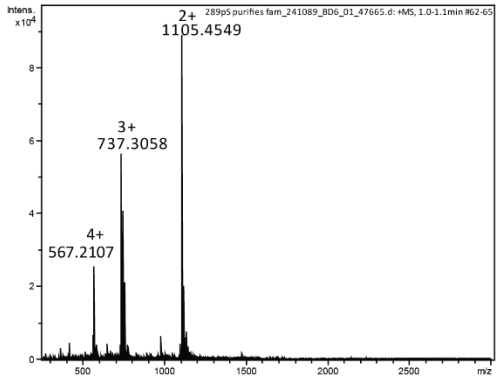

Mw $_{\text{theoretical}}^{\text{found}}$ = 2206.10 +2: 1104.05 +3: 736.37

+2: 1105.45 +3: 737.30

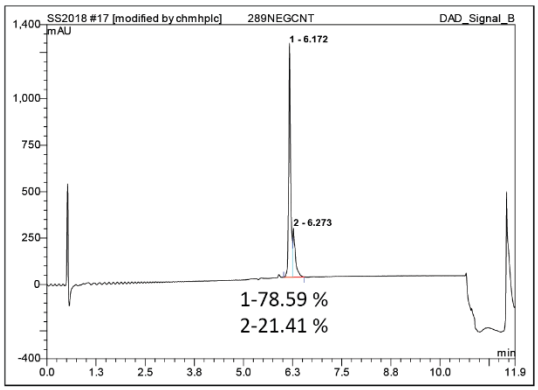

hDMX-289-FAM Negative control

DDLEDSKSLSDDTDV

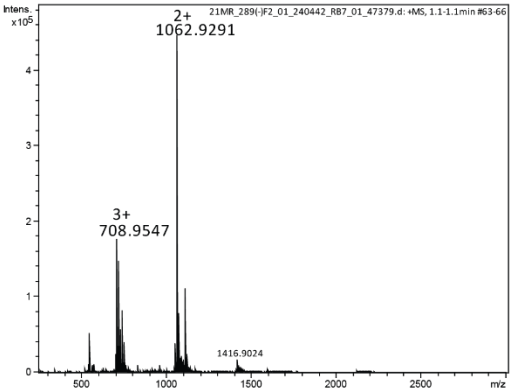

Mw theoretical= 2124.85 +2: 1063.42 +3: 709.28

+2: 1062.93 +3: 708.95

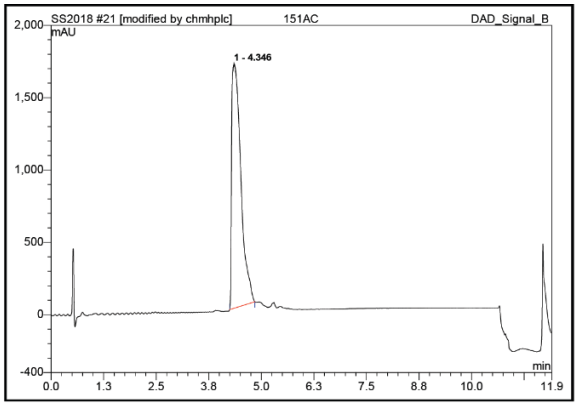

hDMX-151-Ac

STSRKRT(pT)EDDIPTL

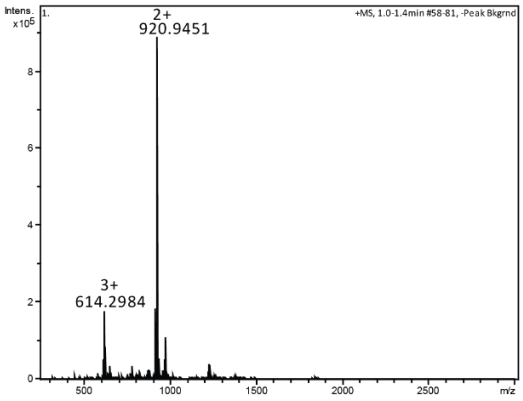

Mw theoretical= 1839.87 +2: 920.93 +3: 614.29

Mw found= +2: 920.94 +3: 614.29

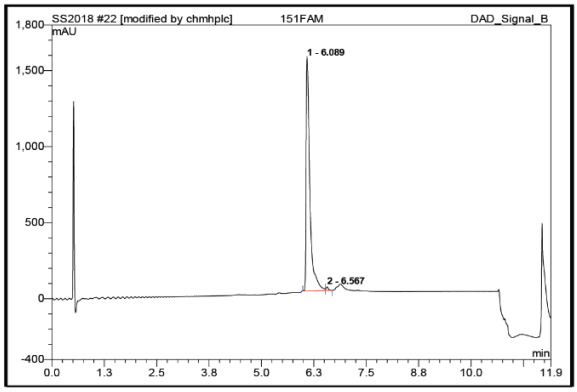

hDMX-151-FAM

STSRKRT(pT)EDDIPTL

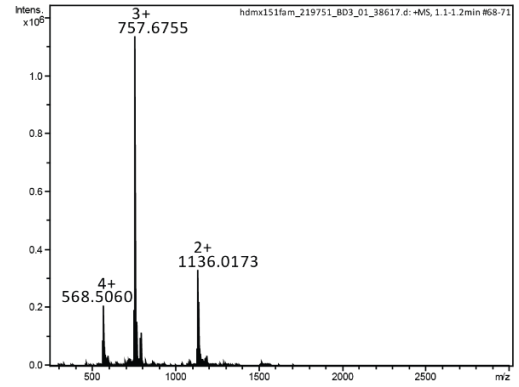

Mw theoretical= 2271.01 +2: 1136.50 +3: 758.00

Mw found= +2: 1136.02 +3: 757.67

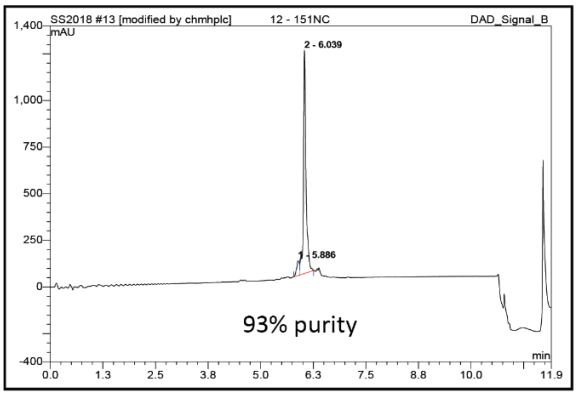

hDMX-151-FAM Negative control

STSRKRTTEDDIPTL

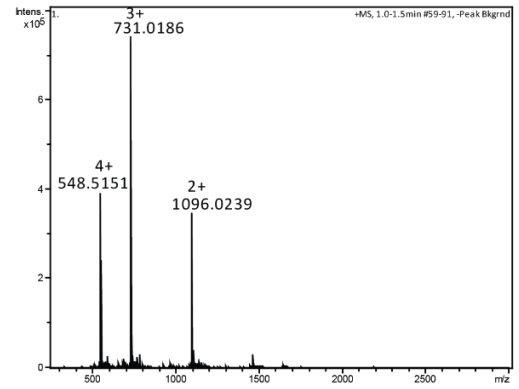

Mw theoretical= 2191.04 +2: 1096.52 +3: 731.35

Mw found= +2: 1096.02 +3: 731.02

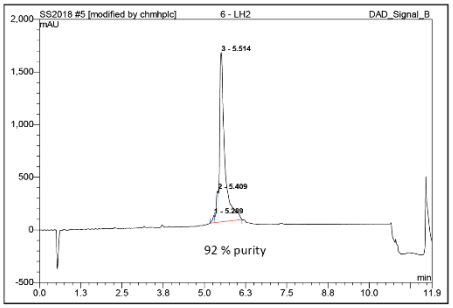

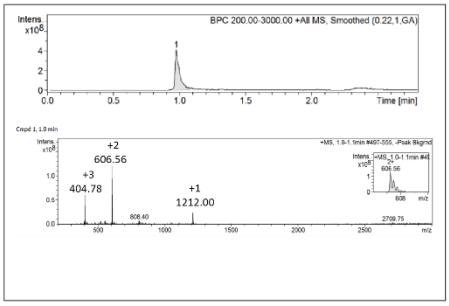

Hydrozide PG-hDMX-367-Ac

Ac-DCRRTI(pS)APG-CONH-NH_2

Mw theoretical= 1211.26 +2: 606.63 +3: 404.75

Mw found= +1 1212.00 +2: 606.56 +3: 404.78

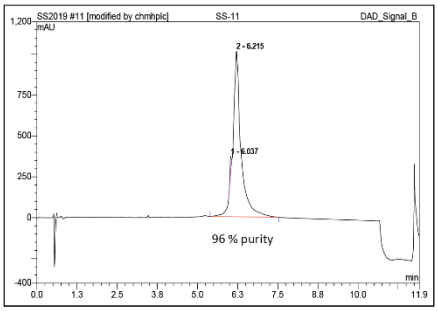

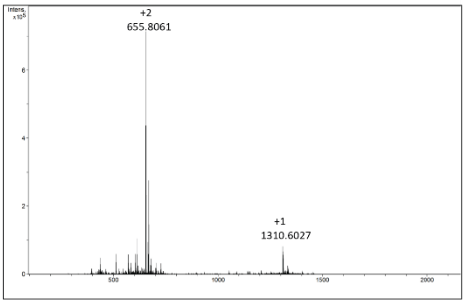

Hydrozide PVG-hDMX-367-Ac

Ac-DCRRTI(pS)APVG-CONH-NH_2

Mw theoretical= 1309.6 +2: 655.80 +3: 437.53

Mw found= +1 1310.60 +2: 655.81

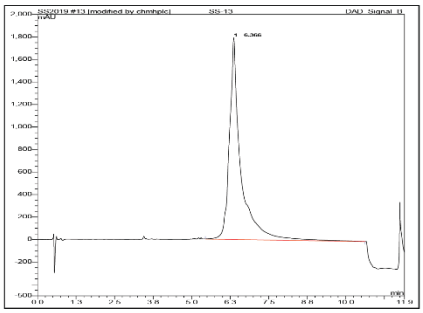

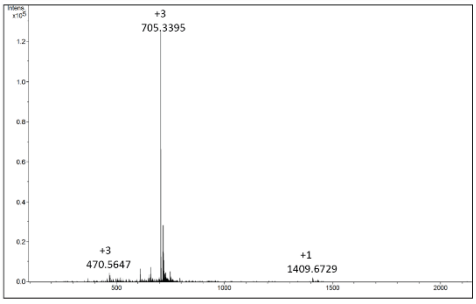

Hydrozide PVVG-hDMX-367-Ac

Ac-DCRRTISAPVVG-CONH-NH_2

Mw theoretical= 1408.66 +2: 705.33 +3: 470.55

+2: 705.34 +3: 470.56

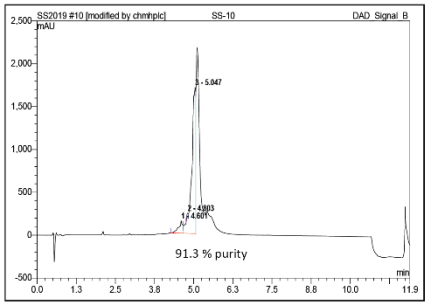

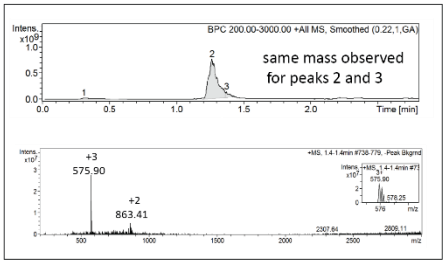

Hydrozide PVG-hDMX-367-FAM

FAM-Ahx-DCRRTI(pS)APVG-$CONH_2$

Mw theoretical= 1725.72 +2: 863.86 +3: 576.24

+2: 863.41 +3: 575.90

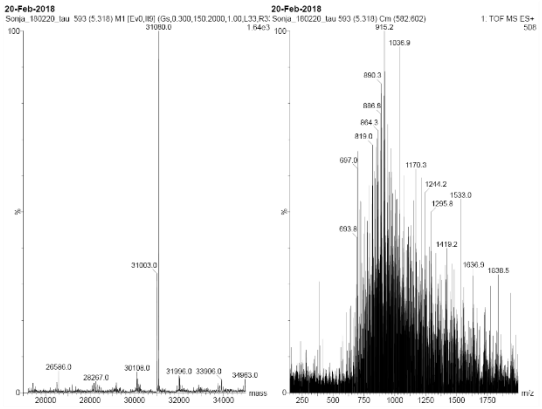

14-3-3 TAU
Mw=31005

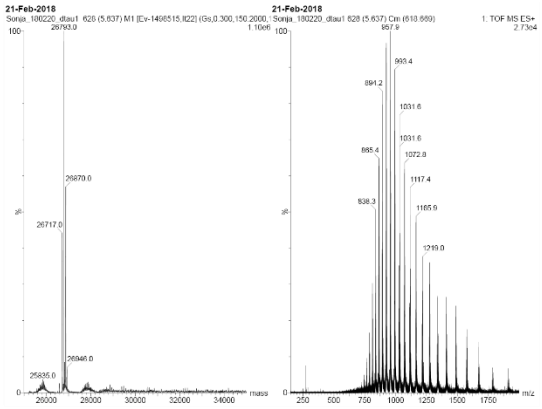

14-3-3 TAU DELTA C
Mw= 26718.3

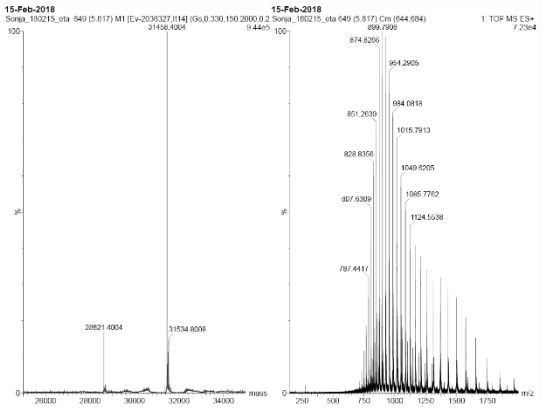

14-3-3 ETA
Mw= 31459

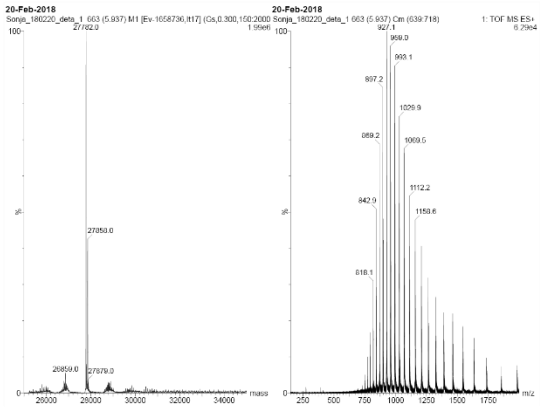

14-3-3 ETA DELTA C
Mw= 27782.4

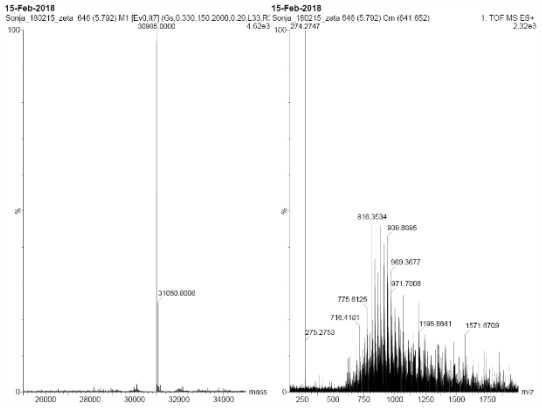

14-3-3 ZETA
Mw= 30985,5

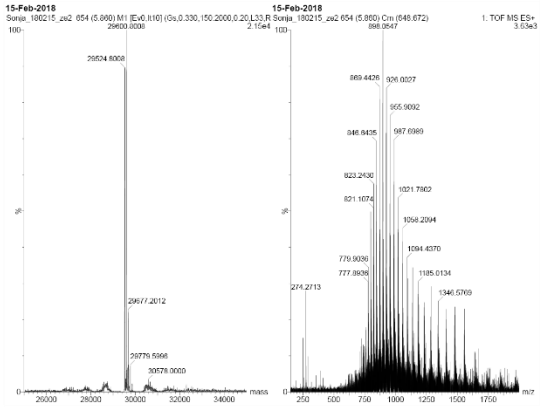

14-3-3 ZETA DELTA C
Mw= 26688.2

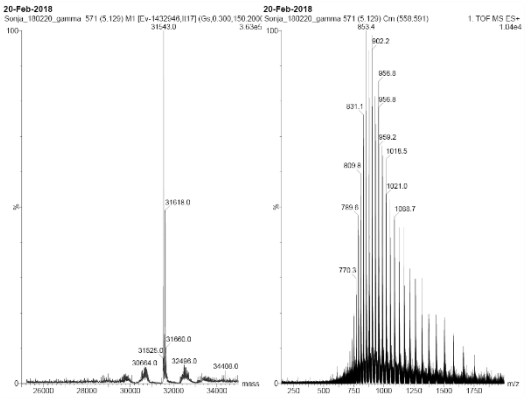

14-3-3 GAMMA
Mw= 31543

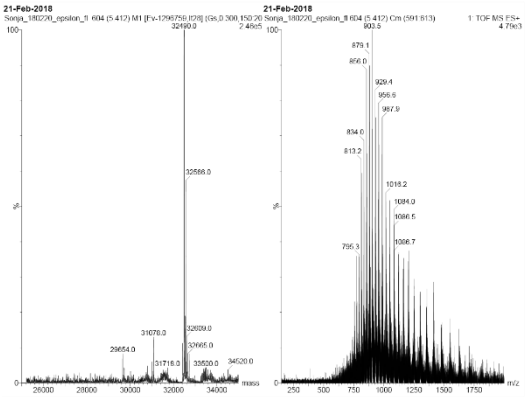

14-3-3 EPSILON
Mw= 32414

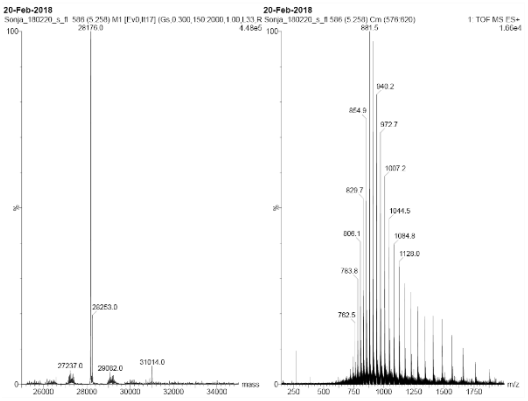

14-3-3 SIGMA
Mw= 31014.4
Major peak is 14-3-3 without his-tag

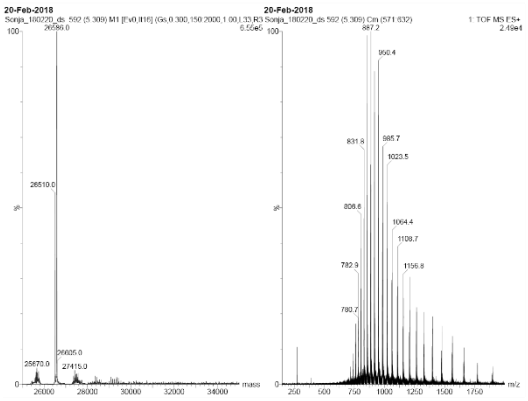

14-3-3 SIGMA DELTA C
Mw=26509.9

A.3 SPR data fitting with BioCore software

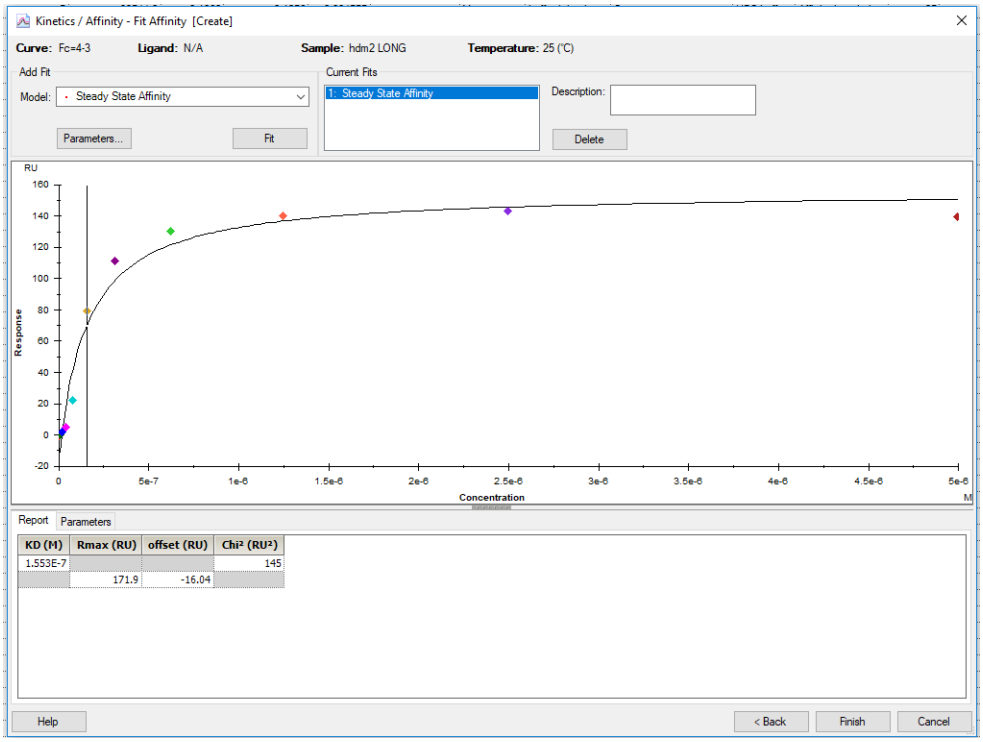

*h*DM2-166+186 peptide

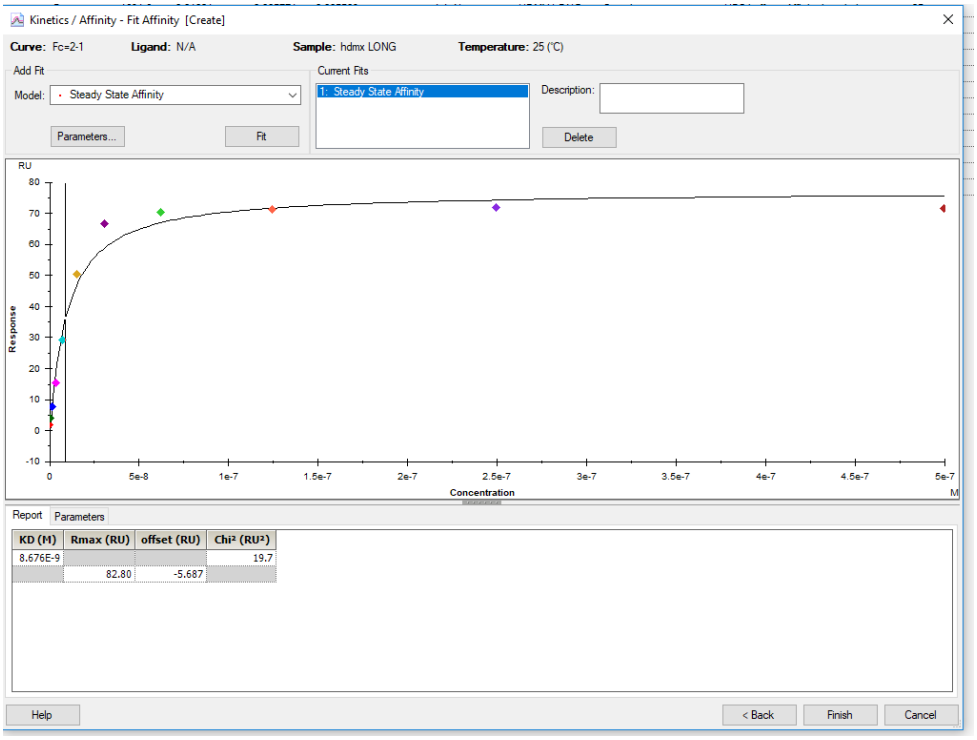

*h*DMX-342+367 peptide

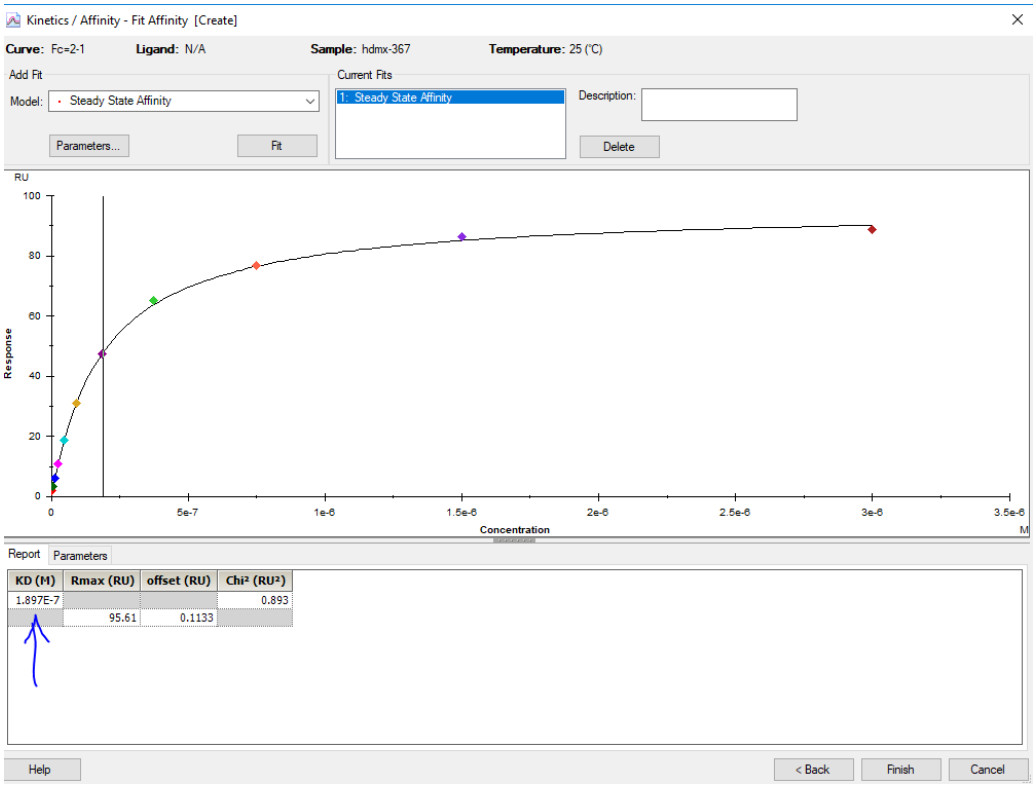

*h*DMX-367 peptide

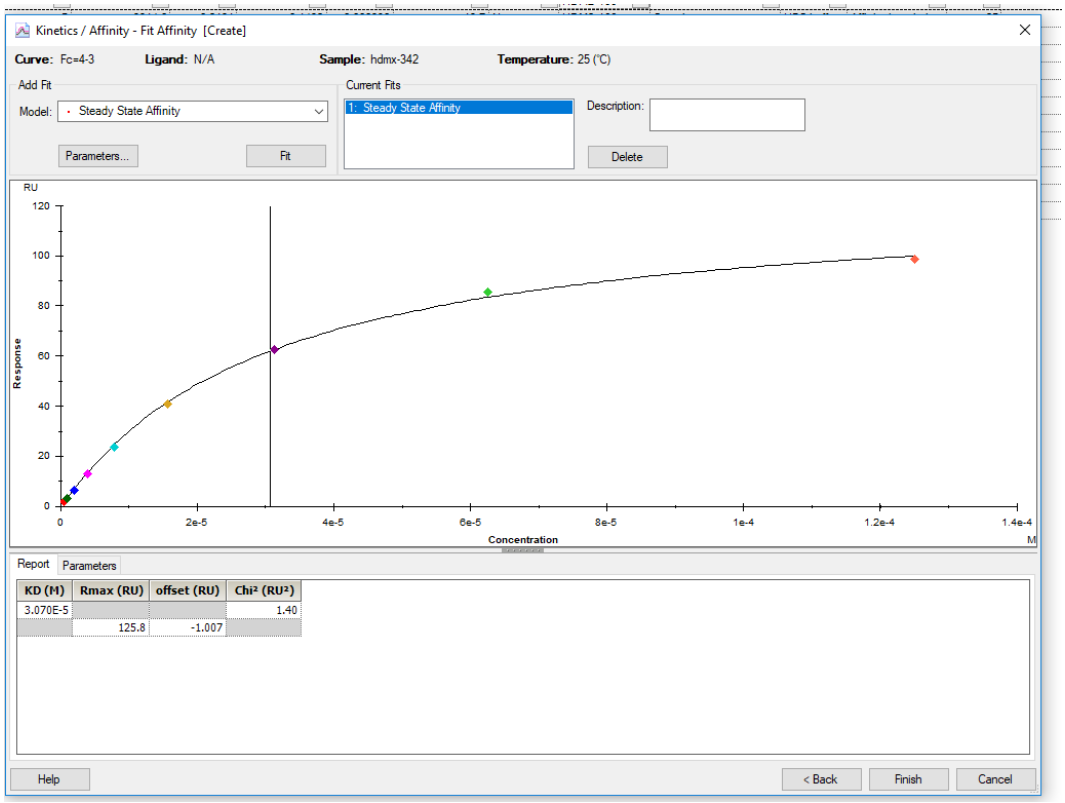

*h*DMX-342 peptide

A.4 Appendix: Crystal structure images

A.4.1 *h*DMX-367 / 14-3-3σ

A. Monomer A

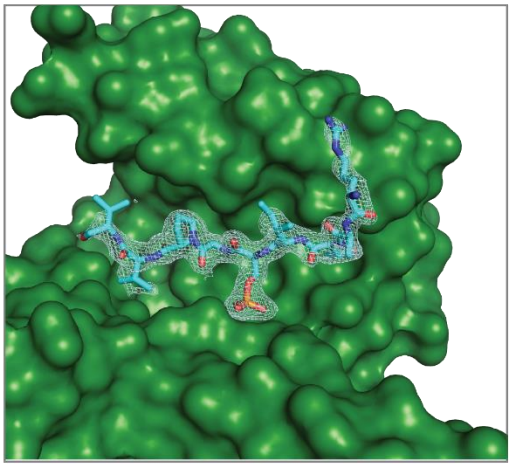

B. Monomer B

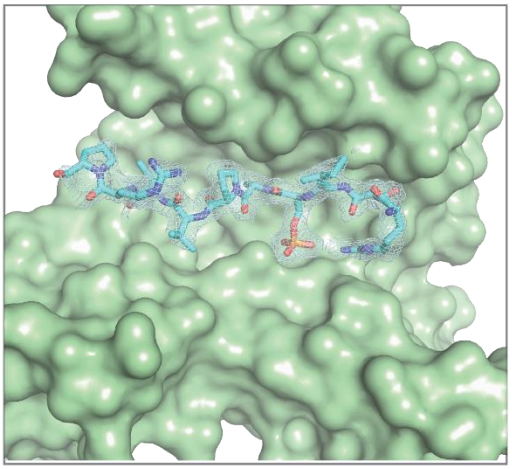

C. Monomer C

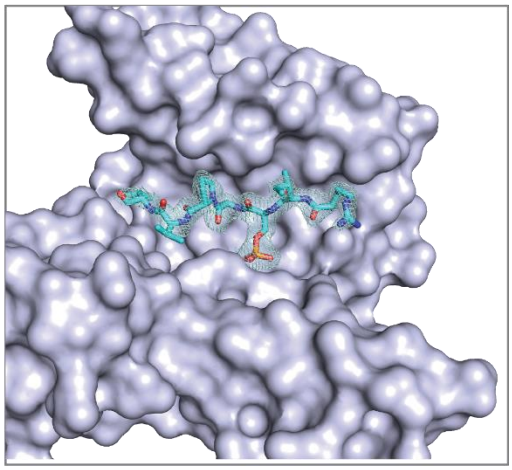

D. Monomer D

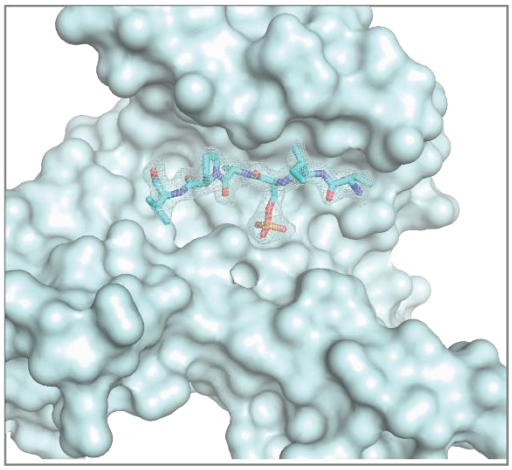

A.4.3 *h*DM2-186/14-3-3σ

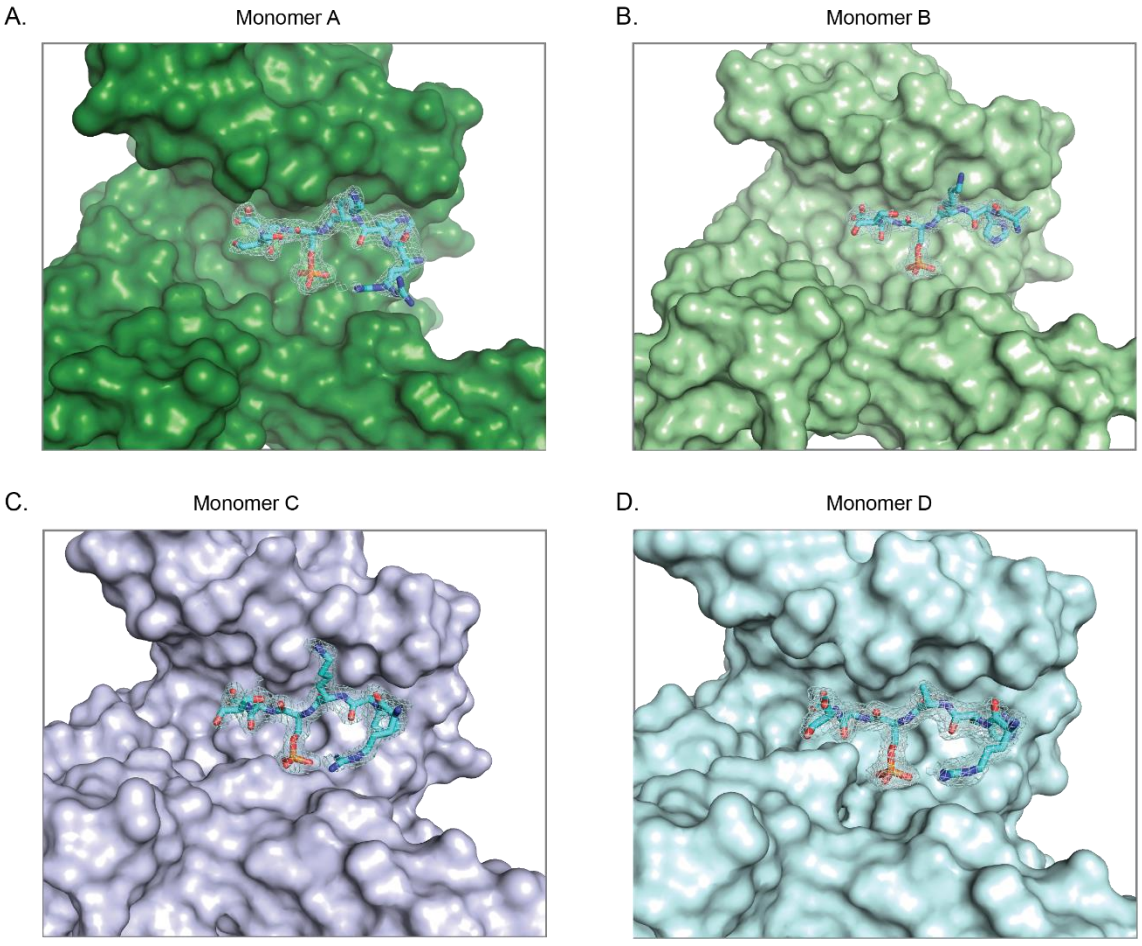

Table A.4 Refinement statistic

	*h*DMX-367	*h*DMX-342+367	*h*DM2-186
Space group	P 1	C 1 2 1	P 1
Cell constants a,b,c, α, β, γ	63.95Å 75.30Å 78.39Å 95.15◦ 113.14◦ 93.84◦	133.11Å 70.21Å 80.63Å 90.00◦ 101.97◦ 90.00◦	63.23Å 74.57Å 77.97Å 98.43◦ 111.09◦ 93.12◦
Resolution (Å)	74.53 - 2.10 71.50 - 2.25	56.26 - 2.10 65.11 - 2.10	56.90 - 1.75 73.26 - 1.75
% Data completeness (in resolution range)	97.3 (74.53-2.10) 97.6 (71.50-2.25)	99.1 (56.26-2.10) 91.2 (65.11-2.10)	94.9 (56.90-1.75) 90.0 (73.26-1.75)
R_{merge}	0.11	0.04	0.07
R_{sym}	-	-	-
< I/σ(I) >	5.36 (at 2.25Å)	0.68 (at 2.10Å)	1.33 (at 1.75Å)
Refinement program	REFMAC 5.8.0230	PHENIX 1.12_2829	PHENIX 1.12_2829, REFMAC 5.8.0238
R, R_{free}	0.198, 0.222 0.206, 0.230	0.212, 0.246 0.213, 0.246	0.199, 0.224 0.198, 0.223
R_{free} test set	2993 reflections (4.85%)	2108 reflections (5.02%)	6318 reflections (5.03%)
Wilson B-factor (Å)	27.3	35.8	25.3
Anisotropy	0.338	0.397	0.241
Bulk solvent k_{sol}(e/Å^3), Bsol(Å^2)	0.30, 31.7	0.36, 40.0	0.41, 47.8
L-test for twinning	< |L| > = 0.47, < L2 > = 0.30	< |L| > = 0.50, < L2 > = 0.34	< |L| > = 0.50, < L2 > = 0.33
Estimated twinning fraction	No twinning to report.	No twinning to report.	No twinning to report.
Fo,Fc correlation	0.93	0.94	0.94
Total number of atoms	7709	7376	15129
Average B, all atoms (Å^2)	34.0	54.0	40.0

A.5 Screening results

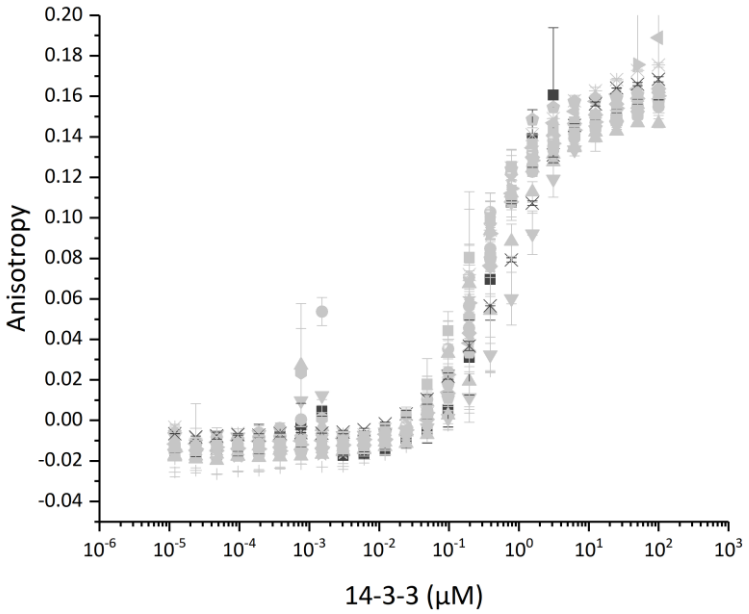

Figure A.5.1 Dose response assay of 50 μM 14-3-3η titrated in the presence of 50 nM *h*DMX-367 peptide and 2.5 mM of fragments identified as hits on Figure 3.4. No significant change in anisotropy was observed for any fragments

Figure A.5.2 Maybridge fragment stabilizers, confirmation of hits by FA and SPR (p.153-155). Each fragment 1-20 is represented with FA followed by SPR dose-response graph. 2.5 mM fragments were titrated against the constant concentration of peptide and tracer (0.2 μM of 14-3-3η and 50 nM of *h*DMX-367 peptide) for FA. For SPR, a serial dilution of fragments (2 mM being the highest concentration, 2% (v/v) DMSO) with a constant concentration of 50 nM of acetylated hDMX-367 peptide was prepared and flown over the protein immobilized on surface.

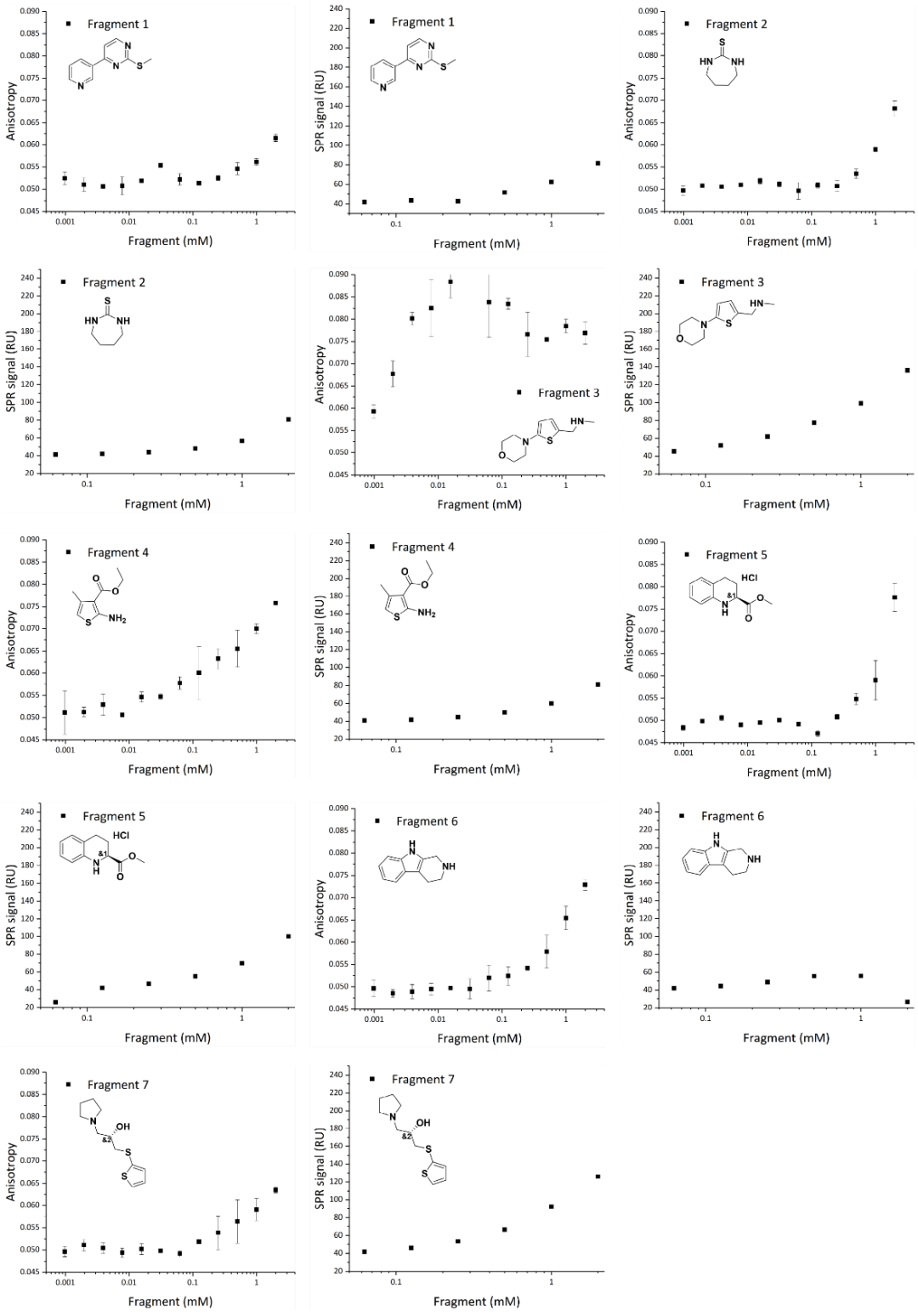

Figure A.5.2 Maybridge fragment stabilizers, confirmation of hits by FA and SPR

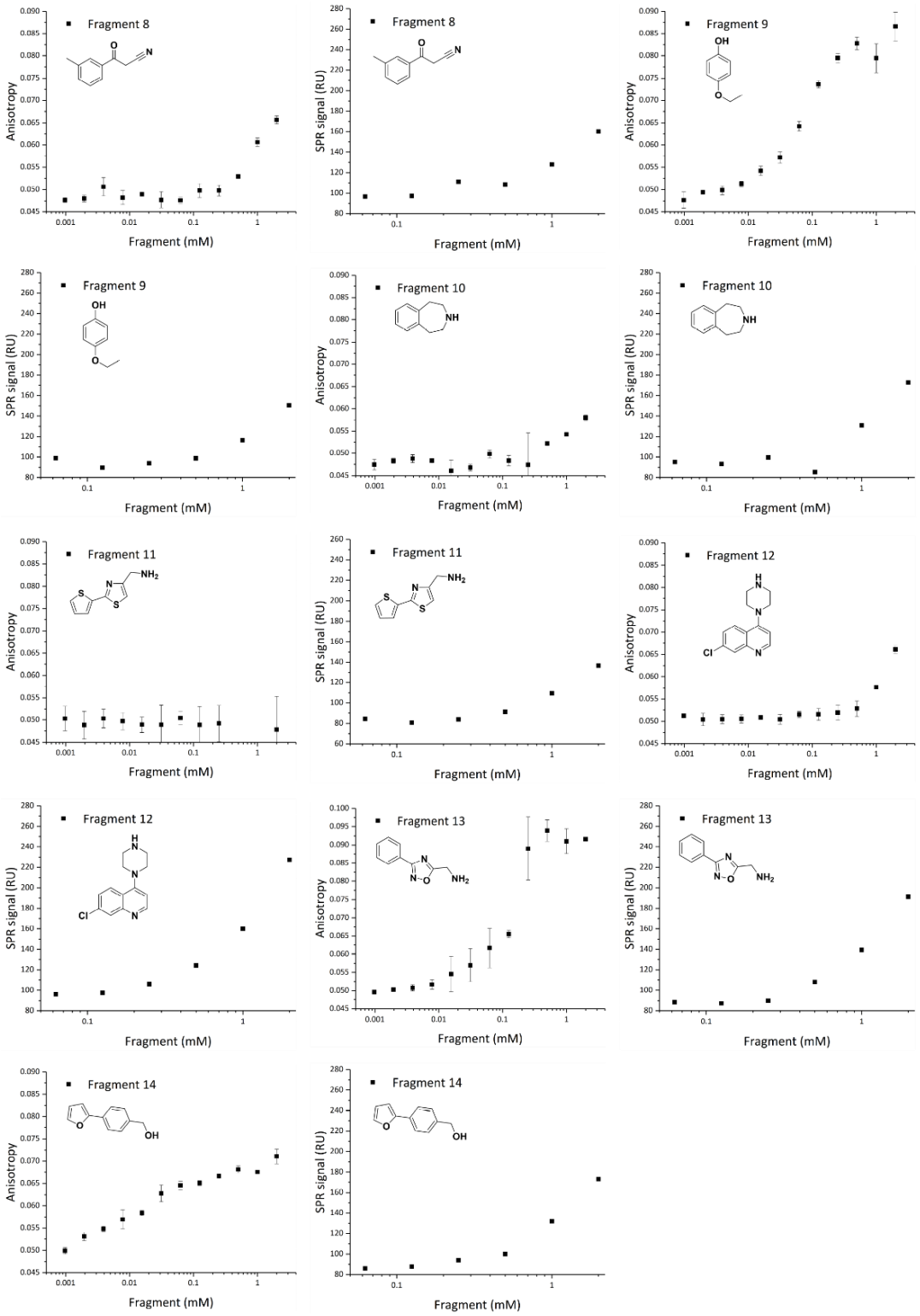

Figure A.5.2 Maybridge fragment stabilizers, confirmation of hits by FA and SPR

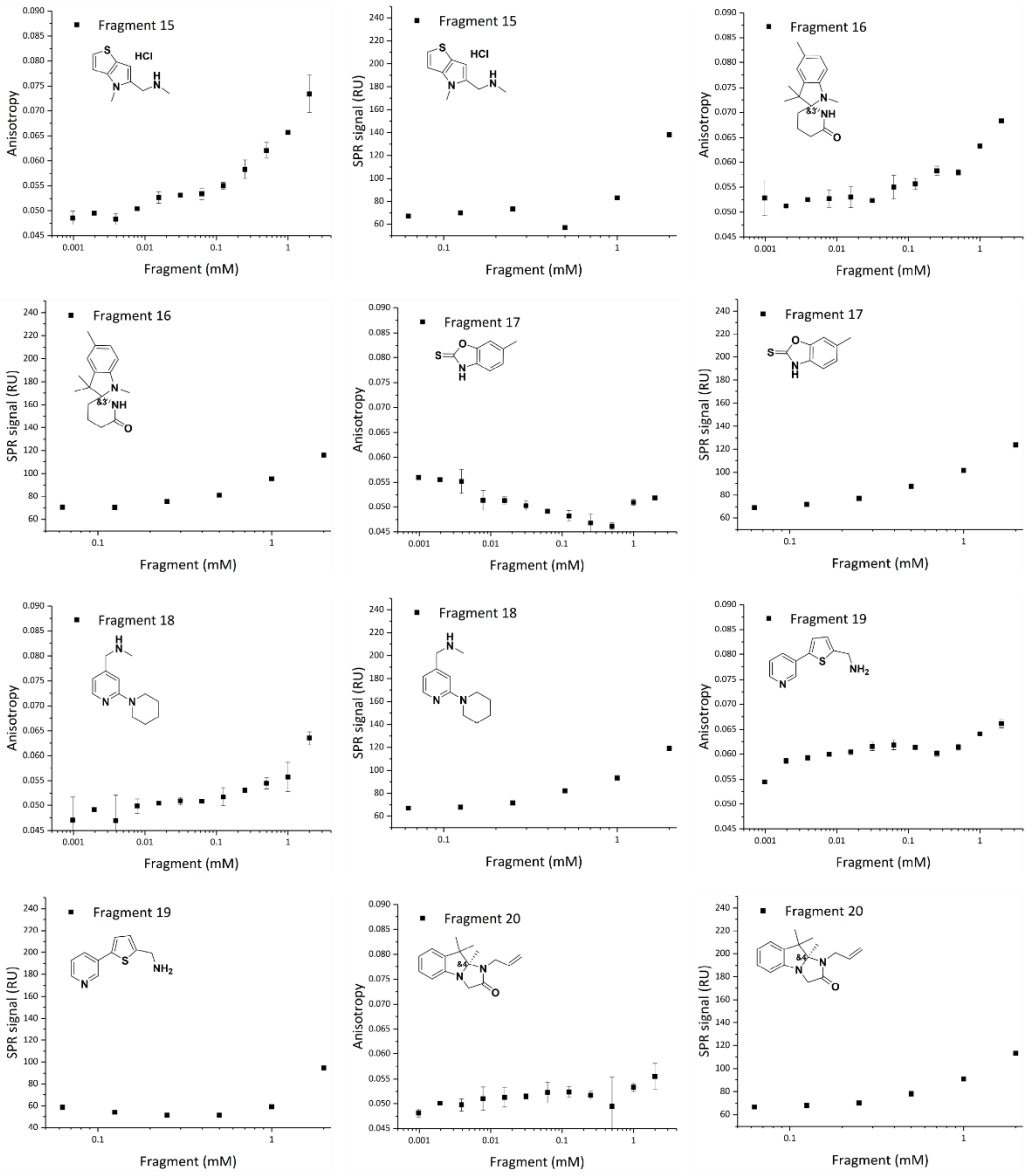

Figure A.5.2 Maybridge fragment stabilizers, confirmation of hits by FA and SPR

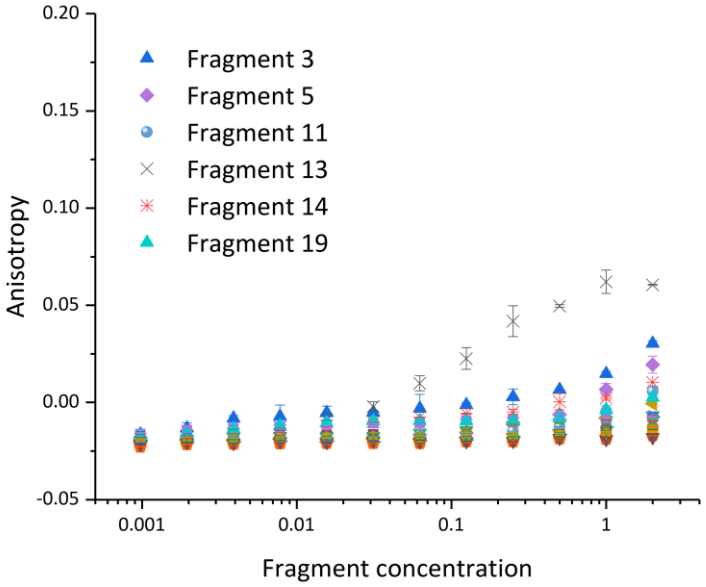

Figure A.5.3 Maybridge fragment stabilizers, control titrations. Fragments were titrated against constant concentration of peptide (2.5 mM fragments, 50 nM tracer). A rise in anisotropy signal suggest compounds interfering with the fluorescently labelled probe. Fragments 3, 5, 13 and 14 were disregarded as false positives.

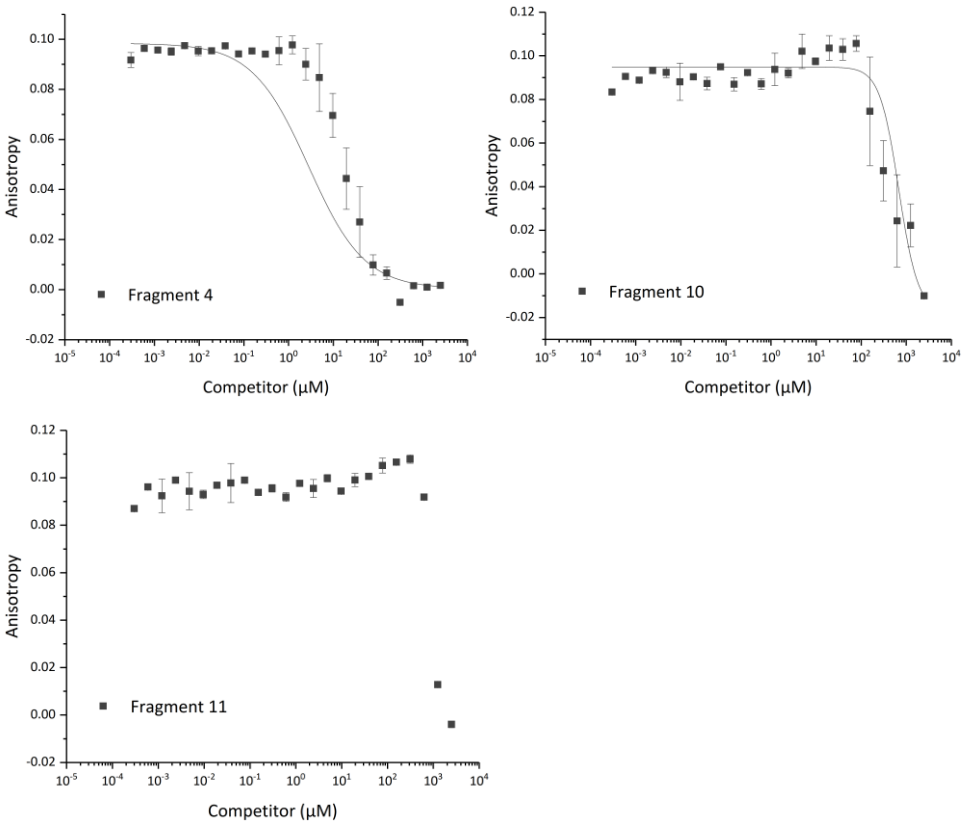

Figure A.5.4 Competition assay for Maybridge fragments identified as inhibitors, where no accurate fir was obtained: 4, 10, 11. Fragments 1 and 2 didn't behave in the assay. 2.5 mM fragments were titrated against a constant concentration of protein and peptide, as used in the a single-point screen (0.2 μM 14-3-3η, 50 nM *h*DMX-367-FAM, in HBS buffer: 10 mM HEPES, 150 mM NaCl, 0.1% Tween 20, pH 7.4).

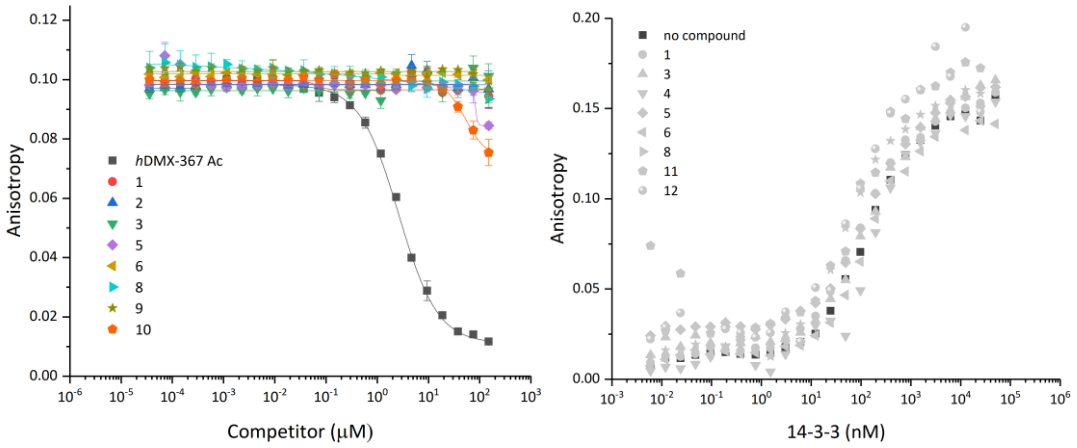

Figure A.5.5 PPI library compounds identified from a single-point screen, tested in a competition assay (150 μM compound or *h*DMX-367-Ac peptide, 0.2 μM 14-3-3η, 50 nM *h*DMX-367-FAM peptide) and a dose-response assay (500 μM compound, 50 μM 14-3-3η, 50 nM *h*DMX-367-FAM peptide).

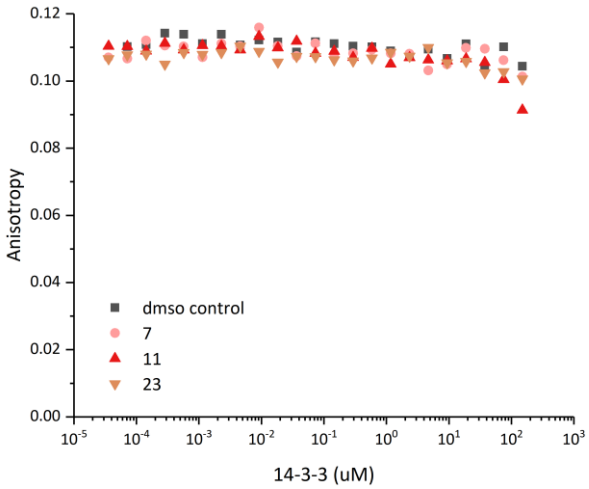

Figure A.5.6 A competition assay of inhibitors from Botta's library (150 μM compound or *h*DMX-367-Ac peptide, 0.2 μM 14-3-3η, 50 nM *h*DMX-367-FAM peptide).

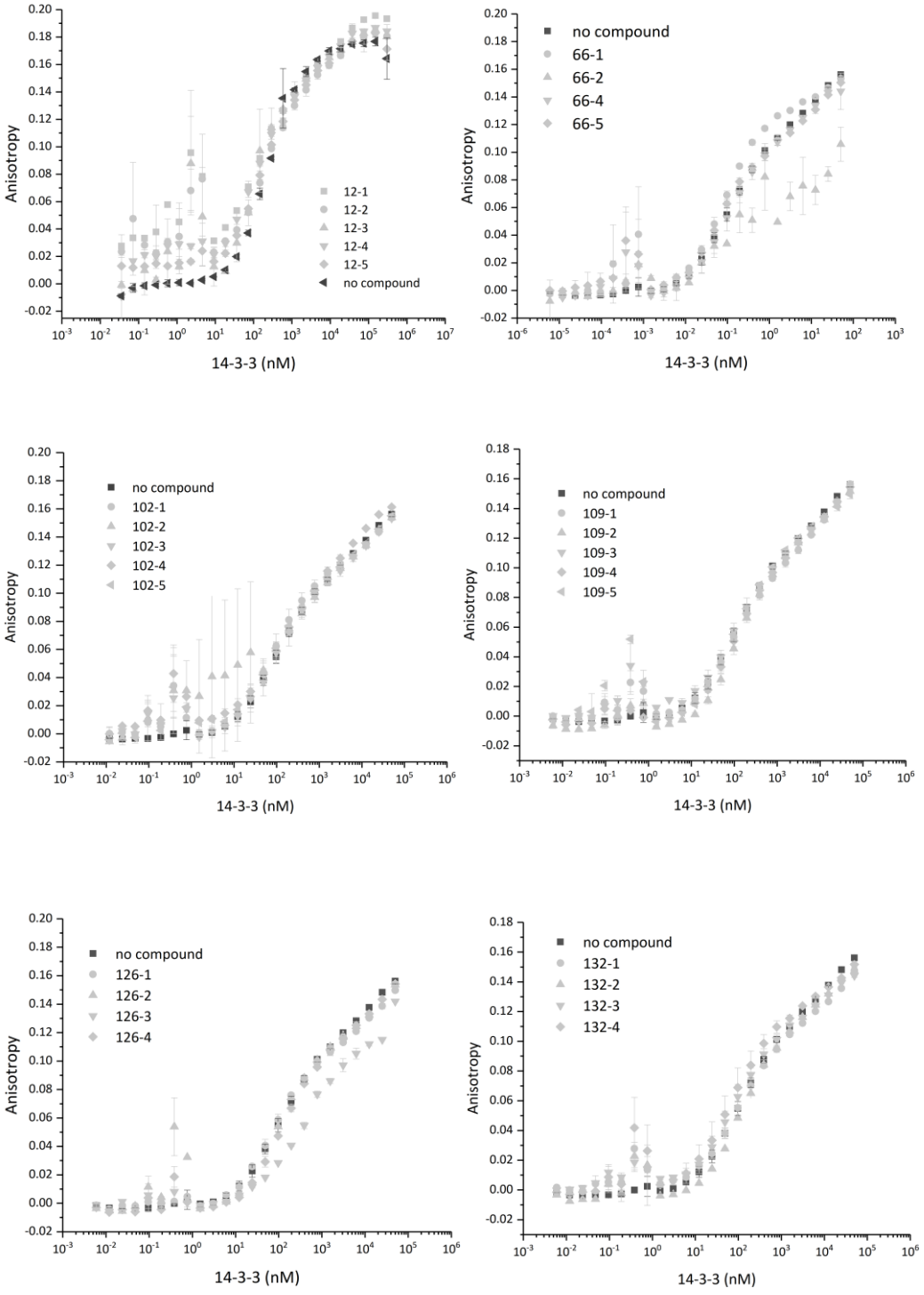

Figure A.5.7 Taros fragments were tested in a direct titration. 14-3-3η protein (200 μM for fragments 12, 50 μM for other fragments) was titrated against the constant concentration of fragments (2.5 mM) and tracer (50 nM *h*DMX-367).

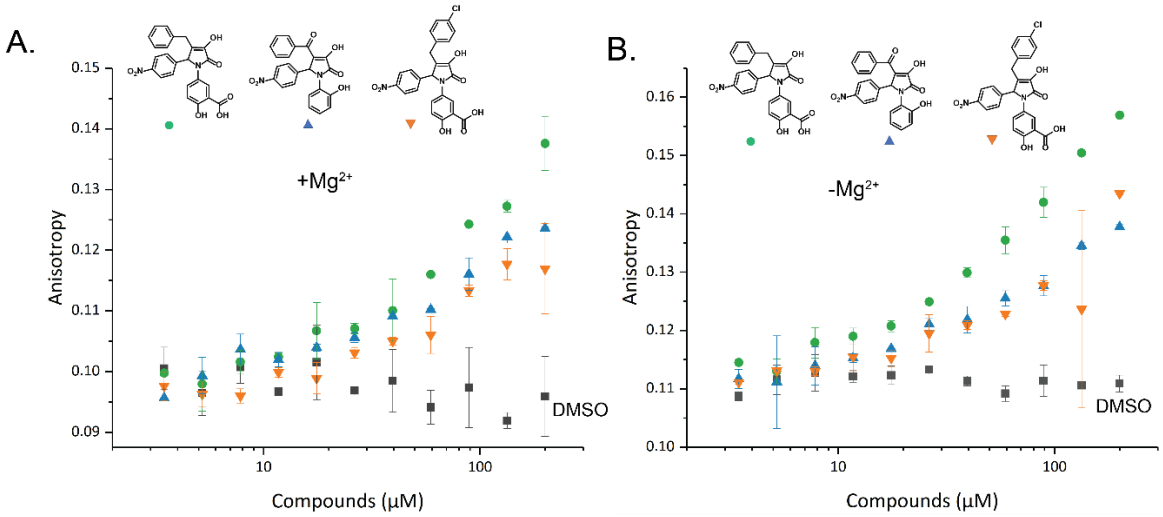

Figure A.5.8 Screening of initial hit compounds in HBS buffer with (panel A) and without (panel B) 10 mM $MgCl_2$. Titration of 200 µM compound (2/3 dilutions) with 200 nM of 14-3-3η and 50 nM of tracer (*h*DMX-FAM).

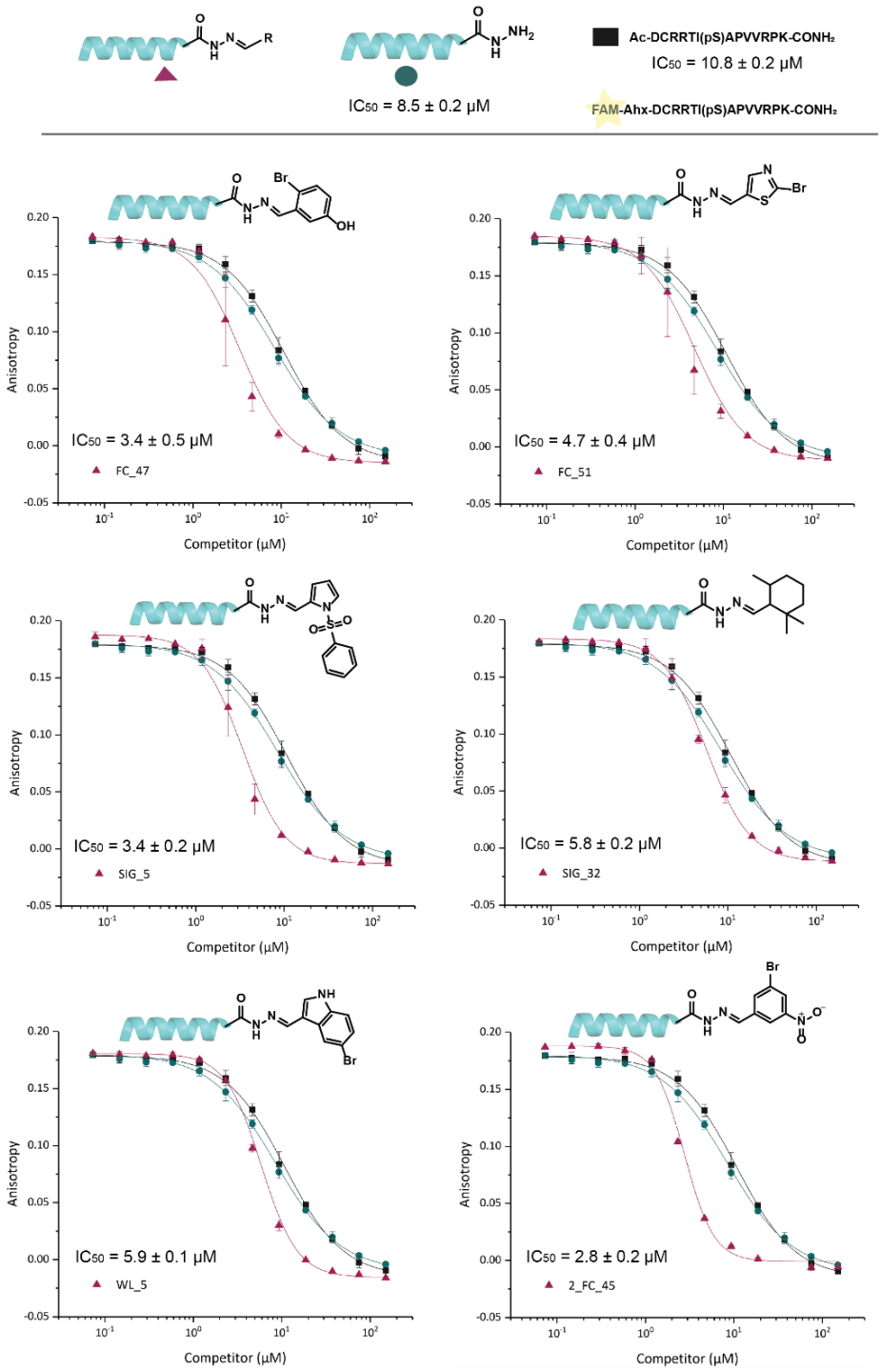

Figure A.5.9 Screening results for PVVG-peptide

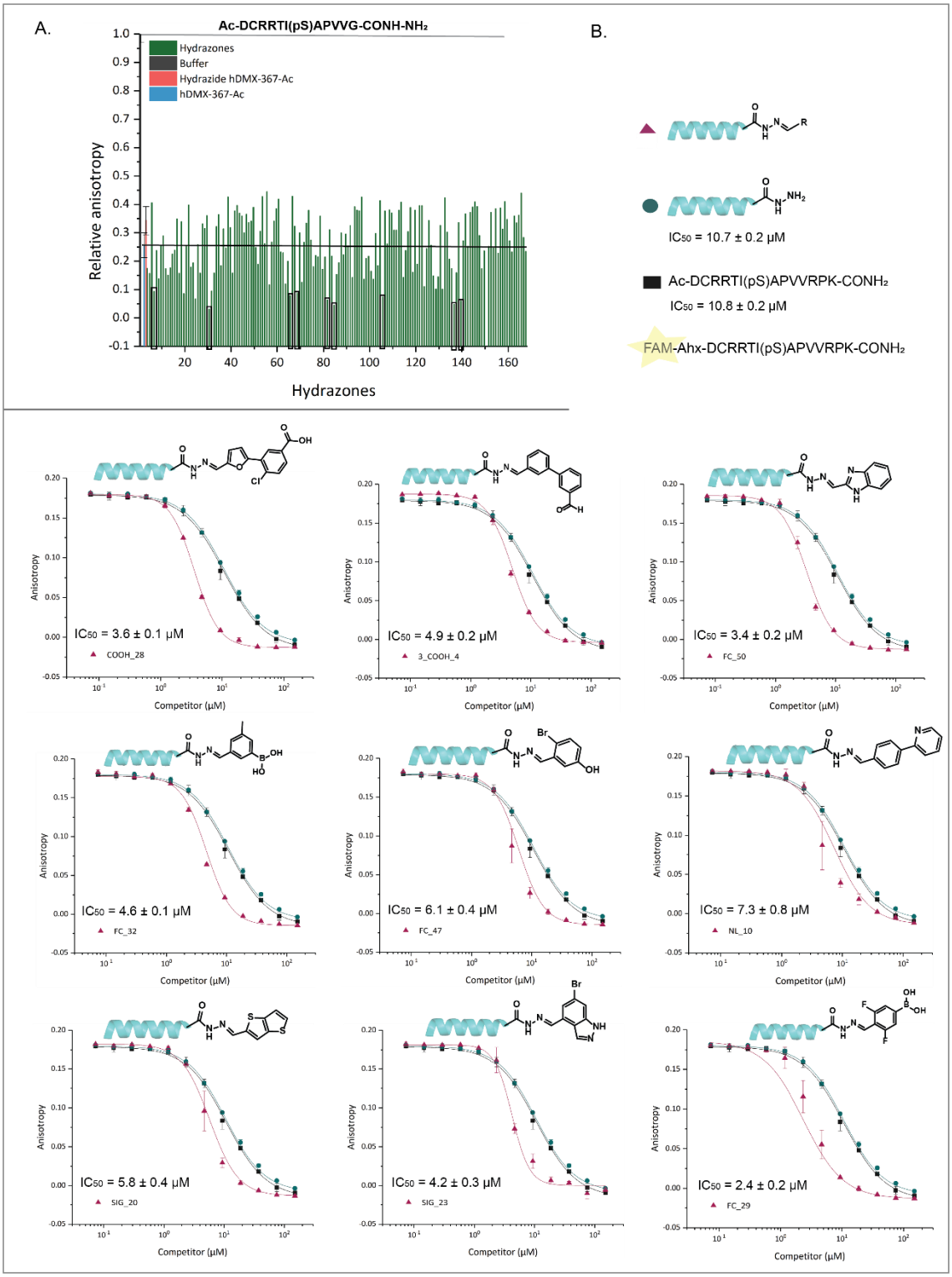

Figure A.5.10 Competition assay for hydrazide hits in comparison to a PVG-peptide